DAMAGE LOCALIZATION IN DATA-DRIVEN VIBRATION-BASED STRUCTURAL HEALTH MONITORING USING LINEAR QUADRATIC ESTIMATION THEORY

Von der Fakultät für Bauingenieurwesen und Geodäsie der Gottfried Wilhelm Leibniz Universität Hannover zur Erlangung des Grades

DOKTOR-INGENIEUR (DR.-ING.)

genehmigte Dissertation von

STEFAN WERNITZ, M.SC.

2022

Referent: Prof. Dr.-Ing. habil. Raimund Rolfes
Korreferentin: Prof. Dr. Eleni Chatzi, ETH Zürich

Tag der Promotion: 11.07.2022

ABSTRACT

Vibration-based Structural Health Monitoring (SHM) is classically approached from two different directions; both involve the acquisition and processing of vibration signals. The first and most popular strategy, which is also followed in the present thesis, relies entirely on the measurements. In contrast, the second approach employs physical models such as finite element (FE) models that are designed based on mechanical principles. In times in which the real-time processing of digital twins for engineering structures becomes more and more realistic, model-based approaches for vibration-based SHM receive increasing attention. Data-driven strategies are still primarily used in vibration-based SHM, and they will remain appealing in situations where precise physical modeling appears cumbersome. Hence, the need for efficient, robust, and reliable data-driven techniques concerning all stages and hurdles of SHM that can prove themselves in practice will never vanish. In this regard, after over 25 years of research, the number of real-life validation studies is still surprisingly low.

As for all SHM strategies, the difficulty concerning damage analysis increases with higher levels of realization. Beginning with the goal of detecting damage, SHM finally seeks to predict the remaining lifetime of a structure. The intermediate steps comprise the localization, classification, and assessment of damage. Without the existence of adequately calibrated physics-based models, the successful implementation of methods tackling the objectives beyond damage localization in an unsupervised data-driven scheme is questionable. The term 'unsupervised' refers to the fact that knowledge about the manifestation of damage is not available. Especially in civil engineering, this situation pertains in general and is considered in the present thesis.

In data-driven SHM, where the area of structural alterations is narrowed down to adjacent sensors, damage localization suffers from the coarse spatial resolution of parsimonious data acquisition systems. Classical modal approaches that hold potential for damage localization require a dense sensor network or significant damage. Originating from the field of fault detection and isolation, estimator- and filter-based methods have proven to be applicable for damage identification of mechanical and civil engineering structures. Notably, they feature an enormous sensitivity towards structural changes when properly designed. Although it remains advantageous for the sake of precise damage localization, these tools such as Kalman or $\mathcal{H}_\infty$ filters do not exhibit the inherent demand for a dense sensor network. Consequently, they promise to be viable techniques for the application in vibration-based SHM.

A central challenge of this discipline is the discrimination between the natural variability of the structure's dynamics and the one caused by damage. The former results from varying environmental and operational conditions (EOCs). Especially highly sensitive methods for damage identification are affected by these natural changes, and thus, rely on an efficient data normalization strategy, which can prove itself in practice.

In light of these challenges, this thesis provides a real-life validation for the application of quadratic estimators in data-driven vibration-based SHM. To this end, an elaborate technique

for estimator-based damage localization is adapted and included in an SHM framework comprising the necessary steps of data normalization and statistical testing. The damage analysis methodology was originally designed for $\mathcal{H}_\infty$ filters, which seem well-suited for use in SHM, as they do not assume specific properties of the excitation acting on the structure nor of the involved disturbances. However, previous studies have shown that, in some cases, the filter performance required to achieve high levels of sensitivity towards localized damage cannot be obtained. This issue can be circumvented by employing well-tuned Kalman filters. Therefore, a novel approach for noise covariance estimation is established at first. The associated estimation scheme constitutes a parametric extension of the popular autocovariance least-squares (ALS) technique. The effectiveness of this estimation technique in the context of Kalman filter-based damage localization is studied first using simulations and laboratory experiments.

The second part is dedicated to the problem of handling EOCs. This body of work proposes an identification scheme for linear parameter-varying systems based on the interpolation of linear time-invariant systems for different operating points. A simulation study demonstrates the applicability for the purpose of data normalization.

Finally, real-life validation of the proposed methods for SHM is conducted. Therefore, a steel lattice mast located outdoors functions as the test object. It is naturally affected by ambient sources of excitation, variability, and uncertainty. The mast, explicitly designed for this validation purpose, is equipped with reversible damage mechanisms that may be activated or removed to reduce the stiffness at multiple locations of the structure. The investigations conducted in this part of the thesis demonstrate proper damage detection of all considered damages as well as localization for the highest degree of severity. These promising results suggest the applicability of the presented methods for Kalman filter tuning, damage localization, and data-normalization in the context of vibration-based SHM.

KEYWORDS: Structural Health Monitoring, vibration-based, data-driven, damage localization, linear quadratic estimation, real-life validation

ZUSAMMENFASSUNG

Die schwingungsbasierte Zustandsüberwachung von Bauwerken (engl.: SHM) wird klassischerweise auf zwei Arten betrieben. Beide Strömungen beinhalten die Erfassung und Verarbeitung von Schwingungssignalen. Die erste und am weitesten verbreitete Strategie, die auch in der vorliegenden Arbeit verfolgt wird, stützt sich vollständig auf Messungen. Im Gegensatz dazu werden bei der modellbasierten Zustandsüberwachung physikalische Modelle wie z. B. FE-Modelle eingesetzt, die auf der Grundlage mechanischer Prinzipien basieren. In Zeiten, in denen die Echtzeitverarbeitung digitaler Zwillinge für Ingenieurbauwerke immer realistischer wird, rücken modellbasierte Ansätze für das schwingungsbasierte SHM zunehmend in den Vordergrund. Nichtsdestotrotz werden nach wie vor vorwiegend datengesteuerte Strategien eingesetzt. Weiterhin ist davon auszugehen, dass diese Methoden auch in Zukunft in Situationen Verwendung finden werden, in denen eine präzise physikalische Modellierung mühsam erscheint. Somit bleibt der Bedarf an effizienten, robusten, zuverlässigen und praxistauglichen datengetriebenen Techniken für alle Phasen und Herausforderungen der Zustandsüberwachung bestehen. Diesbezüglich ist die Zahl der In-situ-Validierungsstudien in der Praxis nach über 25 Jahren Forschung immer noch erstaunlich gering.

Bei allen SHM-Strategien steigt die Herausforderung bezüglich der Schadensanalyse mit zunehmendem Realisierungsgrad. Ausgehend von dem Ziel, Schäden zu erkennen, zielt die Zustandsüberwachung schließlich darauf ab, die verbleibende Lebensdauer einer Struktur vorherzusagen. Die Zwischenschritte umfassen die Lokalisierung, Klassifizierung und Bewertung von Schäden. Ohne das Vorhandensein adäquat kalibrierter physikalischer Modelle ist die erfolgreiche Implementierung von Methoden, die über die Schadenslokalisation hinausgehen, in einem unüberwachten (engl.: unsupervised) datengesteuerten SHM-Ansatz fraglich. Der Begriff ''unüberwacht" bezieht sich auf die Tatsache, dass kein Wissen über die Auswirkung von Schäden vorhanden ist. Im Allgemeinen ist diese Situation im Bauwesen gegeben und wird in der vorliegenden Arbeit berücksichtigt.

Beim datengetriebenen SHM lassen sich Schädigungsorte lediglich auf naheliegende Sensoren eingrenzen. Demzufolge leidet die Schadenslokalisation unter der groben räumlichen Auflösung sparsamer Datenerfassungssysteme. Klassische modale Ansätze, die für die Schadenslokalisation geeignet sind, erfordern ein dichtes Sensornetz oder das Auftreten erheblichen Schäden. Die aus dem Bereich der Fehlererkennung und -isolierung (engl.: FDI) stammenden zustandsschätzer- und filterbasierten Methoden haben sich in der Vergangenheit für die Schadensidentifikation von mechanischen Strukturen bewährt. Sie zeichnen sich, wenn richtig entworfen, insbesondere durch eine hohe Sensibilität gegenüber strukturellen Veränderungen aus. Obwohl diese Werkzeuge wie Kalman- oder $\mathcal{H}_\infty$-Filter für eine präzise Schadenslokalisation vorteilhaft sind, erfordern sie nicht notwendigerweise ein dichtes Sensornetz. Folglich stellen diese Techniken eine vielversprechende Option für die Anwendung im schwingungsbasierten SHM dar.

Eine zentrale Herausforderung dieser Disziplin ist die Unterscheidung zwischen der natürlichen Variabilität der Strukturdynamik und jener, die durch Schäden verursacht wird. Erstere resultiert aus variierenden Umwelt- und Betriebsbedingungen (engl.: EOCs). Gerade hochempfindliche Methoden zur Schadenserkennung werden durch diese natürlichen Veränderungen beeinflusst und sind daher auf eine effiziente Strategie zur Datennormalisierung angewiesen, die sich auch in der Praxis bewährt.

Vor dem Hintergrund dieser Herausforderungen bietet diese Arbeit eine praxisnahe Validierung für die Verwendung linear quadratischer Schätzer in der datengetriebenen schwingungsbasierten Zustandsüberwachung von Bauwerken. Zu diesem Zweck wird ein Verfahren zur schätzerbasierten Schadenslokalisation angepasst und in ein SHM-Konzept integriert, das die notwendigen Schritte der Datennormalisierung und statistischer Tests umfasst. Die adaptierte Schadensanalysemethode wurde ursprünglich für $\mathcal{H}_\infty$-Filter entwickelt, die für den Einsatz im SHM als gut geeignet erscheinen, da sie keine spezifischen Eigenschaften der auf die Struktur wirkenden Erregung oder der beteiligten Störungen voraussetzen. Frühere Studien haben jedoch gezeigt, dass in einigen Fällen die für eine hohe Empfindlichkeit gegenüber lokalisierten Schäden erforderliche Filterperformanz nicht erreicht werden kann. Dieses Problem kann durch den Einsatz von gut abgestimmten Kalman-Filtern umgangen werden. Daher wird zunächst ein neuartiger Ansatz für die Schätzung der Rauschkovarianz-Matrizen entwickelt. Das zugehörige Schätzverfahren stellt eine parametrische Erweiterung der bekannten Autocovariance-Least-Squares-Technik (ALS) dar. Die Wirksamkeit dieses Schätzverfahrens im Zusammenhang mit der Kalman-Filter-basierten Schadenslokalisation wird zunächst anhand von Simulationen und Laborexperimenten untersucht.

Der zweite Teil widmet sich dem Problem des Umgangs mit EOCs. In diesem Teil der Arbeit wird ein Identifikationsschema für lineare parametervariante Systeme vorgeschlagen, das auf der Interpolation linearer zeitinvarianter Systeme für verschiedene Betriebspunkte beruht. Eine Simulationsstudie demonstriert die Anwendbarkeit für den Zweck der Datennormalisierung. Schließlich werden die vorgeschlagenen Methoden für die schwingungsbasierte und datengetriebene Zustandsüberwachung unter realen Bedingungen validiert. Als Testobjekt dient ein im Freien errichteter Stahlgittermast. Dieser wird auf natürliche Weise erregt und unterliegt gleichermaßen natürlicher Variabilität und Unsicherheit der Umgebungsbedingungen. Der ausdrücklich für diesen Validierungszweck konzipierte Mast ist mit reversiblen Schädigungsmechanismen ausgestattet, die aktiviert werden können, um die Steifigkeit an mehreren Stellen der Struktur zu verringern. Die in diesem Teil der Arbeit durchgeführten Untersuchungen zeigen eine korrekte Schadenslokalisation an allen betrachteten Positionen für den höchsten Schweregrad. Diese vielversprechenden Ergebnisse implizieren die Anwendbarkeit der erarbeiteten Methoden zum Kalman-Filter-Entwurf sowie zur Schadenslokalisation und Datennormalisierung im Kontext der schwingungsbasierten SHM.

SCHLAGWORTE: Bauwerksüberwachung, schwingunsbasiert, datengetrieben, Schadenslokalisation, linear quadratische Schätzung, In-situ-Validierung

Alles Wissen und alles Vermehren unseres Wissens endet nicht mit einem Schlußpunkt, sondern mit einem Fragezeichen.

— Herrmann Hesse

ACKNOWLEDGEMENTS

This thesis was composed during my time at the Institute of Structural Analysis (ISD) at the Leibniz University Hannover. For the privilege to pursue and complete this endeavor, I would like to thank Prof. Raimund Rolfes, whom I am particularly grateful for supporting and guiding me throughout my time at his institute. This appreciation must be further passed to Dr. Tanja Grießmann. She spared no effort in providing a comfortable and friendly working environment. Moreover, working alongside her in joint research projects was always inspiring. Special thanks are given to Prof. Armin Lenzen and Dr. Max Vollmering from the University of Applied Sciences Leipzig. They supervised my master thesis with dedication and encouraged me to pursue a doctorate in the first place.

During my PhD, I spent about three months at the Institute of Structural Engineering (IBK) at ETH Zurich in the research group of Prof. Eleni Chatzi. She accepted my request for a research stay without hesitation and welcomed me with open arms. The atmosphere and time in her group inspired me and increased my motivation for research tremendously. I could not have asked for a better scientific environment and place for my research stay. In particular, I would like to thank Prof. Chatzi for her trust and encouragement to believe in my ability as a researcher and her support and guidance posterior to my research stay. My gratitude is also expressed to Dr. Vasileios Ntertimanis, Dr. Konstantinos Tatsis, and Dr. Imad Abdallah for their support and the fruitful discussions during my time at IBK.

It is easy to say that my scientific progress would not have been the same without my colleagues' assistance, discussions, and companionship at ISD. In particular, I would like to thank Dorian Pache, Benedikt Hofmeister, Clemens Jonscher, and Nikolai Penner for sharing their expertise with me. In this regard, a special place is reserved for Michael Treiber, Christian Claußen, Stefan Warnken, and Jan Heinemeyer for their support and help in numerous technical and IT-related matters.

Without a doubt, the path to this dissertation would have been impossible to take without the love, dedication, and support of my parents, brother, and friends! For that, I thank you with all my heart. Filing a list of names of the people involved is a challenge I am not willing to take. Though, one name must be mentioned in the context of this work. I want to thank my dear friend Thomas Seidel who shared my student days from the early beginning and without whom the outcome of this period, which paved the way for my PhD, would have been less successful.

CONTENTS

LIST OF TABLES

NOMENCLATURE

ABBREVIATIONS

AANN	autoassociative neural network
AIC	Akaike's information criterion
ALS	autocovariance least-squares
ANN	aritifical neural network
AR	autoregressive
BAYOMA	Bayesian Operational Modal Analysis
BIBO	bounded-input, bounded-output
CCA	canonical correlation analysis
CDF	cumulative distribution function
DARE	discrete-time algebraic Riccati equation
DFT	discrete Fourier transform
DLV	damage locating vector
DOF	degree of freedom
DTFT	discrete-time Fourier transform
EOC	environmental and operational condition
EOM	equation of motion
EOV	environmental and operational variability
FDD	Frequency Domain Decomposition
FDI	fault detection and isolation
FE	finite element
FFT	fast Fourier transform
FIR	finite impulse response
FRF	frequency response function
GCV	generalized cross-validation
IIR	infinite impulse response
IRF	impulse response function
LLFT	lower linear fractional transform
LMI	linear matrix inequality
LPV	linear parameter-varying
LSCF	Least-Squares Complex Frequency-Domain
LTI	linear time-invariant

LTV	linear time-variant
MA	moving average
MAC	Modal Assurance Criterion
MDOF	multiple degree-of-freedom
MIMO	multiple input/multiple output
MSE	mean squared error
OMA	Operational Modal Analysis
PALS	parametric autocovariance least-squares
PCA	principal component analysis
PCE	Polynomial Chaos Expansion
PDF	probability density function
pLSCF	Poly-Reference Least-Squares Complex Frequency-Domain
PSD	power spectral density
RMS	root mean square
ROC	receiver operator characteristic
SCADA	Supervisory Control and Data Acquisition
SDOF	single degree-of-freedom
SDP	semidefinite programming
SHM	Structural Health Monitoring
SP2E	state-projection estimation error
SSI	Stochastic Subspace Identification
SSI-COV	covariance-driven SSI
SSI-DAT	data-driven SSI
SVD	singular value decomposition
SVM	Support Vector Machine
VAR	vector autoregressive
ZOH	zero-order hold

SCALARS AND SCALAR VALUED FUNCTIONS

f_s	sampling frequency in Hz
e	Euler's number
f_0	undamped natural frequency in Hz
f_D	damped natural frequency in Hz
j	imaginary number $\sqrt{-1}$
$m_{a,i}$	ith statistical moment of stochastic process a
$m'_{a,i}$	ith central statistical moment of stochastic process a

n	number of states, model order
n_D	number of degrees of freedom
p	number of inputs
$P(a)$	cumulative distribution function of random variable a
$p(a)$	probability density function of random variable a
$P_e(a)$	empirical cumulative distribution function of random variable a
$P_{d\mathcal{V}}$	power feature by SP2E
q	number of outputs
s	Laplace variable
t	time
t_s	settling time of impulse response
$r_{d\mathcal{V}}([i_1, i_2])$	variance feature by SP2E
z	complex variable of z-transform
α	real part of Laplace variable s or significance level
δ	decay constant or Kronecker delta
Δt	sampling period
ϑ	$(1-\alpha)$ quantile
θ	substitute variable used for z-Transform ($\theta = \omega\Delta t$)
ζ	modal damping ratio
λ	continuous-time eigenvalue/pole or regularization parameter
μ	discrete-time eigenvalue/pole
σ	singular value
σ_a	standard deviation of stochastic process a
σ_a^2	autocovariance of stochastic process a
τ	time shift/offset
ω	circular frequency in radian
ω_0	undamped natural frequency in radian
ω_D	damped natural frequency in radian

VECTORS

e	estimation error or innovations
f	forces
u	inputs of state-space models or systems
x	states
y	displacements, outputs of state-space model or systems
$\dot{y}$	velocities

$\ddot{y}$	accelerations
θ	scheduling variables of LPV system
μ_a	mean values of stochastic process a
ϕ	mode shape
ψ	eigenvector of system matrix A

MATRICES

A	system matrix of discrete-time state-space model
A_c	system matrix of continuous-time state-space model
B	input matrix of discrete-time state-space model
B_c	input matrix of continuous-time state-space model
C	output matrix of discrete-time state-space model
C_c	output matrix of continuous-time state-space model
$C_{c,a}$	output matrix of continuous-time state-space model leading to accelerations
$C_{c,d}$	output matrix of continuous-time state-space model leading to displacements
$C_{c,v}$	output matrix of continuous-time state-space model leading to velocities
D	feed-through matrix of discrete-time state-space model
D_c	feed-through matrix of continuous-time state-space model
$D_{c,a}$	feed-through matrix of continuous-time state-space model leading to accelerations
$D_{c,d}$	feed-through matrix of continuous-time state-space model leading to displacements
$D_{c,v}$	feed-through matrix of continuous-time state-space model leading to velocities
D_p	proportional damping matrix
H	block Hankel matrix of outputs or output covariances
K	stiffness matrix
K_e	gain matrix for estimation (subscript p for prediction, f for filtering, s for smoothing)
M	mass matrix
N	covariance matrix of future states and current outputs
P_e	state-estimation error covariance of estimation step (subscript p for prediction, f for filtering, s for smoothing)
P_o	projection matrix for SSI
Q	covariance matrix of process noise

R_{ab}	cross-covariance matrix of stochastic processes a and b
R_v	covariance matrix of measurement noise
S	covariance matrix of process and measurement noise
S_1	diagonal matrix of nonzero or selected singular values
$\bar{S}$	diagonal matrix of singular values
T	transformation matrix for similarity transformation
U_1	left-hand singular vectors
V_1	right-hand singular vectors
W_1	left-hand weighting matrix for Stochastic Subspace Identification
W_2	right-hand weighting matrix for Stochastic Subspace Identification
Γ	controllability matrix
Λ	diagonal matrix with discrete-time eigenvalues/poles
Λ_c	diagonal matrix with continuous-time eigenvalues/poles
O	observability matrix
Σ_x	state covariance matrix
Φ	matrix containing eigenvectors on columns
Φ_{ff}	covariance matrix of future outputs
Φ_{pp}	covariance matrix of past outputs
Ψ	modal matrix

OPERATORS

$(\cdot)^*$	complex conjugate of a number or conjugate transpose of a vector or matrix
$\bigoplus$	direct sum
$\|\cdot\|$	Euclidean norm or norm of vector or matrix in general
$\|\cdot\|_{\mathcal{H}_p}$	$\mathcal{H}_p$ norm of complex-valued signal
$\langle a, b \rangle$	inner product of a and b
$(\cdot)^{-1}$	inverse
$\otimes$	Kronecker product
$\|\cdot\|_{\ell_p}$	ℓ_p norm of discrete-time signal
$\|\cdot\|_{\mathcal{L}_p}$	$\mathcal{L}_p$ norm of continuous-time signal
$(\cdot)^\dagger$	pseudoinverse
$(\cdot)^{\mathrm{T}}$	transpose of a vector or matrix
$\bar{\sigma}\{\cdot\}$	extract maximum singular value
$\mathrm{E}\{\cdot\}$	expectation

$\mathcal{F}\{\cdot\}$	Fourier transformation
$\mathcal{F}^{-1}\{\cdot\}$	inverse Fourier transformation
$\mathrm{Im}\{\cdot\}$	extracting the imaginary part of a complex number
inf	infimum
$\mathcal{L}\{\cdot\}$	Laplace transformation
$\mathcal{L}^{-1}\{\cdot\}$	inverse Laplace transformation
$\mathrm{Prob}\{\cdot\}$	probability
$\mathrm{rank}\{\cdot\}$	computing the rank of a matrix
$\mathrm{Re}\{\cdot\}$	extracting the real part of a complex number
sup	supremum
$\mathrm{tr}\{\cdot\}$	trace operator
$\mathrm{var}\{\cdot\}$	variance operator
$\mathrm{vec}\{\cdot\}$	vectorization operator
$\mathrm{vech}\{\cdot\}$	half-vectorization operator
$\mathcal{Z}\{\cdot\}$	z-transformation
$\mathcal{Z}^{-1}\{\cdot\}$	inverse z-transformation

FIELDS AND SPACES

$\mathbb{C}$	field of complex numbers
$\mathbb{D}$	open unit disk in complex plane
$\mathcal{H}_p$	Hardy space of functions and sequences
ℓ_p	Lebesgue space of sequences
$\mathcal{L}_p$	Lebesgue space of functions
$\mathbb{N}$	field of natural numbers
$\mathbb{N}_0^+$	field of nonnegative natural numbers
$\mathbb{N}^+$	field of nonnegative and nonzero natural numbers
$\mathbb{R}$	field of real numbers
$\mathbb{R}_0^+$	field of nonnegative real numbers

1 INTRODUCTION

In vibration-based Structural Health Monitoring (SHM), mechanical systems are continuously observed by acquiring vibration data, e.g., strains or accelerations, at several discrete locations. The goal is to infer the structural integrity by using these measurements and by assessing the structural dynamics of the mechanical system under consideration of varying environmental and operational conditions (EOCs). This objective is approached from two directions, namely by employing calibrated physics-based models, referred to as model-based SHM, or by solely relying on the measured data denoted as data-driven SHM. In civil engineering, where structural excitation is challenging to observe, so-called output-only strategies are particularly relevant. Another limitation is posed by the lack of knowledge regarding the manifestation of potential damage, generally forcing engineers to consider unsupervised approaches for damage identification. This thesis focuses on output-only and unsupervised techniques for data-driven vibration-based SHM. In over 25 years of extensive research in this field, an uncountable number of simulation studies and experiments have been conducted, enabling and promoting the development of elaborate methods to tackle all kinds of problems associated with vibration-based SHM. However, only a few cases exist that can be seen as a real-life benchmark object, which requires the existence of damage and the presence of natural sources of excitation, variability, and uncertainty. For the present work, a long-term measurement campaign of a lattice mast located outdoors has been conducted to enable the real-life validation of a vibration-based damage localization approach using linear quadratic estimation theory. The validation constitutes the central objective of this thesis. The outdoor experiment is well suited for this endeavor because of its excellent data quality and the equipment with reversible damage mechanisms at multiple positions. To highlight the difficulties and hurdles of output-only and unsupervised data-driven vibration-based SHM, in the following, the state of the art is reviewed with particular focus on the damage localization problem. Lastly, the objectives of this thesis are defined, and the outline is formulated.

1.1 DATA-DRIVEN VIBRATION-BASED SHM

Data-driven vibration-based SHM is particularly appealing in situations where precise physical modeling appears cumbersome. It is carried out traditionally within the *statistical pattern recognition paradigm* introduced at the end of the last century [72, 73]. The core of this framework is the acquisition and statistical assessment of so-called damage-sensitive features. Those quantities can be seen as informative proxies of the structure's dynamic behavior analyzed to enable SHM. In general, the problem of SHM can be regarded by defining four main subjects: (i) capturing the short-term dynamics, (ii) capturing the long-term dynamics, (iii) damage analysis, and (iv) uncertainty. This circumstance is summarized in Fig. 1.1. It stands in no contradiction to the established statistical pattern recognition paradigm; in fact, the described segmentation is intrinsically picked up by any existing SHM scheme, cf. [70, 94].

Almost all vibrating structures subject to monitoring undergo varying EOCs such as temperature, humidity, wind speed, etc. [17]. These exogenous effects alter the dynamic behavior of

the structures upon which they act. Thus, they need to be taken into account during monitoring to distinguish between natural and damage-induced changes. Importantly, since EOCs might vary on different time scales and the structural state of the monitored system is to be evaluated continuously, one must consider the dynamics of that system over short and long periods (Subject 1 and 2). The quantitative meaning of this has an individual interpretation, enormously depending on the overall dynamics of the mechanical system affected by varying EOCs, which inherently affects the choice of identification and modeling techniques. However, with simple words and without wanting to state general facts, it can be said that the expression *short-term* is used to refer to seconds, minutes, maybe hours, though, when speaking of *long-term*, the author aims to refer to days, months, and years.

The mentioned overall purpose of SHM is to identify damage (Subject 3). This objective subdivides into five steps ranging from the detection of damage to the prognosis of the remaining lifetime [215]. Damage analysis is enabled through knowledge about the monitored system's general and instantaneous structural dynamics and the consideration of varying EOCs. The associated analyses are performed using damage-sensitive features, also called condition parameters or damage indicators, which are indirectly or directly computed or extracted from the measurements. They comprise modal parameters, residuals, etc. Especially in civil engineering, where damage constitutes complex structural alterations, information about its effect on the applied methods is not available or impossible to determine from an economical and practical point of view. Consequently, an unsupervised damage identification scheme is readily used that does not consider any information in this regard.

Similar to other engineering tasks, the observation and evaluation of complex mechanical systems exposed to all kinds of physical phenomena underlie significant uncertainty. This fact led to the statistical pattern recognition paradigm in the first place. It must be born in mind when conducting any of the three subjects explained before, see Fig. 1.1. In some situations, e.g., in system and modal identification, uncertainty is often inherently considered, for instance, when mathematical models are fitted to measurements by minimizing the error of fit. In view of the main objective of damage analysis, especially of damage detection and localization, the problem of uncertainty is faced by using statistical tests to decide on the structure's state.

The following sections examine the mentioned main subjects of SHM separately. The literature review is limited to methods that are not depending on explicitly measured excitation (output-only). This restriction does not extend to the observation of EOCs. Regarding damage identification, solely unsupervised approaches are considered, as explained before. Since the primary motivation of this work constitutes the real-life validation of an approach for data-driven vibration-based SHM, Section 1.1.3 discusses strategies with the potential of localizing damages.

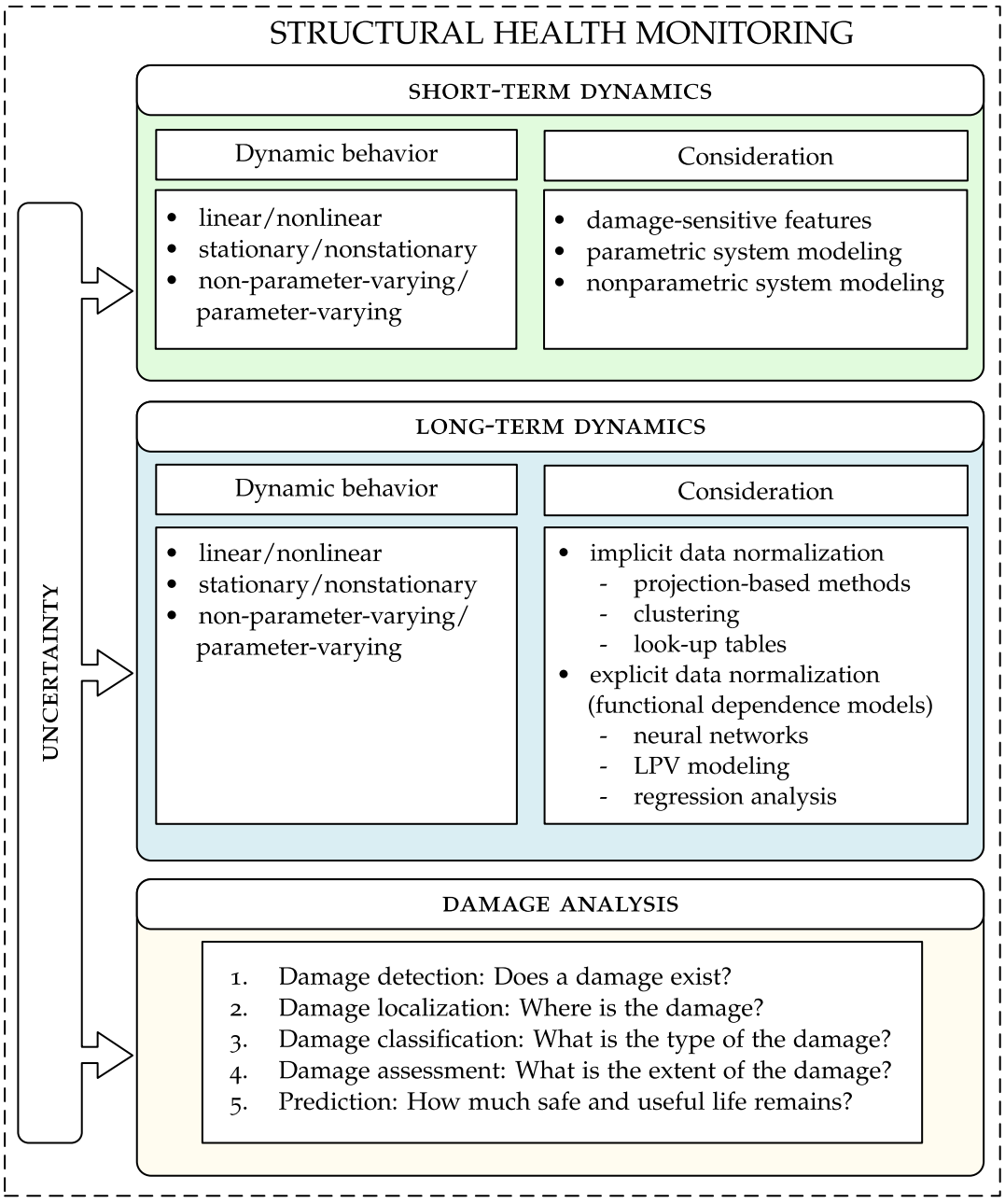

Figure 1.1: Main subjects of SHM.

1.1.1 Capturing short-term dynamics

For a continuous inference of the structural state of monitored mechanical systems based on the structural dynamics, useful information must be gathered regularly. Identifying the dynamics of the observed systems based on snippets of measured vibration data can be seen as producing a snapshot of the current dynamic behavior, which principally enables damage identification. Unfortunately, this picture is hardly interpretable if no information regarding the influence of EOCs is available. Typically, these effects alter the structural behavior naturally, see, e.g., [71]. Therefore, to assess whether the observed system acts normally in terms of its structural dynamics, the usual variation due to exogenous effects must be identified at least to some extent, as will be further discussed in Section 1.1.2.

Short-term dynamics can be captured in two ways. An explicit approach is the repetitive identification of system models based on relatively short measurement intervals. Later, these models can be utilized to identify an overall system representation covering the entire range of environmental and operational variability (EOV) [16, 17]. The second and most common strategy is the implicit approach that strives to extract damage-sensitive features from the measured data, functioning as a proxy of the structure's current dynamic behavior. The list of features applicable for SHM is sheer endless; however, natural frequencies or modal parameters, in general, constitute a classic example. They are determined with the help of system or modal identification techniques.

The present section comprises a summary of parametric and nonparametric methods for system identification, which aim to capture the short-term dynamics explicitly but can also be exploited to derive modal parameters or other quantities representing the current dynamics implicitly. Further, an overview of features extractable from short-term data is presented.

SYSTEM IDENTIFICATION – DEFINITIONS, PROPERTIES, AND CLASSIFICATION

In this thesis, the term system identification is used to denote the data-based realization of functionals representing the time-dependent input-output relationship of a dynamic system. In the context of this section and most parts of this thesis, the latter refers to a mechanical system with time-varying forces on the input side and displacements, velocities, or accelerations on the outputs. Nevertheless, a dynamic system can be generally seen as an operator with specific properties in time and space, representing the transfer between time-varying processes.

System identification techniques can be classified in parametric and nonparametric methods. For the former, parametric mathematical models with certain order (polynomial degree) are fitted to the measured data. Thus, a finite set of coefficients belonging to a particular mathematical structure is determined to represent the associated map from inputs to outputs in the 'best way' possible. Parametric methods feature several advantages such as the compactness of system representation and the improved accuracy, and frequency resolution [74]. Nonparametric approaches, on the other hand, model a system directly based on measurements [163]. Depending on the dynamic behavior of the regarded mechanical system and the level of approximation, the identified models can be linear/nonlinear, time-variant/time-invariant, and parameter-varying/non-parameter-varying, see Fig. 1.1. The term time-variance describes the circumstance that the dynamic properties change with time. In contrast, the expression of

parameter-variance emphasizes the dependence on EOCs such as wind speed, temperature, etc. Thus, time-variance can be seen as a special case of parameter variance, where the so-called scheduling variable, which affects the dynamic properties, is the time. Time-variant and time-invariant systems and models are often denoted as nonstationary and stationary, respectively.

Methods for system identification are further differentiated depending on their degree of physical interpretability. Fully data-driven approaches generally result in so-called *black-box models*, which cannot be directly associated with the physics of the data-generating system (mechanical system). The structure of black-box models is entirely mathematical. They are simply functions computed from or fitted to time or frequency domain data, representing an operator that maps inputs to outputs. Independent of the mathematical nature of black-box models, an indirect physical interpretation in terms of modal properties can often be derived. Contrary to black-box models, *white-box models* are obtained from analytical physical principles. Hence, they are parametric per se. Good examples from the field of structural mechanics are differential equations, which are derived from static and dynamic equilibrium equations, geometric kinematic compatibility equations, and material laws [121]. Equations of motion (EOMs) are determined to describe the dynamic behavior of mechanical systems, depending, e.g., on mass, damping, and stiffness properties. Consequently, the model (EOM) has a direct physical interpretation because of these parameters and their interconnections. In the past years, accelerated through the rise of aritifical neural networks (ANNs), a hybrid model type, namely *gray-box models* received increasing attention. Such models are typically based on simple white-box models designed based on prior physical knowledge of the associated system to be identified. Then they are optimized with the help of data-driven identification techniques [49, 159, 173, 228].

Another way of classifying system identification techniques refers to the type of data used for the identification. Using input and output data is the natural and classic approach to system identification. In civil engineering, or generally in those cases where inputs (excitation data) are difficult to acquire, so-called *output-only strategies* are useful options. Obviously, the input side must be considered to some extent, and thus, the randomness of the inputs, or Gaussianity, in particular, is assumed. Therefore, these methods are readily denoted as *stochastic system identification*. Input-output strategies are often denoted as *deterministic system identification*, see [168]. Output-only identification plays an important role in the realization of linear time-invariant (LTI) systems. Such strategies, linked to the field of Operational Modal Analysis (OMA) are heavily exploited in this thesis, and thus, special attention is paid to summarizing the associated literature.

In the modal analysis community, the term system identification often describes the process of determining modal parameters. This choice of words is somewhat inaccurate since modal analysis does not necessarily imply the identification of system models, e.g., when nonparametric modal identification tools such as the Frequency Domain Decomposition (FDD) are applied, cf. [30]. Further, the construction of dynamic models of mechanical systems based on modal parameters is only feasible in the case of LTI systems when modal scaling factors are known, see [29].

PARAMETRIC AND NONPARAMETRIC SYSTEM IDENTIFICATION

Nonparametric approaches for system identification are generally a good start to get an impression of the complexity of a system's dynamic behavior, as these models impose no particular model structure [158]. The observed systems are modeled as an impulse response function (IRF) in the time domain or frequency response function (FRF) in the frequency domain. The latter and most common approach typically involves the use of H_x estimators depending on the characteristics of the signals used [201]. As mentioned before, all system identification techniques aim to model particular input-output relationships. Nevertheless, some nonparametric system identification techniques belong to the class of output-only methods, that is, the identification without measured excitation. One example constitutes the so-called transmissibilities, see [207]. These models represent the dependence among the output signals, which inherently captures the dynamics of the observed system.

Parametric approaches feature a broad class for system identification resulting in functional dependence models with different structures. Contrary to nonparametric methods, they exhibit a compact and parsimonious representation, and an improved frequency resolution [74]. A popular time-domain identification technique of LTI systems is the *Stochastic Subspace Identification (SSI)*, which was established in the mid-1990s pioneered by the work of van Overschee and de Moor [147, 148]. The application of the SSI helps to identify state-space systems that assume unknown, stationary, white, and Gaussian-distributed excitation [110]. In experimental structural dynamics, the model order must be chosen pragmatically. Therefore, stabilization diagrams are typically applied in the context of SSI, which further enables the discrimination of spurious modes [10].

To receive a polynomial-like representation of the observed system, autoregressive (AR) models might be identified that map the measured data to itself. By that, the dynamics of the output-generating system are inherently captured [27]. If structures are observed with multiple sensors, which is the standard case in SHM, the system is identified as a *multiple input/ multiple output (MIMO)* model. That demands the use of vector autoregressive (VAR) identification techniques. Further, a moving average (MA) part is frequently added to the system representation to model the dynamics in a more parsimonious way [7]. (V)AR/MA models are primarily identified employing a least-squares strategy [74, 122]. Therefore, the model order is determined with the help of information criteria such as Akaike's information criterion (AIC) [3, 186].

For large amounts of data, the application of time-domain techniques can be prohibitively expensive in terms of computational effort. Here, frequency-domain methods might relax this burden. In the presented context, the Least-Squares Complex Frequency-Domain (LSCF) and Poly-Reference Least-Squares Complex Frequency-Domain (pLSCF) method are particularly worth mentioning, which aim to model the FRF of a system as a common-denominator model [163]. The pLSCF method [90], well-known under its commercial name *PolyMAX*, has been celebrated for its computational efficiency and the ability to result in clear stabilization diagrams [153]. Similar to all data-driven system identification techniques, the (p)LSCF estimator was developed for input-output system identification. Though, it was extended to the output-only case by utilizing the positive one-sided power spectral density (PSD) of the measured outputs instead of nonparametric estimates of the FRFs [37].

For completeness, some methods for the identification of linear time-variant (LTV) and linear parameter-varying (LPV) systems shall be briefly reviewed. In the past years, exciting developments regarding the modeling of nonstationary time series (LTV) have been made by applying (V)AR/MA techniques, see [13, 23, 160, 184, 231]. For these kinds of methods, model parameters are generally assumed to follow some sort of structured or unstructured evolution. Hence, the identification is enabled through a functional series expansion and a least-squares scheme. The realization of LPV systems often follows similar strategies, as was shown by Avendaño-Valencia et al. [12, 17].

DAMAGE-SENSITIVE FEATURES

The list of damage-sensitive features employed for SHM is sheer endless. Thus, attempts to provide a complete overview are likely to fail. Before reviewing any of these features, it should be mentioned that the parameters extracted or computed from short-term measurements not necessarily need to function as the features considered for damage analysis. Depending on the strategy of handling EOV, new features might be determined to infer damage eventually. This circumstance is explained in detail in Section 1.1.3. In the following, two standard classes of features are presented that are readily used as a proxy for short-term dynamics. For a more extensive overview, the interested reader is referred to [11, 70].

Modal-based features such as natural frequencies comprise the largest group of damage-sensitive features employed for SHM, as they can be well interpreted from a structural dynamics point of view. However, it must be mentioned that their sensitivity towards small damages is sometimes low. The computation of modal-based features is enabled through system identification techniques or modal identification methods that have been developed particularly for this purpose, such as the FDD [30] or the Bayesian OMA [8, 9]. Cases where natural frequencies are used as a basis for SHM were presented, e.g., in [91, 126, 156, 172, 185, 219]. Mode shapes or the related Modal Assurance Criterion (MAC) [5] have also been used in the context of SHM for damage detection and localization, see, e.g., [105]. However, it is a common opinion that these measures tend to be insensitive towards small damages. Mode shape curvatures, on the other hand, which were initially studied in [149], promise to feature a higher sensitivity in this regard [178]. Many more modal-based features exist. An interesting review of these quantities for damage identification was presented in [69].

A second and lastly presented class of damage-sensitive features comprises model parameters. For their determination, parametric models are fitted to the measured data. The model parameters are then kept for damage identification, constituting a data reduction, which also applies to previously presented features. In [77], Figueiredo et al. used AR coefficients as damage-sensitive features. A similar approach was followed in [67], and in [138] by applying VAR parameters instead.

1.1.2 Capturing long-term dynamics

Capturing the long-term dynamics inherently addresses the problem of handling the effect of EOV on the structure's dynamic behavior, which is often referred to as *data normalization* [70, 182]. In the presented work, a differentiation between implicit and explicit methods is followed. The former seeks to remove the disturbing influence of EOCs on features representing

the short-term dynamics, e.g., modal parameters. Explicit normalization approaches, on the other hand, aim to directly model the long-term variability of the structural dynamics concerning the affecting exogenous conditions [17]. Projection-based data normalization strategies form the most significant class of implicit data normalization techniques and shall therefore be regarded extensively in this section. Explicit methods, also referred to as functional dependence modeling, will be regarded next. One might argue that implicit data normalization does not capture a structure's long-term dynamics, as the corresponding techniques are applied to snippets of continuously acquired vibration data or features extracted from it. However, data normalization tools must be trained with data associated with wide ranges of EOV, and therefore, the long-term dynamic behavior is inherently taken into account.

IMPLICIT DATA NORMALIZATION

Linear projection-based data normalization techniques are appealing since they function in an unsupervised[1] manner such that the affecting EOCs do not need to be measured. Nevertheless, a general understanding of these quantities is required, including information about the number of independent EOCs and whether the acquired data and the altering effects are correlated linearly or nonlinearly. Interesting comparisons of projection-based data normalization techniques can be found in [47, 55, 114].

A well-known projection technique that is readily applied to remove exogenous effects in vibration data is the *principal component analysis (PCA)*, which employs the singular value decomposition (SVD) or eigenvalue decomposition. The PCA is a covariance-based technique, which helps to remove linear correlation caused by EOVs. Therefore, it is also applicable for dimensionality reduction [86]. The method is strongly related to the *factor analysis* [114] and data normalization employing the *Mahalanobis squared distance* [55]. Yan et al. employed the PCA method to remove the linear temperature effects on natural frequencies of a simulated and experimental bridge model, and by that, enabled the successful detection of stiffness reductions and additional local masses [218]. In a companion paper [219], the authors extended the strategy to the case of nonlinear dependence by joining multiple principal components for different intervals of EOCs, which was then applied to natural frequencies of the well-known *Z24 bridge*. Here as well, the normalization strategy facilitated the detection of damage. An alternative strategy for the same validation example was carried out by Reynders et al. [172], using the nonlinear kernel PCA. An interesting extension of the PCA is the probabilistic PCA, which features a couple of advantages, such as the introduction of a likelihood model and the ability to deal with missing data [58]. Other instances of data normalization with the help of PCA can be found in the literature, see, e.g., [178]. Wernitz et al. [213] applied this method to enable the damage localization under varying exogenous conditions with the help of residuals stemming from $\mathcal{H}_\infty$ filters. Criticism on the PCA or factor analysis can be formulated concerning the property of preserving or removing as much variance as possible of the features. As the significant variance is assumed to be caused by EOV, it cannot be precluded that the corresponding principal components cover the effect of minor damages as well [70].

Another projection-based normalization strategy is the *cointegration technique*. This originally econometric method aims to project out nonstationary data components that are not correlated equally. The term cointegration implies that for nonstationary time series, there exists

1 Depending on the context, the term unsupervised exhibits different implications. In general, it states that the data used is unlabeled by an expert.

some linear combination of them which produces a stationary residual [50]. In the context of cointegration, Worden et al. [217] emphasized the issues of heteroscedasticity and nonlinearity. The former refers to the property of time-varying statistical moments, e.g., variance, and the latter describes the problem of EOCs and damage-sensitive features being not correlated in a linear fashion. Both situations represent common problems in the normalization of data in SHM, as was implicitly stated to some extent in this section. The classical cointegration approach was extended to the case of heteroscedastic nonstationary data in [177]. Therein, seasonal effects causing changes in the variance of the data were removed with the help of an additional model representing trends and seasonal components. The problem of nonlinearity of data and the varying EOCs was addressed in [48, 176, 232, 233], where the cointegration technique was applied to natural frequencies of the Z24 bridge and Supervisory Control and Data Acquisition (SCADA) data of a wind turbine.

Besides the mentioned techniques, other projection-based data normalization methods exist. Kullaa presented a missing data model in [113] that comprises an identified mean squared error estimator also relying on the linear correlation of the data to be normalized and the EOCs. Some alternatives to projection-based approaches exist within the class of implicit data normalization, which are worth mentioning. Data clustering or look-up tables are commonly used strategies. There, features are obtained in a training phase for a reasonable range of EOV and then grouped in individual classes of data (clustering). During validation and testing, the newly determined features are first assigned to one of these classes using EOC measurements or reasonable proxies (classification); they are then compared to their pendants from training. An overview of clustering algorithms is given in [95]. Look-up tables can be seen as manual clustering approaches. The data classification is typically carried out with the help of the Euclidean norm to determine the closest cluster available [70]. Instances for the application of clustering approaches for data normalization in the context of wind turbine monitoring can be found in [92, 194, 195, 229].

EXPLICIT DATA NORMALIZATION

As an alternative to removing the varying effects of EOCs on quantities representing the short-time characteristics of the monitored structure (damage-sensitive features), the inherent dependence may be modeled directly. By that, systems are identified that describe the long-term dynamics of the structure under surveillance. Most non-ANN functional modeling approaches require the measurement of the relevant EOCs (supervised data normalization). However, in a few instances, this might not be necessary, see, e.g., [17]. Explicit methods for data normalization can be divided into deterministic and stochastic functional dependence models. Suppose a direct dependence of the varying EOCs and the captured short-term dynamics, e.g., in the form of extracted features, is observable. Then, deterministic dependence models can be derived via functional series expansion or fitting techniques. However, due to unknown excitation, uncertainty, and spatial and temporal sparsity in the observations, the dependence of the structure's dynamic behavior and the EOV might not be sufficiently captured. In these cases, dependence models based on random (stochastic) functions could be identified [17].

Regression techniques are one of the most popular approaches for identifying deterministic functional dependence models. Together with interpolation strategies [216], as another explicit normalization method, and projection-based methods, they have been used for data

normalization since the beginning of extensive research in the field of SHM in the 1990s. They have been applied in many cases ever since. Peeters and De Roeck [152] modeled the temperature dependence of the natural frequencies of the Z24 bridge with the help of an autoregressive model with exogenous inputs (ARX). Similar work was conducted, e.g., for another bridge [126], for the monitoring of a reinforced concrete dam [156], and in the field of wind turbine monitoring [144]. Regarding the latter area of applications, more precisely for the monitoring of jacket structures of offshore wind turbines, Weijtens et al. [208] presented a study employing a nonlinear regression model. An interesting comparison of several nonlinear and piece-wise linear models for temperature-dependent modeling of natural frequencies of a footbridge can be found in [139].

In the context of regression analysis or SHM in general, the so-called Support Vector Machine (SVM)-type regression is worth mentioning. This supervised classification-based tool, rooting from the statistical learning theory, has been widely applied in SHM to model the dynamic long-term behavior of systems [25, 109, 141]. SVMs seek to separate data into two classes by fitting a hyper-plane into the multi-dimensional vector space defined by the data itself. Then, one class represents the intrinsic linear dependency and the other one the remaining information. In the case of nonlinear relationships, the application of kernel functions comes to the rescue [141]. From a numerical point of view, SVM regression is rather appealing since the underlying quadratic optimization problem to be solved is convex [70].

Stochastic functional dependence models for data normalization received considerable attention in the past years because of their flexibility to model all kinds of dependencies. The Polynomial Chaos Expansion (PCE) is particularly well suited for the modeling of uncertain dynamics. To this end, the data to be normalized is expanded on polynomial chaos basis functions, which are orthonormal to the probability space of the EOCs [185]. The PCE method has been applied in SHM to all kinds of structures. In [185], Spiridonakos et al. applied this method to model the nonlinear relationship of the natural frequencies of the Z24 bridge with respect to the measured temperature. Similar work has been conducted on a reinforced viaduct [129]. Bogoevska et al. [24] employed this method to natural frequencies, identified through time-varying ARMA models, and SCADA data of a wind turbine. An interesting extension of the conventional PCE implementation was presented by Dertimanis et al. [57]. They proposed the utilization of B-splines as basis functions and estimated the corresponding parameters with the help of a separable nonlinear least-squares procedure.

Promising explicit normalization results have been further presented within a Gaussian process regression framework [17], which, contrary to the PCE method, considers uncertainty resulting from unmeasurable sources. The associated functional dependency models constitute LPV systems that represent the short- and long-term dynamics of the observed structure with respect to so-called scheduling variables (EOCs). In Gaussian process regression, it is assumed that the EOC-dependent parameters comprising the short-term dynamics follow a Gaussian distribution. An LPV model representing the long-term dynamics is then constructed through functional series expansion. Avendaño-Valencia et al. [17] applied this concept to a bridge featuring LTI short-term dynamics identified as VAR models. Similar efforts have been made for the monitoring of an on-shore wind turbine in [16] using VAR and continuous Wavelet transform models for low- and high-frequency content, respectively.

With the rise of ANNs in all kinds of disciplines related to data processing, their appealing applicability for unsupervised and supervised data normalization was quickly discovered. These tools are applicable to model all types of linear and nonlinear functional dependencies among features and EOCs. Unsupervised normalization is achievable with the help of autoassociative neural networks (AANNs). Setting the size of the bottleneck layer equal to the number of independent EOCs results in capturing the dependency on the unobserved EOCs. An early example of the application of an AANN for data normalization is given in [183], where the neural network is trained by employing temperature-dependent transfer function coefficients. In recent publications, scientists constructed AANNs to represent natural frequencies under varying temperatures [89, 175]. In these instances, the variable temperature was provided as an input to the AANN. A comparative study to non-neural-network-like approaches was presented in [79, 143].

1.1.3 Damage analysis

The primary purpose of SHM is the identification of damage, which constitutes a change of the structure's material and/or geometrical properties leading to a deviation from the ideal condition, cf. [70, 215]. Classically, the damage identification problem describes a hierarchical procedure comprising several steps. Rytter first defined a four-step classification in his PhD thesis [174]. Later Worden and Dulieu-Barton included a fifth step leading to the following widely excepted structure [215]:

1. Damage detection: Does damage exist?
2. Damage localization: Where is the damage?
3. Damage classification: What is the type of damage?
4. Damage assessment: What is the extent of the damage?
5. Prediction: How much safe and useful life remains?

Data-driven vibration-based SHM cannot satisfy all these objectives. The most significant limitation is that no physics-based model is involved, which would provide a more detailed representation of the observed structure compared to the one defined by the sensor network. Consequently, the location of damage, for instance, can only be narrowed down to adjacent sensors. An even more substantial restriction follows from the consideration of unsupervised SHM schemes. According to the third axiom of SHM by Farrar and Worden [70], the localization of damage in the unsupervised case is feasible at best. This approach is generally pursued in civil engineering, which implies that the manifestation of damage with respect to the applied methods is unknown. Since the present thesis is dedicated to the field of unsupervised damage identification, special attention is paid in this section to existing practices with this purpose.

As mentioned before, in data-driven vibration-based SHM, damage is inferred based on damage-sensitive features. The associated *feature extraction process* might as well involve the procedure of data normalization, resulting in a set of characteristic quantities (used for the statistical assessment) that differ from those extracted from the measured data in the first place. Hence, the term damage-sensitive feature is sometimes used inconsistently in the existing lit-

erature. To illustrate the described circumstance, consider the following example: Suppose a structure is monitored using natural frequencies extracted from short-term measurements. These features are sensitive to damage to some extent, but at the same time, they change with varying EOCs. Thus, an implicit data normalization approach that, e.g., applies the PCA method to a certain set of frequencies might be followed. By considering a user-specified number of principal components, the influence of EOCs on the natural frequencies can be removed, leading to a residual of the original and projected natural frequencies, cf. [218]. Under healthy conditions and if the projector is trained adequately, the residual takes a Gaussian distribution, which can be finally tested for the purpose of damage identification. Given this exemplary case, it is arguable that the natural frequencies constitute the actual damage-sensitive features. Instead, the residual should be considered as such. Nevertheless, the denotation is legitimate, as the natural frequencies are indeed affected by damage. Independent of this notational discussion, it can be generalized that, in SHM, damage identification is enabled by assessing the representability of the captured long-term dynamics considering the currently acquired vibration data.

Since the present work contributes to the problem of damage localization in output-only and unsupervised data-driven vibration-based SHM, existing approaches are reviewed in the following. Special attention is paid to the validation of the regarded methods.

As mentioned in Section 1.1.1, modal-based quantities comprise the most intuitive choice of features applicable for damage identification. Attempts to localize damage have been made by employing mode shapes [105] and mode shape curvatures [6, 149, 178, 206] or modal filters [133, 190, 191]. In the output-only context, this class of modal approaches is also related to methods employing flexibility or stiffness matrices such as the popular damage locating vector (DLV) method [20] since these structural parameters can be estimated using OMA techniques, see [21, 221]. Generally, modal-based methods suffer from the sparsity of sensor networks. For mode shape curvatures, which tend to be more sensitive to damage than the mode shapes themselves [149], this issue is often tackled through the application of interpolation schemes. By that, it is hoped to better highlight local changes in the curves. Moreover, the sensitivity of mode shape curvatures towards damage also depends on the level of measurement noise. To overcome this issue, advanced signal processing tools are often applied, see, e.g., [35, 162, 198]. Modal filters promise to hold potential in the view of changing environmental conditions, especially temperature variations. Originally, these filters were constructed from the FRF of the structure under surveillance. The idea is to build up a set of modal filters, each tuned to a different mode by computing linear combination factors. That is, the filter is orthogonal to all modes except one. Thus, the FRFs representing the modal filters feature a single peak at the frequency of the mode they are tuned for. When applied to the measured outputs of the structure, additional peaks arise in the case of local structural changes. On the contrary, if a global change occurs, e.g., caused by a homogenous decrease or increase of temperature, this effect is absent [56], as the mode shapes are unaffected. To overcome the problem of missing input data, the filters can be designed based on PSDs of the outputs or synthesized FRFs [132].

Another class of techniques applied for damage localization stems from the field of fault detection and isolation (FDI) [106, 188] associated with control engineering. The corresponding approaches frequently involve Kalman and $\mathcal{H}_\infty$ filters to detect and localize changes in engi-

neering systems. In output-only problems, such filters can be employed in the observer form, constituting an estimator of the undisturbed outputs. Then, the estimation error exhibits a quantity suitable for damage identification. An early example of Kalman filters used for this purpose in the view of SHM was presented by Yan et al. [220]. For this study, the authors determined the estimators with the help of the SSI. Erazo et al. [68] showed that Kalman filters can be interpreted as modal filters if tuned optimally, and therefore, theoretically exhibit the same insensitivity towards global changes as explained before. A fundamental assumption of Kalman filters is that the excitation and measurement noise represent white noise processes with known statistical properties. Clearly, this assumption does not hold in practice, encouraging the application of more robust estimation schemes. Following this motivation, Lenzen and Vollmering proposed the use of $\mathcal{H}_\infty$ filters for damage identification [117]. Later, the authors extended this strategy through the use of projection techniques [118, 119, 205], leading to an energy-based damage indicator representing the differences in estimation errors.

Other damage localization techniques have been subjected to research. For instance, the applicability of transmissibilities for dispersive and non-dispersive systems was discussed in [43]. An application example is given by Diao et al. [59]. Mosavi et al. [138] proposed damaged localization by applying the Mahalanobis distance to identified VAR parameters. A linear discriminant criterion was then used to evaluate the contribution of the coefficients to structural alterations.

All methods for damage localization mentioned so far have been validated in an experimental context regarding selected batches of data. This even includes large-scale experiments involving a 34 m rotor blade for the utilization of mode shape curvatures [198] or an 80 m footbridge in view of the application of modal filters [133]. The popular Z24 was also subject to Kalman filter-based damage localization, see [220]. These investigations provide valuable justification for the general application of the corresponding methods for data-driven vibration-based SHM, but they do not prove the suitability of the applied methods for long-term monitoring. The reason is that the data used for these studies do not reflect relevant changes of varying EOCs. In the case of [198], the structure was not even excited by ambient sources since it was set up in a laboratory environment. To the knowledge of the author, such studies have so far only been conducted in simulation studies, see, e.g., [116, 178]. This lack of existence of real-life validation examples is addressed in this thesis. Therefore, Kalman and $\mathcal{H}_\infty$ filters are employed within the so-called SP2E framework, and the effect of EOV is handled by means of an interpolation-based LPV modeling approach. The justification for the choice of method is three-fold. Firstly, modal-based methods, in particular, suffer from the sparsity of sensor networks. Without a doubt, dense data acquisition is beneficial for damage identification and damage localization in particular. Nevertheless, energy-based methods tend to cope better with weakly observed structures, cf. [213]. Secondly, a thorough modal identification is not necessarily required, cf. [212, 220], which is appealing for the handling of large sets of data. At last, recent studies have shown that the sensitivity towards localized damage of the proposed damage identification method is high, e.g., compared to a modal curvature-based approach [210].

1.1.4 Uncertainty

It is in the nature of vibration-based SHM that different manifestations of uncertainty are present in all stages and subjects associated with it [39]. Hence, it comes as no surprise that the problem of evaluating the structural integrity of a system given continuously acquired observations is generally approached from a statistical pattern recognition perspective. Nevertheless, the presence of uncertainty needs not only to be faced during the identification of damage. It is also worth considering, reducing, and/or quantifying in all subjects involved, see Fig. 1.1. Possible approaches for coping with uncertainty shall be examined in the following.

UNCERTAINTY AND DYNAMIC MODELING

Uncertainty in the observations might be reduced in the first step during data preprocessing, which among other components, includes data cleansing and data reduction. The former constitutes, for instance, the tasks of filtering signals to remove noise, the removal of spikes, and the treatment of missing data [70, 215]. Uncertainty is intrinsically reduced when modeling the structure's dynamic behavior with parametric techniques. Such techniques aim to fit a mathematical model to the measured data in some optimal sense by reducing the error of fit. From a modal analysis point of view, these models are applicable to extract natural frequencies, damping ratios, and mode shapes, which can be used as features for damage identification. In this regard, approaches exist that quantify the uncertainty associated with the estimated modal parameters. Early contributions were made by Pintelon et al. [157]. Reynders et al. [170] and Döhler et al. [62, 63] published strategies explicitly designed for the SSI. Validation examples are available, e.g., in [169]. Au et al. [8, 9] recently developed an interesting nonparametric approach, leading to the so-called Bayesian Operational Modal Analysis (BAYOMA), which involves the uncertainty quantification of modal estimates.

A final example for the consideration and quantification of uncertainty in system modeling is posed by Gaussian processes. In the regarded context, these stochastic processes assume that the model's parameters follow a Gaussian distribution so that the parameter covariance matrix quantifies the uncertainty of the representation. Valuable contributions in this field have been recently published by Avendaño-Valencia et al. [15, 17] concerning LTI and LPV system modeling.

UNCERTAINTY AND DAMAGE ANALYSIS

Following the statistical pattern recognition paradigm, identifying damage in unsupervised SHM is referred to as novelty, anomaly, or outlier detection. Damage-sensitive features are acquired in a training phase, defining the statistical reference associated with the healthy structure. Generally, this is accomplished with the help of a *hypothesis test*, formulated using a probability density function (PDF) or cumulative distribution function (CDF) of the features acquired during training [93]. In the inspection phase, also called the testing phase, the same kind of features are checked to match this baseline, cf. [70]. To this end, a *confidence interval* must be defined that represents a high likelihood of the structure being undamaged. By using these statistical measures, uncertainty is intrinsically taken into account when implicit approaches are followed.

Control charts exhibit standard tools to visualize the continuous process of outlier detection. They are borrowed from the field of statistical quality control. The charts depict the acquired features over time and stationary upper and lower control limits representing the confidence interval. Once limits are exceeded in either direction, an alarm is triggered, indicating potential damage. An early example of the use in SHM is given by Fugate et al. [81]. An overview of different control charts is available in [70, 137].

Naturally, statistical testing cannot always guarantee the successful identification of damage. This might be caused by the insensitivity of features towards certain types of damage or the minor degree of the damage severity. In any case, for the assessment and/or readjustment of the SHM system, it is beneficial to quantify false detection, manifested as type I errors (false positive detection) and type II errors (false negative detection). The former describes a false alarm, whereas the latter refers to missed damage detection. Clearly, the last case constitutes a more severe error. In SHM, so-called receiver operator characteristic (ROC) curves can be used posterior to the confirmed errors to assess the effectiveness of the applied damage identification scheme and to optimize confidence intervals, see [70].

1.2 ORGANIZATION OF THE PRESENTED WORK

The presented literature review highlights the value of real-life validation cases for SHM. Accordingly, studies that explicitly focus on damage localization in unsupervised data-driven vibration-based SHM have not been presented. Hence, this task defines the central element of this thesis. Linear quadratic estimators form the basis for this endeavor, as they possess a high sensitivity towards localized damage without requiring particularly dense sensor networks. The objectives of this work follow from the necessity to cope with EOV and uncertainty as well as designing proper estimators. The objectives are presented in the following, together with the outline of the thesis.

1.2.1 Objectives

For the overall goal of validating an approach for unsupervised data-driven vibration-based SHM with the potential to localize damage, a strategy shall be developed that focuses on the following goals and hurdles:

- A parametric framework for damage detection and localization is to be adapted for the application in SHM. Therefore, a system theoretic strategy for data normalization shall be developed that enables damage identification under EOV.
- All methods applied must cope with natural sources of variability, excitation, and uncertainty.
- To effectively use Kalman filters within the damage analysis framework, a suitable approach for noise covariance estimation shall be provided.
- The applicability of different kinds of linear quadratic estimators ($\mathcal{H}_2$ and $\mathcal{H}_\infty$ optimal estimators) should be investigated and compared.

- Therefore, criteria shall be derived to enable the a priori assessment of the estimators to be efficiently applied for damage detection and localization.
- Employing the described methods in a practical scenario, challenges should be identified associated with the real-life application of SHM.

By conducting this research in a realistic yet academic context, it is hoped to encourage further studies with a similar focus to quantify the potential and practical effectiveness of vibration-based SHM methods.

1.2.2 Outline

This thesis contains two parts. The first one lays the theoretical foundation for the topics and objectives of this thesis. These are addressed in the second part, which includes simulation and experimental studies for verification and validation purposes. This thesis contributes to all main subjects of SHM directly or indirectly. This circumstance is visualized in Fig. 1.2 with references to the corresponding chapters. The outline of this thesis is as follows:

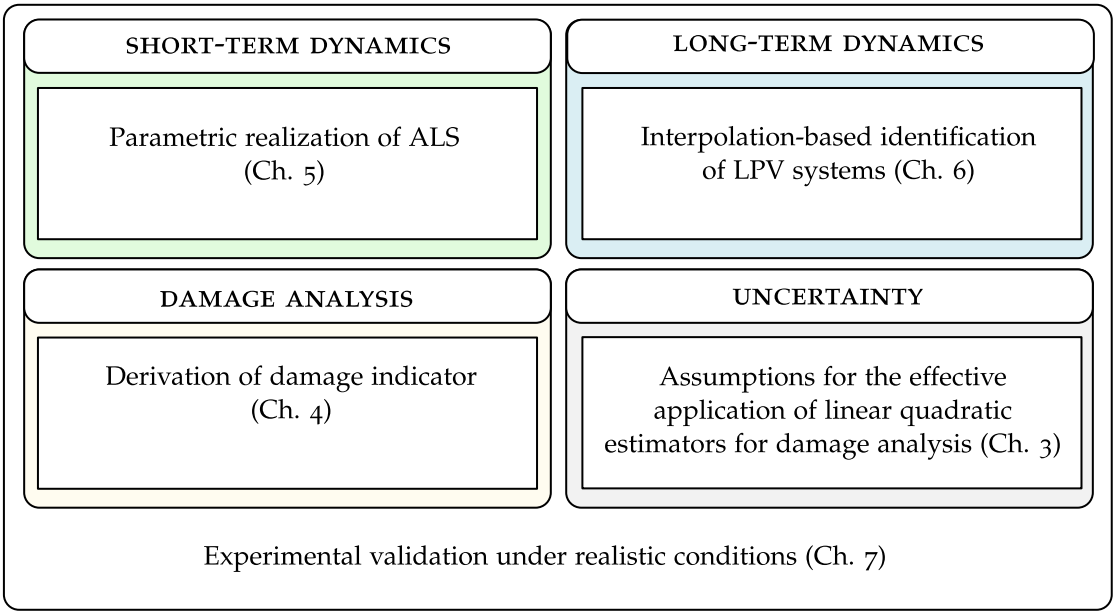

Figure 1.2: Contributions of thesis to SHM.

Chapter 2 — In this thesis, structures are modeled as linear systems with stochastic inputs. Therefore, fundamental structural dynamics of linear systems are presented, and basic properties of random processes are characterized. Finally, the theory and computational steps of the SSI are provided. This method is generally used to identify structures based on short-term observations.

Chapter 3 — The estimation theories behind Kalman and $\mathcal{H}_\infty$ filters are studied. To this end, interpretations of the associated transfer function norms are made within a generalized control framework. A whiteness test for the evaluation of Kalman filter performance is presented.

Chapter 4 — The original damage analysis framework is introduced, which employs quadratic estimators and projection techniques (SP2E) in state space. Based on that, an indicator suitable for damage localization is derived. The framework is regarded in the context of SHM. Therefore, a hypothesis test is proposed for a statistical assessment of the damage indicators. Further, assumptions are postulated concerning the suitability and effective use of the designed filters for effective damage identification.

Chapter 5 — This body of work establishes a parametric extension of the autocovariance least-squares (ALS) method for noise covariance estimation. This enables the convenient design and utilization of Kalman filters within the adapted damage analysis framework. In this context, the whiteness test presented in Chapter 3 is adjusted. The proposed method is validated in a series of simulations and two experiments. The latter demonstrates the effective applicability of tuned Kalman filters within the SP2E framework presented in Chapter 4 for damage detection and localization.

Chapter 6 — This chapter investigates the effect of EOV on damage indicators computed with the help of the damage analysis framework presented before. An LPV identification scheme is developed based on the interpolation of LTI systems for different operating points. Under varying temperatures, this long-term modeling approach is validated using a simulated temperature-dependent LPV system. The applicability of this data normalization strategy in the context of damage detection and localization is demonstrated by introducing small structural changes. A comparison of Kalman and $\mathcal{H}_\infty$ filters is given.

Chapter 7 — SHM is conducted by employing the damage analysis framework by SP2E (Chapter 3) under consideration of the LPV identification scheme (Chapter 6). To this end, Kalman filters tuned with the parametric ALS method (Chapter 5) are applied and compared to $\mathcal{H}_\infty$ filters.

Chapter 8 — This final chapter summarizes and concludes this thesis. Further, an outlook is presented, highlighting aspects to be addressed in future research.

Part I

FUNDAMENTALS

2

LINEAR SYSTEMS AND IDENTIFICATION

Finally, we make some remarks on why linear systems are so important. The answer is simple: because we can solve them!
— Richard Feynman [76, p. 25-8]

In most engineering disciplines, linear models play an essential role in representing system behavior. At the same time, it is common knowledge that these models can never exactly describe the regarded phenomena, as every physical action and reaction features nonlinearities – at least to some extent. Whenever these nonlinear effects can be neglected, ignored, or compensated because of their insignificance, linear models are the first choice from an engineering perspective due to their simplicity, efficacy, and solvability. Since SHM implies the observation and tracking of dynamic properties, a fundamental understanding of structural dynamics is of utmost importance. The relevant theory is given in the first section of this chapter. Inverse system identification techniques are required to model dynamic systems or derive modal properties based on measured data sequences. In this regard, a parametric subspace method is favored throughout this thesis; it is elaborated on in the second section of this chapter.

2.1 FUNDAMENTAL STRUCTURAL DYNAMICS OF LINEAR SYSTEMS

The objective of structural dynamics is to analyze and evaluate the vibration of structures due to time-varying loads. The mathematical tool to address this problem is the equation of motion (EOM) that can be derived from classical or analytical mechanics for continuous-time systems. By leaving the theoretical world of physics and entering the sphere of computer-based engineering analyses, discrete-time representations of vibrating systems become desirable because of their numerical efficacy as well as digital data acquisition. Analyzing a dynamic system, its excitation, or its response in the time domain often leads to limited interpretability of the oscillatory behavior. Therefore, it is advisable to regard the associated signals, or even the system itself in the frequency domain, by performing a Laplace transform or its discrete-time counterpart, the z-transform.

2.1.1 Continuous-time systems

The equation of motion (EOM) is a second-order differential equation that, in the case of mechanical systems, represents the mechanical properties and behavior of a system and allows the computation of vibrations resulting from time-varying external forces. Considering classical mechanics and Newton's second law of motion is the direct approach to derive EOMs for single degree of freedom (SDOF) systems or multi-degree of freedom (MDOF) systems. Newton's second law of motion constitutes that the sum of forces, acting on a point-like particle of mass in a fixed reference frame, is equal to mass times acceleration [151]. With the help of d'Alembert's principle, one can regard a system from a static equilibrium standpoint

for every time t by introducing a fictitious inertia force. This state is referred to as dynamical equilibrium. D'Alembert generalized the principle to any arbitrary mechanical system and not only moving mass particles. The principle further relaxes the necessity of an inertial reference frame, as it permits the introduction of a moving relative system [115]. Other approaches exist to derive EOMs, e.g., the principle of virtual displacement or Hamilton's principle [44].

In the presented work, linear mechanical structures are usually modeled as multiple degree-of-freedom (MDOF) systems. Thus, the corresponding EOM reads

$$M\ddot{y}(t) + D_p\dot{y}(t) + Ky(t) = f(t). \tag{2.1}$$

Therein, $M \in \mathbb{R}^{n_D \times n_D}$ denotes the mass matrix, $D_p \in \mathbb{R}^{n_D \times n_D}$ the viscous and proportional damping matrix and $K \in \mathbb{R}^{n_D \times n_D}$ the stiffness matrix. The vector of external forces $f \in \mathbb{R}^{n_D}$, acting at each of the n_D degrees of freedom (DOFs), is time varying, as well as the displacement $y \in \mathbb{R}^{n_D}$, velocity $\dot{y} \in \mathbb{R}^{n_D}$, and the acceleration $\ddot{y} \in \mathbb{R}^{n_D}$. Note that the dot notation is used to designate the time derivative. Naturally, Eq. 2.1 also applies to single degree-of-freedom (SDOF) systems. The matrix coefficients (M, D_p, K) then reduce to scalar values. The discretization of a structure, e.g. with the finite element (FE) method, highly depends on the presupposed material laws and interconnecting relationships. However, to elaborate on this is beyond the scope of the thesis.

Structures represented by Eq. 2.1 are referred to as linear time-invariant (LTI) systems. That means their mechanical properties (M, D_p, K) are not time-dependent. However, a structure may alter over time. Then, ($M(t)$, $D_p(t)$, $K(t)$) should be considered instead. In this case, the system can no longer be described as LTI but as linear time-variant (LTV). When a linear system changes with respect to its current operational point or environmental conditions, it should be characterized as linear parameter-varying (LPV). Then, the structural parameters are given as a function of the scheduling variable θ such that ($M(\theta)$, $D_p(\theta)$, $K(\theta)$). However, this chapter is only dedicated to LTI systems. LPV systems will be later addressed in Chapter 6.

From a signal processing standpoint, it is often convenient to regard dynamic systems as a general operator that maps some inputs u to some outputs y. This interconnection is displayed in Fig. 2.1, where $\boldsymbol{G}$ denotes some arbitrary system[1]. This illustration condenses the

Figure 2.1: System $\boldsymbol{G}$ with input u and output y.

relationship of u, y, and $\boldsymbol{G}$ to its core. It does not imply any form of representation of $\boldsymbol{G}$ or whether u and y are time- or frequency-domain signals. It simply states that some output y arises when u acts on $\boldsymbol{G}$. From there, the labels single input/single output (SISO) or multiple input/multiple output (MIMO) follow. In the following, important forms of representation are introduced, besides the EOM discussed before. Also, solutions for the map $u \rightarrow y$ are presented.

1 Throughout this thesis, systems are highlighted by bold capital letters.

STATE-SPACE FORMULATION

A practical representation of dynamic systems is the state-space form. This arrangement, developed in control engineering, consists of writing a second-order differential equation in a first-order form and adding an algebraic output equation. To do so, the so-called state vector $x(t)$, which consists of $n = 2n_D$ elements is introduced [214]. At this point, a generic continuous-time LTI state-space system is introduced first that reads

$$\dot{x}(t) = A_c x(t) + B_c u(t) \tag{2.2a}$$
$$y(t) = C_c x(t) + D_c u(t), \tag{2.2b}$$

with

$$x(t) = \begin{bmatrix} x_1(t) \\ x_2(t) \end{bmatrix}, \quad x_2(t) = \dot{x}_1(t). \tag{2.3}$$

Here, the subindex c denotes continuous-time. A_c is the $n \times n$ system matrix, B_c is the $n \times p$ input matrix, C_c is the $q \times n$ output matrix, and D_c represents the $q \times p$ feed-through matrix. All state-space matrices might be complex- or real-valued. Note, that p and q depict the number of inputs $u(t)$ and outputs $y(t)$, respectively. A transformation of Eq. 2.1 into state-space yields

$$\dot{x}(t) = \underbrace{\begin{bmatrix} 0 & I \\ -M^{-1}K & -M^{-1}D_p \end{bmatrix}}_{A_c} \begin{bmatrix} y(t) \\ \dot{y}(t) \end{bmatrix} + \underbrace{\begin{bmatrix} 0 \\ M^{-1} \end{bmatrix}}_{B_c} f(t) \tag{2.4a}$$

$$y(t) = \underbrace{\begin{bmatrix} I & 0 \end{bmatrix}}_{C_{c,d}} \begin{bmatrix} y(t) \\ \dot{y}(t) \end{bmatrix} \tag{2.4b}$$

so that $x_1(t) = y(t)$, $x_2(t) = \dot{y}(t)$, $u(t) = f(t)$, and $D_{c,d} = 0$. In the preceeding equations, 0 depicts a matrix containing only zeros and I is the identity matrix. Note that $x_1(t) = y(t)$, $u(t) = f(t)$, and $D_{c,d} = 0$. All associated variables are real-valued.

In Eq. 2.1, and therefore, in Eq. 2.4b, y refers to displacement, which essentially follows the definition of $C_{c,d}$, where, the subscript d denotes displacement. To yield different quantities as outputs, such as velocity and acceleration, the parameters $C_{c,d}$, and even $D_{c,d}$, must be changed to [152, 204]

$$C_{c,v} = C_{c,d} A_c, \quad D_{c,v} = C_{c,d} B_c, \tag{2.5}$$
$$C_{c,a} = C_{c,d} A_c^2, \quad D_{c,a} = C_{c,d} A_c B_c, \tag{2.6}$$

where the subscripts v and a imply velocity and acceleration, respectively. These definitions follow from the time derivatives of Eq. 2.4b.

TIME DOMAIN SOLUTION

To compute the response of a continuous-time LTI system represented by Eq. 2.2 to an arbitrary input $u(t)$ in time domain, the state equation can be generally solved with [214]

$$x(t) = e^{A_c(t-t_0)} x(t_0) + \int_{t_0}^{t} e^{A_c(t-\tau)} B_c u(\tau) d\tau. \tag{2.7}$$

Here, the first part, $e^{A_c(t-t_0)}x(t_0)$, refers to the homogeneous solution of the first-order differential equation, namely the response to zero input but some initial condition $x(t_0)$ at the starting time t_0. The second part constitutes the particular solution, which represents the output to an arbitrary input signal, whereas the initial state vector $x(t_0)$ is zero. At this point, it must be mentioned that computing e^{A_c} is not trivial at all. However, a solution can be found by employing the Cayley-Hamilton theorem, for instance, [40]. Finally, substituting Eq. 2.7 into Eq. 2.2b yields

$$y(t) = C_c e^{A_c(t-t_0)}x(t_0) + \int_{t_0}^{t} C_c e^{A_c(t-\tau)}B_c u(\tau)d\tau + D_c u(t). \tag{2.8}$$

By assuming that $t_0 = 0$, $x(t_0) = 0$, and $u_i(t) = \delta(t)$, $i \in [1, p]$, with $\delta(t)$ being the Dirac function

$$\delta(t) = \begin{cases} 1, & t = 0, \\ 0, & t > 0, \end{cases} \tag{2.9}$$

one recovers the impulse response function (IRF)

$$G(t) = C_c e^{A_c t}B_c + D_c\delta(t). \tag{2.10}$$

Consequently, an alternative form for Eq. 2.8 follows:

$$y(t) = C_c e^{A_c(t-t_0)}x(t_0) + \int_{t_0}^{t} G(t-\tau)u(\tau)d\tau. \tag{2.11}$$

Note that the second part of the latter is referred to as convolution and is closely related to the *Duhamel's Integral* for the solution of Eq. 2.1 (see, e.g., [44]). The IRF in Eq. 2.10 is a full representation of the system $\boldsymbol{G}$ in the time domain, as it enables the genuine computation of $y(t)$ through convolution with $u(t)$, see Eq. 2.11.

MODAL ANALYSIS

Modal parameters are crucial for the characterization of linear dynamic systems. They comprise natural frequencies, also known as eigenfrequencies, mode shapes, and modal damping ratios. A general way to derive them is to consider Eq. 2.4a for the free-vibration case ($f(t) = 0$) and the possible solution of this first-order homogeneous differential equation [134]:

$$x(t) = \sum_{i=1}^{n} \begin{bmatrix} \phi_i \\ \phi_i\lambda_i \end{bmatrix} e^{\lambda_i t}. \tag{2.12}$$

Here, $\phi_i \in \mathbb{C}^{n_D}$ describes the complex-valued eigenvectors or mode shapes, respectively, and $\lambda_i \in \mathbb{C}$ represents the associated eigenvalues. Both appear in n_D complex-conjugated pairs. The eigenvalues of these n_D so-called normal modes or eigenmodes are defined as

$$\lambda_i, \lambda_i^* = -\zeta_i\omega_{0,i} \pm j\omega_{0,i}\sqrt{1-\zeta_i^2} = \delta_i \pm j\omega_{D,i}, \tag{2.13}$$

where the real part is represented by the decay constant δ_i, and the imaginary part, led by the imaginary number $j = \sqrt{-1}$, contains the damped circular or also-called angular natural frequency $\omega_{D,i}$ (in radian) of the ith eigenmode. $\omega_{0,i}$ depicts the ith undamped circular natural

frequency, and ζ_i is the modal damping ratio. $(\cdot)^*$ denotes the complex conjugate. Note that for mechanical systems with proportional damping, as given by Eq. 2.1, eigenvalues and eigenvectors comprise real-valued quantities since they satisfy the orthogonality property of the normal modes [30, p. 95]. This circumstance implies that the response of the damped MDOF system can be fully described by the superposition of n_D decoupled SDOF systems. Nevertheless, eigenvalues and -vectors become complex-valued when transferring the EOM into state space. The associated eigenvalue problem is similar to the modal decoupling of non-proportionally damped systems, see [30, p. 99 ff.].

Now, substituting Eq. 2.12 into $\dot{x}(t) = A_c x(t)$ (free decay) yields the standard eigenvalue problem

$$\Psi \bar{\Lambda}_c = A_c \Psi, \tag{2.14}$$

with

$$\bar{\Lambda}_c = \begin{bmatrix} \Lambda_c & 0 \\ 0 & \Lambda_c^* \end{bmatrix}, \quad \Lambda_c = \begin{bmatrix} \lambda_i & & \\ & \ddots & \\ & & \lambda_{n_D} \end{bmatrix} \tag{2.15}$$

and

$$\Psi = \begin{bmatrix} \Phi & \Phi^* \\ \Phi\Lambda_c & \Phi^*\Lambda_c^* \end{bmatrix}, \quad \Phi = \begin{bmatrix} \phi_i & \cdots & \phi_{n_D} \end{bmatrix}. \tag{2.16}$$

It follows from Eq. 2.14 and the relations described before that A_c can be diagonalized using the so-called modal matrix Ψ so that $\bar{\Lambda}_c = \Psi^{-1} A_c \Psi$. This procedure is referred to as *modal decoupling* of the state-space form, which comprises a set of n independent first-order differential equations. In fact, an infinite amount of so-called similarity transformations exists for any non-singular matrix $T \in \mathbb{C}^{n \times n}$ that leads to a transformation of the states so that $x'(t) = T^{-1} x(t)$ [214]. The associated state-space matrices then become

$$A_c' = T^{-1} A_c T, \quad B_c' = T^{-1} B_c, \quad C_c' = C_c T, \quad D_c' = D_c. \tag{2.17}$$

Note that the prime marks a vector or matrix after the similarity transformation. With $T = \Psi$, the eigenvalues λ_i can be extracted conveniently from the main diagonal of A_c', as A_c' becomes $\bar{\Lambda}_c$. Based on that and given Eq. 2.13, the circular natural frequencies

$$\omega_{0,i} = |\lambda_i| \tag{2.18}$$

and damping ratios

$$\zeta i = \frac{-\delta_i}{\omega_{0,i}} \tag{2.19}$$

follow. Finally, the projected mode shapes can be found on the columns of $C_c' = C_c \Psi$. To receive the natural frequencies in Hz, the division by 2π is required such that $f_{0,i} = \omega_{0,i}/(2\pi)$ and $f_{D,i} = \omega_{D,i}/(2\pi)$, where $f_{0,i}$ and $f_{D,i}$ denote the ith undamped and damped natural frequency in Hz, respectively.

CANONICAL FORMS AND MODEL REDUCTION

In the case of the modal decoupling with $T = \Psi$, a diagonal canonical form with complex-valued state-space coefficients is derived. Therefore, a model reduction constituting the removal of specific modes from the model is easy to conduct by neglecting the corresponding

rows and columns, respectively, of the state-space matrices. In some applications, real-valued state-space matrices are desired. Then, an alternative canonical form can be computed with [214]

$$T = \begin{bmatrix} \mathrm{Re}\{\psi_i\} & \mathrm{Im}\{\psi_i\} & \cdots \mathrm{Re}\{\psi_n\} & \mathrm{Im}\{\psi_n\} \end{bmatrix}, \tag{2.20}$$

leading to

$$A_c' = T^{-1} A_c T = \begin{bmatrix} \delta_i & \omega_{D,i} & 0 & \cdots & 0 \\ -\omega_{D,i} & \delta_i & 0 & \cdots & 0 \\ 0 & 0 & \ddots & \vdots & \vdots \\ \vdots & \vdots & \vdots & \delta_n & \omega_{D,n} \\ 0 & 0 & \dots & -\omega_{D,n} & \delta_n \end{bmatrix}. \tag{2.21}$$

Note that in Eq. 2.20, ψ_i denotes the eigenvectors of A_c available on the columns of Ψ (Eq. 2.16), the operator $\mathrm{Re}\{\cdot\}$ extracts the real components of complex numbers, and $\mathrm{Im}\{\cdot\}$ the imaginary part. In the case of the described transformation, B_c' and C_c' are real-valued as well, and a modal-based model reduction is feasible similarly to the diagonal canonical form[2].

2.1.2 Discrete-time systems

In SHM, structures of interest are observed with the help of sensors and data acquisition systems. Because of the digital nature of this equipment, the sensed forces, vibrations, meteorological information, etc., are sampled in discrete time. Consequently, the models fitted to this data, e.g., by means of system identification techniques, are defined in discrete time as well. Although these models are appealing for numerical operations, they often become more comprehensible, e.g., in terms of natural frequencies, once converted to continuous time. On the other hand, a conversion from a continuous-time to a discrete-time model might be desired, for instance, to simplify numerical operations. The discretization of signals and systems is enabled by defining $t = k\Delta t$, where Δt denotes the sampling period, and k represents discrete time steps. Further, the type of discretization depends on how the transition of time-dependent processes from one time instance to the next is defined. Assuming a constant value for the duration of one time step $k\Delta t$ is referred to as zero-order hold (ZOH) [168].

When converting continuous-time state-space systems, the input $u(t)$ is assumed constant for $k\Delta t \leqslant (k+1)\Delta t$. By that, the associated discrete-time state-space model can be derived [40]:

$$x_{k+1} = Ax_k + Bu_k \tag{2.22a}$$
$$y_k = Cx_k + Du_k, \tag{2.22b}$$

with parameters

$$A = e^{A_c \Delta t}, \quad B = A_c^{-1}\left(A - I\right) B_c, \quad C = C_c, \quad D = D_c. \tag{2.23}$$

2 It must be remarked that the simplified case is regarded, where a system contains complex-conjugated modes only. For further information and the more complicated scenario, consult [214].

TIME-DOMAIN SOLUTION

By discretizing continuous-time state-space models, e.g., with the help of the ZOH method, the computation of time derivatives is no longer required. Moreover, by processing Eq. 2.22a for some initial time step k_0 yields the discrete-time pendant to Eq. 2.7, which reads

$$x_{k_0+l} = A^l x_{k_0} + \sum_{i=0}^{l-1} A^i B u_{k_0+l-i-1}, \tag{2.24}$$

$$x_k = A^{k-k_0} x_{k_0} + \sum_{i=0}^{k-k_0-1} A^i B u_{k-i-1}, \tag{2.25}$$

with $k = k_0 + l$, $l \geqslant 0$ and $k > k_0$. Further, the output equation as a function of the initial state x_{k_0} and the inputs u_k follows from substituting Eq. 2.25 into Eq. 2.22b such that

$$y_k = CA^{k-k_0} x_{k_0} + \sum_{i=0}^{k-k_0-1} CA^i B u_{k-i-1} + Du_k. \tag{2.26}$$

Here, the similarity to Eq. 2.8 is apparent.

Now, the discrete-time IRF G_k can be found by choosing $k_0 = 0$, $x_0 = 0$, and $u_{i,k} = \delta_k$, $i \in [1, p]$, where δ_k denotes the discrete-time Dirac function defined as

$$\delta_k = \begin{cases} 1, & k = 0, \\ 0, & k \neq 0. \end{cases} \tag{2.27}$$

The discrete-time IRF, also called infinite impulse response (IIR), reads

$$G_k = \begin{cases} D, & k = 0, \\ CA^{k-1}B, & k > 0 \end{cases} \tag{2.28}$$

such that Eq. 2.26 can be written similarly to Eq. 2.11 as

$$y_k = CA^{k-k_0} x_{k_0} + \sum_{i=k_0}^{k} G_{k-i} u_i, \tag{2.29}$$

cf. [40, 145]. This operation is also referred to as discrete convolution. Note that for causal systems, $k \geqslant i$, since the output y_k must be a function of past and present. This system property and some more will be regarded in Section 2.1.4. A last comment is made with respect to the computation of G_k. At first sight, it seems that this procedure is relatively simple. However, because of the matrix exponential A^{k-1}, this operation is numerically demanding.

MODAL ANALYSIS

Eigenvalues and eigenvectors of discrete-time state-space systems can be extracted similarly to the continuous-time case using an eigenvalue decomposition, as stated in Eq. 2.14. However, in this case, the diagonal matrix containing the discrete-time eigenvalues μ_i is denoted $\bar{\Lambda}$ or Λ, respectively. It decomposes to

$$\Lambda = \begin{bmatrix} \mu_i & & \\ & \ddots & \\ & & \mu_{n_D} \end{bmatrix}, \text{ with } \quad \mu_i = e^{\lambda_i \Delta t} \tag{2.30}$$

so that the continuous-time eigenvalues are recovered by

$$\lambda_i = \frac{\ln(\mu_i)}{\Delta t}. \tag{2.31}$$

Then, the classical interpretations in terms of natural frequencies, damping ratios, as well as mode shapes follow from the theory of modal decoupling of continuous-time systems given in Section 2.1.1.

2.1.3 Frequency domain representation and analysis

Signals and systems can also be represented, analyzed, and processed in the frequency domain. To this end, they are regarded as functions of (complex) frequency. The transformation of LTI systems from the time to the frequency domain also paves the way for the computation of system responses in a numerically relaxed manner. In fact, this change of perspective enables interesting interpretations of the nature of signals and systems, and therefore, is readily considered in almost all engineering disciplines. The mathematical operation to conduct such transformations in continuous-time is the *Laplace transform*. For an arbitrary signal $y(t)$, it is defined as [197]

$$y(s) = \int_0^\infty y(t) e^{-st}\, dt. \tag{2.32}$$

The argument $s \in \mathbb{C}$ denotes the so-called Laplace variable or Laplace operator that has the factorization $s = \alpha + j\omega$, where ω denotes the angular frequency in radian and α is some real-valued scalar. In the following, the transformation $y(t) \to y(s)$ is denoted by $\mathcal{L}\{y(t)\}$.

For discrete-time signals, the z-transform ($\mathcal{Z}\{\cdot\}$) must be used instead. Similarly to Eq. 2.32, it is defined as

$$y(z) = \sum_{k=0}^{\infty} y_k z^{-k}. \tag{2.33}$$

Here, the complex scalar variable z is defined that reads $z = e^{s\Delta t}$. If Eqs. 2.32 and 2.33 are considered for the interval $(-\infty, \infty)$, the so-called bilateral or two-sided Laplace or z-transform, respectively, is implied. Both the Laplace and the z-transform possess inverse counterparts such that $\mathcal{L}^{-1}\{y(s)\} = y(t)$ and $\mathcal{Z}^{-1}\{y(z)\} = y_k$, where $\mathcal{L}^{-1}\{\cdot\}$ and $\mathcal{Z}^{-1}\{\cdot\}$ denote the inverse Laplace and z-transform, respectively. For more information on this topic, see [145, 197].

TRANSFER FUNCTION

With the proper mathematical tools at hand, the system response given by Eq. 2.11 for $x(0) = 0$ can be expressed as a function of the complex variable s [40, p. 13 ff.]. Then, it reads

$$y(s) = G(s)u(s). \tag{2.34}$$

Here, $u(s)$ is the Laplace transform of the input signal $u(t)$, and the complex-valued matrix function $G(s)$ is the so-called transfer function of the continuous-time system $\boldsymbol{G}$ represented by the state-space parameters (A_c, B_c, C_c, D_c). It yields

$$G(s) = \mathcal{L}\{G(t)\} = C_c(sI - A_c)^{-1}B_c + D_c. \tag{2.35}$$

Eq. 2.34 reveals a powerful property of the Laplace transform, namely that this operation turns convolution integrals, and even differential equations, into algebraic equations [40, 145]. Consequently, processing signals and systems in the frequency domain is appealing from a numerical perspective. All information can be retained and recovered because of the unitary nature of the Laplace transform [230].

It is easy to show that the transfer functions for discrete-time state-space systems follow similar derivations [40, p. 32 ff.]. To this end, consider the equation of outputs in Eq. 2.29 for $x_0 = 0$ and the z-transform defined in Eq. 2.33. Then,

$$y(z) = G(z)u(z), \quad \text{with} \quad G(z) = \mathcal{Z}\{G_k\} = C(zI - A)^{-1}B + D. \tag{2.36}$$

FREQUENCY RESPONSE FUNCTION

While the transfer function of an LTI system has quite an abstract interpretation because of the complex variables s or z, respectively, the so-called frequency response function (FRF) is a powerful tool to gain insight into how a system reacts to inputs with specific frequencies. By assuming a stationary input and considering the steady-state case[3], the real part of s is chosen to zero ($\alpha = 0$). By that, the FRFs

$$G(j\omega) = C_c(j\omega I - A_c)^{-1}B_c + D_c \tag{2.37}$$

and

$$G(e^{j\omega\Delta t}) = C(e^{j\omega\Delta t}I - A)^{-1}B + D \tag{2.38}$$

are recovered. Hence, the FRFs are simply functions of all real angular frequencies $\omega \in (-\infty, \infty)$ or $\omega \in [0, f_s/2]$ in the discrete-time case, respectively. They show how the system $\boldsymbol{G}$ responds to a sinusoidal excitation with distinct frequency ω and unit amplitude in terms of magnitude $|G(j\omega)|$ and phase $\angle G(j\omega)$. These quantities are defined as

$$|G(j\omega)| = \sqrt{\mathrm{Re}\{G(j\omega)\}^2 + \mathrm{Im}\{G(j\omega)\}^2} \tag{2.39}$$

and

$$\angle G(j\omega) = \arg G(j\omega) = \arctan \frac{\mathrm{Im}\{G(j\omega)\}}{\mathrm{Re}\{G(j\omega)\}}. \tag{2.40}$$

$\angle G(j\omega)$ can be interpreted as the delay to the excitation[4]. These explanations and interpretations hold for the discrete-time case as well. The combined plot of magnitude and phase as functions of frequency is known as *Bode plot*.

FRFs can also be derived with the help of the *Fourier transform*, denoted by $\mathcal{F}\{\cdot\}$, and its discrete-time counterpart, respectively. For the continuous-time case, the associated transformation is defined for an arbitrary signal $y(t)$ as [197]

$$y(j\omega) = \int_{-\infty}^{\infty} y(t)e^{-j\omega t}\,dt. \tag{2.41}$$

3 The steady-state solution of a dynamically excited system comprises the homogeneous solution only and disregards transient effects.

4 In practice, the two-argument arctangent (atan2) is readily applied to determine the unique phase angle within the complex plane.

Obviously, this operation considers the infinite time interval $(-\infty, \infty)$ and yields functions of the real variable ω. Thus, the Fourier transform can be seen as a special case of the Laplace transform for $\alpha = 0$. In the case of the bilateral Laplace transform, $y(t < 0) = 0$ is required, which is satisfied for causal systems. Accordingly, there exist an inverse operation denoted by $\mathcal{F}^{-1}\{\cdot\}$ such that [197]

$$y(t) = \frac{1}{2\pi}\int_{-\infty}^{\infty} y(j\omega)e^{j\omega t}\, d\omega. \tag{2.42}$$

2.1.4 System properties

When analyzing or processing linear dynamic systems, certain properties need to be assumed or assured. In the following, properties that play a fundamental role in the present work are briefly defined and explained. Since discrete-time LTI systems are typically considered in this work, the associated definitions are made in this regard. Nevertheless, the characterization of continuous-time LTI systems follows the same principles in general.

STABILITY

Stability is the most important property of dynamic systems, especially LTI systems. Generally, system theorists distinguish between internal and input-output stability. The former is often referred to as *Lyapunov stability*, whereas the latter type is typically denoted as *bounded-input, bounded-output (BIBO) stability* [102]. In simple words, the internal stability evaluates the system response to some arbitrary initial state x_0. On the other hand, BIBO stability of systems is assessed by contrasting inputs and outputs. Although both kinds of stability share certain similarities, they should not be confused. In the present thesis, Lyapunov stability is implied whenever the stability of systems is regarded. There, the stability of a system depends only on the state matrix A, which constitutes the transmission of states. A discrete-time LTI system described by $x_{k+1} = Ax_k$ is said to be asymptotically stable if and only if all eigenvalues of A have a magnitude strictly smaller than one[5]. On the other hand, the system is unstable if at least one eigenvalue has a magnitude greater than one. States of asymptotically stable systems tend towards zero as the time approaches infinity ($x_k \to 0$ as $k \to \infty$) independent of the initial condition x_0. Thus, the effect of the initial condition diminishes with time. An alternative test for Lyapunov stability follows from the Lyapunov theorem, which states that a discrete-time LTI system is asymptotically stable if for every positive definite $n \times n$ matrix Q, there exist a unique, symmetric, and positive-definite solution P for the following, so-called *discrete-time Lyapunov equation* [102]:

$$A^{\mathrm{T}}PA - P = -Q. \tag{2.43}$$

CAUSALITY AND INVERTIBILITY

Another important characteristic of dynamic systems is the property of causality. A system is causal when the outputs solely depend on past and present inputs. This is generally the case for all passive mechanical systems. In the case of strict causality, the system's output depends on past inputs only. Consider Eq. 2.29, where the output y_k is computed by means of an discrete-time IRF and the inputs u_i. The system $\boldsymbol{G}$ is only causal or *nonanticipatory* if and

5 In the continuous-time case, this refers to strictly negative real parts, which is associated with positive damping, cf. Eq. 2.13.

only if $y_k = 0$ in the case of $i > k$, $u_i \neq 0$. $\boldsymbol{G}$ is strictly causal if and only if $y_k = 0$ for $i \geqslant k$, $u_i \neq 0$.

The property of invertibility can be readily visualized with the help of Eq. 2.36 because of its algebraic nature. This equation also comprises the computation of a system response y for an excitation u, cf. Fig. 2.1. However, the sequences are regarded in the complex frequency domain in this case. The system $\boldsymbol{G}$ is considered invertible if $G(z)^{-*}G(z) = I$, and thus, $u(z) = G(z)^{-*}y(z)$. Here, $(\cdot)^{-*}$ denotes the complex transpose of the inverse. Systems in this work are always considered causal and invertible when not stated otherwise.

OBSERVABILITY AND CONTROLLABILITY

Observability and controllability are essentially important when dealing with control problems. Yet, in the present work, where estimation strategies stemming from the control field are exploited, observability plays a paramount role. Because of the duality to controllability, the necessary statements for this property should also be given.

Typically, the true states x_k of a discrete-time system defined by (A, B, C, D) (see Eq. 2.22) are unknown, and therefore, it might be desirable to estimate x based on measurements y. Therefore, the corresponding system must be observable, which implies that any unknown initial state x_0 can be uniquely reconstructed given a finite sequence of y_k with $k > 0$ [40]. Observability is only linked to the state-space representation's output equation; thus, checking for this property solely involves the pair (A, C). The latter is said to be observable if, e.g., the ($nq \times n$) observability matrix

$$O = \begin{bmatrix} C \\ CA \\ \vdots \\ CA^{n-1} \end{bmatrix} \tag{2.44}$$

has full column rank.

Controllability describes the possibility to steer any state of a system in any direction within the state space in finite time. Contrary to the observability property, this only involves the state equation. A system is controllable if the ($n \times np$) controllability matrix

$$\Gamma = \begin{bmatrix} B & AB & \dots & A^{n-1}B \end{bmatrix} \tag{2.45}$$

has full row rank. Note that besides these binary metrics, the degree of observability and controllability can be assessed by computing the observability and controllability Gramians, respectively, see [102].

2.2 STOCHASTIC PROCESSES AND SIGNAL PROCESSING

Civil engineering structures typically undergo ambient excitation induced by, e.g., wind or exogenous vibration sources, such as traffic. These loads feature random (stochastic) characteristics or are assumed as such. Consequently, they are determined by statistical properties. In particular, these properties comprise statistical moments, probability density functions (PDFs), correlation or covariance functions, and power spectral density (PSD) functions, which are

elaborated on in the following paragraphs. Prior to that, the terms stationarity and ergodicity are introduced, which relate to readily assumed properties. Besides the practical motivation, stochastic processes play an essential role in many problems covered by this work, e.g., hypotheses testing and Kalman filtering. Thus, the theory summarized in this section can be seen as a theoretical foundation for these disciplines. For the sake of clarity, the following theory is mostly summarized for the continuous case. Special notes are made for discrete processes when appropriate.

2.2.1 Stationary and ergodic stochastic processes

To relate the theory of statistics to measured signals, it seems appropriate to overlook the notation one more time and to make some additional nomenclatural definitions. Prior to this section, an arbitrary time-dependent signal or process was denoted as $x(t)$ in continuous-time and as x_k when thought of as a discrete-time function. From a statistical point of view, measured signals are seen as realizations of the stochastic process $x(t)$ or x_k, respectively, and therefore, are denoted as $x_i(t)$ or $x_{i,k}$, where $i \in \mathbb{N}^+$ depicts the number of realizations. Hence, they are called sample functions. The totality $\{x_i(t)\}$ or $\{x_{i,k}\}$ represents an ensemble of these n_e sample functions. This relation is depicted in Fig. 2.2. If t or k is fixed and i is a variable, then any $x_i(t)$ or $x_{i,k}$, respectively, is a random variable [19, 150]. Following this definition

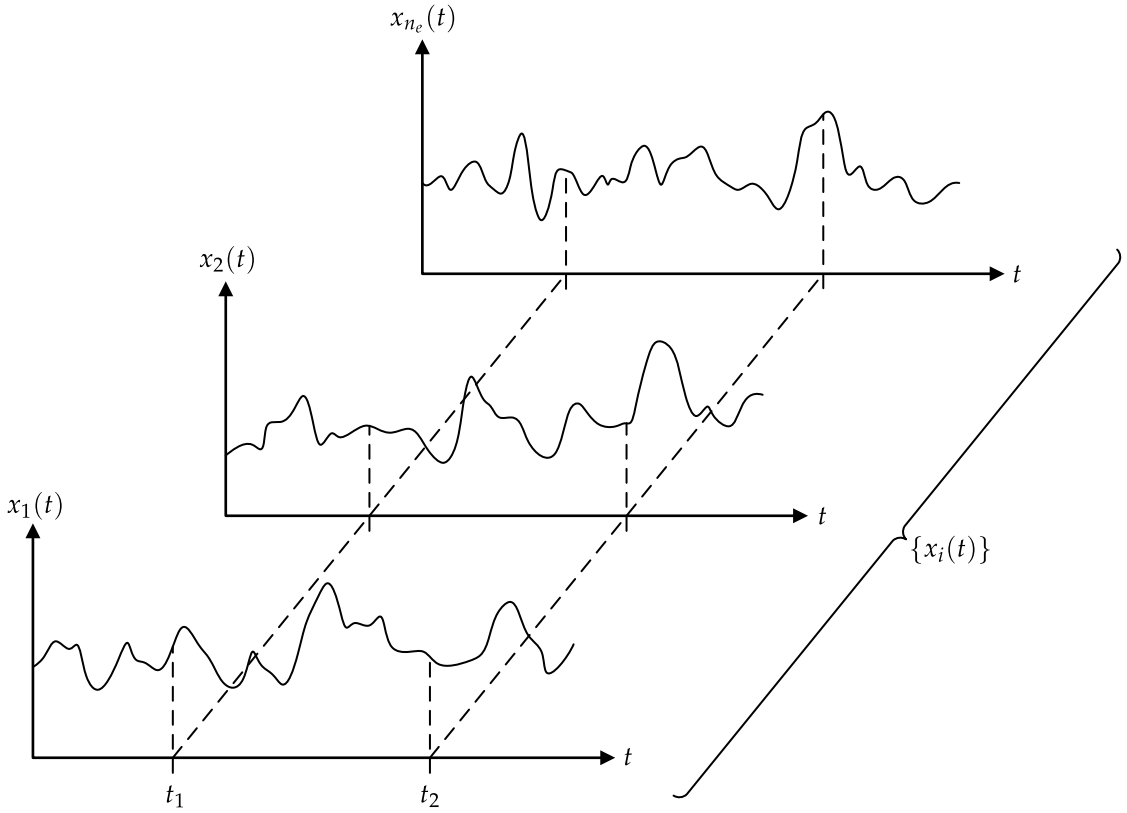

Figure 2.2: Ensemble $\{x_i(t)\}$ of sample functions $x_i(t)$ (adapted from [19, p. 10]).

and regarding Fig. 2.2, it becomes clear that the concept of stochastic processes is somewhat abstract since only an ensemble of infinite sample functions could represent it.

Hence, stochastic processes are typically considered ergodic, as explained in the following paragraph. This assumption pertains to the presented work. Therefore, the stochastic process $x(t)$ or x_k, respectively, can be characterized based on a single sample function, and thus, the index i becomes obsolete. Before continuing, one formal incorrectness should be allowed, namely that measured data is often referred to as a stochastic process and not a realization of such.

For a random process to be ergodic, it must be stationary at first. Stochastic processes are referred to as stationary if certain statistical properties are independent of time. More precisely, they are considered as *weakly stationary* if the mean value and the autocorrelation function are time-independent. Moreover, they are said to be *strongly stationary* if this time-independence holds for all statistical properties [150] (see Section 2.2.2). In this work, the former is typically assumed when considering stationary stochastic processes. To explain this feature, consider the ensemble $\{x_i(t)\}$ of an arbitrary random scalar-valued stochastic process $x(t)$, the expected value $\mu_x(t_l)$ at time instance t_l defined as [19]

$$\mu_x(t_l) = \mathrm{E}\{x_i(t_l)\} = \lim_{n_e \to \infty} \frac{1}{n_e} \sum_{i=1}^{n_e} x_i(t_l) \tag{2.46}$$

and the correlation function

$$R_{xx}(t_l, t_l + \tau) = \mathrm{E}\{x_i(t_l) x_i(t_l + \tau)\} = \lim_{n_e \to \infty} \frac{1}{n_e} \sum_{i=1}^{n_e} x_i(t_l) x_i(t_l + \tau). \tag{2.47}$$

$\mathrm{E}\{\cdot\}$ generally denotes the expectation operator. In the later equation, τ represents a time offset. Now, $x(t)$ is said to be a weakly stationary stochastic process if both the mean and the autocorrelation function are independent of the selection of the fixed time t_l, that is, $\mu_x(t_l) = \mu_x$ and $R_{xx}(t_l, t_l + \tau) = R_{xx}(\tau)$.

Obviously, from an experimental point of view, the stationarity property is hard to prove, or it is cumbersome to estimate the underlying statistical moments. The reason for this is that many realizations would need to be gathered that represent the same experiment conducted in the same way (cf. [29, p. 64]). Fortunately, many physical processes are stationary. A simple example of that could be a building such as a bridge that naturally reacts to some excitation in the exact same chronological manner if the same loads are applied as well as the condition and the initial state of the structure are alike.

As explained above, stationarity of a stochastic process $x(t)$ manifests itself by considering the ensemble $\{x_i(t)\}$ and the corresponding mean and autocorrelation function given by the Eqs. 2.46 and 2.47. Stationary stochastic processes are also ergodic if these ensemble-averaged values are equal to the time-averaged values [19]. Therefore, consider the mean value $\mu_x(i)$ of the ith sample function defined as

$$\mu_x(i) = \mathrm{E}\{x_i(t)\} = \lim_{T \to \infty} \frac{1}{2T} \int_{-T}^{T} x_i(t), \tag{2.48}$$

where T denotes some time interval. Further, consider the corresponding autocorrelation function given by

$$R_{xx}(\tau, i) = \mathrm{E}\{x_i(t) x_i(t + \tau)\} = \lim_{T \to \infty} \frac{1}{2T} \int_{-T}^{T} x_i(t) x_i(t + \tau). \tag{2.49}$$

If $x(t)$ is ergodic, then the choice of the sample function is irrelevant, and thus, $\mu_x(i) = \mu_x$ and $R_{xx}(\tau, i) = R_{xx}(\tau)$. In practice, stationary stochastic processes are typically ergodic as well, which is why, the associated statistical properties can be determined based on a single observation (sample function) [19].

In the following, stationary stochastic processes are implied to be ergodic.

2.2.2 Statistical properties

The probability of a random variable $x(t)$ being smaller or equal than some fixed value x is given by the *probability distribution function* or *cumulative distribution function (CDF)* $P(x) \in [0, 1]$ that is defined as

$$P(x) = \text{Prob}\{x(t) \leqslant x\}. \tag{2.50}$$

Here, $\text{Prob}\{\cdot\}$ denotes the probability of some event. Based on that, the *probability density function (PDF)* can be computed through differentiation such that

$$p(x) = \frac{dP(x)}{dx}. \tag{2.51}$$

Obviously, the latter represents the rate of change of probability for $x(t)$ to take a certain value x [19]. Moreover, the partial integral of $p(x)$ for the interval $[x_1, x_2]$ is equal the probability of $x(t)$ to take any value within that range [29]. This is expressed by

$$\text{Prob}\{x_1 \leqslant x(t) \leqslant x_2\} = \int_{x_1}^{x_2} p(x). \tag{2.52}$$

Thus, the total integral of $p(x)$ from $-\infty$ to ∞ is equal to one.

Both the probability distribution and the PDF inherently depend on the underlying statistics. The most popular probability distribution is the normal or Gaussian distribution with PDF

$$p(x) = \frac{1}{\sigma_x \sqrt{2\pi}} e^{-\frac{(x-\mu_x)^2}{2\sigma_x^2}}. \tag{2.53}$$

Here, σ_x^2 denotes the variance of a univariate random variable $x(t)$, which refers to the second *central statistical moment* of $x(t)$, as shall be explained in the proceeding paragraph. σ_x is the so-called standard deviation. Both the variance and the standard deviation are measures to quantify how close or far the value of a random variable might be from its mean. From Eq. 2.53, it follows that the Gaussian distribution is only defined by two parameters, namely by the mean value and the variance. A random variable $x(t)$ following a Gaussian distribution with mean μ_x and variance σ_x^2 is introduced by $x(t) \sim \mathcal{N}(\mu_x, \sigma_x^2)$.

Probability distribution functions and PDFs are powerful but analytical formulations that can only be approximated given finite amounts of measured data. However, a practical concept to visualize the distribution of random variables are the well-known *histograms*. They are created by dividing the range of measured values into subintervals of uniform span Δx. Then, for each of these so-called bins, the occurrences of x falling within the corresponding range are counted. Despite their appearance, histograms do not function as discrete surrogates for PDFs, as they simply display the number of occurrences of certain events. However, they can

be scaled so that they represent a sample probability density function with sample probability $p_i(x)$ of the ith bin computed by [29]

$$p_i(x) = \frac{n_{s,i}}{n_s}\frac{1}{\Delta x}. \tag{2.54}$$

Histograms do not postulate any specific probability distributions. However, if no information regarding the distribution of data is available, histograms can be used as a basis for deriving such functions.

Another powerful tool for the nonparametric (distribution-free) analysis of random data are *empirical CDFs* denoted as $P_e(x)$, which only assume that the random variables x are independent and identically distributed. Equivalent to its continuous counterpart defined in Eq. 2.50, $P_e(x) \in [0, 1]$. The empirical CDF is determined by sorting the n_s acquired values for x_k in an ascending order. Then the percentile of the ith value is equal to i/n_s so that [54]

$$P_e(x) = \frac{n_{x_k<x}}{n_s}, \tag{2.55}$$

where $n_{x_k<x}$ denotes the number of values of x_k that are smaller than some fixed value x. Empirical CDFs play an important role in hypothesis testing when the distribution of the data is unknown, as will be explained in Section 4.4.2.

STATISTICAL MOMENTS AND CENTRAL STATISTICAL MOMENTS

Both the mean value and the variance constitute statistical moments with certain orders. Statistical moments are parameters that are used to characterize stochastic processes. They are directly related to the shape of PDFs. Given the PDF $p(x)$, e.g. for a Gaussian distribution defined by Eq. 2.53, the ith order statistical moment $m_{x,i}$ is given by [150]

$$m_{x,i} = \mathrm{E}\Big\{x(t)^i\Big\} = \int_{-\infty}^{\infty} x^i p(x)\,dx. \tag{2.56}$$

The mean value of a stationary, ergodic stochastic process $x(t)$ is the first statistical moment:

$$\mu_x = m_{x,1} = \lim_{T\to\infty}\frac{1}{2T}\int_{-T}^{T} x(t) = \int_{-\infty}^{\infty} x^1 p(x)\,dx. \tag{2.57}$$

It can be approximated using n_s samples such that [29]

$$\hat{\mu}_x = \frac{1}{n_s}\sum_{k=1}^{n_s} x_k, \tag{2.58}$$

where $\hat{(\cdot)}$ denotes the estimate.

Furthermore, the central statistical moments depicted as $m'_{x,i}$ are defined similarly to Eq. 2.56 as [29, 150]

$$m'_{x,i} = \mathrm{E}\Big\{\big(x(t) - \mu_x\big)^i\Big\} = \int_{-\infty}^{\infty} (x - \mu_x)^i p(x)\,dx. \tag{2.59}$$

As noted before, the variance σ_x^2 represents the second central statistical moment, that is, $\sigma_x^2 = m'_{x,2}$. Equivalently to Eq. 2.57, the following holds:

$$\sigma_x^2 = m'_{x,2} = \lim_{T\to\infty}\frac{1}{2T}\int_{-T}^{T}(x(t) - \mu_x)^2 = \int_{-\infty}^{\infty}(x - \mu_x)^2 p(x)\,dx. \tag{2.60}$$

Consequently, an estimate can also be found by [19]

$$\hat{\sigma}_x^2 = \frac{1}{n_s - 1} \sum_{k=1}^{n_s} (x_k - \hat{\mu}_x)^2. \tag{2.61}$$

The estimates given by Eqs. 2.58 and 2.61 are crucial for the characterization of discrete-time scalar-valued stochastic processes. Naturally, these sequences are sampled point-wise and characterizations must be made from finite observations. Hence, $\hat{\mu}_x$ and $\hat{\sigma}_x^2$ are often called sample mean and sample variance, respectively. In contrary to Eq. 2.58, in Eq. 2.61, the summation is premultiplied by $1/n_s-1$ to achieve an *unbiased estimate*, that is, the estimated value converges towards the true value [19, p. 79 ff.]. Nevertheless, premultiplying by $1/n_s-1$ or $1/n_s$ does not make a significant difference when large amount of samples are used.

It should be noted that higher-order central statistical moments such as skewness and kurtosis appear to be useful in some disciplines of SHM, e.g., as damage indicators for damage detection [78]. However, in the present work, such parameters are not utilized, and hence, the interested reader is referred to the cited literature for further information.

JOINT AND MULTIVARIATE STATISTICS

Only single and scalar-valued stochastic processes have been regarded in the previous elaborations. However, a common case is that multiple stochastic processes, which are not independent of each other, are involved in certain analyses. Therefore, the theory of joint statistics should be introduced here. Stochastic processes generally manifest themselves as multivariate (vector-valued) processes in the present work. Examples of that are stochastic inputs or outputs of MIMO systems. In these cases, the single univariate processes that form the multivariate process are not independent of each other and, therefore, should be regarded mutually from a statistical point of view. The formulations made before can be extended to the case of joint and multivariate statistics. This paragraph is mainly dedicated to multivariate statistics and only summarizes the most relevant concepts for this thesis.

Consider the scalar-valued, stationary, and ergodic stochastic processes $x(t)$ and $y(t)$ with mean values μ_x and μ_y represented by the first statistical moment defined by Eq. 2.57. Both processes result from a joint PDF $p(x, y)$ so that the covariance can be defined by [19]

$$\sigma_{xy}^2 = \mathrm{E}\{(x(t) - \mu_x)(y(t) - \mu_y)\} = \int_{-\infty}^{\infty}\int (x(t) - \mu_x)(y(t) - \mu_y) p(x, y)\, dx\, dy \tag{2.62a}$$

$$= \lim_{T\to\infty} \frac{1}{2T} \int_{-T}^{T} (x(t) - \mu_x)(y(t) - \mu_y). \tag{2.62b}$$

Obviously, the covariance can be interpreted as a measure of the correlatedness of two stochastic processes. Further, the covariance function $R'_{xy}(\tau)$ can be derived similar to the correlation function given in Eq. 2.49. It is defined as

$$R'_{xy}(\tau) = \mathrm{E}\{(x(t) - \mu_x)(y(t + \tau) - \mu_y)\} = \lim_{T\to\infty} \frac{1}{2T} \int_{-T}^{T} (x(t) - \mu_x)(y(t + \tau) - \mu_y). \tag{2.63}$$

Hereby, the correlation of the stochastic process $x(t)$ and time-shifted versions of $y(t)$ are quantified by introducting the variable τ. Considering Eqs. 2.62, 2.63, 2.60, and 2.49, the following observations can be made:

- $\sigma_{xy}^2 = R'_{xy}(0)$,
- $R'_{xx}(0) = \sigma_x^2$,
- $R_{xy}(\tau) = R'_{xy}(\tau)$ if $\mu_x = 0$ and $\mu_y = 0$,
- $R_{xy}(-\tau) = R_{xy}(\tau)$.

The terms autocovariance or autocorrelation are readily used in the literature when $x = y$. Accordingly, cross-covariance and cross-correlation imply $x \neq y$. In the following, this distinction is not strictly obeyed. However, autocovariance and -correlation will be highlighted by neglecting the second subscript.

The concept of covariance (and correlation) and covariance functions (and correlation functions) can be easily extended to m-dimensional multivariate stochastic processes. Then, e.g., R'_{xy} denotes the (cross-) covariance matrix of the multivariate random variables x and y such that

$$R'_{xy} = \mathrm{E}\Big\{(x(t) - \mu_x)(y(t) - \mu_y)^{\mathrm{T}}\Big\} = \begin{bmatrix} \sigma_{x_1y_1}^2 & \sigma_{x_1y_2}^2 & \dots & \sigma_{x_1y_m}^2 \\ \sigma_{x_2y_1}^2 & \sigma_{x_2y_1}^2 & \dots & \sigma_{x_2y_m}^2 \\ \vdots & \vdots & \ddots & \vdots \\ \sigma_{x_my_1}^2 & \sigma_{x_my_2}^2 & \dots & \sigma_{x_my_m}^2 \end{bmatrix}. \tag{2.64}$$

Equivalently to Eq. 2.61, covariance matrices can be estimated as

$$\hat{R}'_{xy} = \frac{1}{n_s - 1} \sum_{k=1}^{n_s} (x_k - \hat{\mu}_x)(y_k - \hat{\mu}_y)^{\mathrm{T}}, \tag{2.65}$$

which is essential when dealing with discrete-time processes. Therein, $\hat{\mu}_x$ and $\hat{\mu}_y$ are column-vectors computed with help of 2.58 for the associated multivariate processes. An estimator for matrix-valued covariance functions of sampled data is given by [19]

$$\hat{R}'_{xy}(i) = \frac{1}{n_s - i} \sum_{k=1}^{n_s - i} (x_k - \hat{\mu}_x)(y_{k+i} - \hat{\mu}_y)^{\mathrm{T}}, \tag{2.66}$$

where i denotes the time shift operator similar to τ.

A remark should be made for joint PDFs and multidimensional PDFs. Although they inherently play an important role in the context of this work, they are not utilized or derived for any analyses made herein. Therefore, the interested reader is referred to the literature. For Gaussian distributions, see [19, p. 62 ff.].

Notational remark: As implied in the itemization above, correlation is a special case of covariance. Hence, in engineering literature, the terms covariance and correlation are often not properly distinguished. For simplicity, in the later chapters, covariance matrices for mean-free processes are written without a prime. To clarify the underlying computation, the operator $\mathrm{E}\{\cdot\}$ shall be readily used.

2.2.3 Correlation function and power spectral density

Correlation functions comprise potent tools to characterize stationary stochastic processes from a statistical point of view. However, they also allow for a physical interpretation, as the autocorrelation $R_x(0)$ is directly related to the average power of the signal $x(t)$ [29]. The properties of correlation functions can be assessed not only in the time domain but also in the frequency domain. The transformation is realized through the Fourier transform or bilateral Laplace and z-transform by defining $s = j\omega$ or $z = e^{j\omega\Delta t}$, respectively, introduced in Section 2.1.3.

Consider the correlation function $R_{xy}(\tau)$ of two stationary stochastic processes $x(t)$ and $y(t)$. Then, the power spectral density (PSD) function denoted by $S_{xy}(j\omega)$ is defined as

$$S_{xy}(j\omega) = \mathcal{F}\{R_{xy}(\tau)\} = \int_{-\infty}^{\infty} R_{xy}(\tau)e^{-j\omega\tau}\,d\tau, \tag{2.67}$$

cf. Eq. 2.41. For Eq. 2.67 to be feasible, the integral over the interval $(-\infty, \infty)$ of the absolute values of $R_{xy}(\tau)$ must be finite. Further, there exists the inverse operation

$$R_{xy}(\tau) = \mathcal{F}^{-1}\{S_{xy}(j\omega)\} = \frac{1}{2\pi}\int_{-\infty}^{\infty} S_{xy}(j\omega)e^{j\omega\tau}\,d\omega \tag{2.68}$$

that perfectly recovers $R_{xy}(\tau)$, cf. Eq. 2.42. This connection of the correlation function and the PSD through the Fourier transform and inverse Fourier transform was simultaneously proven by the mathematicians Norbert Wiener and Aleksandr Khinchine, and therefore, is known as the *Wiener-Khinchine theorem* [19]. The PSD function given by Eq. 2.67 is also called two-sided PSD as it is defined for $\omega \in (-\infty, \infty)$. The one-sided PSD can be derived by doubling $S_{xy}(j\omega)$ and solely considering the interval $[0, \infty)$. $S_{xy}(j\omega)$ is also referred to as cross-PSD function. Though, considering $R_x(\tau)$ for Eq. 2.67 results in the so-called *auto-PSD function*. Similar to the correlation function, this distinction is not made consistently throughout this thesis. Auto-PSD functions are rather highlighted by omitting one of the redundant subscripts such that $S_x := S_{xx}$. Finally, it should be noted that the auto PSD is a real-valued function, whereas the cross PSD is complex-valued [19]. When multivariate processes are considered, the PSD becomes a symmetric, positive-definite, matrix-valued complex function (cf. Eq. 2.64) containing the auto-PSD entries on the main diagonal and the cross-PSD entries elsewhere.

Estimating correlation functions and PSD functions based on finite amounts of sampled data is crucial for this work. In the previous section, a rather simple but intuitive estimator for correlation functions was introduced, see Eq. 2.66. Regarding Eq. 2.68, an alternative to that could be established through the inverse Fourier transformation of an estimated PSD function. However, given finite amounts of sampled data, two things must be satisfied to realize this. The *discrete Fourier transform (DFT)* and its inverse realization, as well as the *discrete-time Fourier transform (DTFT)* must be utilized. Further, an efficient estimation strategy for PSD functions should be considered. Central element for the derivation of discrete PSD and correlation functions connected through the DFT is the continuous periodic PSD function $S_{xy}(e^{j\omega})$ defined as [167]

$$S_{xy}(e^{j\omega}) = \sum_{i=-\infty}^{\infty} R_{xy}(i)e^{-j\omega i}. \tag{2.69}$$

This function results from a DTFT, which maps an infinite sequence of uniformly sampled data to a continuous function of frequency with a periodicity of 2π. It is symmetric about $\omega = 0$. Similar to Eq. 2.68, this PSD function can be transformed back to the time domain with the help of the inverse Fourier transform such that

$$R_{xy}(i) = \frac{1}{2\pi}\int_{-\pi}^{\pi} S_{xy}(e^{j\omega})e^{j\omega i}\, d\omega. \tag{2.70}$$

Now, suppose that $R_{xy}(i)$ results from the processes x_k and y_k sampled with the sampling frequency $f_s = 1/\Delta t$ (in Hz), then it might be desirable to obtain a PSD function with a periodicity of $2\pi f_s$. This normalization increases the physical interpretability in terms of the average signal power for certain frequency ranges. On the other hand, it enables computations in combination with the discrete-time transfer function of LTI systems (cf. Eq. 2.36), which will be exploited in the following sections. To this end, Eq. 2.69 is modified by considering the sampling period Δt such that [135]

$$S_{xy}(e^{j\omega\Delta t}) = \sum_{i=-\infty}^{\infty} R_{xy}(i)e^{-j\omega i\Delta t}. \tag{2.71}$$

Obviously, this equation is equal to the bilateral z-transform of the discrete-time correlation function with $z = e^{j\omega\Delta t}$, cf. Eq. 2.33. To recover $R_{xy}(i)$, compute

$$R_{xy}(i) = \frac{\Delta t}{2\pi}\int_{-\pi/\Delta t}^{\pi/\Delta t} S_{xy}(e^{j\omega\Delta t})e^{j\omega i\Delta t}\, d\omega. \tag{2.72}$$

It remains the question of how to estimate a discrete PSD function from finite data. A few strategies exist for this purpose. However, one of the most popular approaches is Welch's method, which was published by Peter Welch in 1967 [209]. For this method, the signals x_k and y_k are divided into m possibly overlapping blocks. Then, for each block, a so-called periodogram is computed by multiplying the DFTs of the corresponding signals. Finally, an estimated PSD function $\hat{S}_{xy}(e^{j\omega\Delta t})$ results from averaging the periodograms for all m blocks. Typically, this method is conducted employing the fast Fourier transform (FFT), a numerically efficient version of the DFT. Moreover, additional tools such as windowing or zero-padding are readily applied to avoid leakage effects or to increase the frequency resolution of the PSD functions artificially. For more details on that, see, e.g., [29].

PHYSICAL INTERPRETATIONS

Previously, it was stated that signals in the time and frequency domain are related through the Fourier transform. Obviously, a special case constitutes the transformation of the autocorrelation function to the auto PSD function and vice versa. This connection is known as the Wiener-Khinchine theorem, as mentioned before. Moreover, this theorem is closely related to *Parseval's theorem*, which essentially states that the energy or average power of a signal is conserved in either domain. In case of a stationary random signal x_k, this is demonstrated by considering Eq. 2.72 for $i = 0$. Then, under consideration of the theory presented in Section 2.2.1, one yields

$$R_x(0) = \mathrm{E}\left\{x_k x_k^{\mathrm{T}}\right\} = \frac{\Delta t}{2\pi}\int_{-\pi/\Delta t}^{\pi/\Delta t} S_x(e^{j\omega\Delta t})\, d\omega. \tag{2.73}$$

Consequently, the average power of the signal, which can be written as $\mathrm{E}\{x_k x_k^{\mathrm{T}}\}$, is equal to its correlation and the area under the PSD function. By integrating $S_x(e^{j\omega\Delta t})$ for a certain frequency range, say $[2\pi f_1, 2\pi f_2]$, $f_2 > f_1$, the average power of x_k for this frequency interval can be assessed. Thus, a signal featuring equal power over all frequencies has a constant PSD. Such signals, which play a crucial role in the analysis of random processes and many engineering disciplines, are called *white noise*. The corresponding autocorrelation function yields zero for all $i \neq 0$. It should be mentioned that the terminology of power and energy is only entirely adequate in an electrical sense if x_k refers to voltage. Nevertheless, this formulation is readily used in experimental dynamics and in this thesis. An alternative characterization of signals is often made by means of root mean square (RMS) values, which equal the square root of the autocorrelation.

2.3 SYSTEM IDENTIFICATION

Since the inherent objective of SHM is to identify changes in the dynamic behavior, the repetitive realization of the system and tracking of modal parameters plays an important role. In civil engineering, where the regarded structures typically are of large size and are excited ambiently, a classical determination of the input-output relationship is exceptionally challenging. Hence, so-called *output-only methods* for modal and system identification, which are also referred to as Operational Modal Analysis (OMA), have been developed since the mid-1990s. These techniques only consider the measured system response, which is enabled by the assumption of a stochastic input. Therefore, they quickly gained great popularity. In this work, the Stochastic Subspace Identification (SSI) method is applied for the extraction of modal parameters from structural measurements but, more importantly, for the realization of state-space models. The stochastic realization theory initiated by Akaike [1] and Faurre [75] builds the foundation for that, and hence, is briefly introduced first.

2.3.1 Realization of stochastic systems

Consider the following discrete-time LTI system with finite model order n:

$$x_{k+1} = Ax_k + w_k \tag{2.74a}$$

$$y_k = Cx_k + v_k. \tag{2.74b}$$

Here, the process noise $w_k \in \mathbb{R}^n$ represents the excitation of the underlying system, and the measured signals $y_k \in \mathbb{R}^q$ are disturbed by the measurement noise $v_k \in \mathbb{R}^q$. The noise processes $w_k \sim \mathcal{N}(0, Q)$ and $v_k \sim \mathcal{N}(0, R_v)$ are assumed to be stationary and white. The mutual covariance matrix may be written as

$$M\delta_{kl} = \mathrm{E}\left\{ \begin{bmatrix} w_k \\ v_k \end{bmatrix} \begin{bmatrix} w_l \\ v_l \end{bmatrix}^{\mathrm{T}} \right\} = \begin{bmatrix} Q & S \\ S^{\mathrm{T}} & R_v \end{bmatrix} \delta_{kl} \tag{2.75}$$

$$= \begin{bmatrix} \Sigma_x - A\Sigma_x A^{\mathrm{T}} & N - A\Sigma_x C^{\mathrm{T}} \\ N^{\mathrm{T}} - C\Sigma_x A^{\mathrm{T}} & R_y(0) - \Sigma_x - C\Sigma_x C^{\mathrm{T}} \end{bmatrix} \delta_{kl} \geqslant 0, \tag{2.76}$$

where $S \in \mathbb{R}^{n \times q}$ describes the joint covariance matrix of process and measurement noise, and δ_{kl} denotes the Kronecker delta, which is defined as

$$\delta_{kl} = \begin{cases} 1, & k = l, \\ 0, & k \neq l. \end{cases} \tag{2.77}$$

Eq. 2.76 results by applying expectations to Eq. 2.74. N is the covariance matrix of the future states x_{k+1} and the measured output y_k such that

$$N = \mathrm{E}\left\{x_{k+1} y_k^{\mathrm{T}}\right\} = A\Sigma_x C^{\mathrm{T}} + S. \tag{2.78}$$

Further, $\Sigma_x \in \mathbb{R}^{n \times n}$ denotes the state covariance matrix $\mathrm{E}\{x_k x_k^{\mathrm{T}}\}$, which follows the unique Lyapunov equation [75]

$$\Sigma_x = A\Sigma_x A^{\mathrm{T}} + Q, \tag{2.79}$$

cf. Eq. 2.43.

Because of the randomness of w_k, x_k is a stochastic process as well. Moreover, Eq. 2.74a reveals that x_{k+1} solely depends on the knowledge of x_k and w_k, making x a Markov process, see Section 2.2. By that, it follows that the system represented by Eq. 2.74 is a *Markov model* for the process y. The goal of the stochastic realization is to find all Markov models[6] that simulate the correlation function $R_y(i)$ or the associated PSD function $S_y(z)$ ($z = e^{j\omega\Delta t}$) (cf. Section 2.2.3) [110].

The stochastic realization theory is strongly related to the deterministic realization theory developed by Ho and Kalman [104] in the 1960s. They showed that the IRF of a discrete-time LTI system ordered in a block Hankel matrix is equal to the product of its observability and controllability matrices. Despite the theoretically infinite size of the Hankel matrix, the rank is known to be equal to the system order n.

For the stochastic realization, consider the following infinite-size block Hankel matrix with the correlation function $R_y(i)$:

$$H_\infty = \begin{bmatrix} R_y(1) & R_y(2) & R_y(3) & \dots \\ R_y(2) & R_y(3) & R_y(4) & \dots \\ R_y(3) & R_y(4) & R_y(5) & \dots \\ \vdots & \vdots & \vdots & \ddots \end{bmatrix}. \tag{2.80}$$

As for the deterministic realization theory, it is also assumed that the rank of H_∞ is equal to n [110]. Further, note that under consideration of Eq. 2.74, it follows that

$$R_y(i) = \begin{cases} R_y(0), & i = 0, \\ CA^{i-1}N, & i > 0. \end{cases} \tag{2.81}$$

The derivations of the factorizations of $R_y(i)$ and N are given in Appendix A.1. Akaike [1] showed that there exist a minimal realization (A, N, C, $R_y(0)$) for stochastic systems that

6 Note that by the similarity transformation (see Section 2.1.1), an infinite number of state-space representations exist that yield the same output y_k.

satisfies Eq. 2.81, just as the quadruplet (A, B, C, D) defines the IRF in the deterministic case [104]. This result seems rather intuitive when comparing Eqs. 2.81 and 2.28. As a consequence, a state-space system can be realized using (A, N, C, $R_y(0)$) with Eq. 2.81 being its IRF [110, p. 173]. Finally, the PSD function of y has the parametric factorization

$$S_y(z) = C(zI - A)^{-1}N + R_y(0) + N^{\mathrm{T}}(z^{-1}I - A^{\mathrm{T}})^{-1}C^{\mathrm{T}}, \tag{2.82}$$

where $z = e^{j\omega\Delta t}$.

Following the stochastic realization theory, the SSI and their variants represent powerful numerical tools for the identification of the state-space parameters based on measured data. There, the SVD plays a crucial role in the decomposition of certain block matrices. This procedure was suggested ten years after the publication of Ho's and Kalman's approach by Zeiger and Ewen [223]. Algorithms for the SSI are typically based on the direct application of the deterministic realization approach, as explained before, or on the canonical correlation analysis (CCA) of future and past observations [110]. The latter approach was initiated by Akaike [2, 3] in the 1970s; it led to valuable contributions and algorithms in the 1990s, e.g., by van Overschee and de Moor, and Verhaegen [147, 148, 203]. These projection-based approaches heavily rely on the QR or LQ decomposition [111]. From a stochastic realization viewpoint, the goal of the SSI is to find the minimal realization (A, N, C, $R_y(0)$) that fits the covariance function given in Eq. 2.81 to its measured pendant. Nevertheless, from the perspective of modal analysis or OMA the focus rather lies on the identification of dominant and stable modes, which is typically realized by the use of stabilization diagrams [152]. The SSI is often distinguished between the data-driven SSI (SSI-DAT) and the covariance-driven SSI (SSI-COV), although both approaches are strongly related, as will be shown herein. Nevertheless, to fit this classification of the standard literature on OMA [163], the next two sections follow this differentiation.

POSITIVITY AND REALNESS OF $R_y(i)$

A last remark should be made concerning the positive definiteness of the covariance sequence $R_y(i)$ as a function of (A, N, C, $R_y(0)$), see Eq. 2.81. This sequence should be a positive real sequence, which is identical to the fact that the spectral matrices $S_y(z)$ given by Eq. 2.82 are positive real for every z [147]. The opposite would imply that the measured output has negative power, which has no physical interpretation. The major reason for non-positive covariance sequences lies in using finite measurement time-series to estimate covariances or the computation of a projection matrix. Further discussions on that are made in [52]. Few algorithms exist that guarantee a positive real covariance sequence [110, 147]. In fact, the procedures overviewed in the proceeding sections do not possess this property, which is not problematic, as independent of the choice of method, the positivity cannot be guaranteed after applying model reduction techniques. Further, in an OMA context, this issue is readily disregarded, as the extraction of modal parameters remains feasible. Nevertheless, it should be mentioned that the positivity of $R_y(i)$ plays an important role in the identification of covariance-based Kalman filters constructed by means of the stochastic realization theory and the SSI. In these cases, a stabilizing solution to a discrete-time algebraic Riccati equation (DARE) must be found, which is only possible if $R_y(i)$ is a non-negative definite sequence.

2.3.2 Covariance-Driven SSI

The first identification algorithm presented here is based on the deterministic realization theory by Ho and Kalman [104]. It starts by assembling a block Hankel matrix $H \in \mathbb{R}^{ql \times qm}$ with a user-defined number of block rows l and block columns m with estimated covariance matrices $R_y(i)$ such that

$$H = \begin{bmatrix} R_y(1) & R_y(2) & \dots & R_y(m) \\ R_y(2) & R_y(3) & \dots & R_y(m+1) \\ \vdots & \vdots & \ddots & \vdots \\ R_y(l) & R_y(l+1) & \dots & R_y(l+m-1) \end{bmatrix}. \tag{2.83}$$

The number of block rows and columns should be chosen large enough so that $n < l \leqslant m$ [110, p. 144]. As noted before, $H = O\Gamma$ with

$$O = \begin{bmatrix} C \\ CA \\ \vdots \\ CA^{l-1} \end{bmatrix} \in \mathbb{R}^{ql \times n}, \quad \Gamma = \begin{bmatrix} N & AN & \dots & A^{m-1}N \end{bmatrix} \in \mathbb{R}^{n \times qm}. \tag{2.84}$$

Both the observability matrix O and the controllability matrix Γ can be constructed with the help of the SVD. Therefore, consider the arbitrary weighting matrices $W_1 \in \mathbb{R}^{ql \times ql}$ and $W_2 \in \mathbb{R}^{ml \times ml}$ that can be chosen to implement different versions of the SSI-COV, as will be explained later on. Then, H can be decomposed to

$$W_1 H W_2 = U \bar{S} V^{\mathrm{T}} = \begin{bmatrix} U_1 & U_2 \end{bmatrix} \begin{bmatrix} S_1 & 0 \\ 0 & 0 \end{bmatrix} \begin{bmatrix} V_1^{\mathrm{T}} & V_2^{\mathrm{T}} \end{bmatrix} \simeq U_1 S_1 V_1^{\mathrm{T}}, \tag{2.85}$$

where $U \in \mathbb{R}^{ql \times ql}$ and $V \in \mathbb{R}^{qm \times qm}$ denote the left- and right-hand singular vectors, respectively. $\bar{S} \in \mathbb{R}^{ql \times qm}$ is a rectangular matrix that theoretically contains n non-zero singular values represented by the diagonal matrix $S_1 \in \mathbb{R}^{n \times n}$ [134]. $U_1 \in \mathbb{R}^{ql \times n}$ and $V_1 \in \mathbb{R}^{ql \times n}$ denote the corresponding singular vectors.

In practice, where the model order n is unknown, H has full rank, and the number of the non-singular values is equal to the minimum of ql and qm. Consequently, n must be chosen in advance and S_1 represents the n greatest singular values of $\bar{S}$ with corresponding singular vectors U_1 and V_1 so that O and Γ can be approximated by

$$O = W_1^{-1} U_1 S_1^{1/2} \quad \text{and} \quad \Gamma = S_1^{1/2} V_1^{\mathrm{T}} W_2^{-1}. \tag{2.86}$$

Finally, C and n can be simply extracted from the first q rows or columns of O and Γ, respectively. The system matrix A results from

$$A = \underline{O}^{\dagger} \overline{O}. \tag{2.87}$$

Therein, $\underline{O}$ depicts a subset of O, where the last q columns are omitted. In the case of $\overline{O}$, the first q rows are left aside. $(\cdot)^{\dagger}$ denotes the Moore-Penrose inverse (pseudoinverse) [134].

Before leaving the field of the SSI-COV, possible choices for W_1 and W_2 are presented that result in different versions of the identification method. Essentially, the weighting leads to a specific scaling of the singular values and relations of the subspaces spanned by the singular vectors. For more details on that, see [110]. Tab. 2.1 gives an overview of possible choices for the weighting matrices. In the CCA-based algorithm, Φ_{ff} and Φ_{pp} obey a Toeplitz structure.

Table 2.1: Weighting matrices W_1 with size $ql \times ql$ and W_2 with size $ml \times ml$ according to different realization algorithms of the SSI-COV.

	W_1	W_2
Ho-Kalman-based stochastic realization algorithm [110, p. 198]	I	I
CCA-based stochastic realization algorithm [110, p. 208, 227 ff.]	$\Phi_{ff}^{-1/2}$	$\left(\Phi_{pp}^{-1/2}\right)^{\mathrm{T}}$

They are defined as

$$\Phi_{ff} = \Phi_{pp}^{\mathrm{T}} = \begin{bmatrix} R_y(0) & R_y(1)^{\mathrm{T}} & \dots & R_y(r-1)^{\mathrm{T}} \\ R_y(1) & R_y(0) & \dots & R_y(r-2)^{\mathrm{T}} \\ \vdots & \vdots & \ddots & \vdots \\ R_y(r-1) & R_y(r-2) & \dots & R_y(0) \end{bmatrix}. \tag{2.88}$$

Φ_{ff} and Φ_{pp} must be of appropriate size, and thus, r has to be chosen as l or m, respectively.

2.3.3 Data-Driven SSI

For SSI-DAT, the time sequences of the measurement data are used directly instead of estimated covariance matrices of the output. Hence, projections enable the model realization procedure. The algorithm starts by assembling block Hankel matrices of the past and future outputs with measured data:

$$Y_p = \begin{bmatrix} y_0 & y_1 & \cdots & y_{m-1} \\ y_1 & y_2 & \cdots & y_m \\ \vdots & \vdots & \ddots & \vdots \\ y_{l-1} & y_l & \cdots & y_{l+m-2} \end{bmatrix} \in \mathbb{R}^{ql \times m} \quad \text{and} \quad Y_f = \begin{bmatrix} y_l & y_{l+1} & \cdots & y_{l+m-1} \\ y_{l+1} & y_{l+2} & \cdots & y_{l+m} \\ \vdots & \vdots & \ddots & \vdots \\ y_{2l-1} & y_{2l} & \cdots & y_{2l+m-2} \end{bmatrix} \in \mathbb{R}^{ql \times m}. \tag{2.89}$$

Here, l denotes the number of block rows, and m represents the number of columns, which are both user-defined parameters. It is a common opinion that the latter should be chosen large enough to enable a proper system identification. Moreover, to store all information of a data set with n_s samples, m must be equal to $n_s - 2l + 1$. However, as Priori at al. [161] point out, the computational effort should be considered as well, and therefore, they provide a lower bound for m. Regarding the selection of l, a common approach is to choose this value based on the ratio of the sampling frequency and the lowest natural frequency of interest [171].

The two matrices Y_p and Y_f lay the foundation for the construction of the so-called projection matrix P_o defined as [147]

$$P_o = Y_f Y_p^{\mathrm{T}} \left(Y_p Y_p^{\mathrm{T}} \right)^{\dagger} Y_p. \tag{2.90}$$

This formulation rather follows a geometrical interpretation, that is, the rows of the past outputs Y_p form a reference vector space onto which the rows of the future outputs Y_f are projected. The idea behind it is to retain relevant information from the past to predict the outputs in the future [152]. The relevance of information is quantified through the correlation of past and future, which is essentially represented by $(1/m)Y_f Y_p^{\mathrm{T}}$. In fact, P_o is numerically computed, e.g., with the help of the LQ decomposition, which is the transpose of the QR decomposition [110, 134]. This operation considers the joint block Hankel matrix $H \in \mathbb{R}^{2ql \times m}$ that decomposes to [163]

$$H = \frac{1}{\sqrt{m}} \begin{bmatrix} Y_p \\ Y_f \end{bmatrix} = \begin{bmatrix} L_{11} & 0 \\ L_{21} & L_{22} \end{bmatrix} \begin{bmatrix} Q_1^{\mathrm{T}} \\ Q_2^{\mathrm{T}} \end{bmatrix}. \tag{2.91}$$

Then, the projection matrix finally yields

$$P_o = L_{21} Q_1^{\mathrm{T}} \in \mathbb{R}^{ql \times m}. \tag{2.92}$$

Similar to the decomposition of the Hankel matrix in Eq. 2.85, P_o is decomposed employing the SVD under the consideration of arbitrary weighting matrices such that

$$W_1 P_o W_2 = \begin{bmatrix} U_1 & U_2 \end{bmatrix} \begin{bmatrix} S_1 & 0 \\ 0 & 0 \end{bmatrix} \begin{bmatrix} V_1^{\mathrm{T}} & V_2^{\mathrm{T}} \end{bmatrix} \simeq U_1 S_1 V_1^{\mathrm{T}}. \tag{2.93}$$

In practice, S_1 contains as many non-zero singular values as the minimum dimension of P_o so that n needs to be chosen a priori. Together with the corresponding singular vectors U_1 and V_1, the observability can be constructed according to Eq. 2.86. Note that when conducting the SSI-DAR as presented here and as proposed by van Overschee and de Moor, the controllability matrix has a reversed structure and is thus written as Γ'. It reads [147]

$$\Gamma' = S_1^{1/2} V_1^{\mathrm{T}} W_2^{-1} = \begin{bmatrix} A^{l-1}N & \dots & AN & N \end{bmatrix}. \tag{2.94}$$

Consequently, N is found in the last q columns of Γ'. As for A and C, the identification procedure is identical to the SSI-COV. The entire identification strategy presented here refers to Algorithm 2 in [147].

As in the previous section, different choices for W_1 and W_2 lead to different versions of the identification. A selection of possible weightings is given in Tab. 2.2. Note that the Toeplitz matrices Φ_{ff} and Φ_{pp} with appropriate dimensions ($r = l$) for the realization of the PC and the CVA follow the definitions of Eq. 2.88. Generally, the approaches mentioned in Tab. 2.2 differ in such a way that they yield state-space models, which are balanced in a certain sense, and the obtained singular values can be interpreted differently, see [147, p. 77 ff.].

Table 2.2: Weighting matrices W_1 with size $ql \times ql$ and W_2 with size $ml \times ml$ according to different realization algorithms of the SSI-DAT [147].

	W_1	W_2
Principal component algorithm (PC)	I	$Y_p^{\mathrm{T}} \Phi_{pp}^{-1/2} Y_p$
Unweighted principal component algorithm (UPC)	I	I
Canonical variate algorithm (CVA)	$\Phi_{ff}^{-1/2}$	I

DATA-DRIVEN CCA-BASED SSI

The previous elaborations show that the SSI-COV and SSI-DAT are strongly related. Even though measurement time series are directly utilized for the latter, the projection conducted for the SSI-DAT essentially leads to the estimation and processing of covariance matrices, see Eq. 2.90. Moreover, the CCA-based version of the SSI-COV, based on the work of Akaike and Katayama [2, 3, 110] (see Tab. 2.1), is a data-driven algorithm in its initial configuration. In the following, this balanced realization method is summarized in brevity to emphasize the connection of the general SSI approaches again.

In addition to the block Hankel matrix Y_f given in Eq. 2.89, the block Toeplitz matrix for the past outputs denoted by $\check{Y}_p$ is defined as

$$\check{Y}_p = \begin{bmatrix} y_{l-1} & y_l & \cdots & y_{l+m-2} \\ y_{l-2} & y_{l-1} & \cdots & y_{l+m-3} \\ \vdots & \vdots & \ddots & \vdots \\ y_0 & y_1 & \cdots & y_{m-1} \end{bmatrix} \in \mathbb{R}^{ql \times m}. \tag{2.95}$$

Then, similar to Eq. 2.91, an LQ decomposition yields [110, p. 227]

$$\frac{1}{\sqrt{m}} \begin{bmatrix} \check{Y}_p \\ Y_f \end{bmatrix} = \begin{bmatrix} L_{11} & 0 \\ L_{21} & L_{22} \end{bmatrix} \begin{bmatrix} Q_1^{\mathrm{T}} \\ Q_2^{\mathrm{T}} \end{bmatrix}, \tag{2.96}$$

which forms the basis for the computation of

$$H = \Phi_{fp} = L_{21} L_{11}^{\mathrm{T}}, \tag{2.97}$$

$$W_1 = \Phi_{ff}^{-1/2} = \left(L_{21} L_{21}^{\mathrm{T}} + L_{22} L_{22}^{\mathrm{T}} \right)^{-1/2}, \tag{2.98}$$

and

$$W_2 = \left(\Phi_{pp}^{-1/2} \right)^{\mathrm{T}} = \left(\left[L_{11} L_{11}^{\mathrm{T}} \right]^{-1/2} \right)^{\mathrm{T}}. \tag{2.99}$$

The remainder of the identification process from the SVD to the estimation of (A, C, N) is identical to the steps overviewed in Section 2.3.2.

3

LINEAR QUADRATIC ESTIMATION

In this thesis, linear quadratic estimators are exploited for damage detection and localization. More precisely, filters or predictors for the structure's measured responses are realized, and their corresponding estimation errors are utilized to infer damage. For their synthesis, two different approaches are considered, namely Kalman and $\mathcal{H}_\infty$ filtering. During the design, different cost functions are minimized, which is associated with the minimization of the $\mathcal{H}_2$ or $\mathcal{H}_\infty$ transfer function norms. To lay the basis for that, the necessary signal and system norms are explained first. Secondly, a general control framework is introduced, which enables the interpretations with respect to the system norms. Finally, the estimator design problems are addressed therein and in view of the intended purpose of damage identification.

3.1 SIGNAL AND SYSTEM NORMS AND SPACES

In control and estimation theory, norms, as a measure of size, are utilized to design controllers or estimators in the desired way or to evaluate their behavior and performance. In a few instances, norms are directly computed on systems. However, they are mainly applied to input and output signals, which are time- or frequency-domain functions in a mathematical sense, or to transfer functions, as these quantities are directly related to the systems. The mathematical foundation for the computation of signal and system norms is laid by the theory of *functional analysis*. In the following, the most relevant function spaces and norms are overviewed and interpreted to give a foundation for $\mathcal{H}_2$ and $\mathcal{H}_\infty$ optimal estimation, which is heavily exploited in this work. The concepts and derivations for this section are mainly collected from the textbooks [88, 192, 230].

3.1.1 Normed spaces

Mathematically speaking, signals are measured functions $f(x)$ of some argument x that constitute a map from an input to an output space, that is, $f : \mathcal{X} \to \mathcal{Y}$ with $x \in \mathcal{X}$. It can be said that signals lay within the output space $\mathcal{Y}$, which is a linear vector space over the field of complex numbers $\mathbb{C}$ or real numbers $\mathbb{R}$. To measure the 'size' of these functions in a certain sense, norms, denoted by $\|\cdot\|$, can be determined, which are functions themselves ($\|\cdot\| : \mathcal{Y} \to \mathbb{R}_0^+$) that result in some real scalar value. For a function to be a norm, the following properties must hold [192]:

(i)
$$\|f\| \geqslant 0, \tag{3.1}$$

(ii)
$$\|f\| = 0, \text{ iff } f = 0, \tag{3.2}$$

(iii)

$$\|\alpha f\| = |\alpha| \|f\|, \tag{3.3}$$

(iv)

$$\|f + g\| \leqslant \|f\| + \|g\|, \tag{3.4}$$

where $f, g \in \mathcal{Y}$, $\alpha \in \mathbb{C}$ or $\mathbb{R}$, and $|\cdot|$ denotes the absolute value. A linear vector space $\mathcal{Y}$ associated with a norm $\|\cdot\|$ defines a *normed space*.

3.1.2 Signal norms and spaces

Signals are *Lebesgue measurable* functions in time or frequency domain defined on the interval $[a, b] \in \mathbb{R}$ for which the following norms are given for $1 \leqslant p < \infty$:

$$\|f\|_{\mathcal{L}_p} = \left(\int_a^b \|f(x)\|^p \, dx \right)^{1/p} \tag{3.5}$$

and

$$\|f\|_{\mathcal{L}_\infty} = \sup_{x \in [a,b]} \|f(x)\|. \tag{3.6}$$

Note that in Eq. 3.5 and in the following, $\|\cdot\|$ represents the *Euclidean vector norm* and sup denotes the supremum. Signals are said to lay in the space $\mathcal{L}_p[a, b]$ or $\mathcal{L}_\infty[a, b]$ if the associated norms (Eq. 3.5 and Eq. 3.6) over $[a, b]$ exist and if they are finite [112, 230].

SIGNALS IN TIME DOMAIN

For the purpose of this thesis and for simplicity, vector-valued functions of time t are considered on the finite interval $[0, \infty)$, thus $f : [0, \infty) \to \mathbb{R}^n$, where n represents the number of entries of the vector $f(t)$. Moreover, signals considered in this work are often assumed to lay in $\mathcal{L}_2[0, \infty)$ with the finite norm

$$\|f\|_{\mathcal{L}_2} = \sqrt{\int_0^\infty f(t)^T f(t) \, dt}, \tag{3.7}$$

and therefore, are square-integrable signals. Note that Eq. 3.7 is equal to the computation of energy of a signal, and therefore, signals in $\mathcal{L}_2$ have the natural and practical interpretation of featuring finite energy [192].

This thesis is dedicated to systems that are either modeled or identified as discrete-time systems. Consequently, the corresponding input and output signals are vector-valued sequences $f : \mathbb{N}_0^+ \to \mathbb{R}^n$ and not continuous-time functions. Thus, the integral in Eq. 3.5 must be exchanged by the sum, and the supremum in Eq. 3.6 has to be replaced by the max operator. The $\mathcal{L}_2$ norm in Eq. 3.7 is then expressed by [230]

$$\|f\|_{\ell_2} = \sqrt{\sum_{k=0}^{\infty} f_k^T f_k}, \tag{3.8}$$

Here, k refers to the time steps and denotes the index of the discrete elements f_k within the sequence f. All interpretations of the norms made in continuous time hold in discrete time as well.

SIGNALS IN FREQUENCY DOMAIN

As mentioned in Section 2.1.3, signals in the time domain can be transferred to the frequency domain with the help of the Laplace or z-transform, respectively. Thereby, they become complex-valued functions. In the case of signals in $\mathcal{L}_2[0,\infty)$ and $\ell_2[0,\infty)$, this process is associated with the map from one space to another, namely $\mathcal{L}_2[0,\infty) \to \mathcal{H}_2(j\mathbb{R})$ and $\ell_2[0,\infty) \to \mathcal{H}_2(\mathbb{D})$[1], respectively, where $\mathcal{H}_p$ denotes the *Hardy spaces* [42, 88]. Note that $\mathbb{D}$ refers to the open unit disk in the complex plane ($|z| < 1$). Complex-valued signals in $\mathcal{H}_2$ must have finite norms [88]

$$\|f\|_{\mathcal{H}_2(j\mathbb{R})} = \sqrt{\frac{1}{2\pi}\int_{-\infty}^{\infty} f^*(j\omega)f(j\omega)\,d\omega} \tag{3.9}$$

in the continuous-time case and [42]

$$\|f\|_{\mathcal{H}_2(\mathbb{D})} = \sqrt{\frac{1}{2\pi}\int_{0}^{2\pi} f^*(e^{j\theta})f(e^{j\theta})\,d\theta} \tag{3.10}$$

in the discrete-time case[2]. Here, the Fourier transform is considered ($\alpha = 0$) such that $s = j\omega$ and $z = e^{j\omega\Delta t} = e^{j\theta}$, cf. Section 2.1.3. The $\mathcal{H}_2(j\mathbb{R})$ space contains complex-valued functions $f(s)$ that are analytic on the open right half-plane ($\mathrm{Re}(s) > 0$). This means that $f(s)$ has continuous derivatives of all powers for every s with $\mathrm{Re}(s) > 0$. For a more comprehensive definition of analytic complex functions, see [230, p. 97]. In the discrete-time case, $f(z)$ must be analytic on the open unit disk $\mathbb{D}$ [42].

ISOMORPHISM BETWEEN TIME AND FREQUENCY DOMAIN

Most interestingly, the $\ell_2[0,\infty)$, $\mathcal{L}_2[0,\infty)$, and $\mathcal{H}_2$ spaces induce inner products $\langle\cdot,\cdot\rangle$ making them *Hilbert* spaces. These inner products[3] are defined as [42, 88]

$$\langle f, g\rangle = \int_0^{\infty} f(t)^T g(t)\,dt \tag{3.11}$$

$$= \frac{1}{2\pi}\int_{-\infty}^{\infty} f^*(j\omega)g(j\omega)\,d\omega \tag{3.12}$$

and

$$\langle f, g\rangle = \sum_{k=0}^{\infty} f_k^T g_k \tag{3.13}$$

$$= \frac{1}{2\pi}\int_{0}^{2\pi} f^*(e^{j\theta})g(e^{j\theta})\,d\theta, \tag{3.14}$$

1 $\mathcal{H}_2$ is a subspace of the complex-valued $\mathcal{L}_2(j\mathbb{R})$ space (continuous-time case) or $\mathcal{L}_2(\mathbb{D})$ (discrete-time case).

2 Be aware that integrating a periodic frequency domain signal with argument θ over $[0, 2\pi]$ or $[-\pi, \pi]$ yields the same result because of its symmetry property.

3 Interesting properties can be deduced from inner products such as the angle between two vectors. For a comprehensive description on inner products, see [107, 230].

respectively. Note that the inner products $\langle f, g \rangle$ are preserved when transformed from one domain to the other. Not only the inner products but also the norms remain equal, independent of the signal domain, which makes the Laplace transform (or z-transform) and its inverse counterpart an *isomorphism*. For a more detailed and mathematically elaborated definition of isomorphisms, see [42, p. 87]. The equality of the 2-norms for time- and frequency-domain signals represents what is referred to as Parseval's theorem and can be interpreted as preservation of energy in either domain [88].

3.1.3 Operator norms and spaces

Recall the input-output relationship depicted in Fig. 2.1, which is repeated in Fig. 3.1 for simplicity. There, the output y results from u acting on the linear system $\boldsymbol{G}$. u and y lay within

Figure 3.1: System $\boldsymbol{G}$ with input u and output y.

the normed spaces $\mathcal{U}$ and $\mathcal{Y}$, respectively. As mentioned in Section 2.1.1, it can be assumed that the block diagram implies the following algebra: $y = \boldsymbol{G}u$, although it was shown that in case of time-domain signals, a convolution of the IRF $G(t)$ with $u(t)$ is required, cf. Eq. 2.11. The system $\boldsymbol{G}$ can be seen as a linear operator denoted by $\mathscr{L}(\mathcal{U}, \mathcal{Y})$ that maps signals from $\mathcal{U}$ to $\mathcal{Y}$. To define a normed space of linear operators (systems), the *induced norm*

$$\|\boldsymbol{G}\|_{\mathscr{L}(\mathcal{U},\mathcal{Y})} = \sup_{u \neq 0} \frac{\|\boldsymbol{G}u\|_{\mathcal{Y}}}{\|u\|_{\mathcal{U}}} \tag{3.15}$$

is introduced. Hence, the induced norm $\|\cdot\|_{\mathscr{L}(\mathcal{U},\mathcal{Y})}$ of $\boldsymbol{G}$ is the maximum gain from $u \in \mathcal{U}$ to $y \in \mathcal{Y}$ [192].

3.1.4 Transfer function norms and interpretations

It can be shown that direct relations between the system norm defined in Eq. 3.15 and the $\mathcal{H}_2$ and $\mathcal{H}_\infty$ norms of the transfer functions $G(j\omega)$ and $G(e^{j\theta})$ exist. Thus, certain system properties can be directly inferred by regarding the finite $\mathcal{H}_2$ and $\mathcal{H}_\infty$ norms of the system's transfer function representation.

Before examining these connections, the $\mathcal{H}_2$ transfer function norm is defined by [192]

$$\|\boldsymbol{G}\|_{\mathcal{H}_2(j\mathbb{R})} = \sqrt{\frac{1}{2\pi} \int_{-\infty}^{\infty} \operatorname{tr}\{G^*(j\omega) G(j\omega)\}\, d\omega} \tag{3.16}$$

for the continuous-time case and by [42]

$$\|\boldsymbol{G}\|_{\mathcal{H}_2(\mathbb{D})} = \sqrt{\frac{1}{2\pi} \int_{0}^{2\pi} \operatorname{tr}\{G^*(e^{j\theta}) G(e^{j\theta})\}\, d\theta} \tag{3.17}$$

for the discrete-time case. Here, $\mathrm{tr}\{\cdot\}$ denotes the trace operator. Note that transfer functions of multivariable systems essentially are functions of frequency, and therefore, the signal norms given in Section 3.1.2 are simply extended to matrix-valued functions.

Similarly, the infinity-norms of the transfer function $\boldsymbol{G}$ are given by [88]

$$\|\boldsymbol{G}\|_{\mathcal{H}_\infty(j\mathbb{R})} = \sup_{\omega\in\mathbb{R}} \bar{\sigma}\{G(j\omega)\} \tag{3.18}$$

and [42]

$$\|\boldsymbol{G}\|_{\mathcal{H}_\infty(\mathbb{D})} = \sup_{\theta\in[0,2\pi]} \bar{\sigma}\{G(e^{j\theta})\}, \tag{3.19}$$

respectively, where $\bar{\sigma}\{\cdot\}$ extracts the maximum singular value. The following relationships are established for the discrete-time case, but they also hold for the continuous-time case, see [230].

Again, consider the block diagram given in Fig. 3.1 with $u \in \ell_2[0,\infty)$ and suppose that $y \in \ell_2[0,\infty)$. This appears to be a rather natural case, as the response of the system $\boldsymbol{G}$ to the finite energy signal u should have finite energy too. By considering the isomorphism explained earlier (Parseval's theorem) and the induced system norm

$$\|\boldsymbol{G}\|_{\mathscr{L}(\ell_2[0,\infty))} = \sup_{u\neq 0} \frac{\|y\|_{\ell_2[0,\infty)}}{\|u\|_{\ell_2[0,\infty)}} = \sup_{u\neq 0} \frac{\|\boldsymbol{G}u\|_{\mathcal{H}_2(\mathbb{D})}}{\|u\|_{\mathcal{H}_2(\mathbb{D})}}, \tag{3.20}$$

it becomes obvious that $\|y\|_{\ell_2[0,\infty)} < \infty$ if and only if the transfer function matrix $G(e^{j\theta})$ obeys $\|\boldsymbol{G}u\|_{\mathcal{H}_2(\mathbb{D})} < \infty$ [4]. A sufficient condition for this is that $\|\boldsymbol{G}\|_{\mathcal{H}_\infty(\mathbb{D})} < \infty$, since [88]

$$\|\boldsymbol{G}u\|_{\mathcal{H}_2(\mathbb{D})} = \sqrt{\frac{1}{2\pi}\int_0^{2\pi} \mathrm{tr}\big\{u^*(e^{j\theta})G^*(e^{j\theta})G(e^{j\theta})u(e^{j\theta})\big\}\,d\theta} \tag{3.21}$$

$$\leqslant \sqrt{\sup_\theta \bar{\sigma}\{G(e^{j\theta})\}^2 \frac{1}{2\pi}\int_0^{2\pi} u^*(e^{j\theta})u(e^{j\theta})\,d\theta} \tag{3.22}$$

$$= \|\boldsymbol{G}\|_{\mathcal{H}_\infty(\mathbb{D})}\|u\|_{\mathcal{H}_2(\mathbb{D})}. \tag{3.23}$$

Substituting Eq. 3.23 into Eq. 3.20 shows that

$$\|\boldsymbol{G}\|_{\mathscr{L}(\ell_2[0,\infty))} = \|\boldsymbol{G}\|_{\mathcal{H}_\infty(\mathbb{D})} < \infty \tag{3.24}$$

for mappings of the kind $\ell_2 \to \ell_2$. Eq. 3.24 holds for any causal and stable linear system $\boldsymbol{G}$. In summary, the $\mathcal{H}_\infty$ norm of a transfer function can be referred to as the maximum system gain from an energy-bounded input to an energy-bounded output. Hence, this norm is an excellent design criterion for controllers and estimators.

Another interesting relationship between LTI systems and their transfer functions can be established with respect to the $\mathcal{H}_2$ norm. To this end, again, consider the block diagram depicted in Fig. 3.1, but this time, assume that the input u is white noise with bounded PSD $S_u(e^{j\theta})$, meaning that $\left\|S_u(e^{j\theta})\right\|_{\mathcal{H}_\infty(\mathbb{D})} < \infty$ [5]. As a consequence of the Wiener-Khinchine theorem (see Section 2.2.3), the PSD of the output y can be factorized as [110]

$$S_y(e^{j\theta}) = G(e^{j\theta})S_u(e^{j\theta})G^*(e^{j\theta}). \tag{3.25}$$

4 Note that the notation $\mathscr{L}(\ell_2[0,\infty),\ell_2[0,\infty))$ is reduced to $\mathscr{L}(\ell_2[0,\infty))$ because of equal input and output spaces.
5 Eq. 3.19 is valid for every function of frequency in the discrete-time case.

Now, assume that $S_u = I$ (white noise) and recall from Section 2.2.3 that the average power of the signal y is equal to

$$R_y(0) = \mathrm{E}\Big\{y(t)y(t)^{\mathrm{T}}\Big\} = \frac{1}{2\pi}\int_0^{2\pi} S_y(e^{j\theta})\,d\theta. \tag{3.26}$$

Thus, one may write

$$\mathrm{E}\Big\{y(t)^{\mathrm{T}}y(t)\Big\} = \frac{1}{2\pi}\int_0^{2\pi} \mathrm{tr}\Big\{S_y(e^{j\theta})\Big\}\,d\theta. \tag{3.27}$$

Then, after substituting Eq. 3.25 into Eq. 3.27, and with Eq. 3.17,

$$\mathrm{E}\Big\{y(t)^{\mathrm{T}}y(t)\Big\} = \|\boldsymbol{G}\|^2_{\mathcal{H}_2(\mathbb{D})}. \tag{3.28}$$

Consequently, the $\mathcal{H}_2$ norm of the transfer function of a system $\boldsymbol{G}$ excited by white noise with a constant PSD of I represents the joint average power of the output signal.

3.2 FILTERING AND ESTIMATING AS A SPECIAL CASE OF OPTIMAL CONTROL

A typical objective in modern control is to design feedback systems $\boldsymbol{T}_{z\bar{w}}$, also called closed-loop systems, with certain minimal transfer function norms that map exogenous inputs $\bar{w}$ to regulated outputs z. The former can be seen as disturbance, which is uncontrollable, and the latter is typically expressed by an error or residual, which is desired to go to zero. Therefore, with simple words, the goal of the control problem is rephrased, namely to minimize the effect of $\bar{w}$ on z in a certain sense. A schematic illustration of $\boldsymbol{T}_{z\bar{w}}$ is given by Fig. 3.2. The system

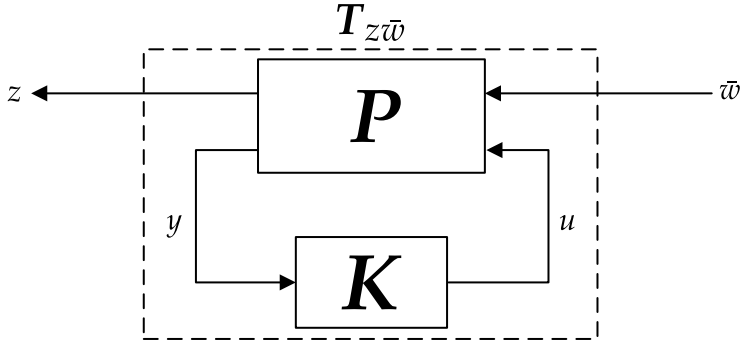

Figure 3.2: Feedback system $\boldsymbol{T}_{z\bar{w}}$ with plant $\boldsymbol{P}$ and controller $\boldsymbol{K}$.

consists of a plant $\boldsymbol{P}$, which itself cannot be changed, and a controller $\boldsymbol{K}$ that maps sensed outputs y to actuator inputs u. For the control system design, the controller $\boldsymbol{K}$ is defined in such a way that the objective, the minimization of some transfer function norm, is met. To illustrate this relationship, consider the following simplified example. The goal may be to design a car's cruise control system that minimizes the worst-case error of measured and desired speed. In this case, $\boldsymbol{P}$ constitutes a model of the car's drive system. z represents the error, namely the difference between the desired speed defined by the user and the measured speed, which is expressed by y. Finally, $\boldsymbol{K}$ controls the throttle represented by u, and is selected in such a way that the infinity-norm of $\boldsymbol{T}_{z\bar{w}}$ is minimized.

This thesis is devoted to using quadratic estimation solutions for vibration-based SHM. Estimation can be seen as a special case of control, and thus, it can be regarded within the general framework introduced before, allowing for a unified formulation, interpretability, and design. In the following, the theoretical foundation is laid, which is then examined in more detail for Kalman and $\mathcal{H}_\infty$ filtering. Therefore, consider this simplified generalized parameterization of $\boldsymbol{P}$ and $\boldsymbol{K}$ given as

$$\boldsymbol{P} = \left[\begin{array}{c|c} \boldsymbol{P}_{11} & \boldsymbol{P}_{12} \\ \hline \boldsymbol{P}_{21} & \boldsymbol{P}_{22} \end{array}\right] = \left[\begin{array}{c|cc} A & B_1 & 0 \\ \hline C_1 & D_{11} & D_{12} \\ C_2 & D_{21} & 0 \end{array}\right] \tag{3.29}$$

and

$$\boldsymbol{K} = \left[\begin{array}{c|c} A_e & B_e \\ \hline C_e & D_e \end{array}\right], \tag{3.30}$$

respectively, where the index e emphasizes the estimation case. The kind of notation used in 3.29 and 3.30 is readily considered throughout this thesis to define transfer functions. Consequently, the general quadruplet of state-space matrices $\left[\begin{array}{c|c} A & B \\ \hline C & D \end{array}\right]$ refers to $C(zI - A^{-1}) + D$, cf. Eq. 2.36.

For the regarded case, the following definitions are made in view of Fig. 3.2:

$$\begin{aligned} y &= y \\ u &= \hat{s} \\ \overline{w} &= \begin{bmatrix} w^{\mathrm{T}} & v^{\mathrm{T}} \end{bmatrix}^{\mathrm{T}} \\ z &= s - \hat{s}, \end{aligned}$$

leading to the state-space representations of Eqs. 3.29 and 3.30 that can be stated in matrix notation as

$$\begin{bmatrix} x_{k+1} \\ z_k \\ y_k \end{bmatrix} = \begin{bmatrix} A & B_1 & 0 \\ C_1 & D_{11} & D_{12} \\ C_2 & D_{21} & 0 \end{bmatrix} \begin{bmatrix} x_k \\ \overline{w}_k \\ \hat{s}_{k|k+m} \end{bmatrix} \tag{3.31}$$

and

$$\begin{bmatrix} x_{e,k+1} \\ \hat{s}_{k|k+m} \end{bmatrix} = \begin{bmatrix} A_e & B_e \\ C_e & D_e \end{bmatrix} \begin{bmatrix} x_{e,k} \\ y_k \end{bmatrix}, \tag{3.32}$$

respectively. Here, s_k denotes an arbitrary signal to be estimated based on past, present, or future observations. This is emphasized by the variable m used as a subscript for the estimate $\hat{s}_{k|k+m}$. x_e denotes the internal states of the estimator defined by (A_e, B_e, C_e, D_e). Depending on the choice of m, the estimator can be used for prediction ($m < 0$), filtering ($m = 0$), or smoothing ($m > 0$) [180]. In this thesis, filters or predictors are derived, for which the subscripts p and f are chosen.

To find the parameterization of the system $\boldsymbol{T}_{z\bar{w}}$, a lower linear fractional transform (LLFT), denoted as $\mathrm{LLFT}(\boldsymbol{P}, \boldsymbol{K})$, is performed, resulting in [88, p. 137]

$$\boldsymbol{T}_{z\bar{w}} = \mathrm{LLFT}(\boldsymbol{P}, \boldsymbol{K}) = \left[\begin{array}{c|c} A_{\mathrm{cl}} & B_{\mathrm{cl}} \\ \hline C_{\mathrm{cl}} & D_{\mathrm{cl}} \end{array}\right] = \left[\begin{array}{cc|c} A & 0 & B_1 \\ B_e C_2 & A_e & B_e D_{21} \\ \hline C_1 + D_{12} D_e C_2 & D_{12} C_e & D_{11} + D_{12} D_e D_{21} \end{array}\right], \tag{3.33}$$

$$\begin{bmatrix} x_{k+1} \\ x_{e,k+1} \\ z_k \end{bmatrix} = \begin{bmatrix} A & 0 & B_1 \\ B_e C_2 & A_e & B_e D_{21} \\ C_1 + D_{12} D_e C_2 & D_{12} C_e & D_{11} + D_{12} D_e D_{21} \end{bmatrix} \begin{bmatrix} x_k \\ x_{e,k} \\ \bar{w}_k \end{bmatrix}.$$

Independent of the applied linear quadratic estimation theory, the overall goal concerning the estimator design for this thesis reads as follows:

Problem 3.1. *Given a linear quadratic estimator $\boldsymbol{K}$ for some signal s, the goal is to derive a strictly proper[6] filter or predictor $\bar{\boldsymbol{K}}_f : y_k \to \hat{y}_{k|k}$ or $\bar{\boldsymbol{K}}_p : y_k \to \hat{y}_{k|k-1}$ with estimation error $e = y - \hat{y}$.*

3.3 KALMAN FILTER THEORY

In this work, Kalman filters are studied and used intensively. These filters can be seen as special cases of $\mathcal{H}_2$ estimators, for which they can be regarded within the control framework presented before. The synthesis is outlined as follows.

Problem 3.2. *Given the pair (A, C), the plant $\boldsymbol{P}$ is defined for $s_k = x_k$ and $\hat{s}_{k|k} = \hat{x}_{k|k}$ such that*

$$\boldsymbol{P} = \left[\begin{array}{c|cc} A & \begin{bmatrix} I & 0 \end{bmatrix} & 0 \\ \hline I & \begin{bmatrix} 0 & 0 \end{bmatrix} & -I \\ C & \begin{bmatrix} 0 & I \end{bmatrix} & 0 \end{array}\right], \quad \begin{bmatrix} x_{k+1} \\ z_k \\ y_k \end{bmatrix} = \left[\begin{array}{c|cc} A & \begin{bmatrix} I & 0 \end{bmatrix} & 0 \\ \hline I & \begin{bmatrix} 0 & 0 \end{bmatrix} & -I \\ C & \begin{bmatrix} 0 & I \end{bmatrix} & 0 \end{array}\right] \begin{bmatrix} x_k \\ \bar{w}_k \\ \hat{x}_{k|k} \end{bmatrix}. \tag{3.34}$$

The goal is to find a filter $\boldsymbol{K} : y_k \to \hat{s}_{k|k} = \hat{x}_{k|k}$ that minimizes the $\mathcal{H}_2$-norm of $\boldsymbol{T}_{z\bar{w}}$ (Eq. 3.33) by taking into account the statistical properties of $\bar{w}_k$ defined as $\mathcal{N}(0, M_k)$. The covariance matrix M_k is given by

$$M_k = \mathrm{E}\left\{ \begin{bmatrix} w_k \\ v_k \end{bmatrix} \begin{bmatrix} w_l \\ v_l \end{bmatrix}^T \right\} = \begin{bmatrix} Q_k & S_k \\ S_k{}^T & R_{v,k} \end{bmatrix} \delta_{kl} \geqslant 0 \tag{3.35}$$

and is assumed as time-invariant, i.e. $M_k = M$. The objective function of this design problem can be formally stated as

$$\underset{\boldsymbol{K}(Q, R_v, S)}{\text{minimize}} \quad J = \|\boldsymbol{T}_{z\bar{w}}\|_{\mathcal{H}_2}. \tag{3.36}$$

From a finite-horizon perspective ($k \in [0, \infty)$), the cost function J formulated in Eq. 3.36 is dual to

$$J_k = \|\tilde{x}_{k|k}\|_2^2 = \mathrm{tr}\{P_{k|k}\}, \tag{3.37}$$

where $\tilde{x}_{k|k}$ denotes the *a posteriori* state-estimation error defined as $\tilde{x}_{k|k} = z_k = x_k - \hat{x}_{k|k}$, and $P_{k|k}$ represents the state-estimation error covariance matrix.

6 The term *strictly proper* implies that the system is asymptotically stable and $D = 0$, see [102, p. 33].

The solution to the filter design problem follows, e.g., from the derivations of the standard time-varying Kalman filter. In the following, the most relevant steps are summarized, starting with the time-varying filter minimizing Eq. 3.37 and finally providing the formulae for the so-called *steady-state Kalman filter*, which constitutes the desired time-invariant solution. For more information on this topic, see, e.g., [180].

The fundamental concept of Kalman filtering is to predict and filter the states in an alternating fashion. Therefore, during filtering, current information from the measurements is introduced with the help of a gain matrix $K_{f,k}$ and an innovation process e_k. Thus, the state prediction reads

$$\hat{x}_{k|k-1} = A\hat{x}_{k-1|k-1}, \tag{3.38}$$

and the filtering comprises

$$e_k = y_k - C\hat{x}_{k|k-1} \tag{3.39}$$

$$\hat{x}_{k|k} = \hat{x}_{k|k-1} + K_{f,k}e_k. \tag{3.40}$$

Now, as stated before, the Kalman filter seeks to minimize the mean squared error (MSE) of the *a posteriori* state estimates (filtering), cf. Eq. 3.37. Hence, $K_{f,k}$ must be determined accordingly. The optimal solution arises by writing $P_{k|k}$ as a function of $K_{f,k}$ [180, p. 85]:

$$P_{k|k} = \mathrm{E}\left\{\tilde{x}_{k|k}\tilde{x}_{k|k}^{\mathrm{T}}\right\} \tag{3.41}$$

$$= (I - K_{f,k}C)P_{k|k-1}(I - K_{f,k}C)^{\mathrm{T}} + K_{f,k}R_{v,k}K_{f,k}^{\mathrm{T}}, \tag{3.42}$$

and then, setting the derivative of Eq. 3.37 to zero with respect to $K_{f,k}$. This results in

$$K_{f,k} = P_{k|k-1}C^{\mathrm{T}}(CP_{k|k-1}C^{\mathrm{T}} + R_{v,k})^{-1}. \tag{3.43}$$

Eq. 3.42 reveals a central property of the Kalman filter recursion. To determine the posterior probability of the estimation errors, the prior likelihood in the form of

$$P_{k|k-1} = \mathrm{E}\left\{\tilde{x}_{k|k-1}\tilde{x}_{k|k-1}^{\mathrm{T}}\right\} = \mathrm{E}\left\{(x_k - \hat{x}_{k|k-1})(x_k - \hat{x}_{k|k-1})^{\mathrm{T}}\right\} \tag{3.44}$$

is taken into account together with information that is currently available. Hence, the Kalman filter is often referred to as a Bayesian filter.

A typical representation of the Kalman filter is given by the one-step form. Therefore, a parameterization of $P_{k+1|k}$ has to be found first, which follows directly from Eqs. 3.40 to 3.44:

$$P_{k+1|k} = \mathrm{E}\left\{(x_{k+1} - \hat{x}_{k+1|k})(x_{k+1} - \hat{x}_{k+1|k})^{\mathrm{T}}\right\} \tag{3.45}$$

$$\begin{aligned}
&= \mathrm{E}\left\{(Ax_k + w_k - A\hat{x}_{k|k-1} - AK_{f,k}Cx_k - AK_{f,k}v_k + AK_{f,k}C\hat{x}_{k|k-1})(...)^{\mathrm{T}}\right\} \\
&= \mathrm{E}\left\{(A\tilde{x}_{k|k-1} - AK_{f,k}C\tilde{x}_{k|k-1} + w_k - AK_{f,k}v_k)(...)^{\mathrm{T}}\right\} \\
&= AP_{k|k-1}A^{\mathrm{T}} - AP_{k|k-1}C^{\mathrm{T}}K_{f,k}^{\mathrm{T}}A^{\mathrm{T}} - AK_{f,k}CP_{k|k-1}A^{\mathrm{T}} + AK_{f,k}CP_{k|k-1}C^{\mathrm{T}}K_{f,k}^{\mathrm{T}}A^{\mathrm{T}} \\
&\quad + Q_k - S_kK_{f,k}^{\mathrm{T}}A^{\mathrm{T}} - AK_{f,k}S_k^{\mathrm{T}} + AK_{f,k}R_{v,k}K_{f,k}^{\mathrm{T}}A^{\mathrm{T}}.
\end{aligned} \tag{3.46}$$

Note that $(...)^{\mathrm{T}}$ is used to avoid the repetition of the first statement within the expectations. Substituting Eq. 3.43 into Eq. 3.46 yields [110, p. 129]:

$$P_{k+1|k} = AP_{k|k-1}A^{\mathrm{T}} - (AP_{k|k-1}C^{\mathrm{T}} + S_k)(CP_{k|k-1}C^{\mathrm{T}} + R_{v,k})^{-1}(CP_{k|k-1}A^{\mathrm{T}} + S_k^{\mathrm{T}}) + Q_k. \tag{3.47}$$

Finally, the one-step Kalman filter is found in the well-known innovations form by substituting Eq. 3.43 into Eq. 3.40 and then into Eq. 3.38. The state-space equations are completed by rearranging Eq. 3.39 such that

$$\hat{x}_{k+1|k} = A\hat{x}_{k|k-1} + K_{p,k}e_k \tag{3.48a}$$
$$y_k = C\hat{x}_{k|k-1} + e_k, \tag{3.48b}$$

where [110, p. 120]

$$K_{p,k} = (AP_{k|k-1}C^{\mathrm{T}} + S_k)(CP_{k|k-1}C^{\mathrm{T}} + R_{v,k})^{-1}. \tag{3.49}$$

The inverse of this system is readily obtained through a small rearrangement and the introduction of $A_{p,k} = A - K_{p,k}C$ so that

$$\hat{x}_{k+1|k} = A_{p,k}\hat{x}_{k|k-1} + K_{p,k}y_k \tag{3.50a}$$
$$e_k = -C\hat{x}_{k|k-1} + y_k. \tag{3.50b}$$

STEADY-STATE KALMAN FILTER

In this work, it is generally assumed that w_k and v_k are stationary processes. Consequently, the covariance matrix must be constant so that $M_k = M$. Thus, in the context of time-invariant parameters (A, C), Eq. 3.47 converges to a constant matrix as $k \to \infty$. In fact, this convergence is obtained quickly in most cases, leading to the so-called steady-state Kalman filter. Therefore, it comes naturally to directly design a time-invariant Kalman filter when the aforementioned criteria are met. The covariance matrix $P_{k+1|k}$ can then be replaced by a unique positive-definite stabilizing solution of the following DARE:

$$P_{k+1|k} \approx P_p = AP_pA^{\mathrm{T}} - (AP_pC^{\mathrm{T}} + S)(CP_pC^{\mathrm{T}} + R_v)^{-1}(CP_pA^{\mathrm{T}} + S^{\mathrm{T}}) + Q \tag{3.51}$$

Then, the time-invariant parameter for Eqs. 3.48 and 3.50 read

$$K_p = (AP_pC^{\mathrm{T}} + S)(CP_pC^{\mathrm{T}} + R_v)^{-1}, \quad A_p = A - K_pC. \tag{3.52}$$

Information regarding the existence conditions and numerical solution of Eq. 3.51 is available in the literature, see e.g. [180] or [101, p. 427] and the citations therein.

Based on these findings, the estimator $\boldsymbol{K}$ that satisfies Problem 3.2 is defined as

$$\boldsymbol{K} = \left[\begin{array}{c|c} A_p & K_p \\ \hline A & 0 \end{array}\right], \quad \begin{bmatrix} \hat{x}_{k+1|k} \\ \hat{x}_{k|k} \end{bmatrix} = \begin{bmatrix} A_p & K_p \\ A & 0 \end{bmatrix} \begin{bmatrix} \hat{x}_{k|k-1} \\ y_k \end{bmatrix}. \tag{3.53}$$

Finally, Problem 3.1 is fulfilled by defining

$$\bar{\boldsymbol{K}}_p = \left[\begin{array}{c|c} A_p & K_p \\ \hline C & 0 \end{array}\right], \quad \begin{bmatrix} \hat{x}_{k+1|k} \\ \hat{y}_{k|k-1} \end{bmatrix} = \begin{bmatrix} A_p & K_p \\ C & 0 \end{bmatrix} \begin{bmatrix} \hat{x}_{k|k-1} \\ y_k \end{bmatrix}. \tag{3.54}$$

3.4 TEST FOR WHITENESS OF INNOVATIONS

In the previous sections, it was assumed that the noise covariance matrices Q_k, $R_{v,k}$, and S_k are known. However, this is rather a theoretical case, and thus, in practice, the noise covariances are either guessed or estimated using noise estimation techniques, as will be elaborated on in Chapter 5. In any case, the performance of the Kalman filter designed with a set of noise covariance matrices can be assessed based on the innovations resulting from that filter. In the optimal case, where the Kalman filter functions as a least-squares error filter, the innovations are white and Gaussian distributed. Special statistical tests exist to test these properties. Regarding the test for Gaussianity, the Kolmogorov-Smirnov or Anderson-Darling tests can be applied [136], for instance. In the context of this thesis, the whiteness property, i.e., the independence or uncorrelatedness of estimation errors, is frequently addressed. Hence, a typical approach for testing this property is explained here.

A classical approach for this endeavor is to consider the normalized estimated covariance function defined as

$$\hat{R}_e(i) = \frac{\sum_{k=1}^{n_s-1} (e_k - \hat{\mu}_e)(e_{k+i} - \hat{\mu}_e)^{\mathrm{T}}}{\sum_{k=1}^{n_s-1} (e_k - \hat{\mu}_e)(e_k - \hat{\mu}_e)^{\mathrm{T}}}, \tag{3.55}$$

and to check whether the weighted and squared covariance function converges in a χ^2 distribution with certain degrees of freedom (DOF)[7]. Note that the numerator and denominator of Eq. 3.55 are slightly different from Eq. 2.66 since they are not multiplied by $1/n_s-i$. The factor cancels out here, and therefore, is not included in Eq. 3.55. The following descriptions contain terms that are strongly related to the random theory covered by Section 2.2 and statistical testing or hypothesis testing, respectively, which is addressed in Section 4.4.2. In the previous equation, n_s denotes the number of measured or processed samples. Note that in the multivariate case, e_k is a vector containing the elements $e_{l,k}$ with $l \in [1, q]$ representing each output channel, and therefore, $\hat{R}_e(i)$ becomes a $q \times q$ matrix with the autocovariance function $\hat{R}_{e_l}(i)$ on the main diagonal. The latter is of interest for the whiteness test, which essentially checks the autocorrelation of the q individual innovations sequences. If $e_{l,k}$ were a white noise process, then $\hat{R}_{e_l}(i)$ would amount to zero for $i > 0$. Various versions of the χ^2 test exist that can be interpreted as modifications of the standard test by Box and Pierce [26]. A good overview of the existing versions, together with suggestions for application, can be found in [53]. The test statistics of the common whiteness test reads

$$r = n_s \sum_{i=1}^{m} \hat{R}_{e_l}^2(i). \tag{3.56}$$

If e_l is a realization of white noise then the sum of the squared correlation function $\hat{R}_{e_l}(i)$ multiplied with the number of samples n_s converges in a χ^2 distribution with m DOF [22]. Now, the null-hypothesis, that is, the hypothesis that the estimation error is white noise, can be stated as $H_0 : r < \vartheta$, where ϑ marks the $(1 - \alpha)$ quantile that is computed from the CDF of the χ^2 distribution with m DOF, cf. Section 4.4.2.

The selection of the value m is not straightforward. Bernal [22] suggests to choose

$$m \approx \frac{f_s}{f_{D,1}}, \tag{3.57}$$

7 Here, the term DOF is used in a statistical sense.

where f_s denotes the sampling frequency and $f_{D,1}$ the lowest measured natural frequency. He also comments on the definition of the significance level α. In the multivariate case, this value might be globally defined as

$$\alpha = 1 - (1 - \bar{\alpha})^{1/q} \tag{3.58}$$

with a uniform significance level $\bar{\alpha}$ for each innovation sequence.

3.5 $\mathcal{H}_\infty$ ESTIMATION THEORY

In practice, Kalman filters, or $\mathcal{H}_2$ estimators in general, exhibit certain drawbacks. It follows from the interpretation of the $\mathcal{H}_2$ transfer function norm (see Section 3.1.4) that both process and measurement noise summarized by $\overline{w}$ are assumed to be white noise processes, which is generally not the case in practice. Moreover, Kalman filtering requires information about the statistical moments regarding these processes. Again, from a practical point of view, this manifests another limitation, as such information is typically not at hand, nor can it be assumed in general that w and v are random processes at all. The estimation of unknown noise covariance matrices is addressed in Chapter 5. Despite likely violations of the underlying assumptions, the Kalman filter is particularly appealing because of its simplicity. Therefore, it has been heavily exploited in many engineering fields since its introduction in 1960 by Rudolf E. Kálmán [108].

An alternative estimator design is posed by the $\mathcal{H}_\infty$ theory, which aims to minimize the $\mathcal{H}_\infty$ norm of $\boldsymbol{T}_{z\overline{w}}$ (Eq. 3.33). According to the explanations made in Section 3.1.4, this design scheme solely requires $\overline{w} \in \ell_2[0,\infty)$ and $z \in \ell_2[0,\infty)$, which implies finite energy of $\overline{w}$ and z. No other assumptions are postulated and noise and even system uncertainties are taken into account [101, 180]. Since the involved processes are not necessarily random processes, Gramian matrices instead of covariance matrices are proper choices to write inner products. The former are denoted by $\langle a_k, b_k \rangle$, where a_k and b_k represent some multivariate, possibly deterministic processes. In the case of a_k and b_k being random processes, $\langle a_k, b_k \rangle = \mathrm{E}\{a_k b_k^{\mathrm{T}}\}$ [210][8].

Similar to Problem 3.2, the objective of the $\mathcal{H}_\infty$ estimator design for this thesis is formulated in view of the control framework presented in Section 3.2.

Problem 3.3. *Given the pair (A, C), the plant $\boldsymbol{P}$ is defined for $s_k = Cx_k$ and $\hat{s}_{k|k} = \hat{y}_{k|k}$ such that*

$$\boldsymbol{P} = \left[\begin{array}{c|cc} A & \begin{bmatrix} I & 0 \end{bmatrix} & 0 \\ \hline C & \begin{bmatrix} 0 & 0 \end{bmatrix} & -I \\ C & \begin{bmatrix} 0 & I \end{bmatrix} & 0 \end{array}\right], \quad \begin{bmatrix} x_{k+1} \\ z_k \\ y_k \end{bmatrix} = \left[\begin{array}{c|cc} A & \begin{bmatrix} I & 0 \end{bmatrix} & 0 \\ \hline C & \begin{bmatrix} 0 & 0 \end{bmatrix} & -I \\ C & \begin{bmatrix} 0 & I \end{bmatrix} & 0 \end{array}\right] \begin{bmatrix} x_k \\ \overline{w}_k \\ \hat{y}_{k|k} \end{bmatrix}. \tag{3.59}$$

The goal is to find a filter $\boldsymbol{K} : y_k \to \hat{s}_{k|k} = \hat{y}_{k|k}$ so that the $\mathcal{H}_\infty$ norm of $\boldsymbol{T}_{z\overline{w}}$ (Eq. 3.33) satisfies an user-defined upper bound γ^2. This is formerly expressed by the objective

$$J = \inf_{\boldsymbol{K}} \|\boldsymbol{T}_{z\overline{w}}\|_{\mathcal{H}_\infty} < \gamma^2. \tag{3.60}$$

8 Note that the differentiation between Gramian and covariance matrices is rather pedantic, as the underlying mathematical operations are identical.

Here, J defines the corresponding cost function and inf denotes the infimum operator. Comparing Eqs. 3.34 and 3.59 reveals that this time, the design problem is formulated to obtain $\hat{y}_{k|k}$, although, in the Kalman filter case, the postulated goal was to receive the state estimates $\hat{x}_{k|k}$. As mentioned before, this has been done to obtain the $\mathcal{H}_2$-optimal estimates $\hat{y}_{k|k}$ and $\hat{y}_{k|k-1}$, respectively, by applying the Kalman filter theory. In the $\mathcal{H}_\infty$ theory, the $\mathcal{H}_\infty$-optimal estimates $\hat{x}_{k|k}$ cannot be employed to receive $\mathcal{H}_\infty$-optimal estimates for y_k by computing $C\hat{x}_{k|k}$, see [180]. Thus, for the sake of comparability, the design problem associated with the $\mathcal{H}_\infty$ theory has to be formulated accordingly. Another remark should be made in view of Eq. 3.60. The attentive reader might wonder why the objective is not formulated to read $\min_K \|\boldsymbol{T}_{z\bar{w}}\|_{\mathcal{H}_\infty}$ instead. The reason is that an $\mathcal{H}_\infty$-optimal solution does not always exist [101], as will be explained later on. Thus, the design problem is relaxed by seeking a suboptimal or so-called γ-optimal solution.

3.5.1 Riccati-based $\mathcal{H}_\infty$ filtering

In the following, a Riccati-based approach is presented for the $\mathcal{H}_\infty$ filter design problem stated above. The underlying theory refers to the problem of indefinite-quadratic estimation, which was established by Hassibi et al. [99–101]. It constitutes an interesting approach, as the synthesis is similar to the Kalman filter design. Solely an indefinite metric space, namely the Krein space, must be considered. As in Section 3.3, the finite-horizon case is regarded first. Secondly, from the converging property of the DARE, a time-invariant solution is derived assuming stationarity of $\bar{w}_k$. For a direct infinite-horizon synthesis, see [101]. As mentioned before, the $\mathcal{H}_\infty$ synthesis strictly depends on the signal to be estimated (s_k). To avoid confusion with derivations from the literature and for the sake of clarity, the general case using $s_k = Lx_k$, where L denotes some arbitrary weighting matrix, is regarded first. Later, the special case of $L = C$ will be considered to meet Problem 3.3, referring to the estimation of the undisturbed measurements.

The time-varying pendant of Eq. 3.60 reads [80, 101]

$$J_k = \sup_{w,v} \frac{\sum_{i=0}^{k} (s_i - \check{s}_{i|i})^{\mathrm{T}} (s_i - \check{s}_{i|i})}{x_0^{\mathrm{T}} \Sigma_{x_0}^{-1} x_0 + \sum_{i=0}^{k} \left(w_i^{\mathrm{T}} Q_i^{-1} w_i + v_i^{\mathrm{T}} R_{v,i}^{-1} v_i \right)} < \gamma^2. \tag{3.61}$$

Here, $\check{s}_{k|k}$ describes the filtered estimate of s_k which is a theoretical process that must not be confused with the actual output of the $\mathcal{H}_\infty$ filter $\hat{s}_{k|k}$, as we will explain later on. A relatively intuitive explanation for $\mathcal{H}_\infty$ filters is the game theory approach by Banavar and Speyer [18]. It constitutes a game between nature and the engineer, where the nature selects w_k and v_k to maximize the estimation error $s_k - \check{s}_{k|k}$, and therefore J_k. The engineer's goal, on the other hand, is to find a good estimate $\hat{s}_{k|k}$ to finally minimize the cost function [180]. In Eq. 3.61, x_0 denotes the initial states and Σ_{x_0} is the corresponding Gramian matrix $\langle x_0, x_0 \rangle$. The Gramian matrices Q_k and $R_{v,k}$ are not required for the $\mathcal{H}_\infty$ filter synthesis, and therefore, do not appear in the original derivations by Hassibi et al. [101]. However, they are introduced here, as suggested by Forssell [80], to establish an interesting relationship with the Kalman filter. Namely, the latter is recovered for $\gamma \to \infty$ and by choosing $L = I$, defining Q_k and $R_{v,k}$ according to Eq. 3.35, and assuming that w_k and v_k are mutually uncorrelated. Though, in the sense of the $\mathcal{H}_\infty$ filter, Q_k and $R_{v,k}$ might function as weighting matrices [179, 180]. That is, if, for instance,

a certain element in w_k is small compared to the other entries, this can be taken into account by choosing the corresponding element in Q_k small relative to the others.

After reordering Eq. 3.61, the following indefinite-quadratic form arises

$$J_k = x_0^{\mathrm{T}} \Pi_0^{-1} x_0 + \sum_{i=0}^{k} \begin{bmatrix} w_i \\ \bar{v}_i \end{bmatrix}^{\mathrm{T}} \overline{M}_i^{-1} \begin{bmatrix} w_i \\ \bar{v}_i \end{bmatrix}, \tag{3.62}$$

with the central Gramian

$$\overline{M}_k = \left\langle \begin{bmatrix} w_k \\ \bar{v}_k \end{bmatrix}, \begin{bmatrix} w_l \\ \bar{v}_l \end{bmatrix} \right\rangle_{\mathcal{K}} = \begin{bmatrix} Q_k & 0 \\ 0 & \overline{R}_{\bar{v},k} \end{bmatrix} = \begin{bmatrix} Q_k & & 0 \\ & \begin{bmatrix} R_{v,k} & 0 \\ 0 & -\gamma^2 I \end{bmatrix} & \\ 0 & & \end{bmatrix} \tag{3.63}$$

and the extended disturbance process

$$\bar{v}_k = \begin{bmatrix} v_k \\ \tilde{s}_{k|k} \end{bmatrix} = \begin{bmatrix} y_k \\ \check{s}_{k|k} \end{bmatrix} - \begin{bmatrix} C \\ L \end{bmatrix} x_k. \tag{3.64}$$

Due to the negative extended Gramian matrix $\overline{R}_{\bar{v},k}$, the Hilbert space, in which Kalman filters are usually defined, is not applicable anymore. Alternatively, the Krein space must be used instead, where negative inner products are allowed [99]. Hence, $\mathcal{K}$ highlights this particular indefinite-metric space.

Most interestingly, the minimum of the deterministic cost function stated in Eq. 3.62 is equivalent to the general solution of least mean-squares problems such as Kalman filtering [204, p. 72]. This minimum is found with the help of a stationary point and yields [101]

$$\min J_k = \sum_{i=0}^{k} \hat{e}_i^{\mathrm{T}} R_{\hat{e},i} \hat{e}_i, \tag{3.65}$$

where $\hat{e}_i$ denotes the extended innovations process defined as

$$\hat{e}_k = \begin{bmatrix} e_{y,k} \\ e_{s,k} \end{bmatrix} = \begin{bmatrix} y_k \\ \check{s}_{k|k} \end{bmatrix} - \begin{bmatrix} \hat{y}_{k|k-1} \\ \hat{s}_{k|k-1} \end{bmatrix} = \begin{bmatrix} y_k \\ \check{s}_{k|k} \end{bmatrix} - \begin{bmatrix} C \\ L \end{bmatrix} \hat{x}_{k|k-1} \tag{3.66}$$

and $R_{\hat{e},k} = \langle \hat{e}_k, \hat{e}_k \rangle$. Note that with a slight abuse of notation, but to match the notation of the cited literature, the internal filter states are written as $\hat{x}$ instead of x_e. This could be seen as a minor imprecision as the objective is not explicitly the estimation of states.

Due to the aforementioned equivalence of solutions to both deterministic and stochastic quadratic-estimation problems, a Krein space state-space system can be defined to which the standard Kalman filter approach (see Section 3.3) is applicable [101, 204]. The corresponding state-space equations read

$$x_{k+1} = Ax_k + w_k \tag{3.67a}$$

$$\begin{bmatrix} y_k \\ \check{s}_{k|k} \end{bmatrix} = \begin{bmatrix} C \\ L \end{bmatrix} x_k + \bar{v}_k, \tag{3.67b}$$

and the estimation results are similar to those presented before – only with extended matrices. In particular, the pendant to the innovations form given in Eq. 3.48 is defined as

$$\hat{x}_{k+1|k} = A\hat{x}_{k|k-1} + \bar{K}_{p,k}\hat{e}_k \tag{3.68a}$$

$$\begin{bmatrix} y_k \\ \check{s}_{k|k} \end{bmatrix} = \bar{C}\hat{x}_{k|k-1} + \hat{e}_k. \tag{3.68b}$$

Further, the gain matrix

$$\bar{K}_{p,k} = AP_{k|k-1}\bar{C}^{\mathrm{T}}(\bar{C}P_{k|k-1}\bar{C}^{\mathrm{T}} + \bar{R}_{\bar{v},k})^{-1} \tag{3.69}$$

results from the Riccati recursion

$$P_{k+1|k} = AP_{k|k-1}A^{\mathrm{T}} - AP_{k|k-1}\bar{C}^{\mathrm{T}}(\bar{C}P_{k|k-1}\bar{C}^{\mathrm{T}} + \bar{R}_{\bar{v},k})^{-1}\bar{C}P_{k|k-1}A^{\mathrm{T}} + Q_k \tag{3.70}$$

with extended matrices $\bar{C} = [C^{\mathrm{T}}\ L^{\mathrm{T}}]^{\mathrm{T}}$ and $\bar{R}_{\bar{v},k}$, and in comparison with Eq. 3.47, with $S_k = 0$.

Unfortunately, these equations do not constitute the final solution for two reasons [101, 204]:

(i) $e_{y,k}$ and $e_{s,k}$ in Eq. 3.66 are not independent ($\langle e_{y,k}, e_{s,k}\rangle \neq 0$), and thus, Eqs. 3.66 and 3.69 have to be decoupled, e.g. with the help of an LDU factorization.

(ii) $\check{s}_{k|k}$ is a theoretical choice only, as it is not available nor measurable in a prediction step. Hence, a pragmatic choice has to be made that ensures that the minimum of the cost function stated in Eq. 3.65 is positive.

Taking care of the first point results in the new extended innovations sequence $\bar{e}_k$ defined as [204]

$$\bar{e}_i = \begin{bmatrix} e_{y,k} \\ \tilde{e}_{s,k} \end{bmatrix} = \begin{bmatrix} y_k \\ \check{s}_{k|k} \end{bmatrix} - \begin{bmatrix} \hat{y}_{k|k-1} \\ \hat{s}_{k|k} \end{bmatrix}, \tag{3.71}$$

with

$$\begin{aligned} \hat{s}_{k|k} &= L\hat{x}_{k|k} \\ &= L\hat{x}_{k|k-1} + LP_{k|k-1}C^{\mathrm{T}}(R_{v,k} + CP_{k|k-1}C^{\mathrm{T}})^{-1}e_{y,k} \\ &= \hat{s}_{k|k-1} + LP_{k|k-1}C^{\mathrm{T}}R_{e_y,k}^{-1}e_{y,k} \end{aligned} \tag{3.72}$$

that satisfies $\langle e_{y,k}, \tilde{e}_{s,k}\rangle = 0$. Eq. 3.71 replaces $\hat{e}_k$ in Eq. 3.68. Further, the gain matrix decomposes to

$$\begin{aligned} &\bar{K}_{p,k} = \begin{bmatrix} K_{py,k} & K_{ps,k} \end{bmatrix}, \\ &K_{py,k} = AP_{k|k-1}C^{\mathrm{T}}R_{e_y,k}^{-1}, \quad K_{ps,k} = AP_{k|k-1}(L^{\mathrm{T}} - C^{\mathrm{T}}(R_{e_y,k}^{\mathrm{T}})^{-1}CP_{k|k-1}L^{\mathrm{T}})R_{\tilde{e}_s,k}^{-1}, \end{aligned} \tag{3.73}$$

where $R_{\tilde{e}_s,k} = \langle \tilde{e}_{s,k}, \tilde{e}_{s,k}\rangle$.

Concerning the selection of $\check{s}_{k|k}$, a reasonable replacement is given through $\check{s}_{k|k} = \hat{s}_{k|k}$, which is equivalent to $\tilde{e}_{s,k} = 0$, cf. Eq. 3.71. Keeping that in mind, a final solution arises by substituting Eqs. 3.71 to 3.73 into Eq. 3.68 so that

$$\begin{aligned}
\hat{x}_{k+1|k} &= A\hat{x}_{k|k-1} + \bar{K}_{p,k}\tilde{e}_k \\
&= A\hat{x}_{k|k-1} + \begin{bmatrix} K_{py,k} & K_{ps,k} \end{bmatrix} \begin{bmatrix} e_{y,k} \\ 0 \end{bmatrix} \\
&= A\hat{x}_{k|k-1} + K_{py,k}e_{y,k} && \text{(3.74a)} \\
\hat{s}_{k|k} &= L\hat{x}_{k|k-1} + LP_{k|k-1}C^{\mathrm{T}}R_{e_y,k}^{-1}e_{y,k}. && \text{(3.74b)}
\end{aligned}$$

It must be mentioned that the existence of Eq. 3.74 is not guaranteed for each time step k given some $\gamma > 0$. Certain existence conditions must be fulfilled, and thus, they must be checked recursively when finite-horizon filtering ($k \in [0, \infty)$) is pursued. For more information on that, see, e.g., [204, p. 90].

Rearranging Eq. 3.74 under consideration of $e_{y,k} = y_k - C\hat{x}_{k|k-1}$ results in a system that maps the measurements y_k to the estimates $\hat{s}_{k|k}$. The corresponding state space formulation reads

$$\begin{aligned}
\hat{x}_{k+1|k} &= A_{p,k}\hat{x}_{k|k-1} + K_{py,k}y_k && \text{(3.75a)} \\
\hat{s}_{k|k} &= L(I - P_{k|k-1}C^{\mathrm{T}}R_{e_y,k}^{-1}C)\hat{x}_{k|k-1} + LP_{k|k-1}C^{\mathrm{T}}R_{e_y,k}^{-1}y_k, && \text{(3.75b)}
\end{aligned}$$

with $A_{p,k} = A - K_{py,k}C$.

STEADY-STATE $\mathcal{H}_\infty$ FILTER

As in Kalman filtering for LTI systems, the recursive Eq. 3.70 converges towards a constant matrix as $k \to \infty$ if, beside other conditions, w_k and v_k are stationary processes, and thus, lead to a stationary central Gramian matrix $\overline{M}_k$ defined in Eq. 3.63. Therefore, a time-invariant $\mathcal{H}_\infty$ filter can be determined by solving the following DARE with the extended matrix $\bar{C} = [C^{\mathrm{T}} \;\; L^{\mathrm{T}}]^{\mathrm{T}}$ and the negative definite Gramian $\bar{R}_{\bar{v}}$ (see Eq. 3.63):

$$P_{k+1|k} \approx P_p = AP_pA^{\mathrm{T}} - AP_p\bar{C}^{\mathrm{T}}(\bar{C}P_p\bar{C}^{\mathrm{T}} + \bar{R}_{\bar{v}})^{-1}\bar{C}P_pA^{\mathrm{T}} + Q \tag{3.76}$$

Then, the time-invariant gain matrix reads

$$K_{py} = AP_pC^{\mathrm{T}}(CP_pC^{\mathrm{T}} + R_{v,k})^{-1} \quad \text{with} \quad A_p = A - K_{py}C. \tag{3.77}$$

The resulting so-called *central filter* can also be used for prediction purposes or in other words as a strictly causal estimator (cf. Section 2.1.4) with $\hat{s}_{k|k-1} = Lx_{k|k-1}$ [101, p. 401]. This is possible since the DARE for the derivations of a strictly causal estimator with output equation $\hat{s}_{k|k-1} = Lx_{k|k-1}$ is equivalent to the DARE of the causal estimator (Eq. 3.76).

Naturally, finding a converging solution for Eq. 3.76 depends, among other conditions explained in [101, p. 436], heavily on the choice of γ. An optimal upper bound can be determined via iteration or with the help of the smoothing solution. Nevertheless, in the regarded case of *filtering signals in additive noise* ($L = C$), a solution for $\gamma = 1$ is always feasible when the convergence conditions for Eq. 3.76 are fulfilled [101, p. 471]. The resulting filter does not

filter at all, but luckily, the predictive performance can be analyzed instead by considering the strictly causal estimator.

In summary, the estimator $\boldsymbol{K}$ that satisfies Problem 3.3 is given by

$$\boldsymbol{K} = \left[\begin{array}{c|c} A_p & K_{py} \\ \hline C(I - P_{k|k-1}C^{\mathrm{T}}R_{e_y,k}^{-1}C) & CP_{k|k-1}C^{\mathrm{T}}R_{e_y,k}^{-1} \end{array}\right],$$
$$\begin{bmatrix} \hat{x}_{k+1|k} \\ \hat{y}_{k|k} \end{bmatrix} = \begin{bmatrix} A_p & K_{py} \\ C(I - P_{k|k-1}C^{\mathrm{T}}R_{e_y,k}^{-1}C) & CP_{k|k-1}C^{\mathrm{T}}R_{e_y,k}^{-1} \end{bmatrix} \begin{bmatrix} \hat{x}_{k|k-1} \\ y_k \end{bmatrix}, \tag{3.78}$$

and Problem 3.1 is fulfilled by

$$\bar{\boldsymbol{K}}_p = \left[\begin{array}{c|c} A_p & K_{py} \\ \hline C & 0 \end{array}\right], \quad \begin{bmatrix} \hat{x}_{k+1|k} \\ \hat{y}_{k|k-1} \end{bmatrix} = \begin{bmatrix} A_p & K_{py} \\ C & 0 \end{bmatrix} \begin{bmatrix} \hat{x}_{k|k-1} \\ y_k \end{bmatrix}. \tag{3.79}$$

3.5.2 LMI-based $\mathcal{H}_\infty$ filtering

A rather modern approach for the design of $\mathcal{H}_\infty$ filters is posed by linear matrix inequality (LMI)-based syntheses. The fundamental idea of these strategies is to linearize the typically nonlinear cost functions and solve the resulting matrix inequalities by means of convex optimization and semidefinite programming. Solving these already relaxed problems still involves elaborate numerical methods such as interior-point methods. For further information, see, e.g., [28]. The optimizations can be conducted by employing open-source software packages such as YALMIP [123] or CVX [33, 87] together with the solvers SEDUMI [187] or SDPT3 [189]. In the following, an LMI-based synthesis for $\mathcal{H}_\infty$ filters is presented in brevity. The proposed strategy follows Problem 3.3 and suffices Problem 3.1 by directly imposing a strictly proper form.

For the LMI-based synthesis of $\mathcal{H}_\infty$ filters, they are considered as special cases of dynamic output feedback controllers. Hence, the corresponding LMIs are adapted for their design [38, p. 139]. A filter $\boldsymbol{K}$ can be designed if there exists a matrix $X = X^{\mathrm{T}} < 0$ such that [83]

$$\begin{bmatrix} -X^{-1} & A_{\mathrm{cl}} & B_{\mathrm{cl}} & 0 \\ A_{\mathrm{cl}}^{\mathrm{T}} & -X & 0 & C_{\mathrm{cl}}^{\mathrm{T}} \\ B_{\mathrm{cl}}^{\mathrm{T}} & 0 & -\gamma I & D_{\mathrm{cl}}^{\mathrm{T}} \\ 0 & C_{\mathrm{cl}} & D_{\mathrm{cl}} & -\gamma I \end{bmatrix} < 0. \tag{3.80}$$

Substituting Eq. 3.33 into this Eq. 3.80 results in a matrix inequality that is not linear in the variables $(A_f,\, B_f,\, C_f, D_f)$ representing $\boldsymbol{K}$, and thus, the nonlinear matrix inequality should be transferred to an LMI to efficiently solve the design problem by means of convex optimization [84]. Several ways exist to perform this conversion, e.g., through a change of variables. For further information, the interested reader is referred to the literature, e.g., [64, 84]. According

to Caverly and Forbes [38, p. 139], a filter that satisfies Problems 3.3 and 3.1 can be found by solving the following set of LMIs:

$$\begin{bmatrix} X_1 & I_n & X_1A+\bar{B}C_2 & \overline{A} & X_1B_1+\bar{B}D_{21} & 0_{n,q} \\ * & Y_1 & A & AY_1 & B_1 & 0_{n,q} \\ * & * & X_1 & I_n & 0_{n,q} & C_1^{\mathrm{T}}+C_2^{\mathrm{T}}\bar{D}^{\mathrm{T}}D_{12}^{\mathrm{T}} \\ * & * & * & Y_1 & 0_{n,q} & Y_1C_1^{\mathrm{T}}+\bar{C}^{\mathrm{T}}D_{12}^{\mathrm{T}} \\ * & * & * & * & \gamma I_q & D_{11}^{\mathrm{T}}+D_{21}^{\mathrm{T}}D_n^{\mathrm{T}}D_{12}^{\mathrm{T}} \\ * & * & * & * & * & \gamma I_q \end{bmatrix} > 0, \quad \begin{bmatrix} X_1 & I_n \\ * & Y_1 \end{bmatrix} > 0. \tag{3.81}$$

Here, $(*)$ was placed in the block lower triangular matrix to emphasize that the symmetric matrices can be easily completed. The identity and zero matrices are given the relevant dimensions to simplify the reimplementation process[9]. The matrices X_1, Y_1, $\overline{A}$, $\bar{B}$, $\bar{C}$, and $\bar{D}$ constitute the variables of the LMI-based optimization problem that result from the linearization procedure. Finally, the filter parameter can be determined as

$$\begin{bmatrix} A_f & B_f \\ C_f & D_f \end{bmatrix} = \begin{bmatrix} X_2 & 0 \\ 0 & I \end{bmatrix}^{-1} \left(\begin{bmatrix} \overline{A} & \bar{B} \\ \bar{C} & \bar{D} \end{bmatrix} - \begin{bmatrix} X_1AY_1 & 0 \\ 0 & 0 \end{bmatrix} \right) \begin{bmatrix} Y_2^{\mathrm{T}} & 0 \\ C_2Y_1 & I \end{bmatrix}^{-1}. \tag{3.82}$$

Now, taking into account Problem 3.1 by defining $D_f = 0$ and $C_f = C$, it follows that $\bar{D} = 0$ and $\bar{C} = CY_2^{\mathrm{T}}$ so that Eq. 3.81 simplifies and the final list of optimization variables reads: X_1, Y_1, Y_2 $\overline{A}$, and $\bar{B}$. X_2 follows with $X_2 = I - X_1Y_1Y_2^{-\mathrm{T}}$. Finally, the LMI-based filter for y_k arises as

$$\boldsymbol{K} = \bar{\boldsymbol{K}}_f = \left[\begin{array}{c|c} A_f & K_f \\ \hline C & 0 \end{array}\right], \quad \begin{bmatrix} x_{f,k+1} \\ \hat{y}_{k|k} \end{bmatrix} = \begin{bmatrix} A_f & K_f \\ C & 0 \end{bmatrix} \begin{bmatrix} x_{f,k} \\ y_k \end{bmatrix}, \tag{3.83}$$

where $K_f = B_f$.

3.6 CONCLUDING REMARKS

In this chapter, two different approaches for linear quadratic estimation were presented, namely Kalman and $\mathcal{H}_\infty$ filtering. Where the former assumes white and Gaussian distributed disturbances and requires the knowledge of the corresponding covariance matrices, $\mathcal{H}_\infty$ filters do not make any assumptions regarding these processes. For this thesis, both strategies are utilized to realize causal and strictly proper estimators (predictors or filters) that map the measured signal y to the estimate $\hat{y}$ so that the estimation error reads $e = \hat{y} - y$. The latter can then be assessed to infer changes in the structure's dynamics resulting from damage. The considered approaches for the realization of $\mathcal{H}_\infty$ filters comprise a Riccati-based and LMI-based synthesis. In either case, special attention is paid to finding the strictly proper form, as is summarized in Fig. 3.3. On the other hand, the Kalman filter theory directly leads to the desired representation by inverting the well-known innovations form.

9 Note that the additional subscripts are only provided in cases where the identification of matrix dimensions appears particularly cumbersome.

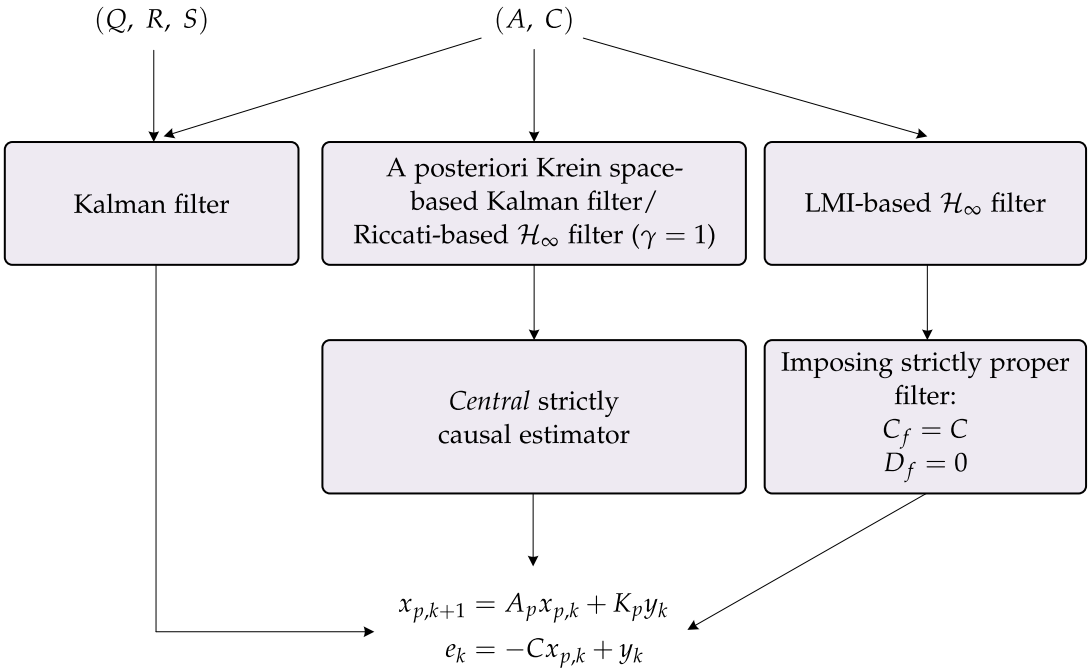

Figure 3.3: Applied predictor syntheses using linear quadratic estimation.

4

DAMAGE ANALYSIS FRAMEWORK

In this chapter, a damage analysis framework developed by Lenzen and Vollmering [118, 119] is introduced. Therein, estimation errors of linear quadratic estimators comprise the basis for damage inference. The framework is inspired by the control-related discipline of fault detection and isolation (FDI); however, two estimators are operated in parallel, unlike conventional approaches. Moreover, instead of processing measurement data, the involved signals are parameterized with the help of the identified system parameters. This parameterization finally enables oblique projections in state space, which further improves the sensitivity and robustness towards damage. Thereby, the method is referred to as state-projection estimation error (SP2E). The resulting estimation errors, or more precisely differences of estimation errors, can be assessed using the average signal power, as initially proposed [118, 119], or by regarding the residual's correlation function, see [210].

In the following, the utilization of multiple estimators and parameterized signals is discussed first. Then, the theory from behind SP2E is briefly summarized in Sections 4.1 and 4.2. The performance of both the power-based and correlation-based damage indicators is discussed and compared using a simulation example in Section 4.3. Finally, in Section 4.3, relevant aspects of the SP2E framework in the context of SHM, such as hypotheses tests, are examined. It is remarked that parts of the proceeding text have been published in [210]. A concise list of the relevant computational steps is given therein as well.

4.1 DAMAGE INDICATORS BY ESTIMATION ERROR RESIDUALS

The considered damage analysis framework is based on the interconnection of state-space systems associated with a reference and analysis state. According to the second axiom of SHM by Farrar and Worden [70, Chapter 13], this differentiation is necessary to enable damage identification. Typically, the structure of interest is considered healthy for a certain period, which is generally referred to as the baseline phase. However, the analysis state does not necessarily relate to the damaged system; it could as well be a further realization of the healthy structure [210]. Signals and systems corresponding to the reference state are indicated by index 1. On the other hand, the analysis state is emphasized with the help of an index 2.

As mentioned before, the SP2E framework is inspired by the control-related discipline of FDI [41]. There, the damage is readily inferred from the estimation performance regarding measured outputs y_k. Hence, a conventional approach is to realize estimators representing the observed and healthy structure and then assess the innovations sequence e_k, also referred to as estimation error, given data acquired under unknown conditions. A null hypothesis for damage identification is generally formulated by considering observations in a training or inspection phase, i.e., data from the healthy structure. This hypothesis is then tested during the inspection phase, as will be explained later in Section 4.4. Since e_k is often assumed to be

Gaussian distributed, a typical approach is to evaluate its mean or covariance $R_{e_k} = \mathrm{E}\{e_k e_k^{\mathrm{T}}\}$ (cf. [41]) where the latter offers the convenient physical interpretation of average power, cf. Section 2.2.3. Now taking into account the aforementioned definitions, the explained conventional residual generator can be illustrated by Fig. 4.1. Here, $\boldsymbol{G}_2$ represents the mechanical

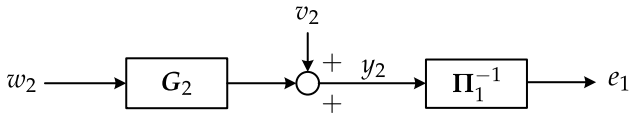

Figure 4.1: Conventional residual generator for damage identification.

system in the analysis state that maps noise processes w_2 and v_2 to the observations y_2. These outputs are used to compute e_1 with the help of the reference estimator $\boldsymbol{\Pi}_1^{-1}$. For completeness, the state-space equations representing both systems are defined as

$$x_{2,k+1} = A_2 x_k + w_{2,k} \tag{4.1a}$$
$$y_{2,k} = C_2 x_{2,k} + v_{2,k}. \tag{4.1b}$$

and

$$x_{e,1,k+1} = A_{e,1} x_{e,1,k} + K_{e,1} y_{2,k} \tag{4.2a}$$
$$e_{k,1} = -C_1 x_{e,1,k} + y_{2,k}. \tag{4.2b}$$

Note that in Eq. 4.2, the general notation for a strictly proper estimator is used (cf. Fig. 3.3) that could be represented as a predictor or filter for y_k. Naturally, the noise processes $w_{2,k}$ and $v_{2,k}$ are unknown but assumed as stationary; they can be characterized by the Gramian matrix

$$M_2 = \left\langle \begin{bmatrix} w_{2,k} \\ v_{2,k} \end{bmatrix}, \begin{bmatrix} w_{2,l} \\ v_{2,l} \end{bmatrix} \right\rangle \tag{4.3}$$
$$= \begin{bmatrix} Q_2 & S_2 \\ S_2^{\mathrm{T}} & R_{v,2} \end{bmatrix} \delta_{kl} \tag{4.4}$$
$$= \begin{bmatrix} \Sigma_{x_2} - A_2 \Sigma_{x_2} {A_2}^{\mathrm{T}} & N_2 - A_2 \Sigma_{x_2} {C_2}^{\mathrm{T}} \\ {N_2}^{\mathrm{T}} - C_2 \Sigma_{x_2} {A_2}^{\mathrm{T}} & R_y(0) - C_2 \Sigma_{x_2} {C_2}^{\mathrm{T}} \end{bmatrix} \delta_{kl} \geqslant 0, \tag{4.5}$$

with $N_2 = \langle x_{2,k+1}, y_{2,k} \rangle = A_2 \Sigma_{x_2} C_2^{\mathrm{T}} + S_2$. Regarding Fig. 4.1 and with the help of the equations given above, the map from y_2 to e_1 can be described with the following equations

$$e_{1,k} = -C_1 \hat{x}_{1,k} + y_{2,k} \tag{4.6}$$
$$= -C_1 \hat{x}_{1,k} + C_2 x_{2,k} + v_{2,k}. \tag{4.7}$$

This shows that for damage identification to be effective, the following conditions must hold: (i) The dynamics represented by the estimator ($A_{e,1}$, $K_{e,1}$, C_1) is linked to the dynamics encompassed in the measurement data y_2. (ii) The characteristics of the noise process $w_{2,k}$, but most importantly, $v_{2,k}$ are truly stationary.

In data-driven SHM, both conditions are likely to be violated at one point or another. In a supervised system identification procedure, poles with no direct structural meaning, e.g.,

those representing the mains hum, are generally discarded. Also, when system identification is automated, physical modes might be neglected by mistake. In these cases, a discrepancy exists between the identified dynamics and the one encompassed in the measurements being processed. Then, these effects end up in the innovations sequence $e_{1,k}$ and are likely to trigger false detections. Instead, the SSI can be exploited that allows the parameterization of the correlation function or PSD of the measured output y_k, see Eq. 2.82. Moreover, an alternative residual $d_k = e_{1,k} - e_{2,k}$ can be considered that follows by employing a second estimator $\mathbf{\Pi}_2^{-1}$, which is designed in the analysis phase and that constitutes the map from y_2 to e_2. In accordance to Eq. 4.7, its estimation error reads

$$e_{2,k} = -C_2\hat{x}_{2,k} + C_2 x_{2,k} + v_{2,k}. \tag{4.8}$$

Computing d_k by subtracting Eq. 4.8 from Eq. 4.7 suppresses the measurement noise $v_{2,k}$, which does not contain any structural information, and hence, increases the robustness of damage identification.

The generation of the signal y_2 as well as the computation of d can be expressed by the overall system $\mathbf{\Omega} : [w_3^{\mathrm{T}}\ v_3^{\mathrm{T}}]^{\mathrm{T}} \rightarrow d$, which is depicted in Fig. 4.2. In fact, Fig. 4.2 describes a more

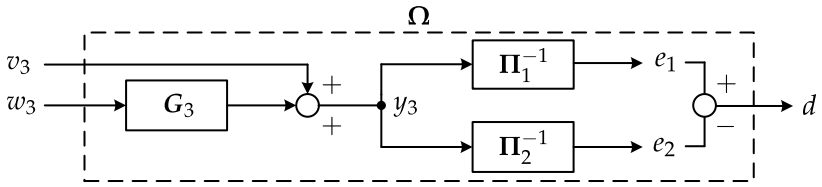

Figure 4.2: Central system $\mathbf{\Omega}$ of the parametric damage analysis framework. Index 1 refers to reference state, index 2 is associated with analysis state.

general scenario by introducing the test signal y_3 that stems from the system $\boldsymbol{G}_3$ exited by w_3 and v_3. The latter processes are characterized by M_3, cf. Eqs. 4.3 - 4.5. This extension via $\boldsymbol{G}_3$ results in an increased flexibility of the damage analysis framework, as will be explained in Section 4.2.2. For now, it should be acknowledged that $\boldsymbol{G}_3$ can be chosen freely, e.g., such that $\boldsymbol{G}_3 = \boldsymbol{G}_2$ so that $w_3 = w_2$, $v_3 = v_2$, and $y_3 = y_2$. This constitutes a natural selection since when SP2E is considered for SHM, $\boldsymbol{G}_2$ is readily available with every incoming data set and system identification conducted.

As mentioned before, damage can be inferred by assessing the correlation function $R_d(i)$. Therefore, processing the measured data $y_{3,k}$ is not required; instead $R_d(i)$ can be computed using the state-space parameters of $\mathbf{\Omega}$ and by making practical choices for the input Gramian M_3 in Eq. 4.3. The latter becomes relevant because the input to $\mathbf{\Omega}$ is unknown. This topic is

addressed at the end of this section. For now, consider the state-space representation of $\mathbf{\Omega}$ defined as

$$\begin{bmatrix} x_{e,1,k+1} \\ x_{e,2,k+1} \\ x_{3,k+1} \end{bmatrix} = \begin{bmatrix} A_{e,1} & 0 & K_{e,1}C_3 \\ 0 & A_{e,2} & K_{e,2}C_3 \\ 0 & 0 & A_3 \end{bmatrix} \begin{bmatrix} x_{e,1,k} \\ x_{e,2,k} \\ x_{3,k} \end{bmatrix} + \begin{bmatrix} 0 & K_{e,1} \\ 0 & K_{e,2} \\ I & 0 \end{bmatrix} \begin{bmatrix} w_{3,k} \\ v_{3,k} \end{bmatrix} \tag{4.9a}$$

$$d_k = \begin{bmatrix} -C_1 & C_2 & 0 \end{bmatrix} \begin{bmatrix} x_{e,1,k} \\ x_{e,2,k} \\ x_{3,k} \end{bmatrix}. \tag{4.9b}$$

By introducing the state-space parameters of $\mathbf{\Omega}$, $A_\Omega \in \mathbb{R}^{n_\Omega \times n_\Omega}$, $B_\Omega \in \mathbb{R}^{n_\Omega \times (n_3+q)}$, and $C_\Omega \in \mathbb{R}^{q \times n_\Omega}$ with model order $n_\Omega = n_1 + n_2 + n_3$, this system of equations can be simplified to

$$x_{\Omega,k+1} = A_\Omega x_{\Omega,k} + B_\Omega u_{\Omega,k} \tag{4.10a}$$

$$d_k = C_\Omega x_{\Omega,k} \tag{4.10b}$$

such that Eqs. 4.10a and 4.10a equal Eqs. 4.9a and 4.9a, respectively. Based on that, the correlation function [210]

$$R_d(i) = \mathrm{E}\left\{ d_k d_{k+i}^\mathrm{T} \right\} = C_\Omega A_\Omega^i \Sigma_{x_\Omega} C_\Omega^\mathrm{T} \tag{4.11}$$

follows, where Σ_{x_Ω} denotes the Gramian matrix of the states $x_{\Omega,k}$, which obeys the following Lyapunov equation:

$$\Sigma_{x_\Omega} = A_\Omega \Sigma_{x_\Omega} A_\Omega^\mathrm{T} + B_\Omega M_3 B_\Omega^\mathrm{T}. \tag{4.12}$$

Here, it is assumed that $\langle x_{\Omega,k}, u_{\Omega,k} \rangle = 0$ for $i \in \mathbb{N}$. As implied before, the computation of this Lyapunov equation requires a certain pragmatism, as the Gramian M_3 is unknown. Suggestions to overcome this hurdle are discussed at the end of Section 4.2.1.

Using Eq. 4.11, the average power of d can be computed by setting $i = 0$ and extracting the diagonal of $R_d(0)$. An alternative damage indicator can be constructed by considering the main diagonal of $R_d(i)$ and computing the variance of the entries for a given interval. In both cases, the sensitivity towards structural damage can be improved by applying oblique projections in state-space, and thereby, reducing the disturbance of the state-estimation error [204]. This procedure is referred to as SP2E and will be explained in the following section, where also the corresponding damage indicators are formally defined.

4.2 STATE PROJECTION ESTIMATION ERROR (SP2E)

The fundamental idea of SP2E is to retain the information contained in x_Ω that is commonly shared by x_1 and x_2, and thus, compute a difference signal $d_\mathcal{V}$ which is condensed to the part relevant for changes (damages) [204]. This is enabled through the use of oblique projection techniques, which, under certain circumstances, can even be conducted with a single estimator. In the following section, the classical approach for SP2E, using two estimators, is explained. In Section 4.2.3, the single-estimator approach is summarized.

4.2.1 SP2E by using two estimators

To comprehend this, it is helpful to see the state vector x_Ω as an element of the vector space $\mathcal{W}$, which is essentially the *direct sum* of the two *complementary subspaces* $\mathcal{U}$ and $\mathcal{V}$, i.e., $\mathcal{U} \cap \mathcal{V} = 0$. In linear algebra, this is denoted by writing $\mathcal{W} = \mathcal{U} \bigoplus \mathcal{V}$, where $\bigoplus$ depicts the direct sum. By regarding x_Ω, as defined in Eq. 4.9a, it can be seen that this state vector consists of $x_{e,1}$ and $x_{e,2}$, both representing the estimates of x_1 and x_2, respectively, and x_3, which is the state vector of the system $\boldsymbol{G}_3$ generating the test signal y_3. Now, $\mathcal{V}$ can be seen as a vector space holding information about the true states of $\boldsymbol{G}_3$. Further, $\mathcal{U}$ is the vector space that governs the states of the estimators $x_{e,1}$ and $x_{e,2}$. Moreover, $\mathcal{U}$ is defined as the direct sum of $\mathcal{U}_1$ ($x_{e,1}$) and $\mathcal{U}_2$ ($x_{e,2}$). These rather complex relations are illustrated in Fig. 4.3

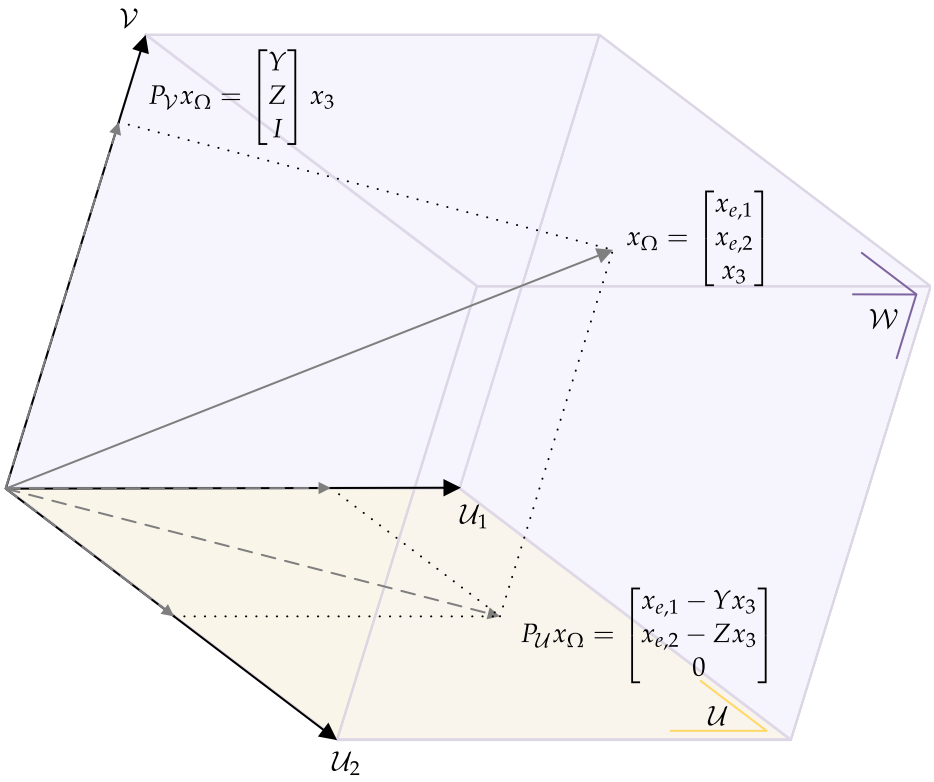

Figure 4.3: Oblique projections of the state vector x_Ω. Adapted from [119]

COMPLEMENTARY SUBSPACES

From an algebraic point of view, the goal of SP2E is to find two unique linear projectors $P_\mathcal{V}$ and $P_\mathcal{U}$. The former maps onto $\mathcal{V}$ along $\mathcal{U}$, and $P_\mathcal{U}$ operates in the opposing direction. The product $P_\mathcal{V} x_\Omega$ leads to $x_{\Omega\mathcal{V}} \in \mathcal{V}$, whereas $P_\mathcal{U} x_\Omega$ is equal to $x_{\Omega\mathcal{U}} \in \mathcal{U}$. Later in this section but also in Fig. 4.3, it can be seen that the sum $x_\Omega = x_{\Omega\mathcal{U}} + x_{\Omega\mathcal{V}}$ is unique, which is an unconditional property of complementary vector spaces and their direct sum, it is equivalent to $\mathcal{U} \cap \mathcal{V} = 0$, see [134]. Since $\mathcal{V}$ strictly refers to x_3 and x_Ω contains both x_1 and x_2, $x_{\Omega\mathcal{V}}$ can be utilized to extract differences in modal information comprised by (A_1, C_1) and (A_2, C_2), cf. [205].

To compute the unique projectors $P_{\mathcal{U}}$ and $P_{\mathcal{V}}$, bases for the complementary subspaces $\mathcal{U}$ and $\mathcal{V}$ must be found. Conveniently, they arise from an eigenvalue decomposition of A_Ω such that

$$A_\Omega = X\Lambda X^{-1} \tag{4.13}$$

$$= \begin{bmatrix} X_1 & X_2 & X_3 \end{bmatrix} \begin{bmatrix} \Lambda_1 & & 0 \\ & \Lambda_2 & \\ 0 & & \Lambda_3 \end{bmatrix} \begin{bmatrix} \overline{X}_1 \\ \overline{X}_2 \\ \overline{X}_3 \end{bmatrix}, \tag{4.14}$$

where X_i denotes the eigenvectors, and Λ_i represents the eigenvalues of A_Ω. The structure of the former follows directly from the composition of A_Ω defined in Eq. 4.9a, and the fact that [204]

$$A_\Omega = \sum_{i=1}^{3} X_i \Lambda_i \overline{X}_i. \tag{4.15}$$

Hence, the matrix containing the eigenvectors on its columns reads

$$X = \begin{bmatrix} \begin{bmatrix} X_{11} & 0 \\ 0 & X_{22} \end{bmatrix} & \begin{bmatrix} X_{13} \\ X_{23} \end{bmatrix} \\ \begin{bmatrix} 0 & 0 \end{bmatrix} & \begin{bmatrix} X_{33} \end{bmatrix} \end{bmatrix} \tag{4.16}$$

X_1, X_2, and X_3 represent the bases of the complementary subspaces $\mathcal{U}_1$, $\mathcal{U}_2$, and $\mathcal{V}$, respectively. The inverse X^{-1} is found by considering X as a 2×2 block matrix, as highlighted in the previous equation, and performing a block-wise Gauss-Jordan elimination [124, 134]. Thus,

$$X^{-1} = \begin{bmatrix} X_{11}^{-1} & 0 & -X_{11}^{-1} Y \\ 0 & X_{22}^{-1} & -X_{22}^{-1} Z \\ 0 & 0 & X_{33}^{-1} \end{bmatrix}, \tag{4.17}$$

with

$$Y = X_{13} X_{33}^{-1} \quad \text{and} \quad Z = X_{23} X_{33}^{-1}. \tag{4.18}$$

Now, it is easy to show that $Z = I$ if $\boldsymbol{G}_3 = \boldsymbol{G}_2$, and $Z = I$ if $\boldsymbol{G}_3 = \boldsymbol{G}_1$. This is an important condition in the derivation of the projectors. An exemplary proof for the case of $\boldsymbol{G}_3 = \boldsymbol{G}_2$ is given in Section A.2.

COMPUTATION OF PROJECTORS

Given the bases for the complementary subspaces $\mathcal{U}$ and $\mathcal{V}$, determined by the eigenvectors of A_Ω, the two projectors are defined as [134]

$$P_{\mathcal{U}} = \begin{bmatrix} U & 0 \end{bmatrix} \begin{bmatrix} U & V \end{bmatrix}^{-1} \quad \text{and} \quad P_{\mathcal{V}} = \begin{bmatrix} 0 & V \end{bmatrix} \begin{bmatrix} U & V \end{bmatrix}^{-1} \tag{4.19}$$

with [204]

$$U = \begin{bmatrix} X_1 & X_2 \end{bmatrix} \quad \text{and} \quad V = X_3. \tag{4.20}$$

Again, $P_{\mathcal{U}}$ constitutes the map onto $\mathcal{U}$ along $\mathcal{V}$, while $P_{\mathcal{V}}$ projects onto $\mathcal{V}$ along $\mathcal{U}$. Substituting Eqs. 4.16 and 4.17 into Eq. 4.19 and under consideration of Eq. 4.20, the projectors arise as

$$P_{\mathcal{U}} = \begin{bmatrix} I & 0 & -Y \\ 0 & I & -Z \\ 0 & 0 & 0 \end{bmatrix} \tag{4.21}$$

and

$$P_{\mathcal{V}} = \begin{bmatrix} 0 & 0 & Y \\ 0 & 0 & Z \\ 0 & 0 & I \end{bmatrix}. \tag{4.22}$$

By means of $P_{\mathcal{U}}$ and $P_{\mathcal{V}}$, x_Ω can be factorized uniquely such that

$$\begin{aligned} x_{\Omega,k} &= P_{\mathcal{U}} x_{\Omega,k} + P_{\mathcal{V}} x_{\Omega,k} && (4.23)\\ &= x_{\Omega\mathcal{U},k} + x_{\Omega\mathcal{V},k} && (4.24)\\ &= \begin{bmatrix} x_{e,1,k} - Y x_{3,k} \\ x_{e,2,k} - Z x_{3,k} \\ 0 \end{bmatrix} + \begin{bmatrix} 0 & 0 & \bar{P}_{\mathcal{V}} \end{bmatrix} x_{\Omega,k} && (4.25)\\ &= x_{\Omega\mathcal{U},k} + \bar{P}_{\mathcal{V}} x_{3,k}, && (4.26) \end{aligned}$$

and thus, information regarding x_3 is removed from $x_{\Omega,k}$ when $P_{\mathcal{U}}$ is applied. On the other hand, $x_{\Omega\mathcal{V},k}$ is solely dependent on x_3. Because of that, the map onto $\mathcal{V}$ along $\mathcal{U}$ by means of $P_{\mathcal{V}}$ constitutes a model reduction. Note that $\bar{P}_{\mathcal{V}}$ was introduced above to denote the relevant parts of $P_{\mathcal{V}}$.

ENHANCED DAMAGE INDICATORS USING STATE PROJECTIONS

$x_{\Omega\mathcal{V}}$ is finally used to define the enhanced difference process $d_{\mathcal{V}}$ as

$$d_{\mathcal{V},k} = C_\Omega x_{\Omega\mathcal{V},k} = (-C_1 Y + C_2) x_{3,k}. \tag{4.27}$$

Equivalently, the projectors $P_{\mathcal{V}}$ or $\bar{P}_{\mathcal{V}}$, respectively, might also be applied to the correlation function given in Eq. 4.11, resulting in the correlation function of the projected difference process [210]

$$\begin{aligned} R_{d\mathcal{V}}(i) = \langle d_{\mathcal{V},k}, d_{\mathcal{V},k+i} \rangle &= C_\Omega P_{\mathcal{V}} A_\Omega^i \Sigma_{x_\Omega} P_{\mathcal{V}}^{\mathrm{T}} C_\Omega^{\mathrm{T}} && (4.28a)\\ &= C_\Omega \bar{P}_{\mathcal{V}} A_3^i \Sigma_{x_3} \bar{P}_{\mathcal{V}}^{\mathrm{T}} C_\Omega^{\mathrm{T}}. && (4.28b) \end{aligned}$$

For damage detection and localization, one can successively analyze the average power of $d_{\mathcal{V}}$ by considering the diagonal of $R_{d\mathcal{V}}(0)$ in Eq. 4.28, as suggested in [118, 119]. However, since the estimation errors are most probably not white, depending on the applied filtering technique and due to practical circumstances, Wernitz et al. [210] proposed to examine $R_{d\mathcal{V}}(i)$ for $i > 0$ instead by considering the variance of the diagonal elements of $R_{d\mathcal{V}}(i)$ for $i \in [i_1, i_2]$ with $i_2 > i_1$ and $i_1 > 0$. This new damage-sensitive feature can be formally defined as

$$r_{d\mathcal{V}}([i_1, i_2]) = \begin{bmatrix} r_{d\mathcal{V},1}([i_1, i_2]) & r_{d\mathcal{V},2}([i_1, i_2]) & \cdots & r_{d\mathcal{V},q}([i_1, i_2]) \end{bmatrix}^{\mathrm{T}} \tag{4.29}$$

with

$$r_{d\mathcal{V},l}([i_1, i_2]) = \mathrm{var}\{R_{d\mathcal{V},ll}([i_1, i_2])\}. \tag{4.30}$$

Here, $\mathrm{var}\{\cdot\}$ is the variance operator and the index l denotes the corresponding output channel. The latter appears twice in the subscript of $R_{d\mathcal{V},ll}$ to denote the entry of the main diagonal. Practical suggestions for choices of i_1 and i_2 are made in Section 4.3.

SELECTION OF GRAMIANS

An important remark is made regarding the definition of input Gramians used for SP2E. To solve Eq. 4.12, the input Gramian M_3 must be chosen at first. Since w_3 and v_3 are unknown, this selection needs to be conducted in a pragmatic way. The noise covariance or Gramian matrices Q_3, $R_{v,3}$, and S_3, which define M_3 (cf. Eq. 4.4), can be estimated, e.g., using the approach presented in Chapter 5, and subsequently used to assemble the input Gramian M_3. This is a reasonable strategy when Kalman filtering is considered. However, as remarked in [210], this might decrease the sensitivity towards structural damage. An alternative approach, which is independent of the applied scheme for linear quadratic estimation, is to define $\Sigma_{x_3} = 0$ at first, and then, factorize M_3 according to Eq. 4.5 instead, and by that, enabling the solution of the Lyapunov equation in Eq. 4.12.

Later, for the computation of $R_{d\mathcal{V}}(i)$ according to Eq. 4.28, Σ_{x_3} is required again. Since the previous and naive choice ($\Sigma_{x_3} = 0$) is not acceptable in this case, the $(2,2)$th block of Σ_{x_Ω}, actually belonging to $\Sigma_{x_{e,2}}$, can be used if $\boldsymbol{G}_3 = \boldsymbol{G}_2$ [119]. Accordingly, if $\boldsymbol{G}_3 = \boldsymbol{G}_2$, the $(2,2)$th block of Σ_{x_Ω} constitutes an appropriate choice. Under the premise that, in Eq. 4.28, Σ_{x_3} can simply be regarded as a weighting matrix, this procedure is justified [205].

4.2.2 Making use of $\boldsymbol{G}_3$

The derivations presented so far take advantage of the central system's ($\boldsymbol{\Omega}$) general structure, see Fig. 4.2 and Eq. 4.9. As mentioned before, employing the system $\boldsymbol{G}_2$ ($\boldsymbol{G}_3 = \boldsymbol{G}_2$) for the generation of the test signal y_3 is an intuitive choice since, e.g., in SHM, the mechanical system in the analysis state is repetitively identified. This strategy was selected in most publications regarding SP2E (see, e.g., [118, 119, 205, 210, 212, 213]). Nevertheless, choosing $\boldsymbol{G}_3$ differently bears tremendous potential for the actual damage identification procedure and can reduce the number of false detections. Although this potential was already anticipated in [119], Lenzen et al. [116] firstly exploited the flexibility arising from the introduction of the system $\boldsymbol{G}_3$ based on results presented in [120].

To comprehend the advantage associated with the introduction of $\boldsymbol{G}_3$, the philosophy of the presented damage analysis framework should be recalled. When designed properly, $\boldsymbol{\Pi}_1^{-1}$ and $\boldsymbol{\Pi}_2^{-1}$ function as modal filters for signals stemming from the identified mechanical system in the reference ($\boldsymbol{G}_1$) and analysis state ($\boldsymbol{G}_2$), respectively. Thus, when $\boldsymbol{G}_3 = \boldsymbol{G}_2$ is defined and y_2 is analytically fed through $\boldsymbol{\Pi}_1^{-1}$ and $\boldsymbol{\Pi}_2^{-1}$, e_1 will differ significantly from e_2 when $\boldsymbol{G}_2$ and $\boldsymbol{\Pi}_2^{-1}$ are related to an altered mechanical system. Otherwise, e_1 and e_2 will be similar in terms of the damage indicators presented. Now, for this mind game to hold true in a practical application, one of the following conditions should hold:

(i) $\boldsymbol{G}_1$ and $\boldsymbol{G}_2$, and thus, $\boldsymbol{\Pi}_1^{-1}$ and $\boldsymbol{\Pi}_2^{-1}$ comprise the exact same set of modes (qualitatively).

(ii) $\boldsymbol{G}_2$, and thus, $\boldsymbol{\Pi}_2^{-1}$ do not represent any modes that are not covered by $\boldsymbol{G}_1$ and $\boldsymbol{\Pi}_1^{-1}$, respectively.

Notably, from an SHM perspective, either condition must pertain at all times and independently of the structural state of the system under surveillance. To satisfy this constraint is not trivial at all: While it is almost impossible to repetitively realize systems representing the same set of modes (option (i)), the alternative is to over-determine $\boldsymbol{G}_1$ and $\boldsymbol{\Pi}_1^{-1}$ by choosing particularly high model orders. Besides an inherent decrease in computational time, this strategy reduces the user's control regarding the model selection. Hence, false detections might occur that are difficult to explain.

Now, the flexibility that follows from the general system $\boldsymbol{\Omega}$ depicted and described by Fig. 4.2 and Eq. 4.9 can be exploited to lower the practical hurdles by combing the options mentioned before. To this end, the definition $\boldsymbol{G}_3 = \boldsymbol{G}_2$ can be reconsidered at first. Then, by performing a modal-based model reduction, an analytical test signal y_3 can be determined, representing the dynamics that is mutually shared or related to by both estimators $\boldsymbol{\Pi}_1^{-1}$ and $\boldsymbol{\Pi}_2^{-1}$. The challenge that arises here is to find some reasonable Σ_{x_3} that solves Eq. 4.28b. Unlike discussed in the final paragraph of Section 4.2, defining $\Sigma_{x_3} = \Sigma_{x_{e,2}}$ for this operation is not feasible, as $n_3 \neq n_2$. However, since $\boldsymbol{G}_3$ is a reduced version of $\boldsymbol{G}_2$, $\Sigma_{x_3} = \overline{\Sigma}_{x_{e,2}}$ can be chosen instead, where $\overline{\Sigma}_{x_{e,2}}$ is derived from $\Sigma_{x_{e,2}}$ by removing the rows and columns that represent the neglected modes. To this end and from an algorithmic point of view, the structure of Z introduced in Eq. 4.18 comes in handy. Because of the connection of $\boldsymbol{G}_3$ and $\boldsymbol{G}_2$, this $(n_2 \times n_3)$ matrix only contains ones and zeros, cf. Section A.2. Thus, the appropriate rows and columns of $\Sigma_{x_{e,2}}$ to be discarded can be directly determined from the structure of Z.

4.2.3 SP2E by using one estimator

According to the derivations summarized before, the SP2E method can be applied even when the identified systems ($\boldsymbol{G}_i$) and estimators ($\boldsymbol{\Pi}_i^{-1}$), respectively, feature different model orders. In the context of SHM, this property is beneficial, which follows from the discussions made in Section 4.2.2. Nevertheless, if one could guarantee the identification of comparable dynamics and constant model orders, e.g., in simulation studies or probably at the cost of neglecting a significant amount of identification results, the SP2E technique can be employed in a single-estimator mode. Therefore, Vollmering and Lenzen [205] showed that if $\boldsymbol{G}_3 = \boldsymbol{G}_2$ the relevant projectors can readily be determined without needing to compute an estimator in the analysis state ($\boldsymbol{\Pi}_2^{-1}$). Nevertheless, the identification of $\boldsymbol{G}_2$ via, e.g., SSI is still required. Depending on the applied theory for linear quadratic estimation and the number of channels and modes to be considered, this approach might drastically reduce the computational effort. The single-estimator mode for SP2E is also applicable if $\boldsymbol{G}_3 = \boldsymbol{G}_1$ or if $\boldsymbol{G}_3$ constitutes a reduced form of $\boldsymbol{G}_2$ or $\boldsymbol{G}_1$, cf. Section 4.2.2. However, for the sake of simplicity, the following derivations refer to the case that $\boldsymbol{G}_3 = \boldsymbol{G}_2$.

It follows from Section 4.2.1 that the core of SP2E is to determine a projector that maps onto $\mathcal{V}$ along $\mathcal{U}$, namely, in the regarded case ($\boldsymbol{G}_3 = \boldsymbol{G}_2$), the matrix $Y \in \mathbb{R}^{n_1 \times n_2}$, see Eq. 4.22. Consequently, if one were able to construct this matrix solely given $\boldsymbol{\Pi}_1^{-1}$ and $\boldsymbol{G}_2$, $R_{d\mathcal{V}}(i)$ and $r_{d\mathcal{V},i}([i_1, i_2])$ defined in Eqs. 4.28 and 4.30, respectively, could be computed equivalently. In this regard, consider the system depicted in Fig. 4.1 that maps the unknown processes w_2 and

v_2 to the estimation error e_1. This system shall be called $\overline{\mathbf{\Omega}}$, and it is similar to $\mathbf{\Omega}$ defined by Eq. 4.9. The corresponding state transition matrix $A_{\overline{\Omega}}$ reads

$$A_{\overline{\Omega}} = \begin{bmatrix} A_{e,1} & K_{e,1}C_2 \\ 0 & A_2 \end{bmatrix}, \tag{4.31}$$

with state vector

$$x_{\overline{\Omega},k} = \begin{bmatrix} x_{e,1,k} \\ x_{2,k} \end{bmatrix}. \tag{4.32}$$

Now, according to the concept of complementary spaces and direct sums, $x_{\overline{\Omega}}$ could be regarded as an element of $\overline{\mathcal{W}}$, where $\overline{\mathcal{W}} = \overline{\mathcal{U}}_1 \bigoplus \overline{\mathcal{V}}$. Again, $\overline{\mathcal{V}}$ is dedicated to x_2 and $\overline{\mathcal{U}}_1$ refers to the states of $\mathbf{\Pi}_1^{-1}$, namely $x_{e,1}$. Hence, analogously to Eqs. 4.13 to 4.16, bases of $\overline{\mathcal{U}}_1$ and $\overline{\mathcal{V}}$ can be determined via eigenvalue decomposition of $A_{\overline{\Omega}}$. Suppose that the resulting eigenvalues are represented by $\overline{\Lambda}$ and the eigenvectors are denoted by V such that $A_{\overline{\Omega}} = V\overline{\Lambda}V^{-1}$, then [124]

$$V = \begin{bmatrix} V_{11} & V_{12} \\ 0 & V_{22} \end{bmatrix} \quad \text{and} \quad V^{-1} = \begin{bmatrix} V_{11}^{-1} & -V_{11}^{-1}V_{12}V_{22}^{-1} \\ 0 & V_{22}^{-1} \end{bmatrix}. \tag{4.33}$$

Note that $V_{11} = X_{11}$ and $V_{22} = X_{33}$, and thus, $V_{12} = X_{13}$. Therefore, $Y = V_{12}V_{22}^{-1} = X_{13}V_{33}^{-1}$. Consequently, $P_{\mathcal{V}}$ and $\bar{P}_{\mathcal{V}}$ might be computed accordingly.

As good as this seems, obstacles arise when seeking practical choices for Σ_{x_2}, see the final paragraph in Section 4.2.1. There it was claimed that defining $\Sigma_{x_2} = \Sigma_{x_{e,2}}$ after solving Eq. 4.12 is admissible to process Eq. 4.28b, as in this case, Σ_{x_2} can simply be regarded as a weighting matrix. From this perspective, it also seems legitimate to choose $\Sigma_{x_2} = \Sigma_{x_{e,1}}$ when only $\mathbf{\Pi}_1^{-1}$ and the corresponding state covariance matrix is available [205]. Obviously, this procedure is only feasible if and only if $n_1 = n_2$.

4.3 ANALYZING CORRELATEDNESS AND POWER

As mentioned before, damage detection and localization are enabled by analyzing $R_{d\mathcal{V}}(i)$. On the one hand, one could assess the main diagonal of $R_{d\mathcal{V}}(0)$ [118, 119], which refers to the average power of $d_{\mathcal{V}}$ denoted as $P_{d\mathcal{V}}$. During the actual damage analysis process, values for the damage indicator must be compared to some threshold. This problem will be addressed in the proceeding section. Without a doubt, the power-based damage indicator is most suitable if e_2 is always a white noise process. However, from a practical standpoint, this can hardly be guaranteed, which is why the utilization of the feature defined in Eq. 4.30 might be beneficial.

To elaborate on that, consider the following example. A 3DOF system is given in the form of the spring-mass chain depicted in Fig. 4.4. The mass and stiffness matrices are given by

$$M = \begin{bmatrix} m_1 & & 0 \\ & m_2 & \\ 0 & & m_3 \end{bmatrix} \quad \text{and} \quad K = \begin{bmatrix} k_1 + k_2 & -k_2 & 0 \\ -k_2 & k_2 + k_3 & -k_3 \\ 0 & -k_3 & k_3 \end{bmatrix}, \tag{4.34}$$

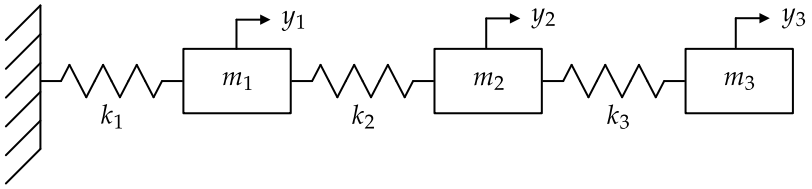

Figure 4.4: 3DOF system as spring-mass chain with masses m_i, spring stiffnesses k_i, and outputs y_i.

where each m_i was chosen as 1 kg and k_i as $100\,\mathrm{N\,m^{-1}}$. Proportional damping was defined by a damping rate $\delta_i = 0.01$ for each of the three eigenmodes. The 3DOF system was transferred to state-space according to Eq. 2.4 and converted to a discrete-time LTI system using Eq. 2.23. Finally, the output equation was altered to enable the simulation of acceleration, see Eq. 2.6. Damage was realized by decreasing the stiffness k_2 by 10 %. The proposed damage analysis framework is generally applied to identified systems with state-space representation as given in Eq. 4.1. Therefore, inputs and outputs of the model depicted in Fig. 4.4 were repetitively simulated for a duration of 10^4 samples at a sampling frequency of 50 Hz (200 s). To this end, each mass was excited with Gaussian white noise, featuring a variance of $0.1\,\mathrm{N}^2$. To each simulated output, a white measurement noise was added, taken from a Gaussian distribution with a variance of $5 \times 10^{-6}\,\mathrm{m}^2/\mathrm{s}^4$. In a second step, the system was identified by means of the CCA-based SSI-DAT (see Section 2.3.3) and with a model order of $n = 6$. The number of rows and columns for the assembly of the block-Hankel matrices defined in Eq. 2.89 were selected according to the suggestions given in Section 2.3.3. To determine a baseline for damage detection, 100 realizations of the intact system were identified.

Before performing the actual damage analysis according to Section 4.2.1 and with $\boldsymbol{G}_3 = \boldsymbol{G}_2$, the spectra, or more precisely the PSDs, of the relevant signals concerning the difference process d (cf. Fig. 4.2) shall be examined. This includes y_2, where, in the regarded case, $\boldsymbol{G}_2$ actually refers to the damaged system. The list continues with e_1 and e_2; additionally, y_1 is considered. Both estimators $\boldsymbol{\Pi}_1^{-1}$ and $\boldsymbol{\Pi}_2^{-1}$ were designed using the Riccati-based $\mathcal{H}_\infty$ synthesis for filtering signals in additive noise, as described in Section 3.5.1. The energy-bound γ (see Eq. 3.60) was set to one, and the filters were transferred to a strictly causal form so that they function as predictors. Throughout this section, the healthy system's first realization was considered as the reference system (index 1). The PSDs were determined by employing Eq. 2.82 and computing

$$S_{e_i}(z) = \Pi_i^{-1}(z) S_{y_2}(z) \Pi_i^{-*}(z) \tag{4.35}$$

for $i = 1$ and $i = 2$, where $z = e^{j\omega\Delta t}$. The analytical PSDs of the first channel associated with S_{y_1}, S_{y_2}, S_{e_1}, and S_{e_2} are depicted in Fig. 4.5. Firstly, it can be realized that the stiffness reduction (10 %) has an altering effect on the system's dynamics (softening), as the peaks of S_{y_2} referring to the natural frequencies of the model depicted in Fig. 4.4 are shifted to the left. For orientation, the PSD of the output y_1 used to identify the system in the reference state ($\boldsymbol{G}_1$) is presented in Fig. 4.5 as well using the grey line. Further the spectra of the estimation errors e_1 and e_2 can be seen. Note that these are computed with the help of the test signal y_2. Because of the introduced damage, the information encompassed in the output y_2 (A_2, C_2) does not match the dynamics of the reference system (A_1, C_1), and thus, the different dynamics are caught up by the estimation error e_1, which becomes visible through the spikes

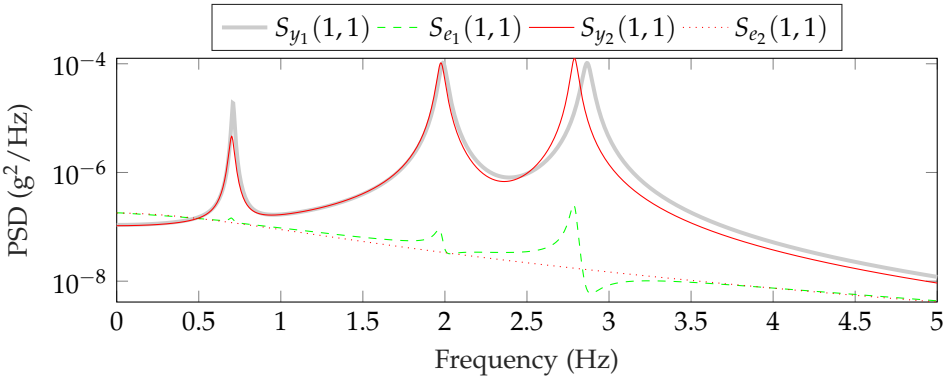

Figure 4.5: Analytical PSDs of signals associated with the computation of the difference signal d. PSD of the output used to identify the reference system $\boldsymbol{G}_1$ (S_{y_1}) given for orientation.

of the dashed green line. The PSD S_{e_2}, on the other hand, clearly corresponds to a random signal. Consequently, by analyzing the difference $d = e_1 - e_2$ the change in dynamics can be identified. Naturally, baseline values are required, which can be determined by repetitively considering realizations of the healthy system for ($\boldsymbol{G}_1$), as mentioned before.

A final remark is made in view of the analysis of d. Clearly, assessing $R_d(0)$ (or $R_{d\mathcal{V}}(0)$), which is essentially the area under $S_d = S_{e_1} - S_{e_2}$, is plausible. However, as pointed out before, the difference in dynamics is mainly manifested by the spikes of S_{e_1}, and thus, of S_d. Therefore, analysing $R_d(i)$ (or $R_{d\mathcal{V}}(i)$) for $i > 0$ seems to be a powerful alternative. To investigate this assumption, both $R_{d\mathcal{V}}(0)$ and the new damage feature given by Eq. 4.30 were computed. For the latter, i_1 was set to 1 and $i_2 = 72$. The last value corresponds to Eq. 3.57. Since the central idea is to somewhat distinguish d from a white-noise signal, this choice is justified.

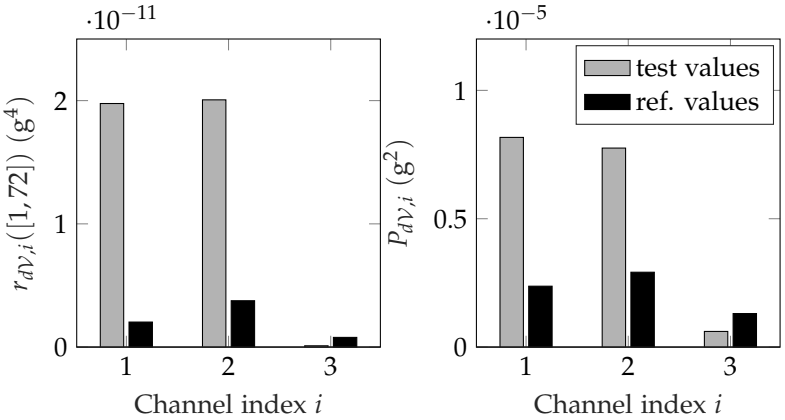

Figure 4.6: Variance-based (left) and power-based (right) damage indicators by SP2E for damage detection and localization at 3DOF system.

Fig. 4.6 contains two bar charts depicting $r_{d\mathcal{V},i}([1,72])$ and $P_{d\mathcal{V}}$. The latter constitutes the average power of $d_{\mathcal{V}}$, which is found on the main diagonal of $R_{d\mathcal{V}}(0)$. These values were determined by applying the SP2E method described before to the healthy reference system ($\boldsymbol{G}_1$) and the damaged system in the analysis state ($\boldsymbol{G}_2$). The reference values highlighted in black result from a training phase, where the remaining 99 realizations of the healthy

system were assigned to G_2. For the sake of simplicity, the maximum values regarding each channel computed during these analyses were set as baseline values. Since, in both cases, the corresponding black bars are exceeded by at least one channel, damage detection can be confirmed. The damage location might be associated with the channel featuring the maximum value of the damage indicators. Because of the fact that k_2 was reduced, it comes as no surprise that two channels display significantly high values, as k_2 reflects the spring connecting the lumped masses related to the first and second output channel, cf. Fig. 4.4. This phenomenon should be kept in mind when performing damage localization in the context of data-driven SHM; it appears less dominant when a denser sensor network is used. As for $r_{d\mathcal{V},i}([1,72])$, the reference values are exceeded more clearly, which implies a higher sensitivity towards damage. Hence, in this thesis, the damage-sensitive feature $r_{d\mathcal{V},i}([i_1,i_2])$ is mostly used for damage identification instead of $P_{d\mathcal{V}}$.

4.4 SP2E IN THE CONTEXT OF SHM

Applying SP2E in the context of data-driven SHM requires some deliberation regarding the choice of estimators and the decision-making for damage detection and localization. In the previous section, more precisely, in the previous example, Riccati-based $\mathcal{H}_\infty$ estimators were used without questioning this choice. This initial decision can be justified since damage detection and localization were successful. But, in an unsupervised problem, where the effect of damage is unknown prior to the damage analysis, it is helpful, or maybe even necessary, to have some criteria to decide upon whether the selection of estimators holds the desired potential for damage identification to be carried out. This problem is discussed in the following section. Attention should also be paid to a statistically profound damage analysis and the definition of threshold values for damage detection. In the previous example, damage detection was confirmed as damage indicators exceeded the maximum values obtained in a training phase. Clearly, the proper damage detection would have been complicated if these extreme values were particularly high, e.g., because of erroneous computations of some sort. Therefore, Section 4.4.2 discusses the role of hypotheses testing. Lastly, Section 4.4.3 is dedicated to formerly define a procedure for damage analysis considered in the chapters to come, especially Chapters 6 and 7.

4.4.1 Design and selection of filters and system identification

Essentially, linear quadratic estimators strive to track the dynamics of an observed system within noisy signals. Therefore, it can generally be assumed that estimators that feature a good estimation performance are most suitable for SP2E. This is expressed by the following assumption.

Assumption 4.1. *Linear quadratic estimators are most suitable for damage analysis via SP2E, when*

(i) the estimation errors are not correlated with the measured outputs,

(ii) the variance of the estimation errors is low.

The first point refers to the estimators' ability to successfully distinguish the system dynamics from the corrupting noise. If an estimator fails in this regard, harmonic components will arise

in the estimation error that refers to the natural frequencies of the observed system. These deterministic components lead to a strongly oscillating correlation function. In the frequency domain, this is manifested by distinct spikes of the corresponding PSD that one typically wants to take advantage of when applying the test signal y_3 to the reference estimator $\mathbf{\Pi}_1^{-1}$, cf. Fig. 4.5. This addresses the scenario where $\boldsymbol{G}_3$ is derived from $\boldsymbol{G}_2$. If $\boldsymbol{G}_3 = \boldsymbol{G}_1$ or $\boldsymbol{G}_3$ is a reduced form of $\boldsymbol{G}_1$, then deterministic components are expected to be contained in e_2.

The second point in Assumption 4.1 further addresses the denoising quality of estimators. It is fair to assume that the parts of measured signals representing the system dynamics feature much higher variance[1] than the contaminating noise, e.g., measurement noise. Hence, the estimation error variance should be low and should not exceed the variance of the measured signal in general or in spectral intervals associated with the system's poles. Otherwise, the corresponding estimator would exhibit an amplifying effect.

Both properties discussed here can be assessed numerically. One way to do that is to contrast the variance of the estimation error and the one of the measured signal. Further, the correlation function of the estimation error might be evaluated by means of whiteness tests, see Section 3.4 or Section 5.5. However, since a purely white estimation error can hardly be expected depending on the applied linear quadratic estimation theory and due to practical reasons, the corresponding test would require the definition of an acceptable threshold for the test statistics. Hence, such a procedure is not straightforward to apply. Nevertheless, in the experience of the author, a good strategy is to design different estimators such as Kalman or $\mathcal{H}_\infty$ filters and to assess the criteria from Assumption 4.1 visually. Suppose none of the mentioned properties is clearly violated by at least one of the estimators. Then, the setup corresponding to the best estimator should be considered for the entire damage analysis. This practical approach is followed throughout this thesis.

Naturally, the best-designed estimators are useless if those employed for the computation of d or the corresponding damage indicators refer to different dynamic features. This circumstance was already discussed in Section 4.2.2 and shall be generally expressed with the help of a second assumption:

Assumption 4.2. *SP2E performs best if the estimators $\mathbf{\Pi}_i^{-1}$ employed for damage analysis are designed based on models representing the same set of vibration modes.*

Since SP2E seeks to identify changes in the dynamic behavior of a structure, a poor damage identification performance is to be expected if the aforementioned assumption is strongly violated. Notably, and as mentioned before, repeatedly identifying the same set of modes in a monitoring scenario is challenging. Therefore, Assumption 4.2 could be considered by, e.g., taking advantage of the flexibility associated with $\boldsymbol{G}_3$, see Section 4.2.2.

4.4.2 Hypotheses testing

In SHM, hypotheses tests are typically employed as a statistical measure to infer the state of the monitored structure, see, e.g., [93, 213]. Naturally, a null hypothesis H_0 is formulated based on damage-sensitive features from the training phase. Therefore, the acquired data

1 The variance of a signal is proportional to its average power. In fact, these quantities are equal if the considered signal features zero mean.

is related to some statistical model. If the underlying statistical distribution, e.g., Gaussian, Weibull, χ^2 distribution, etc., is known, one might fit the data to PDFs or CDFs. Then, during testing, values of damage indicators are checked to be represented by the identified statistical models. If this is true, H_0 is accepted, and the structure is considered as healthy; however, in the opposite case, H_0 is rejected, and the structure is considered damaged. Significance levels defined by $\alpha \in [0,1]$ can be chosen to adjust the acceptance regions of values associated with the damage indicator [29]. In other words, if α is increased, the statistical model corresponding to H_0 is trusted less, whereas, if $\alpha = 0$, only quantities of values that were unseen during training can trigger an alarm for damage during testing. In often cases, such as in the regarded context of SP2E, the distribution of the features considered for damage identification is unknown, so distribution-free statistical tests should be applied. One way to do that is to consider empirical CDFs instead, see Section 2.2.2. The following paragraph will explain the concept of hypothesis testing through the previous example.

To this end, the empirical CDF was determined using training data (99 samples) for the second element of $r_{d\mathcal{V}}([1,72])$, referring to the second output channel of the 3DOF system. The empirical CDF of $r_{d\mathcal{V},2}([1,72])$ is depicted in Fig. 4.7. However, first, consider the corresponding

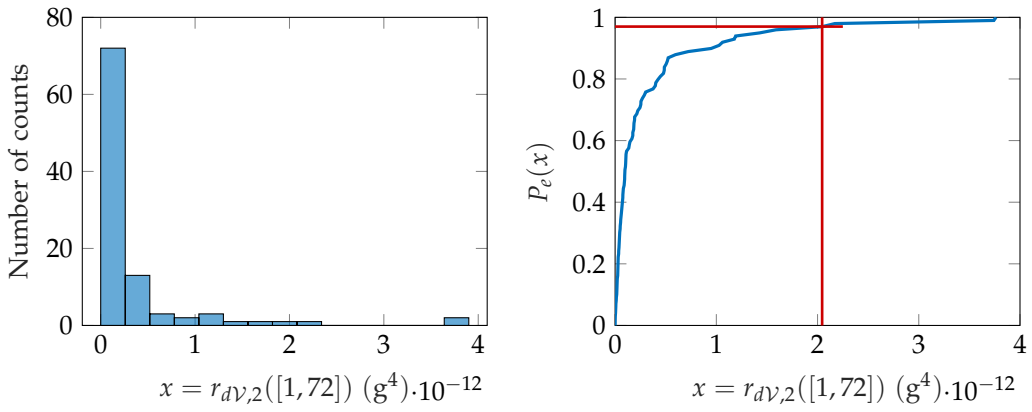

Figure 4.7: Histogram with 15 bins (left) and empirical CDF (right) of $r_{d\mathcal{V},2}([1,72])$ from training phase. Confidence interval corresponding to $\alpha = 3\%$ highlighted by red line.

histogram given in the same figure, which was generated using 15 bins. Assigning a specific distribution to the underlying data does not come naturally, although the histogram might be linked to some χ^2 distribution. Nevertheless, considering a distribution-free statistical test seems to be a sound decision. Therefore, the empirical CDF was computed as explained before. In Fig. 4.7, also the confidence interval of approximately 97 % corresponding to $\alpha \approx 3\%$ is displayed with the help of the red line. It constitutes the area under the blue curve for $r_{d\mathcal{V},2}([1,72])$ from 0 to $2.04 \times 10^{-12}\,\mathrm{g}^4$. Note that the black bar depicted in Fig. 4.6 is equivalent to $\alpha = 0$. Now, a hypothesis for damage detection could readily be defined based on these findings, e.g. by stating H_0 (healthy): $r_{d\mathcal{V},2}([1,72]) \leqslant 2.04 \times 10^{-12}\,\mathrm{g}^4$. However, this work proposes an alternative by considering the training values for all channels, as will be explained in the following section. A final remark is made concerning the significance level α. It is recommendable to define some $\alpha > 0$ to discard the effect of outliers. Nevertheless, one should keep in mind that increasing α also increases the chance of false-positive alarms, also called type I errors. On the contrary, the number of false negatives might rise if α is set too low.

4.4.3 Proposed statistical assessment of damage indicators

The following strategy for a statistically profound damage analysis is applicable for both multivariate damage features $P_{d\mathcal{V}}$ and $r_{d\mathcal{V}}([i_1, i_2])$ introduced in this chapter. For simplicity and in the present section only, the general damage indicator $DI \in \mathbb{R}^q$ is introduced that might represent either of the SP2E-related features or any other multivariate damage-sensitive feature applicable for damage detection and localization. The proposed statistical decision-making procedure comprises a training, validation, and testing phase, which is standard practice in machine decision-making/learning. In the first two stages, only sets of DI are considered that reflect the observed structure under healthy conditions . During testing, DI represents the potentially damaged structure, i.e., the corresponding values might be associated with the healthy or damaged structure . The three phases of damage analysis applicable for SHM are summarized in the following.

TRAINING

Gather n_{healthy} samples of DI and split this data into a subset of training (n_{train}) and validation (n_{val}) data such that $n_{\text{healthy}} = n_{\text{train}} + n_{\text{val}}$ and $n_{\text{train}} \geqslant n_{\text{val}}$. A reasonable segmentation would be such a one that obeys $n_{\text{train}}/n_{\text{val}} \geqslant 2$. For all n_{train} sets of DI, compute $\sum_{i=1}^{q} DI_i$, where i refers to any entry of DI. Thus, the vector DI is condensed to a scalar, which is subsequently used for the determination of a statistical model applicable for the decision making in terms of damage detection. To this end, compute the empirical CDF given the n_{train} values of $\sum_{i=1}^{q} DI_i$. After defining some significance level α, the corresponding $(1-\alpha)$ quantile ϑ is obtained. Based on that, formulate the null-hypothesis such that

$$H_0 \text{ (healthy):} \quad \sum_{i=1}^{q} DI_i < \vartheta. \tag{4.36}$$

On the contrary, the observed structure is assumed to be damaged if

$$H_1 \text{ (damaged):} \quad \sum_{i=1}^{q} DI_i > \vartheta. \tag{4.37}$$

VALIDATION

The purpose of the validation phase is to evaluate whether the obtained statistical model (empirical CDF) is valid for a representation of the observed structure under healthy conditions. Therefore, the remaining n_{val} sets of DI (representing the healthy structure) are considered. After computing $\sum_{i=1}^{q} DI_i$, the previously stated null hypothesis can be tested. If this hypothesis is rejected, that is, $\sum_{i=1}^{q} DI_i > \vartheta$, the presence of damage is mistakenly assumed. This case is called false-positive detection or type I error. The relative number of these kinds of errors should not significantly exceed the degree of $\sum_{i=1}^{q} DI_i$ values discriminated in the training phase through the definition of α. Since the false-positive rate depends directly on α, this value might be readjusted before testing.

TESTING

The testing phase deals with the detection of damage but also with its localization. So far, the latter was not regarded, as it only becomes relevant once the null-hypothesis stated in Eq. 4.36

is rejected during testing. Therefore, the detection procedure is equal to the one described in the previous paragraph for incoming sets of DI, representing a potentially damaged structure. The location of damage might be associated with the entry in DI accommodating the maximum value. The underlying assumption is that the channel closest to damage exhibits the greatest difference compared to the healthy reference. Indeed, other metrics for damage localization (and detection) are plausible and worth considering. However, a discussion on that is left for future studies.

Part II

NOVELTIES, VALIDATIONS, AND APPLICATIONS

5

PARAMETRIC AUTOCOVARIANCE LEAST-SQUARES METHOD FOR NOISE COVARIANCE ESTIMATION

For Kalman filters to function properly, the noise covariance matrices Q, R_v, and S must be known. Practically, this information is not available, and thus, noise estimation strategies received plenty of attention from the moment the Kalman filters' potential was recognized for control and other engineering disciplines. Classically, noise covariance estimation methods can be divided in four groups: correlation methods, maximum-likelihood methods, covariance matching methods, and Bayesian methods [131]. Other strategies such as subspace methods, prediction error methods, and minmax approaches could be added to this list [66]. Among all these approaches, the correlation methods stand out because of their theoretical optimality and efficient numerical solvability with the help of convex optimization tools. They are particularly attractive for LTI systems. In this section, the so-called ALS method by Odelson et al. [142] is adapted for the estimation of noise covariance matrices to design Kalman filters based on identified state-space models for damage detection and localization within the framework presented in Chapter 4. Therefore, a parametric alternative to the originally data-driven approach was developed and presented in [210]. In this chapter, the general formulation of the ALS approach is summarized first. Then, the extensions leading to the so-called parametric autocovariance least-squares (PALS) strategy are presented. In what follows, both the ALS and PALS methods are compared for damage identification as well as for state estimation and filtering, respectively, in simulation and experimental studies. Parts of this chapter have been published in [210, 213].

5.1 MOTIVATION AND BACKGROUND

Kalman filters are powerful tools for state estimation and filtering, given certain conditions are satisfied relating to their $\mathcal{H}_2$ optimality, see Chapter 3. Besides the Gaussian distribution and whiteness of process and measurement noise, which is already hard to satisfy or guarantee in practice, the statistics of these processes must be known a priori. Noise estimation describes the discipline of estimating the covariance matrices of process and measurement noise that enables the design of optimal or least suboptimal Kalman filters. This discipline covers multiple types of algorithms, as described before. A good overview of existing methods can be found in [65]. The selection of noise covariance estimation methods also depends on the dynamics of the underlying system. Correlation approaches are readily applied for LTI systems; the so-called ALS technique represents the standard for these kinds of systems. Nevertheless, extensions and advancements of this method also exist for nonlinear and time-varying systems [85, 166]. An interesting approach, especially in the context of this thesis, is the estimation of noise covariances with the help of subspace techniques such as the SSI. In the present work, mechanical systems are identified with the help of this method. Hence, it feels natural to estimate the noise covariances in the process. To do so, SSI algorithms must be chosen that guarantee a positive real sequence $R_y(i)$, as only then the triple of the noise covariance matrices Q, R_v, and S is positive definite as well, and a Kalman filter can be found.

Algorithms that guarantee this positive-definite property were presented by van Overschee and de Moor [147, p. 85 ff] and Katayama [110, p. 228 ff]. In practice, where identified state-space models are typically reduced to a representation covering only physically interpretable modes, the SSI-based approach for noise covariance estimation is problematic. The reason is that the positive definiteness can only be assured for a predefined model order that typically includes physical but also purely mathematical eigensolutions. Therefore, the estimation of noise covariance matrices via SSI is not appropriate in the presented context. Alternatively, these quantities shall be estimated with the help of the ALS method, a representative of the so-called correlation methods.

Correlation-based methods root back to the developments of Mehra in the early 1970s [130, 131]. This innovations-based approach was quickly taken up by several authors such as Carew and Bélanger [36], and Neethling and Young [140]. The original multi-step procedures by Mehra and Carew and Bélanger for the estimation of Q and R_v involve two least-squares solutions, which leads to high variances of the estimates. Neethling and Young [140] first improved this point using only a single least-squares computation. This was later taken up by Odelson et al. [142] who introduced the so-called ALS method. Moreover, the latter criticized and corrected the uniqueness conditions given by Mehra [130] and cited by Carew and Bélanger [36]. Both parties, Neethling and Young [140] as well as Odelson et al. [142], proposed imposing the symmetry and positive definiteness of the autocovariance matrices Q and R_v to relax the computational burden, to reduce the variance of the estimates, and to decrease the set of solutions to a physically reasonable level. It is not reported how Neethling and Young [140] approached the least-squares problem to achieve only positive definite solutions, but Odelson et al. [142] suggested solving the problem within a semidefinite programming (SDP) optimization framework. The original contribution to the ALS method resulted in interesting advancements. Rajamani [164], and Rajamani and Rawlings [166] contributed to identify the disturbance structure of state-space models. Åkesson et al. [4] extended this method to a generalized framework to cover the case of correlated process and measurement noise. The optimal weighting of the least-squares approach was discussed in [166, 222]. Wernitz et al. [210] proposed a parametric computation of the innovations' correlation function for state-space models identified via SSI. They utilized the tuned Kalman filters in the context of damage detection and localization of LTI systems.

Solving the ALS problem using convex optimization and semidefinite programming [28, 200] has become a standard because of its numerical efficacy. For instance, Åkesson et al. [4] presented a predictor-corrector algorithm to solve the constrained ALS problem. For Matlab applications, open-source toolboxes such as the CVX framework [33, 87] in combination with semidefinite solvers like SeDuMi [187] or SDPT3 [189] can be employed, see [31]. Also, commercial optimization tools such as Matlab's `fmincon` [125, 146] have been utilized to solve the associated least-squares problem [210]. Because of the general nonlinear nature of `fmincon`, the semidefinite constraints need to be formulated as eigenvalue-based inequalities to assure positive definiteness of the noise covariance triple. Despite the considered optimization tools, the ALS problem remains convex and linear in the parameters, see [164].

In this chapter, the strategy of employing the PALS method [210] is revisited and compared to the classical ALS approach, where the innovations covariance sequences are estimated using batches of measured data. However, at first, the potential of the ALS method for the

estimation of true noise covariance matrices is demonstrated in simulation studies for the cases of uncorrelated and correlated process and measurement noise. The effectiveness of both the ALS and PALS approaches in the context of damage localization is then analyzed in two experiments. In these applications, the knowledge of the true covariances is of less interest. Moreover, the goal is rather to design Kalman filters that are in line with Assumption 4.1. For the analyses made herein, the CVX framework and SDPT3 are employed. Although good results have been achieved by using Matlab's nonlinear optimization toolbox (`fmincon`, cf. [211]), the aforementioned tools constitute the more natural choice given the explicitly convex nature of the optimization problem[1] and the numerically efficient ability of CVX to handle semidefinite constraints.

5.2 GENERALIZED ALS FORMULATION

In the following, the underlying theory of the ALS method is presented. The given formulation is based on [4, 32, 142, 164].

Consider a system with the following state-space representation:

$$x_{k+1} = Ax_k + G_w w_k \tag{5.1a}$$
$$y_k = Cx_k + v_k. \tag{5.1b}$$

Here, G_w represents a so-called noise shaping matrix that maps the process noise w_k, acting on the inputs, to the states x_k. Note that in case of a system identified with the help of the SSI, $G_w = I_n$, where I_n denotes an $n \times n$ identity matrix, cf. Eq. 2.74. However, when the system is modelled based on mechanical principles using the parameters M, K, and D_p, then $G_w = B$, cf. Eq. 2.4.

For the ALS technique, the evolution of the state-estimation error $\tilde{x}_{k|k-1} = x_k - \hat{x}_{k|k-1}$ is considered [142], which can be written in state-space formulation as

$$\tilde{x}_{k+1|k} = (A - K_p C)\tilde{x}_{k|k-1} + \begin{bmatrix} I & K_p \end{bmatrix} \begin{bmatrix} G_w w_k \\ v_k \end{bmatrix} \tag{5.2a}$$
$$= A_p \tilde{x}_{k|k-1} + \bar{B}\bar{w}_k \tag{5.2b}$$
$$e_k = C\tilde{x}_{k|k-1} + v_k \tag{5.2c}$$

with

$$X = \mathrm{E}\left\{\bar{w}_k \bar{w}_l^{\mathrm{T}}\right\} = \begin{bmatrix} G_w Q G_w^{\mathrm{T}} & G_w S \\ S^{\mathrm{T}} G_w{}^{\mathrm{T}} & R_v \end{bmatrix} \delta_{kl} \geqslant 0. \tag{5.3}$$

Here, X denotes the general covariance matrix of the extended input process $\bar{w}$ that contains the unknown noise covariances to be estimated. The covariance of the state-estimation error follows the Lyapunov equation

$$P = A_p P A_p^{\mathrm{T}} + \bar{B} X \bar{B}^{\mathrm{T}}, \tag{5.4}$$

which can be broken down to [4]

$$P = A_p P A_p^{\mathrm{T}} + G_w Q G_w^{\mathrm{T}} - K_p S^{\mathrm{T}} G_w^{\mathrm{T}} - G_w S K_p^{\mathrm{T}} + K_p R_v K_P^{\mathrm{T}}. \tag{5.5}$$

1 `fmincon` does not necessarily assume global minima (convexity) and can also cope with nonconvex problems.

Now, the general idea of the ALS method is to parametrize the covariance or correlation function of the innovations[2] with the help of the state-space system given in Eq. 5.2, and from there, construct an overdetermined linear set of equations that can be solved as a least-squares problem. The mentioned correlation function of the innovations reads [32]

$$R_e(i) = \mathrm{E}\left\{e_k e_{k+i}^{\mathrm{T}}\right\} = \begin{cases} CPC^{\mathrm{T}} + R_v, & i = 0 \quad (5.6a) \\ CA_p^i PC^{\mathrm{T}} + CA_p^{i-1} G_w S - CA_p^{i-1} K_p R_v, & i > 0. \quad (5.6b) \end{cases}$$

If the Kalman filter is tuned ideally, i.e., if K_p is optimal, this function yields zero for every $i > 0$ [130]. A vectorized version of Eq. 5.6 can be found with the help of the Kronecker product denoted by $\otimes$ [128] so that

$$\mathrm{vec}\{R_e(i)\} = \begin{cases} (C \otimes C)\mathrm{vec}\{P\} + \mathrm{vec}\{R_v\}, & i = 0 \quad (5.7a) \\ (CA_p^i \otimes C)\mathrm{vec}\{P\} + (I_q \otimes CA_p^{i-1} G_w)\mathrm{vec}\{S\} \\ \qquad -(I_q \otimes CA_p^{i-1} K_p)\mathrm{vec}\{R_v\}, & i > 0. \quad (5.7b) \end{cases}$$

Here, $\mathrm{vec}\{\cdot\}$ represents the column-wise stacking of a matrix. By substituting the vectorized state-estimation covariance (Eq. 5.5) defined as

$$\begin{aligned} \mathrm{vec}\{P\} = [I_{n^2} - A_p \otimes A_p]^{-1}[(G_w \otimes G_w)\mathrm{vec}\{Q\} + (K_p \otimes K_p)\mathrm{vec}\{R_v\} \\ -(G_w \otimes K_p)\mathsf{K}_S\mathrm{vec}\{S\} - (K_p \otimes G_w)\mathrm{vec}\{S\}] \end{aligned} \quad (5.8)$$

into Eq. 5.7, one yields a linear set of equations

$$\underbrace{\begin{bmatrix} \mathrm{vec}\{R_e(0)\} \\ \mathrm{vec}\{R_e(1)\} \\ \vdots \\ \mathrm{vec}\{R_e(n_l)\} \end{bmatrix}}_{b} = \underbrace{\left\{ \begin{bmatrix} \mathcal{A}_{Q,0} \\ \mathcal{A}_{Q,1} \\ \vdots \\ \mathcal{A}_{Q,n_l} \end{bmatrix} \quad \begin{bmatrix} \mathcal{A}_{R_v,0} \\ \mathcal{A}_{R_v,1} \\ \vdots \\ \mathcal{A}_{R_v,n_l} \end{bmatrix} \quad \begin{bmatrix} \mathcal{A}_{S,0} \\ \mathcal{A}_{S,1} \\ \vdots \\ \mathcal{A}_{S,n_l} \end{bmatrix} \right\}}_{\mathcal{A}} \underbrace{\begin{bmatrix} \mathrm{vec}\{Q\} \\ \mathrm{vec}\{R_v\} \\ \mathrm{vec}\{S\} \end{bmatrix}}_{\chi}. \quad (5.9)$$

Here, the variables are represented by χ, $\mathcal{A}$ denotes the coefficient matrix, and the vectorized correlation function for a user-defined number of lags n_l is gathered in b. Further, the commutation matrix K_S in Eq. 5.8 depicts a $n \times q$ matrix containing only ones and zeros that helps to reorganize $\mathrm{vec}\{S\}$ so that $\mathsf{K}_S\mathrm{vec}\{S\} = \mathrm{vec}\{S^{\mathrm{T}}\}$ [128]. The coefficient matrix $\mathcal{A}$, contains the three submatrices $\mathcal{A}_Q$, $\mathcal{A}_{R_v}$, and $\mathcal{A}_S$ with subelements for each lag i. They decompose to

$$\mathcal{A}_{Q,i} = \left(C \otimes CA_p^i\right)\left[I_{n^2} - A_p \otimes A_p\right]^{-1}(G_w \otimes G_w), \quad (5.10)$$

$$\mathcal{A}_{S,i} = \begin{cases} (C \otimes C)\left[I_{n^2} - A_p \otimes A_p\right]^{-1}[-(G \otimes K_p)\mathsf{K}_S - K_p \otimes G_w], & i = 0 \quad (5.11a) \\ \left(C \otimes CA_p^i\right)\left[I_{n^2} - A_p \otimes A_p\right]^{-1}[-(G_w \otimes K_p)\mathsf{K}_S - K_p \otimes G_w] \\ \qquad +I_q \otimes CA_p^{i-1} G_w & , i > 0, \quad (5.11b) \end{cases}$$

and

$$\mathcal{A}_{R_v,i} = \begin{cases} (C \otimes C)\left[I_{n^2} - A_p \otimes A_p\right]^{-1}(K_p \otimes K_p) + I_{q^2}, & i = 0 \quad (5.12a) \\ \left(C \otimes CA_p^i\right)\left[I_{n^2} - A_p \otimes A_p\right]^{-1}(K_p \otimes K_p) \\ \qquad -I_q \otimes CA_p^{i-1} K_p, & i > 0. \quad (5.12b) \end{cases}$$

2 Since the innovations are readily assumed as mean-free processes, it is fair to use both the terms covariance and correlation function.

5.3 NUMERICAL SOLUTION OF ALS METHOD

A simple and straightforward solution to Eq. 5.9 can be achieved by considering the standard least-squares problem described by the objective

$$\underset{\chi}{\text{minimize}} \quad \|\mathcal{A}\chi - b\|_2^2. \tag{5.13}$$

It has the well-known solution [28]

$$\chi = \left(\mathcal{A}^{\mathrm{T}}\mathcal{A}\right)^{-1}\mathcal{A}^{\mathrm{T}}b, \tag{5.14}$$

which can be computed, e.g., with the help of the pseudoinverse. Unfortunately, following this strategy will most likely lead to unsatisfactory results, as the positive definiteness of X is not guaranteed. Moreover, bad conditioning of $\mathcal{A}$ caused by the finite length of data is to be expected, which decreases the accuracy of the solution [4, 32]. The latter is a common problem in the least-squares theory, typically remedied with the help of regularization strategies. Then, the associated objective reads

$$\underset{\chi}{\text{minimize}} \quad f_0(\chi) = \|\mathcal{A}\chi - b\|_2^2 + \lambda^2\|\chi - \chi_0\|_2^2, \tag{5.15}$$

where λ is the so-called regularization parameter, and χ_0 contains the initial guesses of the noise covariances that are used to construct the arbitrary Kalman filter. Eq. 5.15 is linked to the popular Thikonov regularization, where the regularization parameter can be computed in multiple ways, e.g., via the generalized cross-validation (GCV) or the L-curve method [32, 97]. Both procedures are implemented in the Matlab regularization toolbox by Hansen introduced in [96, 98].

Conditioning the initial least-squares problem stated in Eq. 5.13 is a decisive step to increasing the accuracy of the estimations. However, to guarantee positive definiteness of X, the regularized problem in Eq. 5.15 must be constrained, leading to the problem stated as

$$\begin{aligned} \underset{\chi}{\text{minimize}} \quad & f_0(\chi) = \|\mathcal{A}\chi - b\|_2^2 + \lambda^2\|\chi - \chi_0\|_2^2, \\ \text{s.t.} \quad & X \succcurlyeq 0. \end{aligned}$$

Typically, the solution is efficiently realized through SDP within a convex optimization framework [28, 200]. Powerful open-source tools exist for this purpose, as was described in Section 5.1. The underlying optimization algorithms, such as the interior-point methods [200, Chapter 11], are gradient-based strategies that might be accelerated by providing the analytical derivative of the objective function defined as[3]

$$\nabla f_0(\chi) = 2\left(\mathcal{A}^{\mathrm{T}}\mathcal{A} + \lambda I\right)\chi - 2\mathcal{A}^{\mathrm{T}}b - 2\lambda\chi_0. \tag{5.16}$$

At this point, it should be mentioned that, as for every least-squares problem, there are certain conditions for the estimates' uniqueness. For ALS, these rules are presented diligently by Rajamani [164]. In the context of this work, where identified state-space models are involved, it is rather irrelevant to check the uniqueness conditions, as the goal is to find noise covariance

3 The gradient of the objective function can, e.g., be considered by Matlab's `fmincon` [125, 146].

matrices that lead to improved Kalman filter performance (see Assumption 4.1) instead of identifying the true covariances. In the literature, the problem of unknown noise shaping matrices G_w (see Eq. 5.1), which inherently arises when techniques such as the SSI are involved, is often referred to as *disturbance structure identification*. They are readily tackled as a rank-minimization problem, see, e.g., [164, 165]. However, in this work, the latter is not necessarily pursued because of the mentioned goal of improved Kalman filter performance.

When solving the ALS problem, it is advisable to impose the symmetry or even diagonality of the covariance matrices Q and R_v to increase the accuracy of the estimates and to relax the computational burden by reducing the number of unknowns. Diagonality of the covariance matrices can be easily achieved by canceling the columns of $\mathcal{A}$ associated with off-diagonal entries of Q and R_v. It is advisable to consider diagonalization if the process or measurement noise is not inherently cross-correlated or if a decrease of variables leads to similar estimation performance of the tuned Kalman filters, see [210]. Symmetry should be imposed on A_Q and A_{R_v} by employing duplication matrices (cf. [164]), as autocovariance matrices are inherently symmetric. Duplication matrices contain only ones and zeros, such that [127]

$$\text{vech}\{E\} = \mathsf{D}_\mathsf{E}\text{vec}\{E\} \quad \text{and} \quad \text{vec}\{E\} = \mathsf{D}_\mathsf{E}^\dagger\text{vech}\{E\}. \tag{5.17}$$

Here, E denotes some $m \times m$ symmetric matrix, whereas the $\left(m^2 \times \left(m\left[m+1\right]/2\right)\right)$ duplication matrix D_E extracts the $m(m+1)/2$ unique values denoted by the half-vectorization $\text{vech}\{E\}$.

5.4 PARAMETRIC ESTIMATION OF THE INNOVATIONS' CORRELATION FUNCTION

In the classical ALS approach, the innovations' correlation function $R_e(i)$ is estimated, e.g., with the help of the sample-covariance defined in Eq. 2.66. Alternatively, when noise covariance matrices are estimated for Kalman filter design based on state-space parameters identified via SSI, a parametric estimation of $R_e(i)$ might be advantageous. This proposition is further supported in the context of damage detection and localization utilizing the damage analysis framework presented in Chapter 4, as the estimation-error analysis is purely parametric. The argumentation for parametric estimation of noise covariance matrices for the Kalman filter synthesis is based on the following points:

- When the model structure, namely the state-space matrices A and C do not account for the entire dynamics encompassed in the measurement data, e.g., because of a selective model reduction, then additional information can have a disturbing effect on the estimation of the noise covariances.
- A parametric representation of $R_e(i)$ solely depends on the identified system dynamics, which is often defined by a low-order model. Consequently, fewer lags of this correlation function need to be considered. Practically, that can lead to a decrease in computational time and fewer iterations of the optimization algorithm.

For a parametric computation of the innovations' correlation function, recall the Wiener-Khinchine theorem (see Section 2.2.3) expressed by

$$R_e(i) = \mathcal{F}^{-1}\{S_e(z)\}, \tag{5.18}$$

where $S_e(z)$ denotes the PSD of e and $z = e^{j\omega\Delta t}$. Conveniently, $S_e(z)$ can be computed through the following algebraic operation:

$$S_e(z) = \Pi^{-1}(z) S_y(z) \Pi^{-*}(z). \tag{5.19}$$

Here, $\Pi^{-1}(z)$ represents the FRF of the Kalman filter, which, to set up the least-squares problem, is constructed using Q_0, $R_{v,0}$, and S_0. A parametric formulation for $S_y(z)$ is readily available from the SSI, see Eq. 2.82. Thus, by substituting Eq. 2.82 into Eq. 5.19 and applying the inverse Fourier transform (or bilateral z-transform) according to Eq. 5.18, one can estimate the innovations' correlation function solely based on the identified state-space parameters. However, special attention should be paid to the definiteness of $S_y(z)$ and $S_e(z)$, respectively. As mentioned before, most SSI algorithms do not guarantee the positive definiteness of $S_y(z)$, which can lead to implausible physical interpretations (see Section 2.2.3) and numerical inaccuracies. Consequently, a correction procedure should be applied that checks if $S_e(z) \geqslant 0$ for every z and enforces positive semidefiniteness if $S_e(z) < 0$. One way to do this is to replace the corresponding matrix with its nearest symmetric positive semidefinite version. Such matrices can be computed by applying the algorithm presented in [103]. A Matlab implementation is available in [51]. An alternative strategy to enforce positive semidefiniteness of $S_e(z)$ was presented by Vaccaro and Vukina [199].

REMARK ON IMPLEMENTATION

When reimplementing this parametric approach for estimating the innovations' correlation function, questions might arise regarding the number of sample points n_f for the computation of $S_y(z)$ and $S_e(z)$. This choice should be made in view of $R_y(i)$, which is defined by Eq. 2.81. Recall that this function represents the IIR of the system identified via SSI. Thus, it must be ensured that n_f is large enough to allow a computation through $R_y(i) = \mathcal{F}^{-1}\{S_y(z)\}$ without any loss of information regarding the dynamics of the underlying identified system. Since the maximum number of lags n_l[4] for $R_y(i)$, $i \in [0, n_l]$ is equal to n_f, the problem of selecting this parameter is equivalent to representing the identified system through a finite impulse response (FIR) because of the discrete nature of the approximation problem. Therefore, n_l must be found so that the FIR ($R_y(i)$, $i \in [0, n_l]$) contains no less information than the IIR ($R_y(i)$, $i \in [0, \infty)$). Moreover, since $S_y(z)$ as well as $S_e(z)$ are two-sided PSDs, n_f should finally be chosen as two times n_l.

A perfect orientation for that is the so-called *settling time* t_s. This measure refers to the time elapsed until the IIR enters a $\pm 2\,\%$ error band. It can be approximated by [214]

$$t_{s,i} \approx \frac{4}{\zeta_i \omega_{0,i}}. \tag{5.20}$$

Since MIMO systems are generally considered, which are represented by multiple modes (i), n_f should be selected such that

$$n_f > 2 \max t_{s,i} f_s, \tag{5.21}$$

where f_s represents the sampling frequency.

Depending on the quantities used for Eqs. 5.20 and 5.21, n_f become quite large. Therefore, it is advisable to define a maximum value for n_f, say 40.000. However, it should be borne in mind that this comes at the cost of reduced precision regarding the noise covariance estimates.

4 Here, n_l is not necessarily the value that is eventually used to set up the linear set of equations in Eq. 5.9.

5.5 TESTING FOR WHITENESS IN THE CONTEXT OF PALS

As mentioned in Section 3.4, the Kalman filter performance can be evaluated with the help of whiteness tests. Especially when the underlying noise covariance matrices are estimated, this might be taken into account to check and perhaps improve the estimates by repeating the computations with different settings. In the case of a parametric estimation of the innovations' correlation function, the application of the χ^2-test summarized in Section 3.4, or any statistical test in general, is slightly unorthodox, as only state-space parameters and no sampled data is involved in the entire noise estimation process. Nevertheless, an altered χ^2 test can be applied, which is explained and demonstrated exemplarily in the following.

For a whiteness test in the context of PALS, consider the estimated innovations' correlation function $\hat{R}_e(i)$ determined as explained in the previous section. Given some m, e.g. via Eq. 3.57, the next step is to compute the test statistics r for each channel using Eq. 3.56 and the squared normalized innovations' correlation function $(\hat{R}_{e_l}[i]/\hat{R}_{e_l}[0])^2$, see Eq. 3.55. At this point, confusion might arise, as the number of samples n_s is not intuitively defined. Typically, when whiteness tests are applied to sampled data, n_s follows directly from the amount of data gathered to estimate the correlation function. If $\hat{R}_e$ is a parametric function, this is rather different. Nevertheless, since the parameters for constructing this function are state-space parameters identified given a finite set of measurements, they should be defined according to the length of the corresponding data minus m.

This procedure shall be justified with the help of the following example. To this end, consider measurements on the first output of the 3DOF system presented in Section 4.3. Fig. 5.1 shows the PSD of the simulated acceleration data ($S_y(z)$) as well as of the innovations ($S_e(z)$) resulting from a Kalman filter designed with an arbitrary and suboptimal choice of covariance matrices ($Q = I$, $R_v = I$, $S = 0$). These matrices could as well be estimated with PALS. Both $S_y(z)$ and $S_e(z)$ were determined using Welch's method, cf. Section 2.2.3. In Fig. 5.1, $S_{y,\mathrm{SSI}}(z)$ and $S_{e,\mathrm{analy}}(z)$ are depicted as well, which denote their analytical counterparts. Obviously, $\mathbf{\Pi}^{-1}$

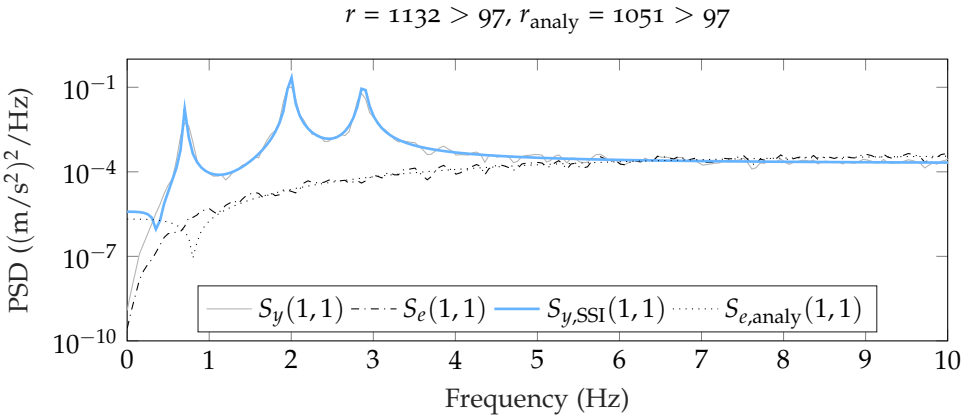

Figure 5.1: Measured and analytical spectra of 3DOF system.

does not perform in an $\mathcal{H}_2$ optimal sense, as the PSD referring to the estimation errors $S_e(z)$ and $S_{e,\mathrm{analy}}(z)$ do not form a constant line. It can be observed that the graphs associated with the analytical spectra follow the PSDs of the corresponding measured (simulated) quantities. Due to the parametric nature, the typical jitter caused by finite-length data is not apparent. The

test statistics r referring to whiteness tests described in Section 3.4 and above (r_{analy}) are given above the plot. It can be seen that the null hypothesis is rejected in either case, as the threshold value $\vartheta = 97$ corresponding to a 0.95 % quantile is exceeded. Only slight differences between the test statistics can be observed, which approves the approach for testing the whiteness in the context of PALS suggested herein.

5.6 SIMULATION STUDIES

In output-only system identification, process and measurement noise might be statistically independent ($S = 0$) or not ($S \neq 0$). It depends on the type of the acquired measurement data and must be taken into account when estimating noise covariance matrices for Kalman filtering. Therefore, the proceeding sections cover the cases of uncorrelated and correlated process and measurement noise. The statistical relationship of these noise processes becomes more apparent regarding the state-space structure of the output-generating system and the Kalman filter. This will be explained in the following.

Since, in this work, inputs are always considered unknown, and therefore, the SSI technique is applied, Kalman filters must assume that the outputs y_k result from a system represented by

$$x_{k+1} = Ax_k + w_k \tag{5.22a}$$
$$y_k = Cx_k + v_k. \tag{5.22b}$$

Now, consider the case of measured displacement. Then, the state-space model of the data-generating mechanical system in discrete-time reads

$$x_{k+1} = Ax_k + Bw_{1,k} \tag{5.23a}$$
$$y_{d,k} = C_d x_k + v_{1,k}, \tag{5.23b}$$

cf. Eqs. 2.4 and Eq. 2.23. Here, the subscript d highlights the qualitative nature of the outputs, namely, the displacements. The process noise in Eq. 5.23a is depicted by $w_{1,k}$ and characterized by the covariance matrix $\mathrm{E}\left\{w_{1,k}w_{1,l}^{\mathrm{T}}\right\} = Q_1\delta_{kl}$ to distinguish it from the one in Eq. 5.22a. Similarly, the measurement noise is depicted by $v_{1,k}$ with covariance $\mathrm{E}\left\{v_{1,k}v_{1,l}^{\mathrm{T}}\right\} = R_{v_1}\delta_{kl}$. Obviously, the noise covariance matrices for a Kalman filter that acts on $y_{d,k}$ and assumes a system structure given by Eq. 5.22, implies noise covariance matrices defined as

$$\mathrm{E}\left\{\begin{bmatrix} w_k \\ v_k \end{bmatrix}\begin{bmatrix} w_l \\ v_l \end{bmatrix}^{\mathrm{T}}\right\} = \begin{bmatrix} Q & S \\ S^{\mathrm{T}} & R_v \end{bmatrix}\delta_{kl} = \begin{bmatrix} BQ_1B^{\mathrm{T}} & 0 \\ 0 & R_{v_1} \end{bmatrix}\delta_{kl}. \tag{5.24}$$

Hence, the process noise w_k and measurement noise v_k considered for Kalman filtering in Eq. 5.22 can be assumed as uncorrelated since $\mathrm{E}\left\{w_{1,k}v_{1,k}^{\mathrm{T}}\right\} = 0$ is readily presumed. Moreover, another classical assumption is that both $w_{1,k}$ as well as $v_{1,k}$ are not internally cross-correlated, and therefore, Q_1 and R_{v_1} possess diagonal structures, which also pertains for R_v.

If accelerations are measured or simulated instead, the output equation of the output-generating system reads

$$x_{k+1} = Ax_k + Bw_{1,k} \tag{5.25a}$$
$$y_{a,k} = C_d A_c^2 x_k + C_d A_c B_c w_{1,k} + v_{1,k} \tag{5.25b}$$
$$= C_a x_k + D_a w_{1,k} + v_{1,k}. \tag{5.25c}$$

Here, the subscript a emphasizes acceleration. It can be seen that the output matrix C_a and the feedthrough matrix D_a are assembled using the continuous-time state-space parameters A_c and B_c. This follows from the theory presented in Sections 2.1.1 and 2.1.2. Given this state-space representation, the noise covariance matrices decompose to

$$\mathrm{E}\left\{ \begin{bmatrix} w_k \\ v_k \end{bmatrix} \begin{bmatrix} w_l \\ v_l \end{bmatrix}^{\mathrm{T}} \right\} = \begin{bmatrix} Q & S \\ S^{\mathrm{T}} & R_v \end{bmatrix} \delta_{kl} = \begin{bmatrix} BQ_1B^{\mathrm{T}} & BQ_1D_a^{\mathrm{T}} \\ D_aQ_1B^{\mathrm{T}} & D_aQ_1D_a^{\mathrm{T}} + R_{v_1} \end{bmatrix} \delta_{kl}. \tag{5.26}$$

Hence, when Kalman filtering is pursued using acceleration data and output-only identified state-space models, process and measurement noise must be assumed to be mutually correlated, i.e., $S \neq 0$. As in the case of simulated displacements, Q_1 and R_{v_1} possess diagonal structures. This property even pertains to R_v since Eqs. 2.4a, 2.5, and 2.23 show that $D_a = I$. However, this is only valid for the here considered type of representation and discretization of mechanical systems and cannot generally be assumed.

In the following, both the uncorrelated and correlated process and measurement scenarios shall be regarded. Thereby, the performance of the ALS and PALS techniques for noise covariance estimation is evaluated. Since the mechanical system is known in the simulation case in terms of the physical parameters (A, B, C, D), the ALS method can be applied to estimate the true noise covariance matrices. This will be demonstrated through repeated simulations. Therefore, the goal of ALS is to estimate Q_1, R_v when displacements are considered, cf. Eqs. 5.23, 5.1, and 5.24. Thus, the noise shaping matrix is defined as $G_w = B$. In the case of simulated accelerations, the matrices Q_1, R_v, and S shall be estimated, cf. Eqs. 5.25, 5.1, and 5.26.

The advantages of PALS mainly manifest themselves in the experimental case when identified systems are involved. This will be studied in Section 5.7. Nevertheless, a comparison to the classical ALS approach is given here as well by examining the RMS of prediction errors for a set of simulations. Therefore, slight modifications to the simulation setup must be considered. That is, systems will be realized using the SSI and the simulated data. Further, the noise shaping matrix G_w must be defined as identity so that the goal of ALS and PALS is to estimate Q, R_v in the case of simulated displacements. This list must be extended by S when acceleration data is considered. Thus, the number of unknowns increases significantly, and diagonality of Q should not be assumed in either case, see Section 5.6.

5.6.1 The case of uncorrelated process and measurement noise

First, to demonstrate the necessity of noise covariance estimation in the context of Kalman filtering, regard the example depicted in Fig. 5.2. Therein, a segment of simulated displacements (y_{meas}) is given, which was obtained by simulating the 3DOF system introduced before.

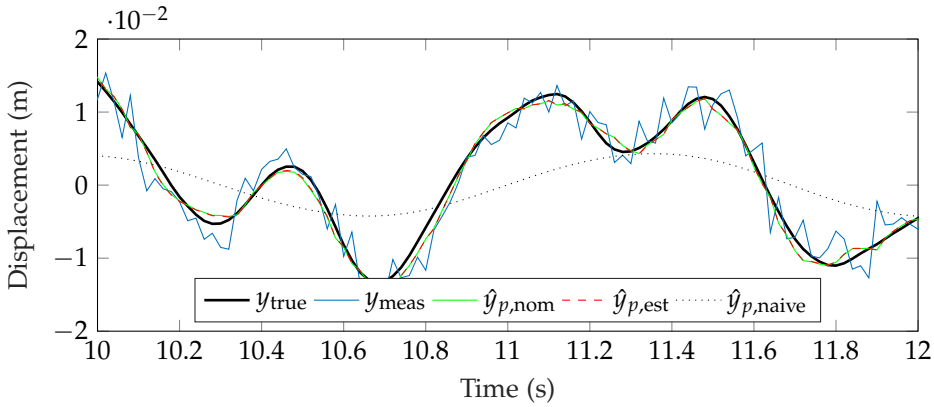

Figure 5.2: True and measured displacement of 3DOF system. Comparison of predicted output using Kalman filter tuned with true noise covariances ($\hat{y}_{p,\text{nom}}$), estimated noise covariances ($\hat{y}_{p,\text{est}}$), and naive selection of noise covariances ($\hat{y}_{p,\text{naive}}$).

Therefore, $w_{1,k}$ and $v_{1,k}$ (see Eq. 5.23) were generated from a Gaussian distribution with zero mean and covariance matrices

$$Q_1 = \begin{bmatrix} 0.1 & & 0 \\ & 0.1 & \\ 0 & & 0.1 \end{bmatrix} \quad \text{and} \quad R_{v_1} = 1e^{-6} \begin{bmatrix} 5 & & 0 \\ & 5 & \\ 0 & & 5 \end{bmatrix}. \tag{5.27}$$

Three different Kalman filters were designed to conduct predictions $\hat{y}_p$ of the true outputs $y_{\text{true}} = Cx_k$. The list of estimators comprises a naive predictor designed with $Q_{1,0} = I$ and $R_{v,0} = I$ ($\hat{y}_{p,\text{naive}}$), one that takes into account the true noise covariance matrices given above ($\hat{y}_{p,\text{nom}}$), and a last one that was tuned with ALS estimates ($\hat{y}_{p,\text{est}}$). The naive Kalman filter was also considered to initialize the ALS technique. It can be seen that both the Kalman filter tuned with true and the one with estimated noise covariance matrices perform well; the predicted outputs $\hat{y}_{p,nom}$ and $\hat{y}_{p,est}$ are close to the true value. The estimator designed with $Q_0 = BQ_{1,0}B^{\mathrm{T}}$ and $R_{v,0}$ ($\hat{y}_{p,\text{naive}}$), on the other hand, fails to produce reasonable predictions. Consequently, applying noise estimation schemes is worth the effort, as Kalman filters tuned with estimated noise covariance matrices most likely feature a reasonable prediction and filtering performance.

In order to evaluate the ability of the ALS method to estimate the true noise covariances, 300 simulations were carried out. In each run, the process and measurement noise was generated and fed through the state-space representation of the 3DOF system. Then, the ALS method was applied using Kalman filters designed with the state-space parameters corresponding to the true mechanical parameters and the initial values $Q_{1,0}$ and $R_{v,0}$. Thus, no system identification was conducted. The solutions to the least-squares problem with semidefinite constraints were computed using convex optimization employing the CVX framework [33, 87] in combination with SDPT3 [189]. The number of lags n_l (Eq. 5.9) was set to 100. As mentioned before, the noise shaping matrix G_w was set to B. The corresponding results are given in Figs. 5.3 and 5.4, where the estimated diagonal entries of the estimated noise covariance matrices (blue dots) are compared with the true values (red lines). For Fig. 5.3, diagonality of Q_1 and R_v was imposed, which is in line with the structure of the true noise covariance matrices

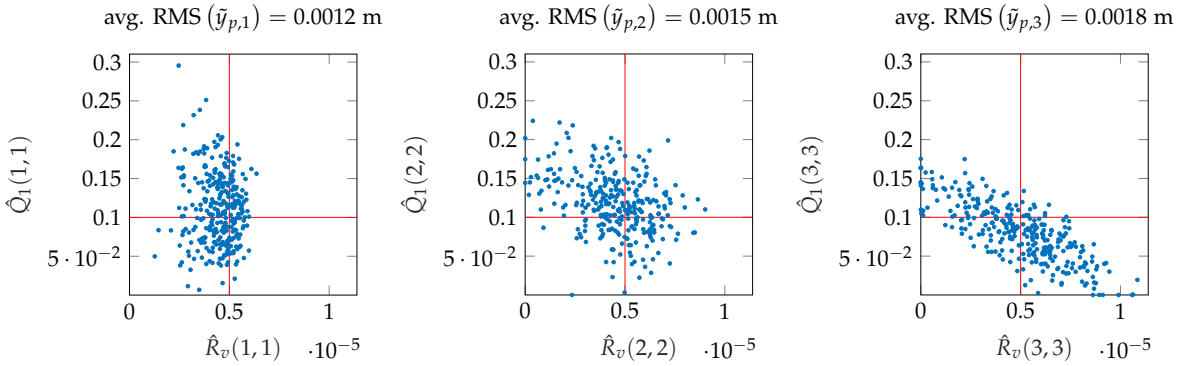

Figure 5.3: Estimated noise covariances (uncorrelated process and measurement noise) for 3DOF system by ALS with enforced diagonality. Estimated values in blue dots, true values depicted by red lines. Average RMS of prediction errors $\tilde{y}_p = Cx_k - C\hat{x}_{k|k-1}$ given above each subplot ($\tilde{y}_{p,nom} = 0.0011$ m).

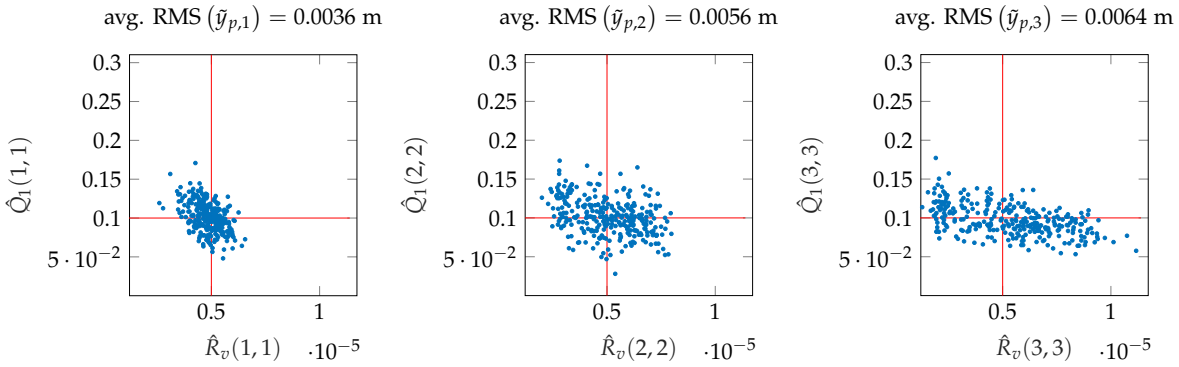

Figure 5.4: Estimated noise covariances (uncorrelated process and measurement noise) for 3DOF system by ALS. Estimated values in blue dots, true values depicted by red lines. Average RMS of prediction errors $\tilde{y}_p = Cx_k - C\hat{x}_{k|k-1}$ given above each subplot ($\tilde{y}_{p,nom} = 0.0011$ m).

given in Eq. 5.23. In contrary, for Fig. 5.4, only the symmetry of the covariance matrices was enforced to test the robustness of the ALS method when the linear set of equations becomes undetermined.

It can be observed that the autocovariance estimates gather around their corresponding true values, which is desired. Nevertheless, some significant scattering is visible in either figure. Hence, the average RMS of the prediction errors $\tilde{y}_p = Cx_k - C\hat{x}_{k|k-1}$ are additionally provided to enable the proper assessment of deviations from the true values. The prediction errors can be best compared to those referring to the nominal Kalman filter, which amounted to approximately 0.0011 m. Consequently, the predictors tuned with ALS-estimated noise covariance matrices function almost optimally when diagonality is imposed (see Fig. 5.3), which is in line with the inherent matrix structures discussed in Section 5.6. Apparently, the quality of covariance estimation decreases when unnecessarily raising the number of variables and imposing only symmetry constraints, see Fig. 5.4. This behavior is to be expected, as Q_1 and R_v are indeed diagonal matrices. Nevertheless, it should be mentioned that by simply comparing the distributions of the blue dots in Figs. 5.3 and 5.4, one would expect the fully populated covariance matrices to lead to the better predictions.

As mentioned before, in this work, the ALS method is neither applied to estimate true values of covariances nor to identify the disturbance structure of identified systems. Instead, the goal is solely to identify noise covariance matrices that improve the estimation performance of Kalman filters employed within the damage analysis framework presented in Chapter 4, cf. Assumption 4.1. To this end, the PALS technique was developed by the author. The influence on the detection and localization of damage shall be investigated in an experiment later on. Concerning the simulation case, the ALS and PALS methods are compared based on the prediction error RMS values. Therefore, another 100 simulations were conducted. For noise covariance estimation, the diagonality R_v was enforced. However, since $G_w = I$, Q was estimated instead of Q_1, which is not a diagonal matrix. In each run, a state-space model with an order of $n = 6$ was identified using the CCA-based SSI-DAT, see. Section 2.3.3. Then, Kalman filters were designed based on noise covariance matrices estimated with the ALS and PALS methods. The nominal Kalman filter was again processed in parallel. Finally, the RMS of prediction errors $\tilde{y}_p = Cx_k - C\hat{x}_{k|k-1}$ was computed. Fig. 5.5 depicts these RMS values of the estimation errors for each of the three output channels and for the different Kalman filters, respectively. There, it can be seen that the prediction performance of the Kalman filters tuned with estimated covariance matrices is almost as good as the ones of the nominal filter, referring to the optimal case. Notably, there is almost no visible difference in the RMS of estimation errors concerning the Kalman filter tuned with PALS estimates and the nominal filters. The estimators tuned with ALS estimates perform slightly worse, especially in view of the output at the third channel. This highlights the effectiveness of the proposed PALS technique. In the following section, the case of correlated process and measurement noise is regarded, representing the situation of acceleration measured at a mechanical system. Since this is a common practice in SHM, the corresponding investigations have greater relevance.

5.6.2 The case of correlated process and measurement noise

The investigations presented in this section were conducted analogously to Section 5.6.1, but this time, because of simulated accelerations, the optimization problem stated in Eq. 5.16 was given the flexibility to estimate the joint covariance matrix S as well. Therefore, the noise estimation procedures were initialized with $S_0 = 0$.

First, the ability of estimating the true noise covariance matrices is regarded. The corresponding results of a series of simulations comprising 300 runs are given in Figs. 5.6 and 5.7. As in the previous study, two investigations were conducted in parallel. Therefore, Fig. 5.6 represents the case of imposed diagonality of Q_1 and R_{v_1}, whereas for Fig. 5.7 no such constraints were enforced, i.e., a fully populated and symmetric structure was assumed. By that, the robustness of noise covariance estimation shall be examined. Note that, contrary to the previous studies, the true values for R_v are marked at $1 + 5e^{-6}$ instead at $5e^{-6}$ because of the factorization of $R_v = D_a Q_1 D_a^{\mathrm{T}} + R_{v_1}$, cf. Eqs. 5.26 and 5.27. The estimates for the diagonal entries of Q_1 and R_{v_1} gather around the corresponding true values, except for the values associated with the third channel. There, a significant bias in the estimates is observable. Nevertheless, this issue is slightly relaxed when the diagonality constraint is lifted. A possible explanation for that could be found in the linear system of equations, which is already underdetermined because of $S \neq 0$. Adding more equations to the systems might increase the flexibility of the least-squares problem, leading to slightly better results. However, such a phenomenon can

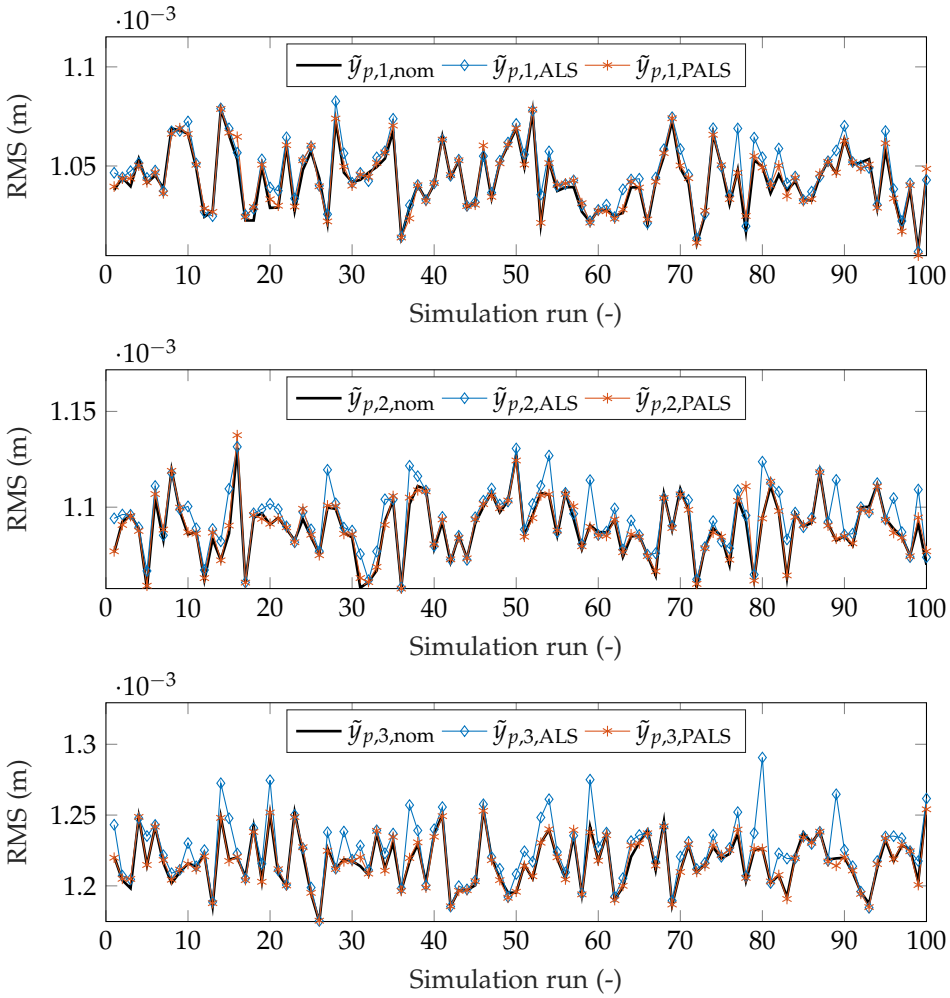

Figure 5.5: Comparison of prediction performance of Kalman filters designed for identified 3DOF models and ALS- and PALS-estimated noise covariance matrices (uncorrelated process and measurement noise). Nominal Kalman filter for true system designed with true noise covariance matrices as reference.

barely be expected when real measurements are considered. Moreover, the average prediction errors depicted above each subplot of Fig. 5.6 are computed as $\tilde{y}_{p,k} = C_a x_k - C_a \hat{x}_{k|k-1}$, see Eq. 5.25c. Again, the RMS of estimation errors is best compared with those associated with the nominal Kalman filter, which amounts to approximately $0.033\,\mathrm{m\,s^{-2}}$. Given that, it is realized that, on the one hand, dropping the diagonality constraint leads to slightly better results. On the other hand, it can be observed that the general prediction performance with estimated noise covariance matrices is significantly worse (almost by a factor of 3) than the one of the nominal Kalman filter. This observation contrasts the previous example of the uncorrelated process and measurement noise and can be explained by the number of unknowns in the least-squares problem. Note that no plots are presented that contrast estimated entries in S with their true counterparts. According to Eq. 5.26, S is directly related to Q_1, and thus, the estimation performance of the joint covariance matrix S can be derived from Q_1.

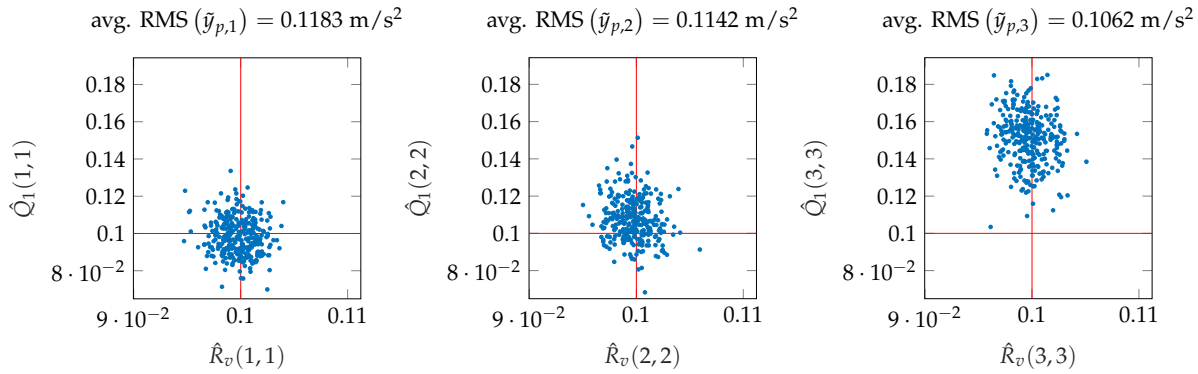

Figure 5.6: Estimated noise covariances (correlated process and measurement noise) for 3DOF system using the CVX toolbox and enforcing diagonality. Estimated values in blue dots, true values depicted by red lines. Average RMS of prediction errors $\tilde{y}_p = C_a x_k - C_a \hat{x}_{k|k-1}$ given above each subplot ($\tilde{y}_{p,nom} = 0.033\,\mathrm{m\,s^{-2}}$).

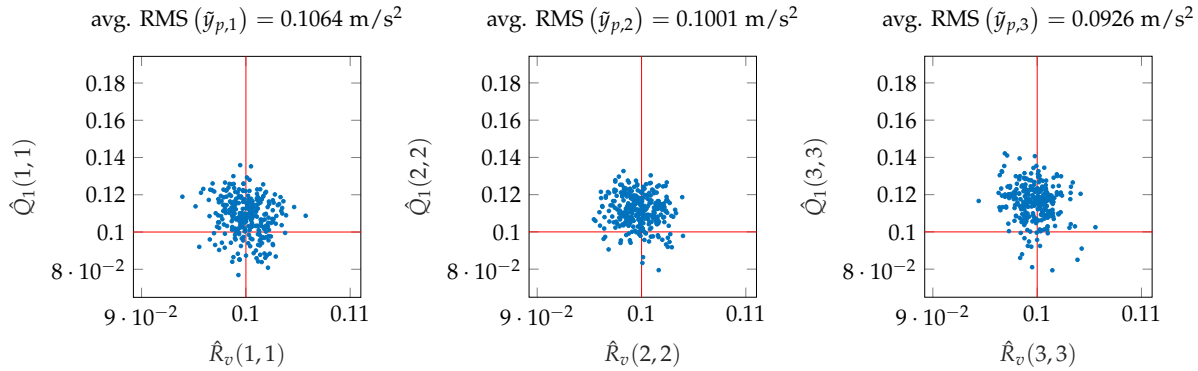

Figure 5.7: Estimated noise covariances (correlated process and measurement noise) for 3DOF system using the CVX toolbox. Estimated values in blue dots, true values depicted by red lines. Average RMS of prediction errors $\tilde{y}_p = C_a x_k - C_a \hat{x}_{k|k-1}$ given above each subplot ($\tilde{y}_{p,nom} = 0.033\,\mathrm{m\,s^{-2}}$).

In the next step, the performance of ALS and PALS in the context of noise estimation for identified state-space models is observed. To this end, again, 100 new simulations were conducted. Then, systems were identified using the acceleration data and the CCA-based SSI-DAT technique with a model order of $n = 6$. Since $G_w = I$ and $D_a = I$, only the diagonality of the measurement noise covariance was assumed. The RMS values of the prediction error $\tilde{y}_{p,k} = C_a x_k - C_a \hat{x}_{k|k-1}$ of the Kalman filters tuned with estimated noise covariance matrices are presented in Fig. 5.8 with reference values resulting from a nominal Kalman filter. As in the case of uncorrelated process and measurement noise investigated in the previous section, the Kalman filters tuned with PALS-estimated covariance matrices perform better than those designed with covariance estimates resulting from ALS. The difference is even more significant (cf. Figs. 5.6 and 5.7), which can be explained with the increased number of variables caused by estimating S and the (6×6) and fully populated matrix Q instead of the (3×3) diagonal matrix Q_1. Both ALS and PALS fail to tune Kalman filters that get close to the performance of the Kalman filter designed with the true system model and true noise covariance matrices.

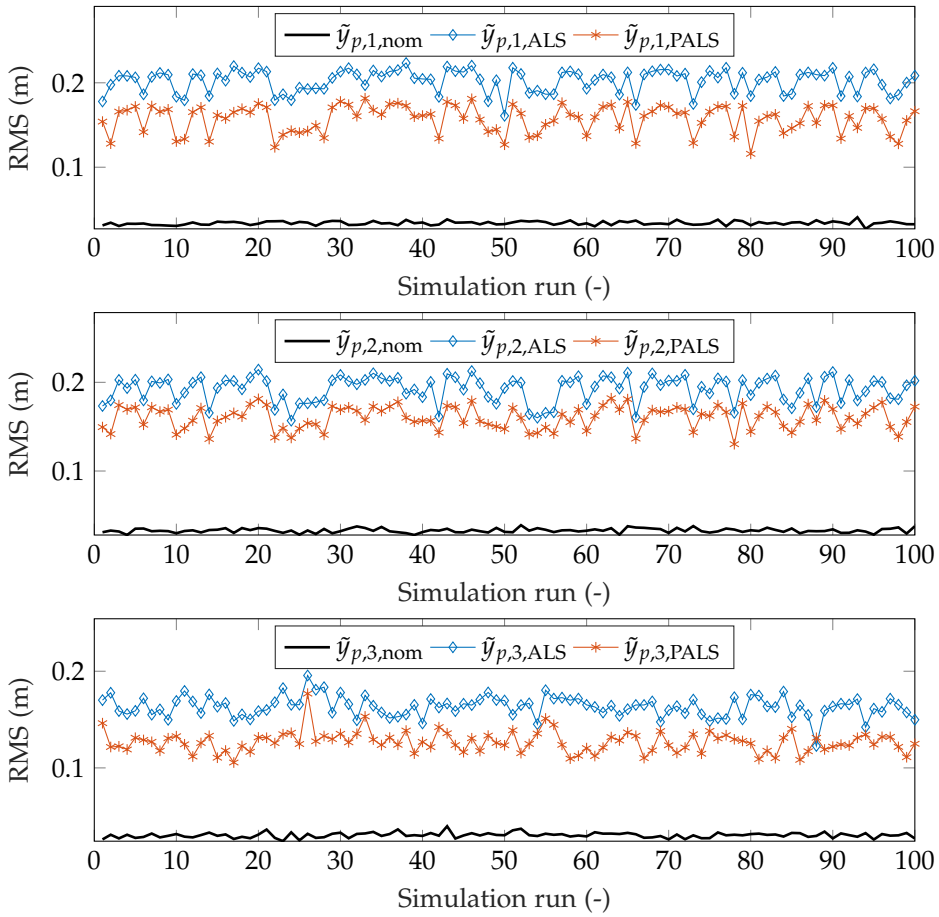

Figure 5.8: Comparison of prediction performance of Kalman filters designed for identified 3DOF models and ALS- and PALS-estimated noise covariance matrices (correlated process and measurement noise). Nominal Kalman filter for true system designed with true noise covariance matrices as reference.

5.7 EXPERIMENTAL VALIDATION

In the previous sections, both the ALS and PALS techniques were compared, e.g., in terms of prediction performance in several simulations. For that, the CVX framework was employed. The corresponding studies were conducted for the cases of uncorrelated and correlated process and measurement noise. It was found that both optimization schemes produce reasonable noise covariance estimates. Moreover, in connection with the correlated process and measurement noise and identified state-space models, which is the standard case throughout this thesis, the PALS technique led to Kalman filters that performed slightly better than those based on ALS estimates. In the following, the noise estimation techniques are regarded in relation to damage analysis, utilizing the framework presented in Chapter 4. Therefore, experimental data is considered instead of simulations. Minor stiffness alterations at a cantilever beam in a laboratory setting shall be detected and localized in a first study. The specimen was already considered in a previous publication [210]. A second experimental study is dedicated to detecting and localization of an added mass at a different cantilever beam.

5.7.1 Localizing stiffness alterations

The central element of a recent publication was the steel cantilever beam subjected to localized stiffness changes. For more details, see [210]. For convenience, the experimental setup is again depicted in Fig. 5.9, and described in the following. The monolithic beam has di-

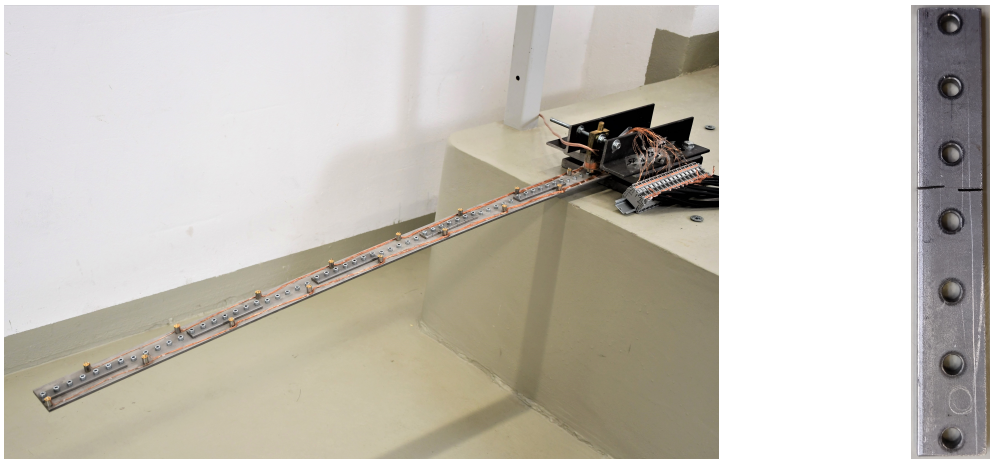

(a) (b)

Figure 5.9: Photograph of the experimental setup of a cantilever beam with exchangeable lugs (a) and exchangeable lug with centered saw-cut (b).

mensions $(l, w, t) = (1.2\,\text{m}, 60\,\text{mm}, 5\,\text{mm})$. To controllably vary the local stiffness properties in a modular manner, nine exchangeable steel lugs were bolted along the beam, alternating at the top or bottom with an overlap of 10 mm. These feature a length of 130 mm, a width of 20 mm, and a thickness of 5 mm. Local damages were introduced by removing these lugs and replacing them with a modified version subjected to minor damages realized by saw-cuts of approximately 1 mm in width, severing about 75 % of the lug's cross-section. The beam remained intact. An exemplary photograph of such a damaged lug is presented in Fig. 5.9. Along the beam, 15 piezoelectric accelerometers were placed at every 75 mm, starting at the tip of the cantilever beam. The sensors were oriented at the left and right edges of the steel beam. An illustration of the measurement layout is given in Fig. 5.10. A broadband excitation

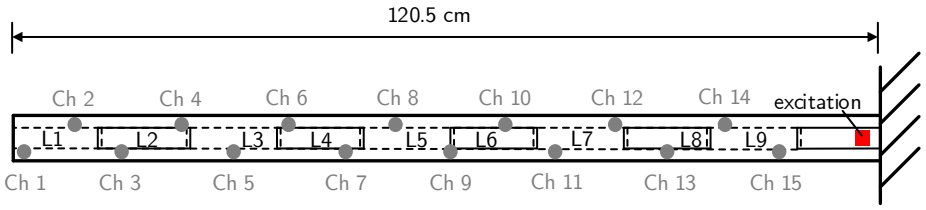

Figure 5.10: Elevation view of the experimental steel cantilever with exchangeable lugs (L) at top and bottom (dashed line).

up to 250 Hz was realized using a contactless electromagnetic shaker placed at the root of the beam. The data acquired in the experiments comprises at least one hour of data recorded at a sampling rate of at 1200 Hz and split into segments of 10 min for each configuration (reference and damaged).

Before conducting the damage analyses, the Kalman filters, later used for this procedure, shall be evaluated exemplarily based on the PSDs of the corresponding innovations. To this end, consider Fig. 5.11, which contains the PSD of the measured acceleration (S_y) at channel 1 as well as its analytical pendant computed with identified parameters resulting from the SSI ($S_{y,\mathrm{SSI}}$). It should be noted that the identified model does not capture the entire dynamics encompassed in the data. In fact, the first peak, at a frequency of about 5 Hz, refers to the first natural frequency, which the identified model does not realize. However, since the corresponding power comprised by that mode is comparatively low, the disturbing effect concerning ALS is expected to be neglectable. The spectra of the innovations (S_e), given in the figure, refer to Kalman filters tuned with noise covariance matrices estimated with either ALS ($S_{e,\mathrm{ALS}}$) or PALS ($S_{e,\mathrm{PALS}}$) employing Matlab's `fmincon`. The reason for selecting another optimization scheme was that the nonlinear optimization tool outperformed the CVX framework with respect to Assumption 4.1, i.e., it led to Kalman filters resulting in less correlated innovations. The PSDs were computed analogously to Eq. 5.19 using $S_{y,\mathrm{SSI}}$ instead of S_y, which explains the smooth nature of the graphs. The noise covariance matrices were estimated

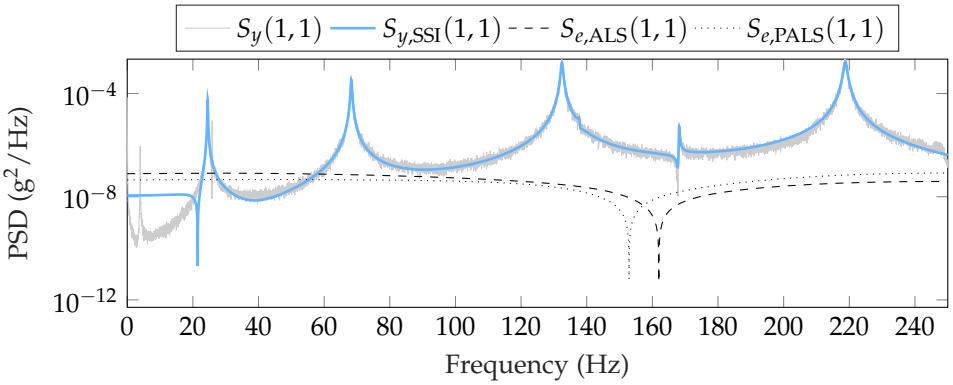

Figure 5.11: PSD of measured acceleration (S_y), analytical PSD using identified system ($S_{y,\mathrm{SSI}}$), and PSD of innovations from Kalman filter ($S_{e,\mathrm{ALS}}$ and $S_{e,\mathrm{PALS}}$). Noise covariances estimated with `fmincon`.

similarly as described in [210]. That is, both ALS and PALS were initialized with $Q_0 = I$, $R_v = I \cdot \min \operatorname{diag}\{R_y(0)\}$, and $G_w = I$ was defined. Further, diagonality of R_v was imposed, and process and measurement noises were assumed to be uncorrelated ($S = 0$). Note that this assumption somewhat contradicts the theoretical elaborations presented at the beginning of Section 5.6. Because of the fact that acceleration data was acquired, process and measurement are inherently correlated ($S \neq 0$). However, as was shown in [210], the additional estimation of S does not always lead to significantly improved filtering performance, and it comes at the cost of increased computational effort. Hence, the simplification was justified in this case.

Both PSDs of the estimation errors (S_e) almost indicate whiteness of the innovations. However, they feature a valley located in the proximity of 160 Hz. Note that these singularities do not result from zeros of the estimators' transfer functions, as could be expected. Notably, zeros can generally be found at the locations of the poles of the underlying systems $\boldsymbol{G}_i$ (cf. [22, 68]) and nowhere else since only stable estimators are considered. However, during the filter synthesis, additional poles might arise that can lead to artifacts observed in Fig. 5.11. In the

regarded context, these phenomena are not problematic, as they have no amplifying effect. Finally, no significant difference between the estimation errors' PSDs can be recognized, and thus, according to Assumption 4.1, it can be suspected that the ability of Kalman filters tuned with ALS and PALS estimates to detect damage is similar. To investigate this assumption, consider Figs. 5.12 and 5.13. The former contains damage detection and localization results for Kalman filters tuned with ALS-estimated noise covariance matrices. The latter refers to the estimators tuned with PALS estimates. Each figure represents the replacement of all nine lugs with a damaged version of it, cf. Figs. 5.10 and 5.9. The damage detection and localization procedures are in line with the routines summarized in Section 4.4.3. Therefore, the SP2E-based damage-sensitive feature $r_{d\mathcal{V}}([i_1, i_2])$ was considered, where i_1 was set to one, and, according to Eq. 3.57, i_2 was chosen as 70. Because of the low degree of uncertainty, the significance level for hypothesis testing was defined as $\alpha = 0$.

Comparing Figs. 5.12 and 5.13, it can be seen that damage detection is successful in all regarded cases. The Kalman filters tuned with ALS estimates are able to pinpoint the damage in all cases but for the exchanged lugs 5, 3, and 2. On the contrary, the estimators tuned with noise covariance matrices estimated via PALS fail to localize the damage introduced at lugs 5, 2, and 1. However, the results associated with ALS are slightly more pronounced in some cases (damage at lugs 6 to 9). Nevertheless, in the regarded example, no significant advantage of either approach can be realized. Finally, an interesting phenomenon shall be discussed. For the damage case concerning lugs 2, 3, and 5, particularly high values of the damage indicator can be observed for the first channel. This phenomenon can be occasionally observed for the damage identification scheme presented in Chapter 4 and probably also for different residual-based damage localization techniques. A possible explanation can be derived from the structure of the considered mechanical system. Generally, the tip of the cantilever (channel 1) exhibits strong oscillations that manifest themselves as a high variance of the adjacent channels. Moreover, identifying the corresponding values of the mode shapes is associated with significant uncertainty, as only neighboring channels exist in one direction. Hence, when damage occurs that does not alter only the local but also the global dynamic properties, residual average power might be picked up at those channels that are particularly influenced. In the case of damage at lugs 2, 3, and 5, it is to be expected that the change of the global dynamics regarding the first channel is more dominant than the local alteration observed in the proximity of the damages.

Although in this experiment, the PALS technique shows to be a proper alternative to the classical ALS method, the experiment does not seem to be entirely suitable to highlight the advantages of PALS. The reason for that was mentioned earlier. It refers to the fact that the identified system covers the predominant dynamics encompassed in the data, cf. Fig. 5.11. However, the PALS technique was developed for the case where a significant difference between the modeled or identified dynamics and the measured dynamics is present. Therefore, the proceeding experiment constitutes a good example.

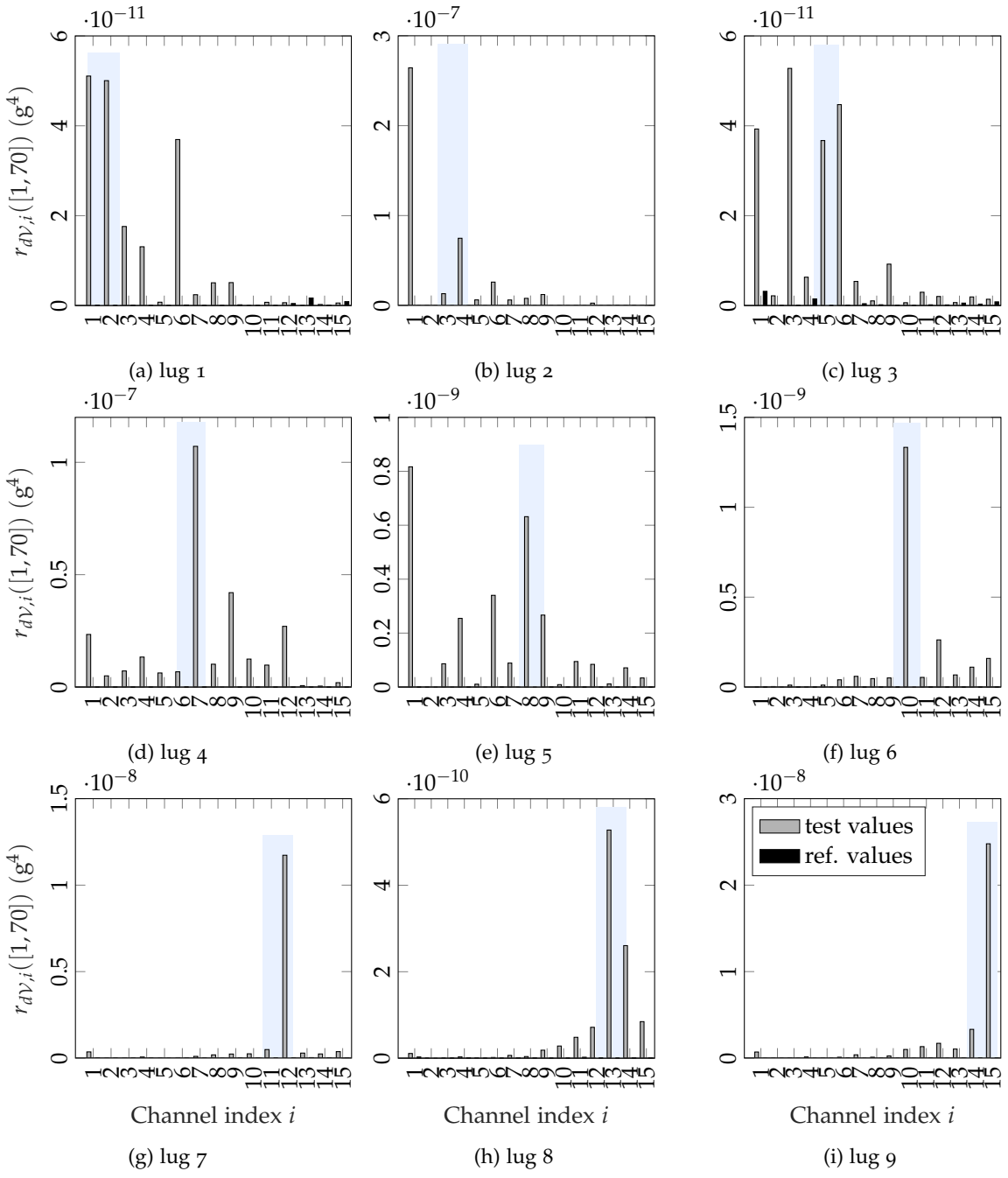

(a) lug 1 (b) lug 2 (c) lug 3

(d) lug 4 (e) lug 5 (f) lug 6

(g) lug 7 (h) lug 8 (i) lug 9

Figure 5.12: Variance feature by SP2E for localization of stiffness alteration using Kalman filters tuned with noise covariance matrices estimated with the ALS method using `fmincon`. Colored areas depict the severed lugs.

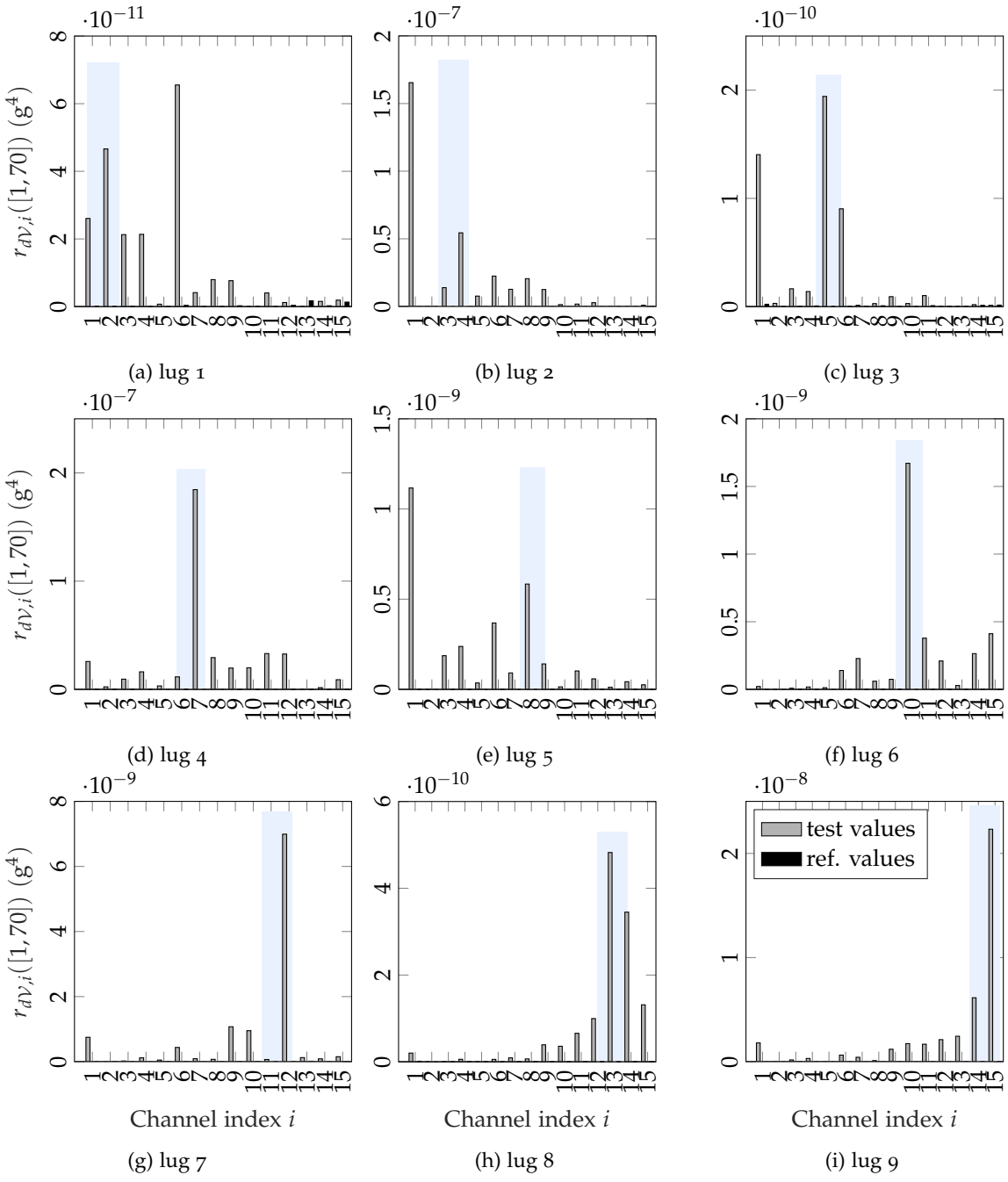

(a) lug 1 (b) lug 2 (c) lug 3

(d) lug 4 (e) lug 5 (f) lug 6

(g) lug 7 (h) lug 8 (i) lug 9

Figure 5.13: Variance feature by SP2E for localization of stiffness alteration using Kalman filters tuned with noise covariance matrices estimated with the PALS method using `fmincon`. Colored areas depict the severed lugs.

5.7.2 Localizing mass alterations

Considerable structural alterations do not always manifest themselves as a local change of stiffness but also as a mass change. An obvious example from the domain of civil engineering, or systems situated outdoors in general, is the case of icing. Therefore, an experiment in a laboratory environment was conducted to test the detectability of localized additional masses. The associated experiment was the subject of an article published earlier, see [213]. However, for clarity, the setup is briefly described in the following. The considered cantilever beam is depicted in Fig. 5.14. It featured a rectangular profile with a width of 60 mm and a thickness

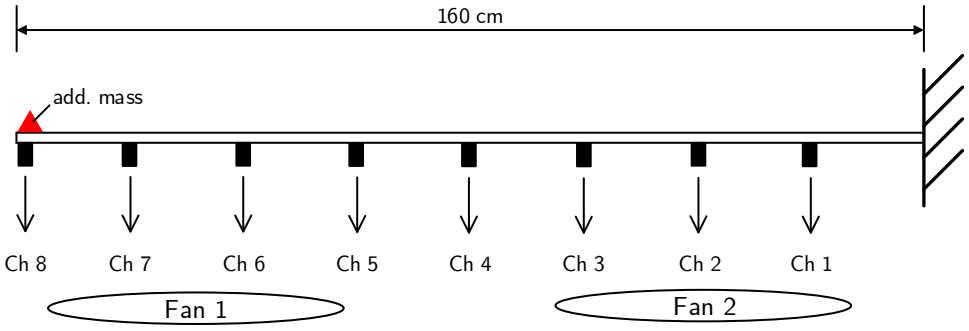

Figure 5.14: Sketch of experimental steel cantilever excited by two fans with additional mass at the tip of the beam.

of 6 mm. It was equipped with eight accelerometers sampled at a frequency of 1652 Hz and stored as 5 min data blocks. Measurements were acquired in both a reference and an altered state. For the latter, single masses weighing 24 g and 96 g, respectively, were placed at the tip of the beam. The excitation was realized using airflow by employing two regular fans positioned underneath the cantilever.

Before performing the actual damage analysis, the filtering performance of two exemplary Kalman filters is again examined. They were realized given the noise covariance matrices estimated using the ALS and PALS approach within the CVX framework. PSDs of the measurement response (S_y) as well as its analytical counterpart ($S_{y,\mathrm{SSI}}$) using identified state-space parameters are therefore depicted in Fig. 5.15. It is noted that the identified model does not capture the entire dynamics encompassed in the data. In fact, the first peak, at a frequency of about 2 Hz, refers to the first natural frequency, which the identified model does not realize despite high signal power. This circumstance might disturb the noise covariance estimation when the ALS approach is pursued, as shall be observed later on. In addition, the spectra of the estimation errors associated with ALS ($S_{e,\mathrm{ALS}}$) and PALS ($S_{e,\mathrm{PALS}}$) are also given in Fig. 5.15 as well. For the noise covariance estimation, diagonality of R_v was imposed, and both process and measurement noise were assumed to be mutually correlated ($S \neq 0$). Further, both ALS and PALS were initialized with $Q_0 = I$, $R_v = I$, and $G_w = I$ was defined. Despite the fact that both Kalman filters lead to almost white innovation series, the filter tuned with noise covariance matrices estimated with PALS leads to innovations corresponding to a spectrum with a more even distribution over all frequencies.

Considering these findings from the visual inspections of Figs. 5.15 and in view of Assumption 4.1, it can be postulated that the Kalman filters tuned with PALS-estimated noise covari-

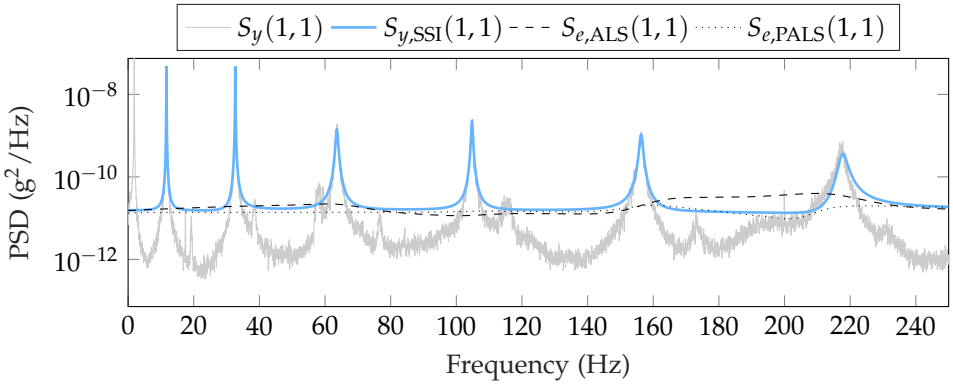

Figure 5.15: PSD of measured output using identified system ($S_{y,\mathrm{SSI}}$) as well as PSD of innovations from Kalman filter ($S_{e,\mathrm{ALS}}$ and $S_{e,\mathrm{PALS}}$). Noise covariance matrices estimated with CVX toolbox.

ance matrices are most probably more suitable for the damage analysis. This is confirmed through Fig. 5.16 for the case of an additional mass of 24 g and through Fig. 5.17 for 96 g.

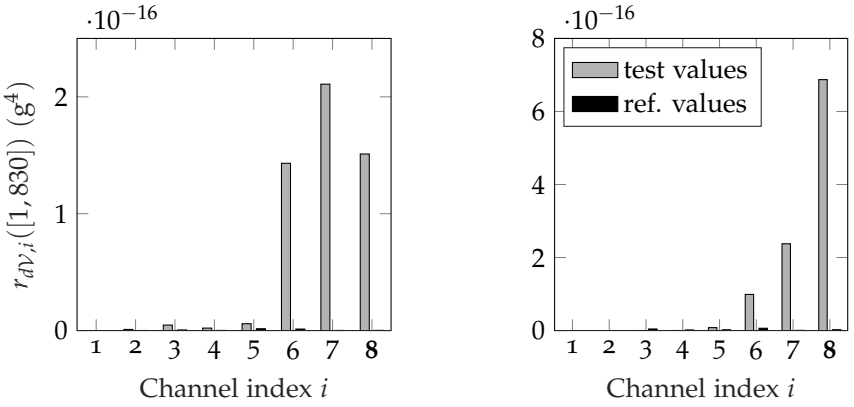

(a) ALS (b) PALS

Figure 5.16: Variance feature by SP2E for localization of additional 24 g at tip of cantilever beam (channel index 8) using Kalman filters tuned with noise covariance matrices estimated with the ALS (a) and PALS (b) method using CVX toolbox.

Note that the damage analysis procedure is equivalent to the one from the preceding investigation. Though, according to Eq. 3.57, i_2 for $r_{dV}([i_1, i_2])$ had to be altered to 830 because of a different lowest natural frequency (approximately 2 Hz). Although the identified systems do not represent this mode, this value is reasonable for comparability reasons concerning the ALS method.

Indeed, damage detection is successful with respect to either noise estimation scheme, as expected. However, the Kalman filters tuned with noise covariances resulting from PALS pinpoint the location of the structural alteration, whereas, in the case of the ALS estimates, the precision of the damage localization is less convincing. Interestingly, by comparing the magnitudes of the damage feature, a qualitative connection to the degree of structural alteration (24 g versus 96 g) can be recognized. However, the circumstance that the damage indicators do not take the fourfold value when increasing the additional mass by a factor of four sug-

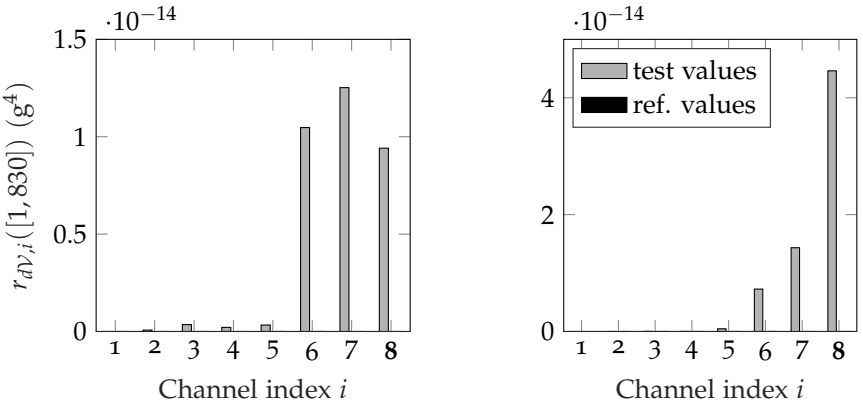

(a) ALS (b) PALS

Figure 5.17: Variance feature by SP2E for localization of additional 96 g at tip of cantilever beam (channel index 8) using Kalman filters tuned with noise covariance matrices estimated with the ALS (a) and PALS (b) method using CVX toolbox.

gests that the proposed damage analysis technique needs adjustment (if even possible) when precise damage quantification is pursued.

5.8 CONCLUDING REMARKS

The presented chapter introduced the PALS method, a parametric extension of the ALS method for noise covariance estimation of state-space models. The PALS approach can be utilized in combination with systems identified with the help of SSI techniques. Contrary to the original ALS method, the correlation function of the innovations, which forms the basis for the least-squares problem, is estimated by employing the identified state-space parameters and performing an inverse Fourier transform.

Both the ALS and PALS were utilized in the context of simulation and experimental studies to predict signals and, most importantly, for detecting and localizing structural alterations. Also, the estimation of the actual covariance matrices for the case of known systems, or such that is modeled by first principles, employing ALS was demonstrated and investigated.

Estimating noise covariance matrices by ALS (and PALS) requires solving an optimization problem with semidefinite constraints. For this endeavor, several optimization toolboxes can be applied. The open-source optimization framework CVX and Matlab's optimization toolbox were employed for the present chapter. In one example (Section 5.7.1), the optimization problem was tackled utilizing the Matlab function `fmincon`, which is a tool for solving constrained nonlinear optimization problems. Since the underlying optimization problem is explicitly convex and demands semidefinite constraints, CVX or similar frameworks constitute intuitive choices since they have been particularly designed for these problems; and they enable a numerically efficient realization of the semidefinite constraints. However, the commercial and generic tool (`fmincon`) was applied because of a better performance regarding Assumption 4.1. In this case, a reasonable computation time could be achieved. However, to the author's experience, CVX performs more efficiently when systems with high model orders are considered.

The PALS technique was validated as a proper replacement for the classical ALS approach for damage detection and localization. It was shown that the sensitivity toward localized damage can be improved when the identified system models do not cover modes that are significantly encompassed in the acquired signals, see Section 5.7.2. The explanation for that results from the theory of ALS. There, a Kalman filter is employed, which, on the one hand, represents the identified or modeled dynamics of the observed mechanical system and, on the other hand, constitutes a filter for the acquired measurements. When computing the innovations by feeding the measured data through the initially designed Kalman filter to estimate the innovations' correlation function (ALS), perturbations are picked up if the dynamics represented by the Kalman filter are not linked to those encompassed in the data. More precisely, even if the initially chosen Kalman filter were designed optimally by accident, the resulting innovations sequence would not be a white noise process. Hence, the PALS technique was developed to cope with such scenarios. By synthesizing the innovations' correlation function with the help of identified state-space parameters, the utilization of actual measurements is bypassed. Thus, it can be concluded PALS is more suitable for the application in SHM.

6

A LOCAL LPV APPROACH FOR DAMAGE LOCALIZATION IN LONG-TERM MONITORING

A major challenge in SHM is manifested by varying EOCs that naturally alter the dynamic behavior of mechanical systems. Linear and even nonlinear dependencies might characterize the underlying relationship between dynamic properties and exogenous conditions. Hence, implicit or explicit data normalization strategies are readily applied to features extracted from short-term data to remove or handle these natural variations. In the past years, growing attention has been paid to the identification of linear parameter-varying (LPV) systems. These models account for the dependency on so-called scheduling variables, such as temperature or wind speed, and the corresponding dynamics of the observed system. Two identification strategies exist, namely global and local approaches. In the former, an LPV model with some presumed structure is directly derived from a finite amount of data that covers a reasonable variety of the scheduling EOCs as well as the system's dynamics. Whereas for the latter approach, the interpolation between locally stationary models (LTI models) is carried out, resulting in a different global representation. In the context of the damage localization framework presented in Chapter 4, an LPV approach to handle long-term variations caused by EOV is particularly appealing, as it matches the system theoretic background. Moreover, applying an interpolation scheme enables the representation of nonlinear dependencies, which frequently occur in SHM. Unfortunately, this intuitive and simple concept faces strong hurdles in identifying LPV state-space systems due to the coherence requirement of local models. Therefore, in this chapter, a recently presented interpolation method is adapted to identify LPV estimators suitable for damage localization within the SP2E framework. In the following, this approach is presented, validated, and further investigated by means of a simulation study of an LPV system under varying temperatures.

6.1 MOTIVATION AND BACKGROUND

In the past years, the direct modeling of the functional dependence of EOCs and representatives of the short-term dynamics of structures under surveillance (system parameters or features) received increasing attention in SHM to enable the damage identification under EOV, see Section 1.1.2. An exciting strategy constitutes the modeling of LPV systems, as it incorporates varying dynamic properties, and therefore, is closely related to the predominant physical phenomena. Relevant literature in the context of SHM has been published recently, e.g., by Avendaño-Valencia et al. [12–14, 17]. For these modeling approaches, the observed structure is regarded as a system depending on the scheduling variable θ and featuring linear dynamic behavior at different operating points represented by the set $[\bar{\theta}_1, \bar{\theta}_2, \cdots \bar{\theta}_l]$. This circumstance is depicted by the flowchart given in Fig. 6.1. There, u represents the excitation and y depicts the output of the LPV system $\boldsymbol{G}(\theta)$. Obviously, y depends on the scheduling variable θ, as the output-generating system behaves differently for varying θ. This circumstance is further illustrated by Fig. 6.2, where a fictive ith system pole λ_i representing the dynamic behavior of $\boldsymbol{G}(\theta)$ is plotted versus θ. There, also the operating points represented by $\bar{\theta}_i$ are depicted. In

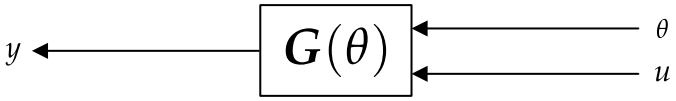

Figure 6.1: LPV system $\boldsymbol{G}(\theta)$ with input u, scheduling variable θ, and output y.

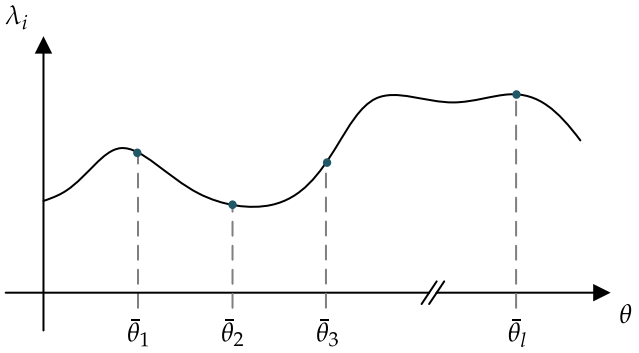

Figure 6.2: Dependence of system pole λ_i (representing $\boldsymbol{G}(\theta)$) on the scheduling variables θ.

the illustrated example, the dependency on the scheduling variable is clearly nonlinear. That highlights a major advantage of LPV modeling approaches, as they are suitable for nonlinear problems as long as the dynamic behavior at a local operating point represented by $\bar{\theta}_i$ is linear. This property makes LPV models particularly attractive for nonlinear control problems [193]. But also in SHM, where the observed structures might vary their dynamic behavior significantly with respect to changing EOCs, LPV identification schemes are applicable for data normalization by explicitly modeling the functional dependence of relevant EOCs on the dynamic properties over long periods, or more precisely, for a wide range of EOV.

For the identification of LPV systems, two general strategies exist: the *global* and *local approach*. The former refers to the realization of LPV systems through data representing the expected range of the scheduling parameter θ. The local approach, on the other hand, relies on the interpolation of so-called *frozen* LTI systems that refer to different operating points. In either case, a single global model arises. It should be mentioned that the identification process might be accompanied by statistical methods such as Gaussian process models to consider uncertainty in the parameters, see [14] and the citations therein. Global approaches can struggle to represent long-term trends in SHM, as they readily involve huge amounts of data. Therefore, interpolation-based strategies might perform better in these cases.

In this chapter, the SP2E method summarized in Chapter 4 shall be incorporated into an LPV framework that accounts for EOV so that data normalization is performed explicitly. That is, the dependence of EOCs and some damage-sensitive features is modeled directly. Therefore, the local approach is appealing as, in the regarded cases, LTI models are continuously identified. Thus, the framework becomes extendable for newly experienced EOCs. Unfortunately, the interpolation-based realization of a single global LPV model involving multiple state-space models is not a trivial task, as the considered local models must be *coherent*. This expression refers to the circumstance that the state-space systems feature the same state-space basis. Typically, this is faced by transforming the corresponding state-space models into some

canonical form [193] applying a similarity transformation with the help of $T_i \in \mathbb{R}^{n\times n}$ so that for a system defined by $[A(\bar{\theta}_i), B(\bar{\theta}_i), C(\bar{\theta}_i), D(\bar{\theta}_i)]$

$$A'(\bar{\theta}_i) = T_i A(\bar{\theta}_i) T_i^{-1}, \quad B'(\bar{\theta}_i) = T_i B(\bar{\theta}_i), \quad C'(\bar{\theta}_i) = C(\bar{\theta}_i) T_i^{-1}, \quad D'(\bar{\theta}_i) = D(\bar{\theta}_i), \tag{6.1}$$

cf. Eq. 2.17. Zhang et al. concluded in [227] that in practice, a single transformation matrix T must be found, which is valid for all local state-space models in the sense that the input-output relation is in line with the actual (measured) behavior of the observed LPV system. Further studies by Zhang and Ljung [225, 226] showed that a common matrix T could be derived from measurements at the regarded operating points. The approach is based on the work of Verdult and Verhaegen [202]. Although promising numerical results were presented in these publications, for the present work, the coherence issue is circumvented by combing local LTI models into a global system and solely interpolating the output with the help of a distance-based weighting. Thus, no interpolation of the system matrices is pursued. The corresponding procedure is described and validated in the following. An investigation of the strategy presented in [225, 226] in the regarded context is left out for future research.

6.2 INTERPOLATION OF LOCAL LTI SYSTEMS IN THE CONTEXT OF SP2E

As mentioned before, the goal is to operate the SP2E method summarized in Chapter 4 in a normalized manner so that the identification of damage (detection and localization) is enabled under varying EOCs. In previous studies presented by the author [213], an implicit data normalization strategy based on the PCA was applied that allowed for the localization of structural alterations under environmental variability. However, given the system-theoretic nature of the SP2E framework and the fact that EOV might manifest itself in a nonlinear alteration of the dynamic behavior, an explicit normalization approach with the potential of coping with these kinds of dependencies is desirable. To this end, an interpolation approach by Zhang [224] is adapted for this thesis. An alternative, look-up-table-like strategy was presented in [116].

For the interpolation-based SP2E framework, consider the interconnection of systems as given in Fig. 4.2. At the risk of repetition, it is remarked that $\mathbf{\Pi}_1^{-1}$ refers to an estimator, e.g., designed using Kalman or $\mathcal{H}_\infty$ filter theory, representing the monitored structure in the reference state (emphasized by index 1). $\mathbf{\Pi}_2^{-1}$, on the other hand, represents the potentially damaged structure referred to as the structure in the analysis state (index 2). Now, the idea is to substitute $\mathbf{\Pi}_1^{-1}$, which is typically given by an LTI system associated with a particular working point, with an LPV system representing a wide range of EOV. The latter is constructed with the help of l local LTI systems referring to different operating points ($\bar{\theta}_i$). The output of $\mathbf{\Pi}_1^{-1}$ triggered by some test signal y_3 on the input side is then determined through weighting. This relation is illustrated in Fig. 6.3. The corresponding state-space equations read

$$x_{e,k+1} = \bar{A} x_{e,k} + \bar{B} y_{3,k} \tag{6.2a}$$

$$e_{1,k} = \bar{C}(\theta) x_{e,k} + \bar{D} y_{3,k}, \tag{6.2b}$$

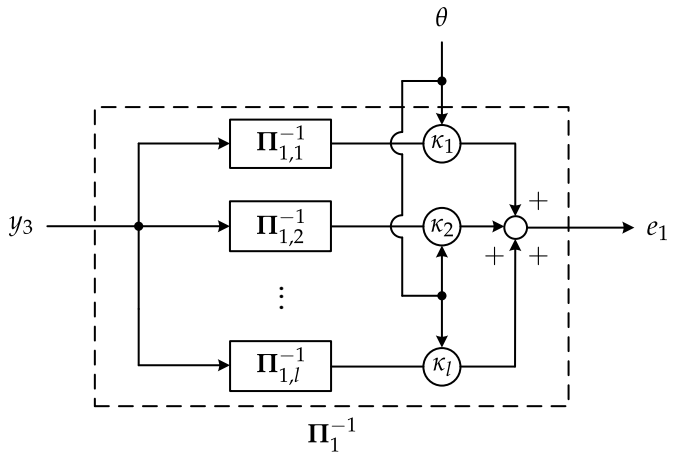

Figure 6.3: Construction of reference estimator $\mathbf{\Pi}_1^{-1}$ as LPV system via interpolated LTI systems.

where

$$\bar{A} = \begin{bmatrix} A_e(\bar{\theta}_1) & & 0 \\ & \ddots & \\ 0 & & A_e(\bar{\theta}_l) \end{bmatrix}, \; \bar{B} = \begin{bmatrix} K_e(\bar{\theta}_1) \\ \vdots \\ K_e(\bar{\theta}_l) \end{bmatrix}, \tag{6.3}$$
$$\bar{C}(\theta) = \begin{bmatrix} -\kappa_1(\theta)C(\bar{\theta}_1) & \cdots & -\kappa_l(\theta)C(\bar{\theta}_l) \end{bmatrix}, \; \bar{D} = I.$$

Thus, e_1 is equal to the weighted sum of the outputs of the local LTI models defined by $[A(\bar{\theta}_i), K_e(\bar{\theta}_i), C(\bar{\theta}_i)]$. Recall that θ depicts the continuous scheduling variable, whereas $\bar{\theta}_i$ describes discrete values of θ representing a single operating point, namely a snapshot of θ observed, e.g., when identifying the local LTI models. In Eq. 6.3, $\kappa_i(\theta)$ depicts the weightings for interpolation. It can be seen that the proposed design of the LPV model is different from conventional approaches (cf. e.g. [34]) since $\bar{A}$, $\bar{B}$, and $\bar{D}$ are not a function of the continuous scheduling variable θ, only $\bar{C}(\theta)$ varies. Hence, this interpolation approach is not influenced by different state-space bases of the local LTI models referring to $\bar{\theta}_i$, and no special care must be taken to make these systems coherent. Consequently, the LPV design problem is reduced to a proper selection of the weightings $\kappa_i(\theta)$ for the current values of θ, which is explained in the following. The corresponding Algorithm 1 is presented in Section A.3.

The proposed weighting selection is based on a simplex inclusion metric and is illustrated with the help of Fig. 6.4. Consider $\theta = [\theta_1 \; \cdots \; \theta_m]^\mathrm{T}$ to be an m-dimensional variable representing m EOCs that affect the dynamics of the monitored structure. In the first step, a grid of l local LTI models is constructed, where each model refers to a different working point given by $\bar{\theta}_i \in \mathbb{R}^m$. To this end, the EOC space is divided into segments, for which $\Delta\theta$ is defined, cf. Fig. 6.4. This parameter contains the segment widths for all m EOC dimensions. During monitoring, it is to be expected that multiple identified models fall into a single EOC segment. Therefore, the 'best' representative should be selected for the LPV system realization. Clearly, the choice depends on the case of application; however, local LTI models that represent a wide range of structural dynamics and are close to the segment center are attractive for the LPV design.

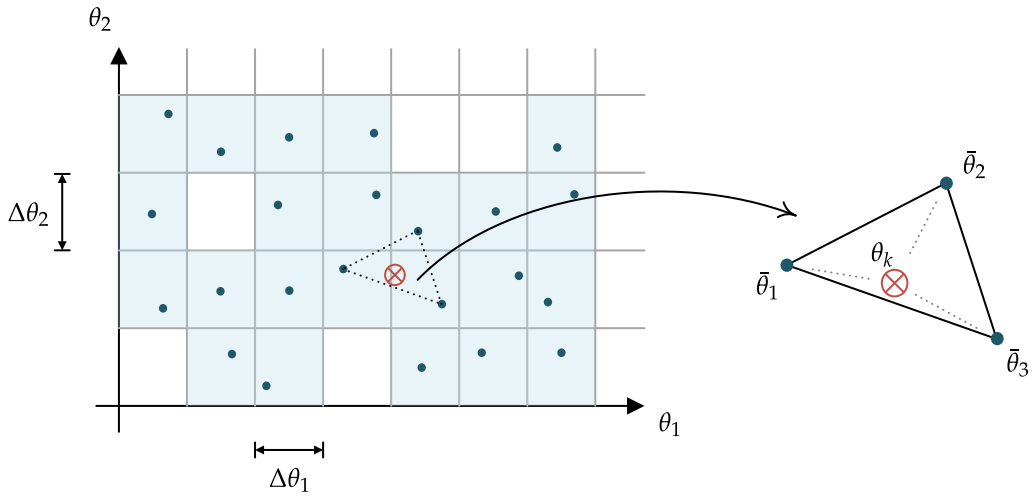

Figure 6.4: Grid of local LTI models (blue dots) and interpolation in a 2D EOC space via Barycentric coordinates.

For the actual interpolation step, weightings $\kappa_1(\theta)$ to $\kappa_l(\theta)$ must be found for a given $\theta = \theta_k$ to assemble $\bar{C}(\theta_k)$. A simple strategy for that is to find the $m+1$ local LTI models whose working points $\bar{\theta}_i$ form a convex hull which includes θ_k. The corresponding weightings are then defined in such a way that

$$1 = \sum_i \kappa_i(\theta_k). \tag{6.4}$$

All other $l - m - 1$ weightings are set to zero. A convenient choice of convex hulls is given by m-dimensional simplexes, which are generalizations of polyhedra [28]. That is, if, e.g., $m = 1$, the associated geometric shape is a line, if $m = 2$, the simplex is equivalent to a triangle, and so forth. The number of vertices ($\bar{\theta}_i$) amounts to $m+1$. Most interestingly, a point included in an m-dimensional simplex can be transformed into the *barycentric coordinate system*, allowing for interesting interpretations concerning the vertices defining the simplex. This circumstance is elaborated on in the following.

For simplicity, the 2-dimensional case is regarded, where a triangle gives the corresponding simplex, cf. Fig. 6.4. The barycentric coordinates of a point lying within this triangle (θ_k) can be imagined to correspond to masses placed at the vertices $\bar{\theta}_1$, $\bar{\theta}_2$, and $\bar{\theta}_3$. If all barycentric coordinates for that point are equal, it represents the center of mass and the geometric center. Moreover, a point included in a triangle divides this shape into three sub-triangles. The area of each sub-triangle normalized with respect to the overall area of the triangle is equivalent to the barycentric coordinates of the dividing point, cf. [46, p. 216]. Hence, the weightings $\kappa_i(\theta_k)$ concerning the $m+1$ surrounding reference working points $\bar{\theta}_i$ can be determined by normalizing the EOC space and then computing the barycentric coordinates for θ_k. This operation is enabled by an affine transformation [196]. The idea is that barycentric coordinates

should be equal before and after the transformation. Thereby, the generic property defined in Eq. 6.4 is presupposed, leading to the following linear set of equations:

$$\begin{bmatrix} \theta_k \\ 1 \end{bmatrix} = \begin{bmatrix} V_{\bar{\theta}} \\ J_{1,m} \end{bmatrix} \kappa(\theta_k) \tag{6.5}$$

$$\begin{bmatrix} \theta_{k,1} \\ \vdots \\ \theta_{k,m} \\ 1 \end{bmatrix} = \begin{bmatrix} \bar{\theta}_{1,1} & \bar{\theta}_{2,1} & \cdots & \bar{\theta}_{m+1,1} \\ \vdots & \vdots & \ddots & \vdots \\ \bar{\theta}_{1,m} & \bar{\theta}_{2,m} & \cdots & \bar{\theta}_{m+1,m} \\ 1 & 1 & \cdots & 1 \end{bmatrix} \begin{bmatrix} \kappa_1(\theta_k) \\ \vdots \\ \kappa_m(\theta_k) \\ \kappa_{m+1}(\theta_k) \end{bmatrix} \tag{6.6}$$

Here, $V_{\bar{\theta}}$ depicts a matrix containing the vertices of the m-dimensional simplex and $J_{1,m}$ denotes a row vector of ones positioned in m columns. $V_{\bar{\theta}}$ is assembled with the help of the normalized values of the operating points $\bar{\theta}_i$ that surround θ_k, which is also normalized with respect to the considered EOC grid. The second subindex of θ_k and $\bar{\theta}_i$ refers to the associated value for each EOC. Note that with a slight abuse of notation, in Eq. 6.6, the index i is replaced by numbers starting at 1, strictly referring to the vertices of the surrounding simplex. Finally, the weights can be computed by

$$\kappa(\theta_k) = \begin{bmatrix} V_{\bar{\theta}} \\ J_{1,m} \end{bmatrix}^{-1} \begin{bmatrix} \theta_k \\ 1 \end{bmatrix} \tag{6.7}$$

or with the help of Cramer's rule, see [196].

Very importantly, it should be mentioned that to determine the weightings $\kappa(\theta_k)$ with the proposed interpolation scheme, the segmentation of the EOC space via $\Delta\theta$ is not necessary, cf. Eq. 6.6. Moreover, the motivation to realize an EOC grid is twofold:

(i) The 'best' estimators can be defined as a local reference by comparing those associated with the same EOC segment, e.g., by regarding the model order.

(ii) Reasonable values of $\Delta\theta$ can be readily determined in preliminary studies, e.g., by investigating natural frequency fluctuations with respect to EOCs. In case of an incomplete representation of the EOC space, $\Delta\theta$ can be conveniently considered to assess the meaningfulness of interpolations.

To elaborate on the latter issue, suppose the following circumstance: In the context of SHM, a complete grid of local LTI models is often hard to achieve (cf. Fig. 6.4), especially if the LPV modeling approach is pursued adaptively. In cases where the distance of even the closest reference models is comparatively far and the dependence of system dynamics and relevant EOCs is nonlinear, interpolation might be problematic. That is, the values of the damage indicators introduced in Section 4.2.1 might increase because of EOC-related alterations (not damage) of the estimators' dynamics in the reference and analysis state. Hence, it is suggested to check the following criterion for all $l \in [1, m+1]$:

$$\theta_{k,l} - \bar{\theta}_{i,l} < 2\Delta\theta_l. \tag{6.8}$$

Another challenging scenario occurs when θ_k lies outside the considered EOC grid. Then, interpolation is not feasible and a pragmatic strategy must be found to enable damage analyses

beyond the yet observed EOC space. A simple solution for that is to consider a maximum of the m nearest points (local reference systems) that obey

$$\theta_{k,l} - \bar{\theta}_{i,l} < \Delta\theta_l \tag{6.9}$$

and perform a distance-based weighting instead, see Algorithm 1. Obviously, the criteria defined in Eqs. 6.8 and 6.9 can be adjusted depending on the application scenario. Moreover, the proposed normalization scheme might be modified to enable proper extrapolation.

A final remark is made in view of implementing the simplex inclusion algorithm. This procedure involves the identification of encasing m-dimensional simplexes. Thus, the m-dimensional grid of $\bar{\theta}$ must be divided into a finite set of simplexes first. Secondly, the simplex must be identified that accommodates θ_k. The first problem can be tackled via a triangulation approach such as the *Delaunay triangulation*, and the latter constitutes a convex hull inclusion problem. Because of the possible high dimensionality, one must consider advanced geometric algorithms. Elaborating on that would by far exceed the scope of this thesis. Nevertheless, for the implementation of the proposed interpolation scheme the Matlab functions `delaunayn` and `tsearchn` have been utilized.

6.3 SIMULATION AND ANALYSIS OF AN LPV SYSTEM UNDER VARYING CONDITIONS

A series of simulations were performed to validate the proposed interpolation-based LPV approach. Therefore, the system depicted in Fig. 6.5 was modeled as a temperature-dependent LPV system with five two-noded Euler-Bernoulli beam elements and a diagonal (5×5) mass matrix. The Young's modulus and second moment of inertia were set to 21×10^7 kPa and $1.7932 \times 10^{-7}\,\mathrm{m}^4$, respectively. Further, the modal damping ratios ζ_i were set to 0.5 %. Note that the simulation model is not linked to any of the cantilever systems investigated in Chapter 5. The LPV simulation was carried out via Simulink [181] after defining a grid of local LTI

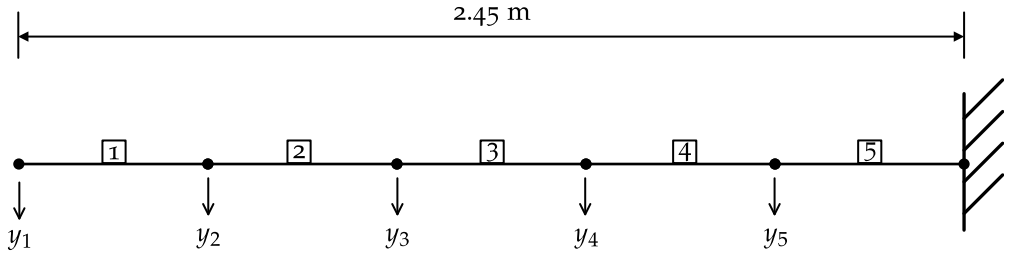

Figure 6.5: Cantilever simulation model as LPV system.

models in Matlab [45].

Two different temperature dependency functions were considered and realized by scaling the stiffness matrices of the local LTI models with a scalar factor α_K. Thus, it is assumed that the temperature effect manifests itself in a uniform and global change in the structural dynamics. For the investigations, a smooth sinusoidal fluctuation of the temperature was simulated, ranging from $-30\,°\mathrm{C}$ to $30\,°\mathrm{C}$. The different imaginary temperature dependencies are represented by a linear and nonlinear (quadratic) functional relationship to the stiffness-altering parameter α_K. These relations are depicted in Fig. 6.6. It can be seen that the temperature rises from $-30\,°\mathrm{C}$ to $30\,°\mathrm{C}$ within a period of 12 h. After this time, it reduces to $-30\,°\mathrm{C}$ again.

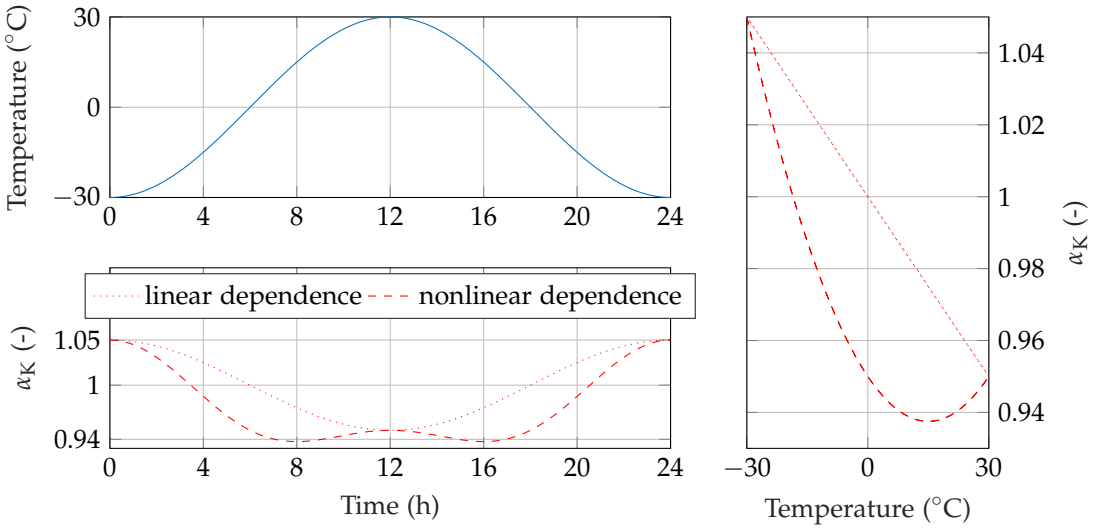

Figure 6.6: Temperature dependence of LPV system (expressed by stiffness-altering factor α_K) and temperature profile.

The corresponding factor α_K changes within 1.05 to 0.95 for the linear and approximately to 0.94 for the nonlinear case, respectively. For the studies made herein, the LPV system was simulated for 24 h under healthy and locally altered conditions at a sampling frequency of 800 Hz. For each state, the entire range of environmental variability was considered by passing the temperature to the Simulink model as well as a random excitation signal. The outputs are comprised of acceleration data that were computed through linear interpolation of the LPV system. Measurement noise was added featuring a variance of $R_v = 5e^{-6}\,(\mathrm{m/s^2})^2$. Stationary and nonstationary excitation was considered for the present investigations. The former is defined by a constant variance of $Q_1 = 0.5\,\mathrm{N}^2$ (cf. Eq. 5.26) for the entire simulation period of 24 h. The nonstationary excitation, on the other hand, is characterized by a changing intensity as depicted in Fig. 6.7. An exemplary plot of the simulated accelerations at the cantilever's tip for the cases of least and most intense excitation is presented in Fig. 6.8.

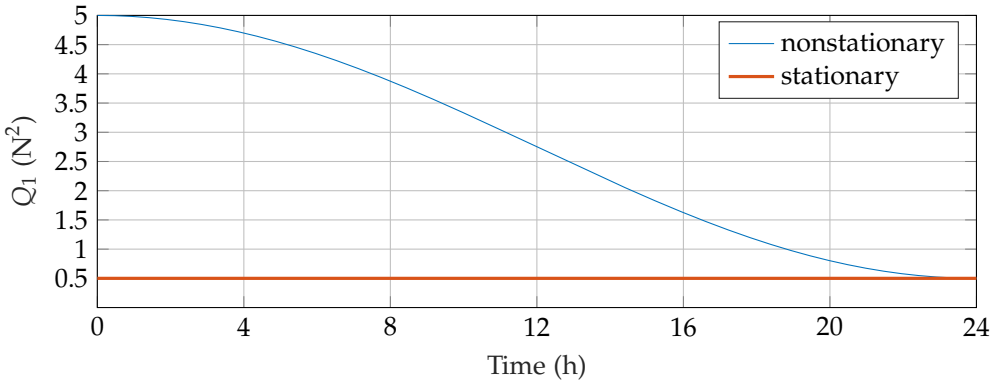

Figure 6.7: Nonstationary and stationary variance Q_1 of random excitation $w_{1,k}$, cf. Eqs. 5.25c and 5.26.

Finally, as the overall goal is to detect and localize damages under varying EOCs, changes to the system illustrated in Fig. 6.5 were introduced in the form of a reduced element stiffness

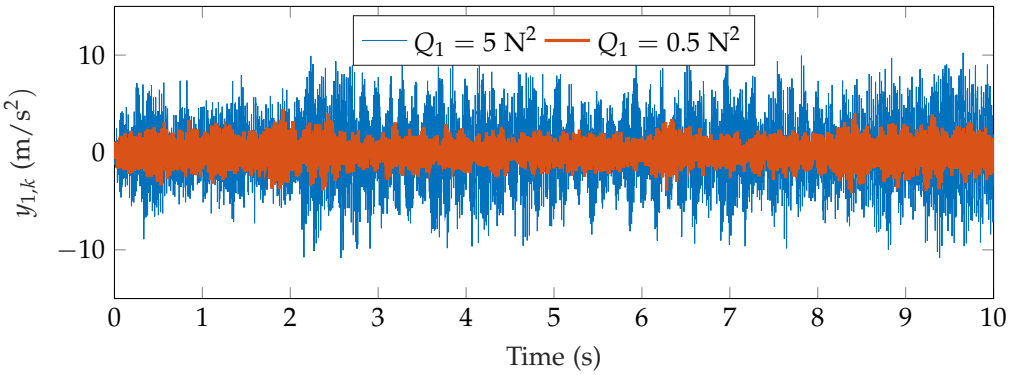

Figure 6.8: Exemplary time series of the output $y_{1,k}$ at cantilever tip (cf. Fig. 6.5) for excitation with minimal and maximal variance.

and an increased mass. More precisely, the stiffness of the third element was decreased by 5 %. The second damage state constitutes an increased mass of the same element by 2 %.

Separate analyses are presented in Section 6.5 to observe the effect of the simulated phenomena (linear/nonlinear temperature dependence, stationary/nonstationary excitation, local change of stiffness/mass) individually. The scopes of these studies are summarized in the following list:

- Section 6.5.1 presents the results of the damage analysis procedure described in Section 6.2 for the case of linear temperature dependence and stationary excitation. The results cover both damage scenarios.
- Section 6.5.2 is dedicated to the problem of nonlinear temperature dependence in combination with stationary excitation. Both damage scenarios are considered.
- Section 6.5.3 extends the previous problem by considering nonstationary excitation instead. Only the case of localized stiffness alteration is regarded for simplicity.
- Since interpolation techniques depend on the density of the sampling grid, a sensitivity study is performed in Section 6.5.4 There, results obtained in Sections 6.5.1 and 6.5.2 are reevaluated for different choices of $\Delta\theta$, cf. Fig. 6.4.

DAMAGE ANALYSIS PROCEDURE

The applied damage analysis strategy is based on subsequent processing and evaluation of small batches of simulated measurement data. To this end, the simulated data was divided into segments of 10 min resulting in a total of 144 data sets representing the system under healthy conditions and 144 data sets for the damaged state. Each unit of 144 data sets covers the entire range of temperature and excitation intensity variation depicted in Figs. 6.6 and 6.7, respectively, depending on the investigated problem. According to Section 4.4.3, the damage analysis procedure is divided into training, validation, and testing phase. Hence, the data set representing the healthy system is split in half so that the first 72 data sets comprise the training set, and the remaining 72 batches are associated with the validation set. The testing set is solely defined by the data representing the damaged model.

The estimator $\mathbf{\Pi}_1^{-1}$ depicted in Figs. 4.2 and 6.3 must be constructed as an LPV model to enable monitoring using the interpolation-based SP2E method. Therefore, in the present example, the system is gradually identified using the unweighted SSI-COV (see Tab. 2.1) and a model order of $n = 10$. The identified state-space parameters were labeled with the mean temperature of the corresponding data set and subsequently used to derive estimators $\boldsymbol{K}$ using quadratic estimation theory. To compare the different techniques presented in the aforementioned chapter, Kalman filters as well as Riccati-based and LMI-based $\mathcal{H}_\infty$ filters were constructed following the design guidelines summarized in Fig. 3.3. For the former, fully populated noise covariance matrices were estimated with the PALS method presented in Chapter 5. To this end, the CVX toolbox and SDPT3 were employed, and the number of lags n_l was set to 100. The method was initialized with $Q_0 = I$, $R_v = I \cdot \min \operatorname{diag}\{R_y(0)\}$, and $S_0 = 0$, and $G_w = I$ was defined. Note that this chapter does not aim to compare the PALS and ALS techniques. This topic was already covered by Sections 5.6 and 5.7. Besides, since this simulation study somewhat constitutes an ideal scenario for both noise covariance estimation techniques, similar results concerning the damage analysis could be expected. The LMI-based $\mathcal{H}_\infty$ filters were designed using YALMIP and SDPT3. Next, to define a grid of local reference estimators, the EOC space was divided in 12 segments with boundaries of -30, -25, ..., 25, and 30 °C by setting $\Delta\theta = \Delta T = 5\,\mathrm{K}$. The estimators associated with the training data that are closest to these 13 boundaries were defined as the local reference estimators considered for the identification of $\mathbf{\Pi}_1^{-1}$ according to Fig. 6.3.

For damage analysis, $\boldsymbol{G}_3 = \boldsymbol{G}_2$ was defined and $r_{d\mathcal{V}}([i_1, i_2])$, $i_1 = 1$ and $i_2 = 133$, was computed using the SP2E framework in combination with the proposed LPV identification scheme. During training, the models initially chosen for the grid of local LTI models were spared, which resulted in 59 executions of damage analysis. Each time, the mean temperature (θ_k) associated with the data set used to identify $\boldsymbol{G}_2$ and $\mathbf{\Pi}_2^{-1}$ was taken into account to determine the weightings $\kappa_i(\theta_k)$ to construct the LPV reference estimator $\mathbf{\Pi}_1^{-1}$ defined by Eqs. 6.2 and 6.3, cf. Fig. 6.3. Then, a CDF of $\sum_{i=1}^{q} r_{d\mathcal{V},i}([1, 133])$ was determined given a significance level $\alpha = 3\,\%$. Based on this statistical model, damage analysis in the validation and testing phase is conducted.

6.4 PRELIMINARY INVESTIGATIONS

Before presenting the actual results of the damage analyses, some preliminary investigations will be shown. Fig. 6.9 illustrates the fluctuation of the natural frequency with respect to the varying temperature. In the upper plot of Fig. 6.9, the mean temperature for each of the 144 data sets referring to the healthy and damaged structure are displayed. The lower plot contains the identified values for the third undamped natural frequency for both structural states. These quantities vary about 5 %, demanding the consideration of data normalization strategies. As for the damage scenarios, only the stiffness alteration is depicted in Fig. 6.9. However, the local change of mass resulted in a slightly more significant decrease in the natural frequency. This can be further regarded in Tab. 6.1, where the actual values for all five natural frequencies are given for all structural states at $-30\,°\mathrm{C}$. The maximum frequency deviation amounts to 1.2 % for the fifth mode of system with locally increased mass and 0.7 % for the same mode caused by the change of element stiffness. The MAC value was merely

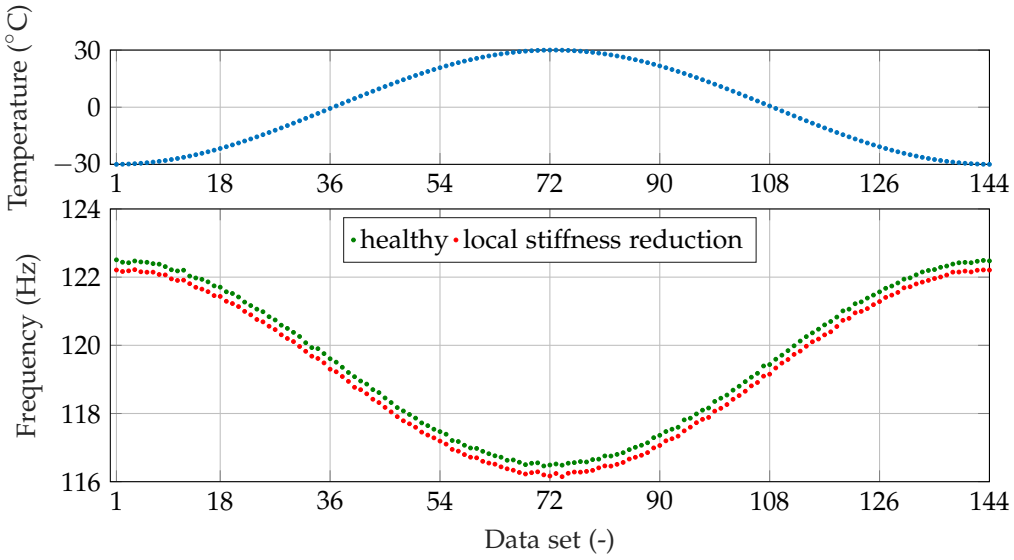

Figure 6.9: Temperature-dependent variation of third undamped natural frequency for the healthy and structurally altered system (local stiffness reduction).

affected and did not result in values below 0.997 with respect to the mode shapes of the healthy structure.

Table 6.1: Undamped natural frequency of simulated cantilever at −30 °C ($\alpha_K = 1.05$) under healthy and damaged conditions. Stiffness reduction highlighted by K, increase of mass emphasized by M.

Mode i	$f_{0,i}$ of healthy system	... damaged system (K)	... damaged system (M)
1	6.77 Hz	6.75 Hz	6.73 Hz
2	43.23 Hz	42.88 Hz	42.53 Hz
3	122.49 Hz	122.21 Hz	122.11 Hz
4	236.71 Hz	235.58 Hz	234.27 Hz
5	352.52 Hz	350.14 Hz	348.29 Hz

Further, special attention is paid to Assumption 4.1, where the suitability of linear quadratic estimators for damage identification is addressed. In this regard, the PSD of the estimation error (S_e) for an exemplary data set is examined, stemming from all three estimators introduced in Chapter 3. Fig. 6.10 depicts these quantities referring to the first channel. For orientation purposes, the PSDs of the simulated output (S_y) and its analytical pendant ($S_{y,\mathrm{SSI}}$) are given as well. It can be seen that the model realized using SSI-COV fits the simulated data flawlessly. The estimation error e features a comparatively small variance for all three estimators. However, the more important property is the correlation with the outputs, which could be quantified with the help of a whiteness test, cf. Section 5.5. This step is skipped for the sake of conciseness. Instead, the spectra depicted in Fig. 6.10 are assessed visually[1]: The Kalman filter and the Riccati-based $\mathcal{H}_\infty$ filter seem not correlated with the simulation data at all. Whereas

1 As mentioned earlier, in the experience of the author, this step is generally sufficient.

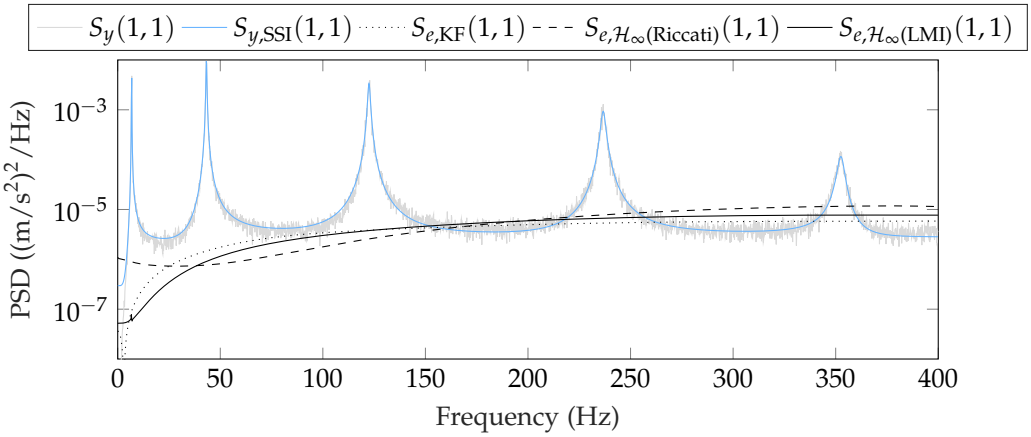

Figure 6.10: PSD of simulated measurement from LPV system (S_y), analytical PSD using identified system ($S_{y,\mathrm{SSI}}$), and PSD resulting from estimators (S_e).

the PSD of the estimation error stemming from the LMI-based $\mathcal{H}_\infty$ filter features a little spike in the area of the first resonance frequency, indicating some degree of correlation. The PSD of the estimation error stemming from the Kalman filter exhibits a small valley at a slightly lower frequency. As discussed in Section 5.7.1, this phenomenon is not problematic for the intended purpose. Following Assumption 4.1, it can be concluded that the Kalman and Riccati-based $\mathcal{H}_\infty$ filter is likely to be the most suitable for damage identification, as the estimation error is small and close to white. Due to a slight degree of correlation with the simulated data, the LMI-based $\mathcal{H}_\infty$ filter is expected to perform the worst.

EMPHASIZING THE NECESSITY OF DATA NORMALIZATION

As mentioned before, the change of dynamic properties illustrated and implied by Fig. 6.9 suggests the consideration of data normalization schemes. In the following sections, this issue shall be tackled through the LPV-based modeling of a structure under EOV. A damage analysis was performed by employing the SP2E framework and PALS-tuned Kalman filters to emphasize the necessity of strategies that account for the long-term variability of structural dynamics. Therefore, the predictor designed using the first data set of the healthy structure was defined as $\mathbf{\Pi}_1^{-1}$. Training, validation, and testing were conducted as described before but without applying any interpolation of local LTI models. The corresponding results are depicted in Fig. 6.11. Therein, the value of the damage feature $\sum_i^q r_{dv,i}([1,133])$ is plotted for all simulated data sets. It can be seen that, without a surprise, the damage indicator varies tremendously throughout the training phase, resulting in a particularly high threshold value. The corresponding statistical model is confirmed in the validation phase. However, only 23 % of the data sets representing the damage system (stiffness reduction of the third element) are identified as such. Moreover, damage localization was mostly unsuccessful in these instances, as spikes appeared predominately for channel 5 instead of channels 3 and 4. In the following sections, it will be shown that the consideration of the proposed LPV-based data normalization strategy leads to a significant improvement in damage detection and localization performance.

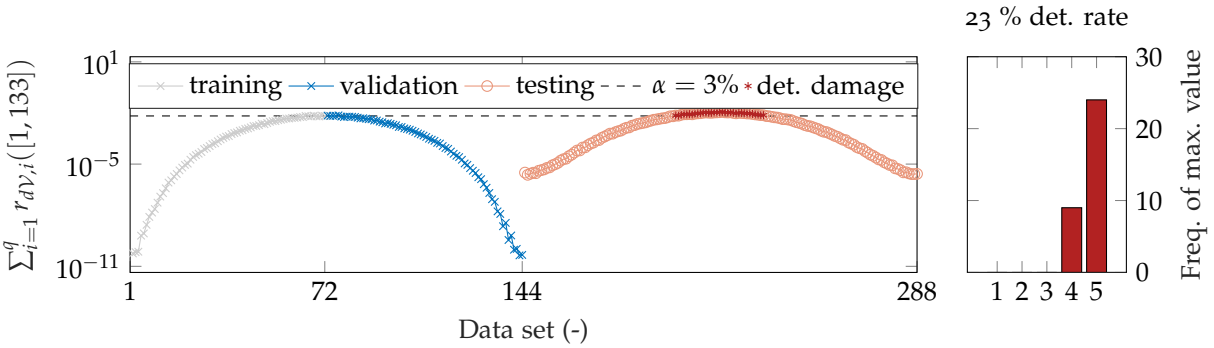

Figure 6.11: Damage localization of 5 % stiffness reduction of third element via SP2E using tuned Kalman filters and no normalization scheme. Linear temperature dependence and stationary excitation. $\sum_{i=1}^{q} r_{dV,i}$ in $\mathrm{m}^2/\mathrm{s}^4$.

6.5 RESULTS OF INTERPOLATION-BASED DAMAGE IDENTIFICATION BY SP2E

The damage identification performance is investigated using different quadratic estimators in the following sections. This section starts with the case of linear dependence of the structural dynamics on the temperature under stationary excitation. In the following Sections, the problem is extended successively to more complicated scenarios.

6.5.1 Linear effect of exogenous conditions

At first, the case of a linear relation between dynamic behavior and environmental conditions is examined. Therefore, simulations were conducted following the descriptions made in Section 6.3 under stationary excitation. Damage analysis with intrinsic data normalization was performed by applying the LPV-based SP2E method according to Section 6.2. In Fig. 6.12, the results for damage detection and localization are plotted involving PALS-tuned Kalman filters as well as Riccati-based and LMI-based $\mathcal{H}_\infty$ filters. This figure is dedicated to the case of the reduced element stiffness of the third element, whereas Fig. 6.13 contains the results for the locally increased mass.

In both cases, data normalization is successful, which manifests itself in a rather constant progression of the depicted damage-sensitive feature, cf. Fig. 6.11. This pertains to all estimators. Regarding the damage identification, the Kalman and Riccati-based $\mathcal{H}_\infty$ filters help to detect damages for all test data sets leading to a detection rate of 100 %. Comparing the threshold value for detection (dashed line) with the values of the damage indicator in the case of damage suggests that the sensitivity towards damage of the Kalman and Riccati-based $\mathcal{H}_\infty$ filters are similar. This statement cannot be repeated for the LMI-based $\mathcal{H}_\infty$ filters, where the damage is only detected in 7 % of the test data sets for the case of the reduced element stiffness and 40 % in the case of the locally changed mass. Apparently, the design of the LMI-based $\mathcal{H}_\infty$ filters via optimization fails to realize estimators with similar properties, which leads to outliers that result in a rather great variance of the damage indicators compared to the other estimators. Nevertheless, damage localization was successful whenever damage was detected. This applies to all estimators.

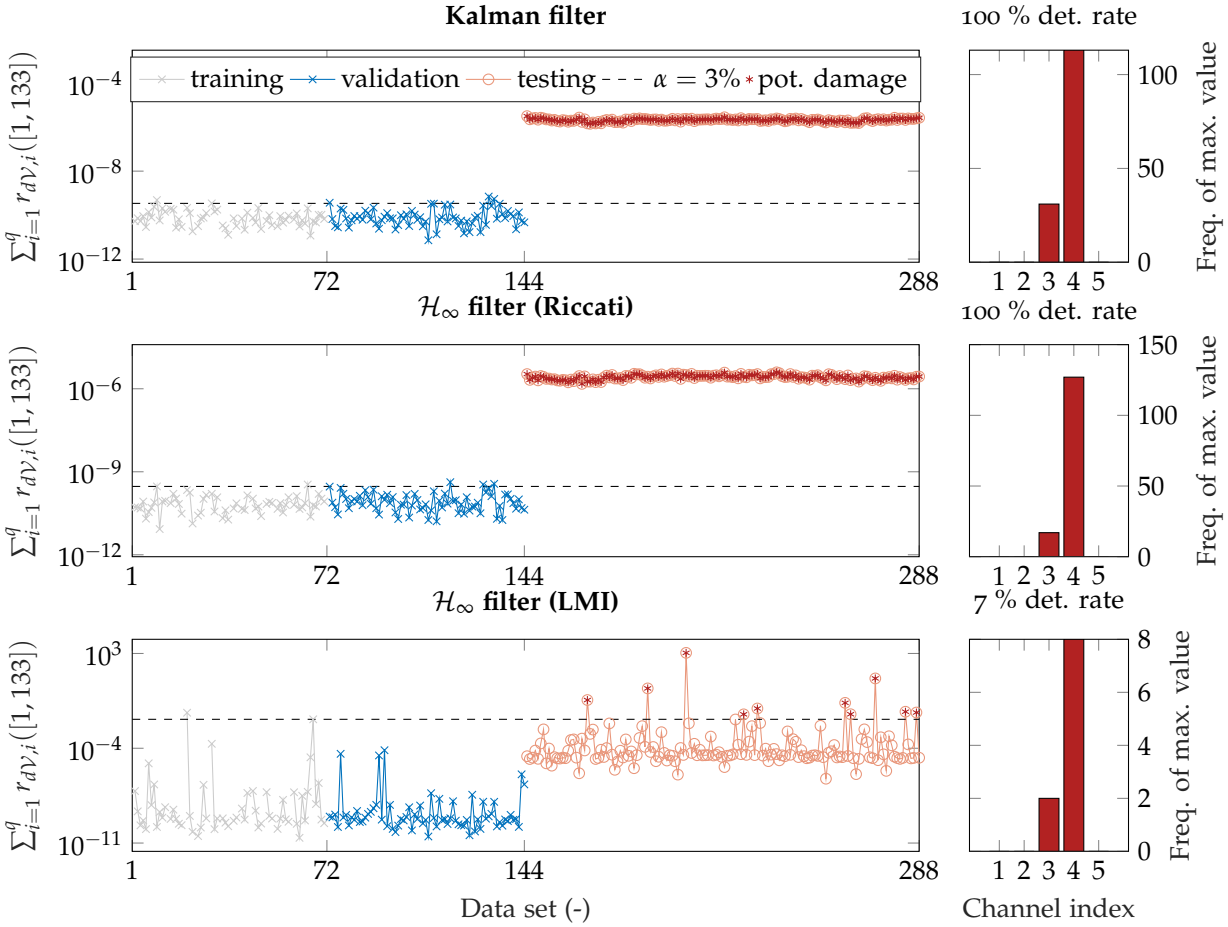

Figure 6.12: Damage localization of 5 % stiffness reduction of third element via SP2E using different types of interpolated estimators ($\Delta T = 5\,\mathrm{K}$). Linear temperature dependence and stationary excitation. $\sum_{i=1}^{q} r_{d\mathcal{V},i}$ in $\mathrm{m}^2/\mathrm{s}^4$.

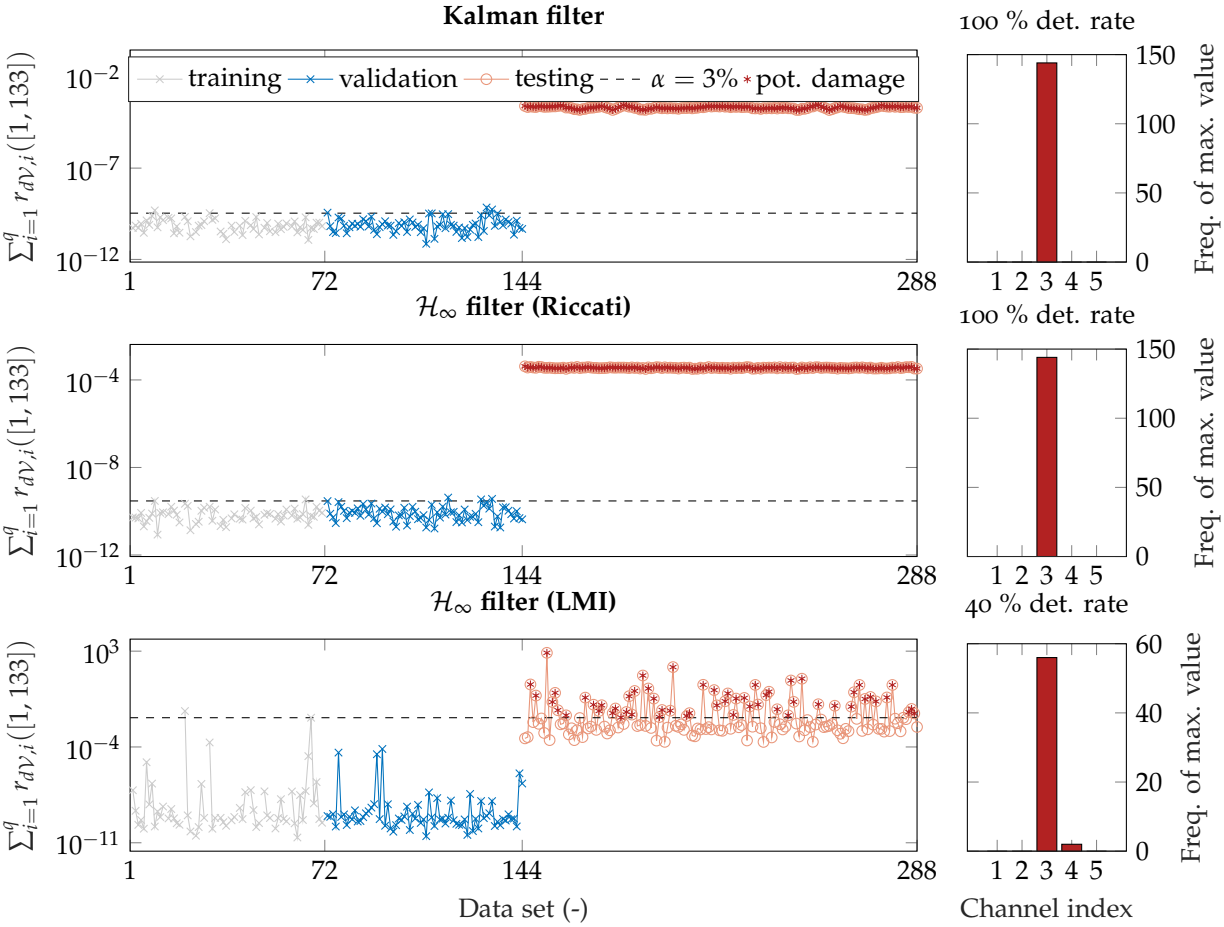

Figure 6.13: Damage localization of 2 % mass reduction of third element via SP2E using different types of interpolated estimators ($\Delta T = 5\,\mathrm{K}$). Linear temperature dependence and stationary excitation. $\sum_{i=1}^{q} r_{dv,i}$ in $\mathrm{m}^2/\mathrm{s}^4$.

6.5.2 Nonlinear effect of exogenous conditions

The same analyses as in the previous section were performed for the simulated nonlinear relationship between global dynamic behavior and temperature. Clearly, this scenario is more challenging when it comes to data normalization, but it is also more realistic since such phenomena can be frequently observed, see, e.g., [154, 155]. The results for each damage case (local stiffness and mass alteration) are given in Figs. 6.14 and 6.15

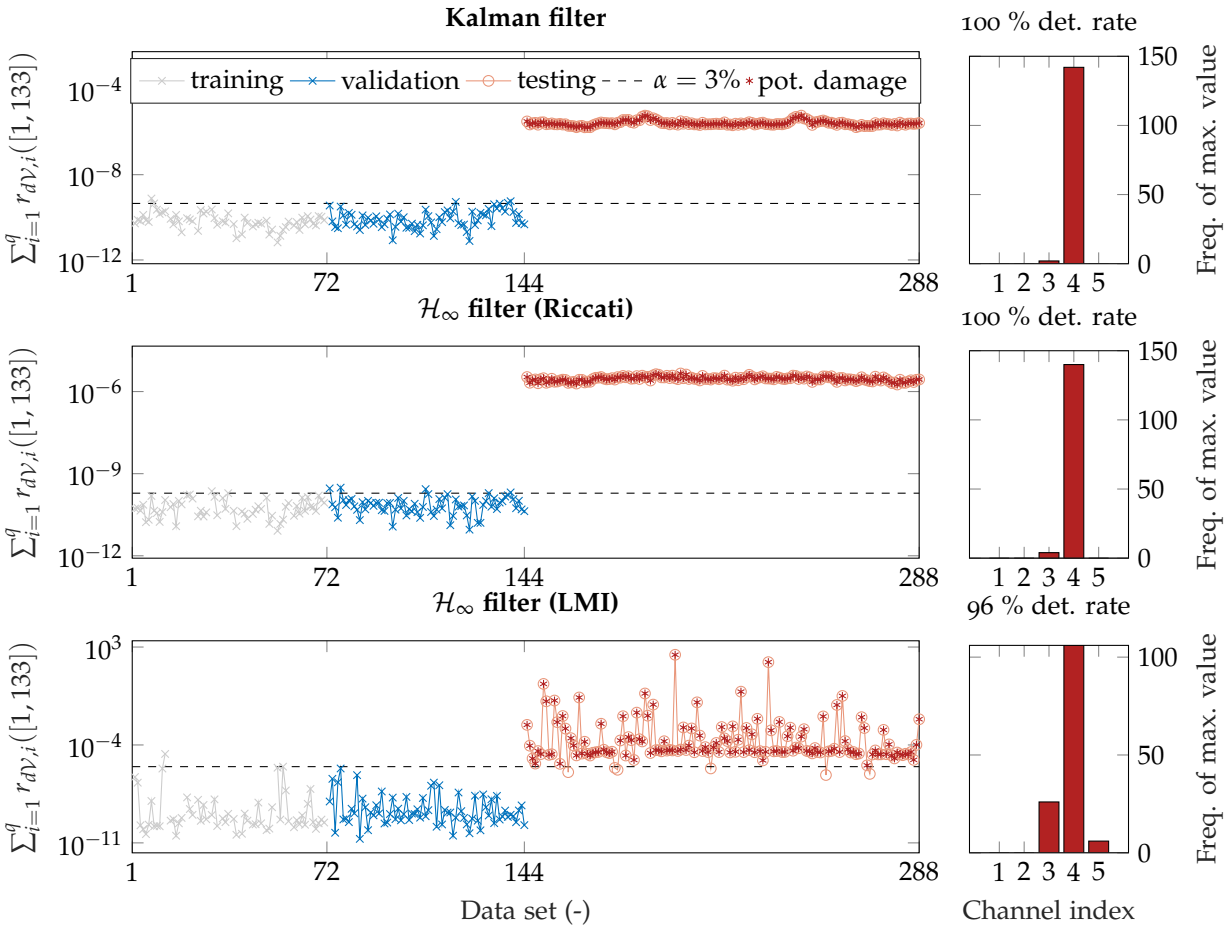

Figure 6.14: Damage localization of 5 % stiffness reduction of third element via SP2E using different types of interpolated estimators ($\Delta T = 5\,\mathrm{K}$). Nonlinear temperature dependence and stationary excitation. $\sum_{i=1}^{q} r_{dV,i}$ in $\mathrm{m}^2/\mathrm{s}^4$.

Regarding the Kalman and Riccati-based $\mathcal{H}_\infty$ filters, nearly no difference can be observed compared to the previous investigation regarding the linear dependency. Solely the results for damage localization vary, as the maximum value of $r_{dV,i}$ appears more frequently for channel 4 in the case of the reduced element stiffness. However, this is not an issue, as maximum values at the third and the fourth entry are legitimate for proper damage localization. The damage identification results received using LMI-based $\mathcal{H}_\infty$ filters differ significantly compared to the previous investigations. Most interestingly, the detection rate increased drastically from 7 to 96 % in the case of reduced stiffness and from 40 to 100 % in the second damage scenario (mass alteration). In both cases, damage localization is almost always successful. A reason for that

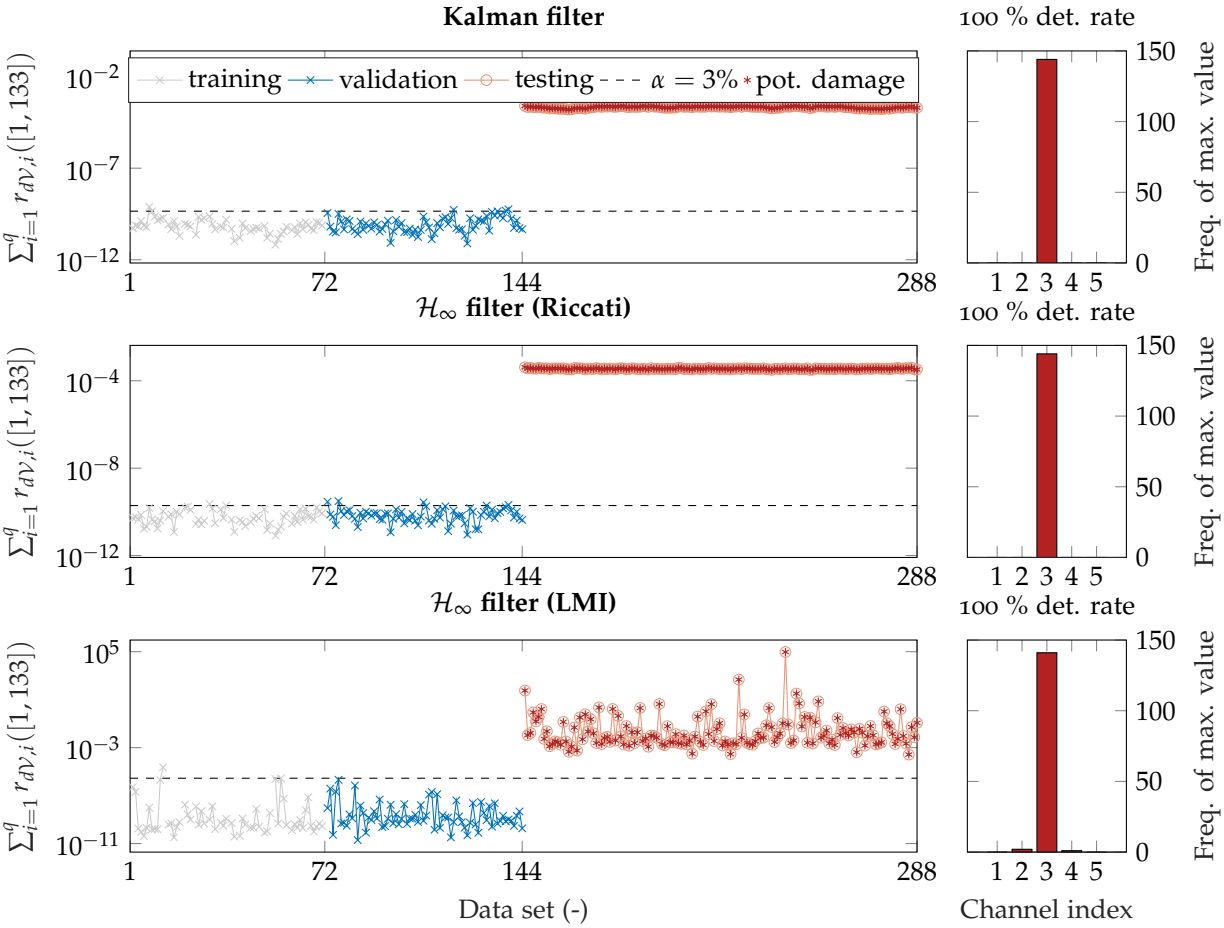

Figure 6.15: Damage localization of 2 % mass reduction of third element via SP2E using different types of interpolated estimators ($\Delta T = 5\,\mathrm{K}$). Nonlinear temperature dependence and stationary excitation. $\sum_{i=1}^{q} r_{dV,i}$ in $\mathrm{m}^2/\mathrm{s}^4$.

is difficult to find. Nevertheless, it can be recognized that the threshold value decreased when the nonlinear dependence was realized. Still, regarding the significance of damage detection, Kalman and Riccati-based $\mathcal{H}_\infty$ filters outperform the LMI-based $\mathcal{H}_\infty$ filters significantly. This circumstance emphasizes the different sensitivity to damage.

6.5.3 Considering nonstationary excitation

Data normalization does not only play a role when it comes to varying EOCs. Also, changing excitation intensities might significantly affect the outcome of damage identification. Hence, it is advisable to account for different levels of excitation by conducting some data normalization in this regard, see, e.g., [61]. To investigate the necessity of such procedures, the analysis presented in the previous section, corresponding to Fig. 6.14, was repeated for the case of nonstationary excitation. Therefore, the variance of the inputs was simulated according to Fig. 6.7. Fig. 6.16 depicts the corresponding damage identification results. Therein, it can be seen that the magnitude of the damage indicator reduces with decreasing intensity of excitation. Thus, the threshold for damage detection rises as the variance of the damage-sensitive

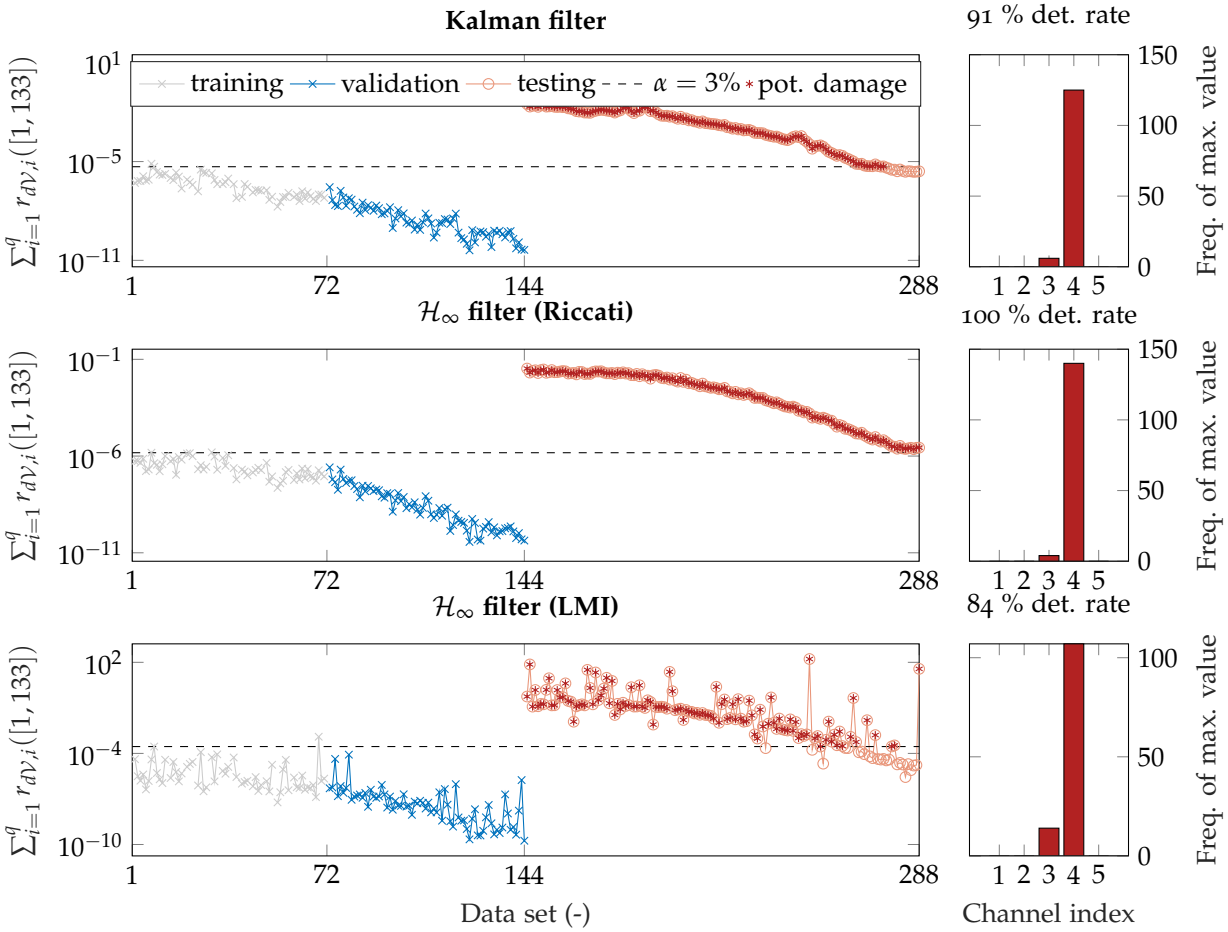

Figure 6.16: Damage localization of 5 % stiffness reduction of third element via SP2E using different types of interpolated estimators ($\Delta T = 5\,\mathrm{K}$). Nonlinear temperature dependence and nonstationary excitation. $\sum_{i=1}^{q} r_{d\mathcal{V},i}$ in $\mathrm{m}^2/\mathrm{s}^4$.

feature increases. As a consequence, a reduced sensitivity towards localized damage can be observed in Fig. 6.16, which, in the case of the applied Kalman filters (and LMI-based $\mathcal{H}_\infty$ filters), resulted in a reduction of the detection rate by 9 %. Though, the precision with respect to damage localization was not affected. In total, these results suggest a further normalization of the data considered for damage identification concerning the excitation intensity.

A classic approach for this is to divide each channel of measured or simulated outputs by its standard deviation so that the variance becomes unity, cf. [70]. By that, different levels of excitation are taken into account inherently. In the context of system identification via SSI-COV, a convenient way to realize the aforementioned data normalization constitutes the computation of Hankel matrix weightings [82]

$$\overline{W}_1 = I_l \otimes R_y(0)^{1/2}, \quad \overline{W}_2 = I_m \otimes R_y(0)^{1/2} \tag{6.10}$$

so that Eq. 2.85 becomes to $W_1 \overline{W}_1 H \overline{W}_2 W_2$. In Eq. 6.10, l and m denote the number of block rows and columns, respectively, and $(\cdot)^{1/2}$ represents the matrix square root.

From the author's experience, such a normalization strategy is problematic in the context of parametric system identification, as information regarding the internal transfer behavior gets lost. Hence, an alternative approach is proposed. Regarding Fig. 4.2 highlights that both the reference system $\mathbf{\Pi}_1^{-1}$ as well as $\mathbf{\Pi}_2^{-1}$ are fed with the same input – namely y_3. Therefore, dividing the resulting estimation errors e_1 and e_2 by the summed power of y_3 should remove the effect of varying magnitudes of excitation. Based on this analysis, the amplitude-normalized damage indicator can be formally defined as

$$\bar{r}_{d\mathcal{V}} = r_{d\mathcal{V}} \frac{1}{\mathrm{tr}\{R_{y_3}(0)\}}. \tag{6.11}$$

This normalization was considered for the data belonging to Fig. 6.16 leading to results depicted in Fig. 6.17. Clearly, the normalization according to Eq. 6.11 led to an improvement

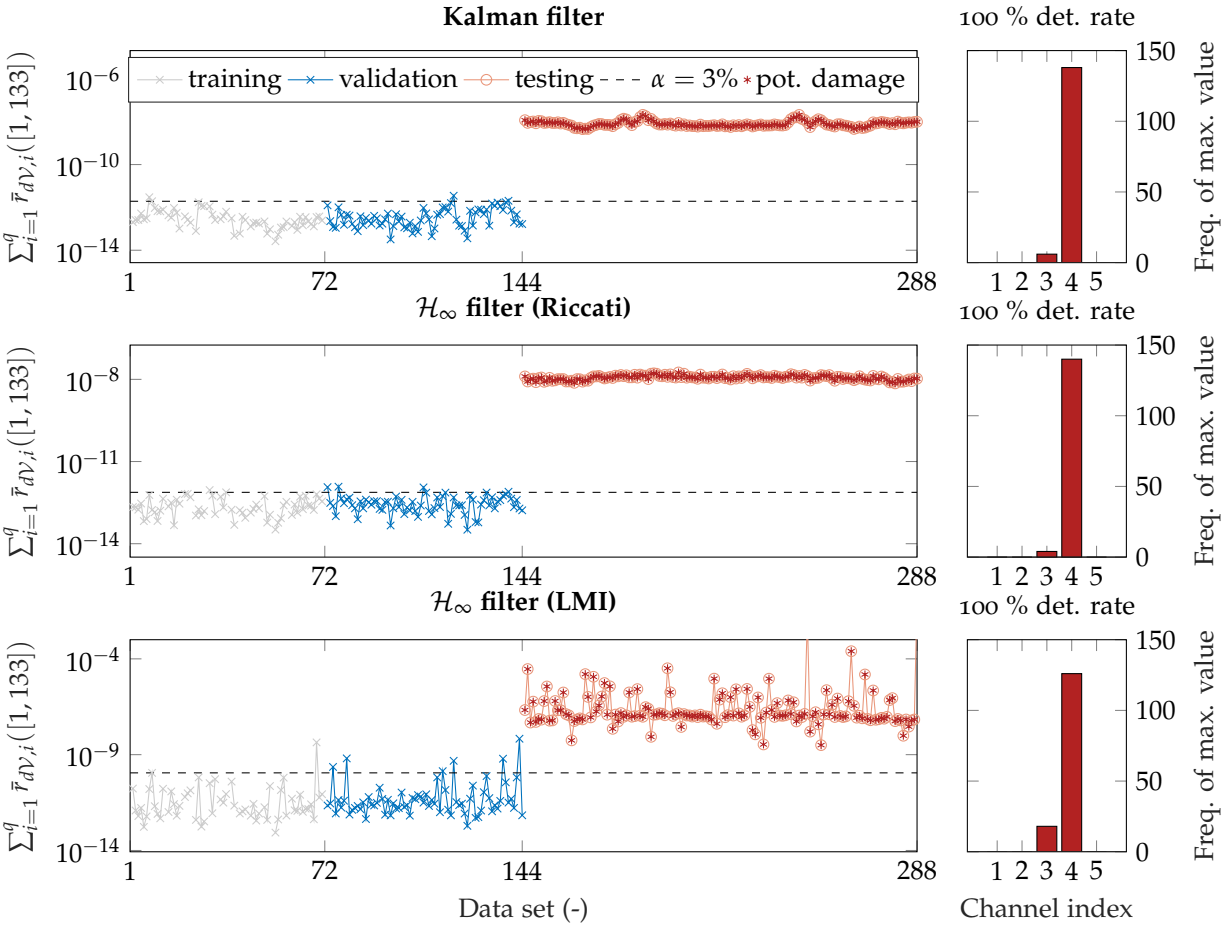

Figure 6.17: Damage localization of 5 % stiffness reduction of third element via SP2E using different types of interpolated estimators ($\Delta T = 5\,\mathrm{K}$). Nonlinear temperature dependence and nonstationary excitation, normalized. $\sum_{i=1}^{q} \bar{r}_{d\mathcal{V},i}$ in $\mathrm{m}^2/\mathrm{s}^4$.

in the damage detection performance, as no trends caused by varying levels of excitation are visible. Further, the sensitivity towards damage was increased to the maximum, which is now similar to the corresponding case under stationary excitation, cf. Fig. 6.19. The ability to localize damage did not suffer from the excitation normalization since the damage indicator's

values associated with each channel were scaled equally. This is not the case when Eq. 6.10 is considered.

6.5.4 Influence of the sampling point density

Naturally, the interpolation methods applied here depend on the chosen distance between sampling points. For the previous investigations, the grid of local reference systems was defined with $\Delta\theta = \Delta T = 5\,\mathrm{K}$. This setting led to satisfactory results. However, it is to be expected that a coarser grid worsens the data normalization performance – especially in the case of nonlinear temperature dependence, resulting in a reduced sensitivity towards damage under the presence of EOV. On the other hand, a more refined grid might improve that.

To test this property in the context of the applied methods, additional simulations were performed for both cases of linear and nonlinear dependence on temperature. At first, results calculated for a finer grid by choosing $\Delta T = 3\,\mathrm{K}$ are examined. Figs. 6.18 and 6.19 show these for the linear and nonlinear temperature dependence, respectively. Comparing Figs. 6.18

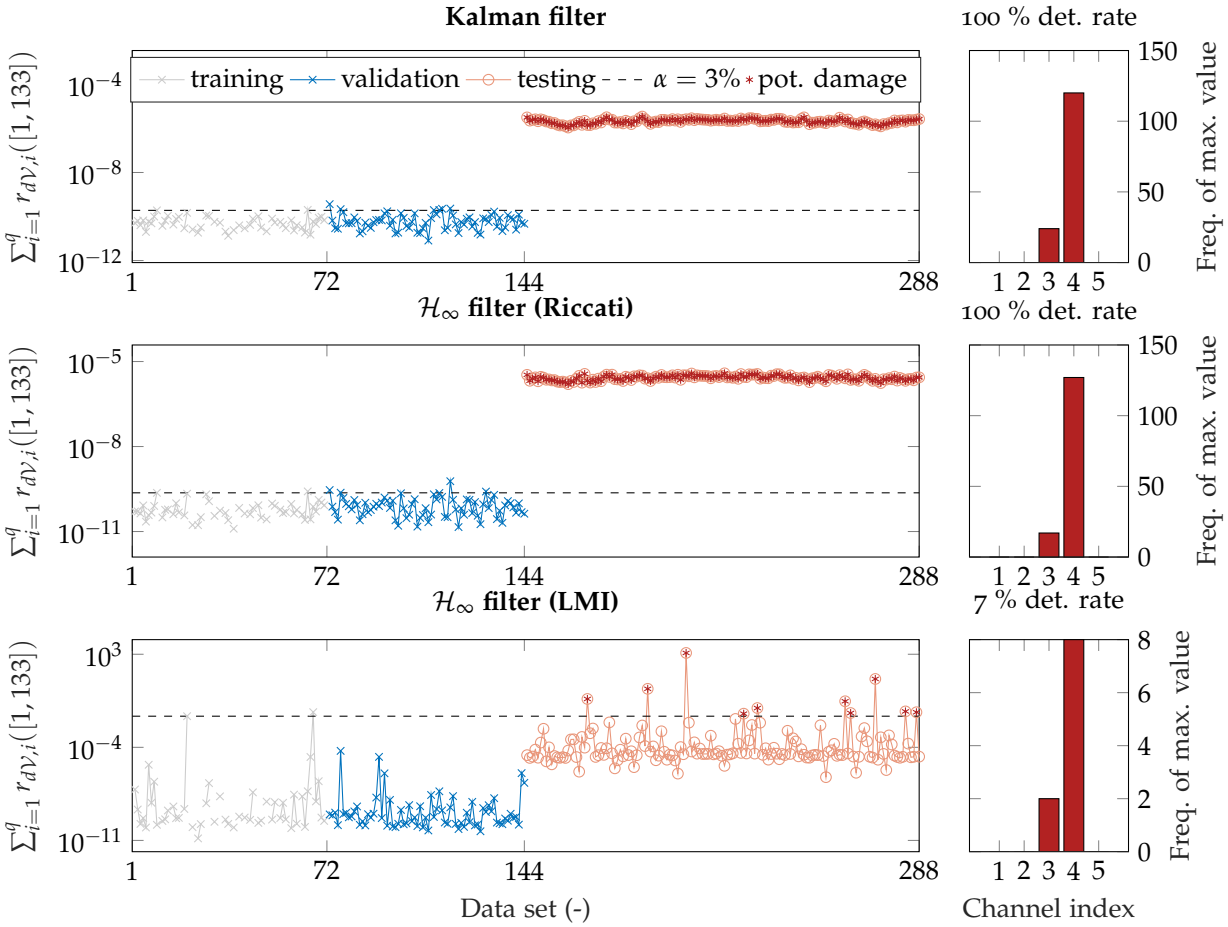

Figure 6.18: Damage localization of 5 % stiffness reduction of third element via SP2E using different types of interpolated estimators ($\Delta T = 3\,\mathrm{K}$). Linear temperature dependence and stationary excitation. $\sum_{i=1}^{q} r_{d\mathcal{V},i}$ in $\mathrm{m}^2/\mathrm{s}^4$.

and 6.12 reveals no significant improvement for the increase of the sampling point density.

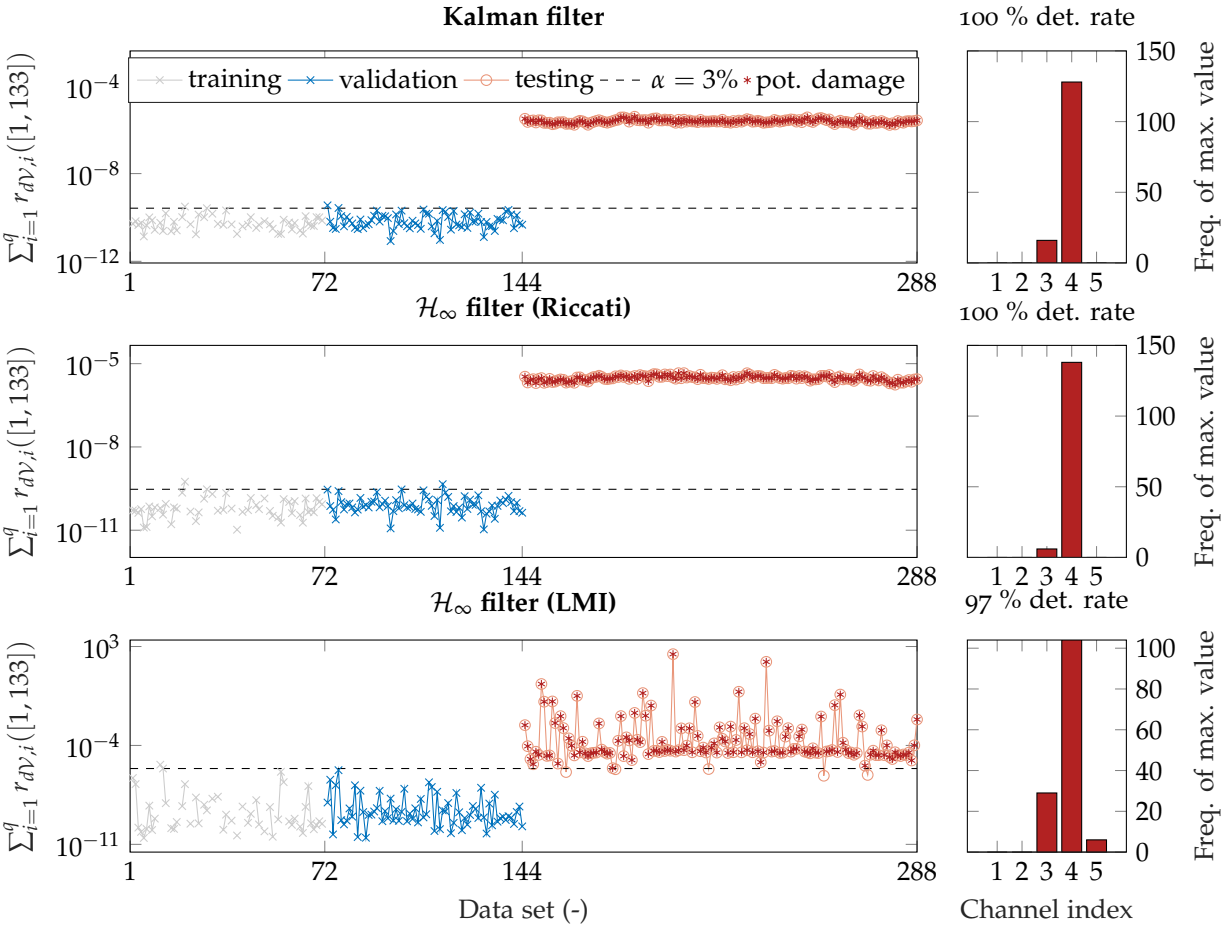

Figure 6.19: Damage localization of 5 % stiffness reduction of third element via SP2E using different types of interpolated estimators ($\Delta T = 3\,\mathrm{K}$). Nonlinear temperature dependence and stationary excitation. $\sum_{i=1}^{q} r_{dV,i}$ in $\mathrm{m}^2/\mathrm{s}^4$.

Though it must be mentioned that this comes to no surprise, as the simulated system features linear dynamics, and the temperature dependence and interpolation are linear as well. Even in the case of the nonlinear dependence on the temperature, no relevant improvement can be realized for either of the applied estimators, cf. Fig. 6.14. However, the detection rate of the LMI-based $\mathcal{H}_\infty$ filters increased by 1 %. It can be concluded that the sampling grid distance of $\Delta T = 5\,\mathrm{K}$ was a reasonable choice for this example. It should be remarked that an excessive increase of grid density is not recommendable, as the corresponding LTI models should be excluded from the computation of the damage indicator during training, which might result in an erroneously low threshold value for damage detection.

An even more interesting investigation is realized by drastically increasing the sampling grid distance for interpolation. To this end, ΔT was increased to 30 K. Again, Figs. 6.20 and 6.21 show the results for the linear and nonlinear dependence, respectively. Even though the grid distance was increased by a factor of six, resulting in a grid of three local LTI models only, the damage detection performance for the case of linear dependence on temperature is shown in Fig. 6.20 is still good. Indeed, temperature fluctuation appears within the training and validation phase values. However, the threshold value is still fairly small, which leads to a

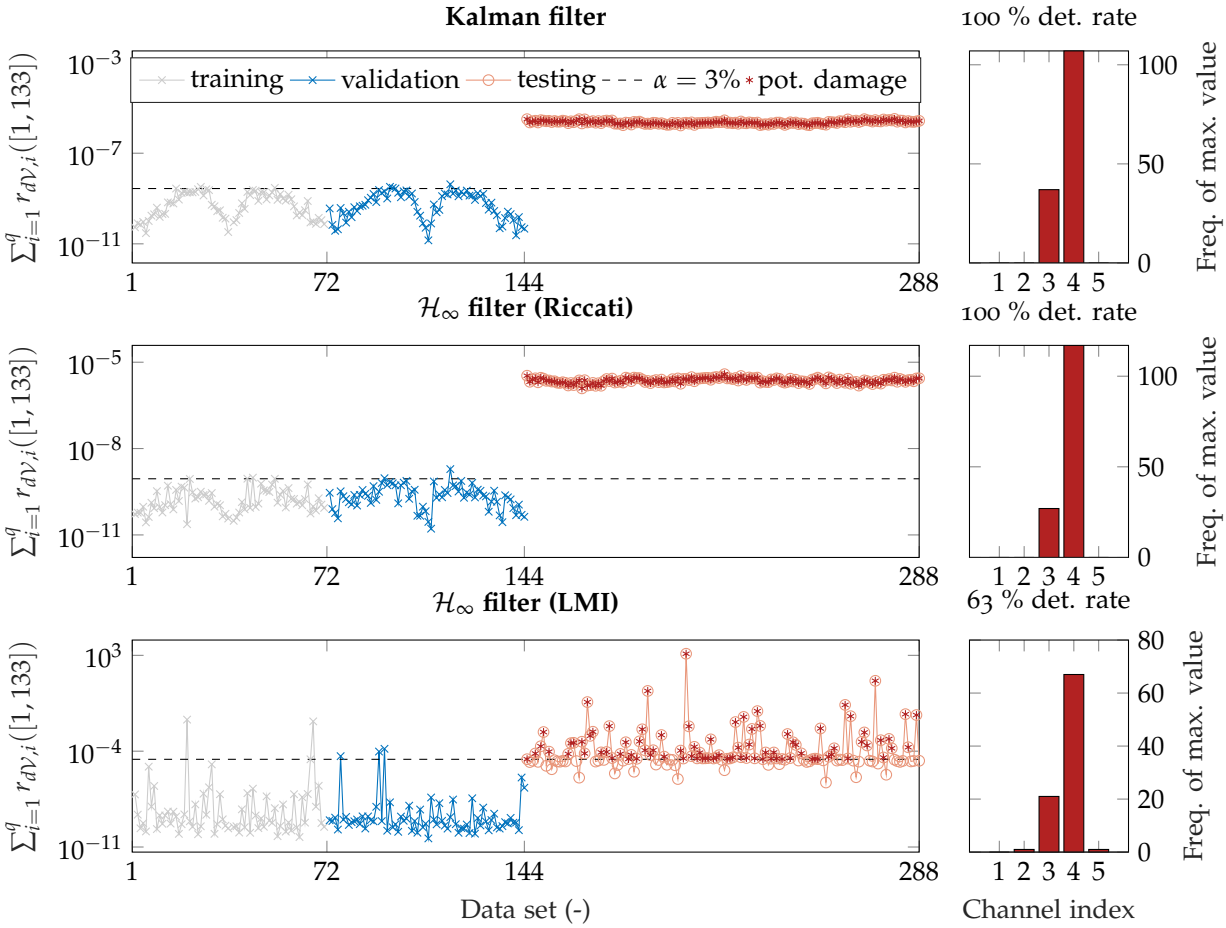

Figure 6.20: Damage localization of 5 % stiffness reduction of third element via SP2E using different types of interpolated estimators ($\Delta T = 30\,\mathrm{K}$). Linear temperature dependence and stationary excitation. $\sum_{i=1}^{q} r_{dV,i}$ in $\mathrm{m}^2/\mathrm{s}^4$.

good sensitivity towards damage. Interestingly, the damage detection rate for the LMI-based $\mathcal{H}_\infty$ filters increased in the regarded case. That gives rise to the suspicion that rather a global change in the dynamics has been detected. In this case, the estimators possibly pick up local differences since the damage position is always pointed out correctly.

Fig. 6.21 contains the damage identification results for the case of the nonlinear temperature dependence and $\Delta T = 30\,\mathrm{K}$. As expected, the choice of the sampling grid distance affects the outcome more clearly. Indeed, both the tuned Kalman filters and Riccati-based $\mathcal{H}_\infty$ filters succeed in detecting and localizing the introduced damage. However, the sensitivity towards damage decreased tremendously compared to Fig. 6.14. In the case of the LMI-based $\mathcal{H}_\infty$ filters, this led to 69 % less correct detections.

Given these observations, it can be concluded that if the dependence on the relevant EOCs is linear, the effect of the user-defined sampling grid distance $\Delta\theta$ is minor. However, in the nonlinear case, a rather dense grid of local LTI models should be defined if feasible to enable a proper data normalization and increase the sensitivity towards damage.

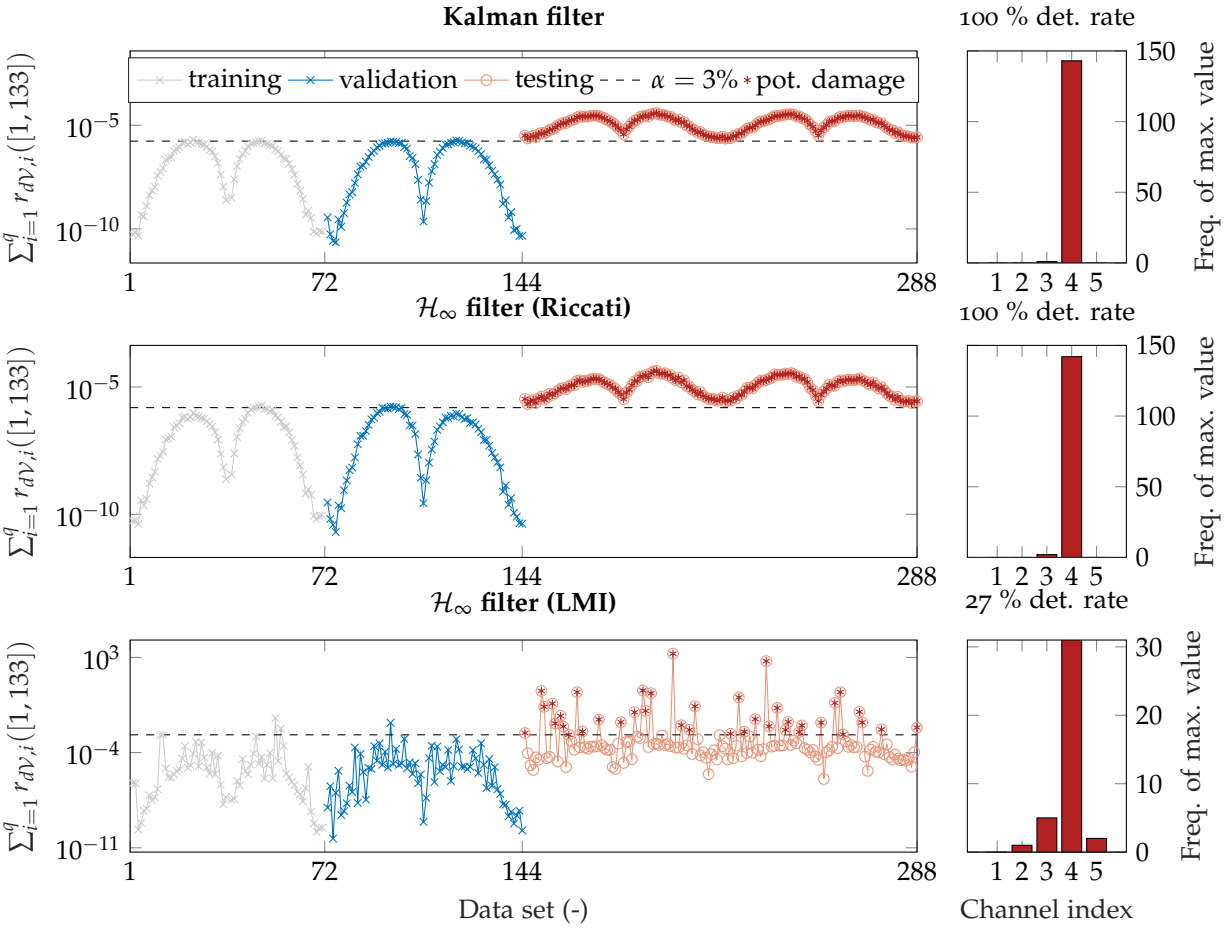

Figure 6.21: Damage localization of 5 % stiffness reduction of third element via SP2E using different types of interpolated estimators ($\Delta T = 30\,\mathrm{K}$). Nonlinear temperature dependence and stationary excitation. $\sum_{i=1}^{q} r_{dV,i}$ in $\mathrm{m}^2/\mathrm{s}^4$.

6.6 CONCLUDING REMARKS

In the present chapter, an explicit data normalization technique was introduced that enables damage identification by SP2E under EOV. Therefore, the reference estimator $\mathbf{\Pi}_1^{-1}$, which typically refers to a single operating point only, is replaced by an LPV model representing the entire range of EOCs experienced during training. The output of this LPV system is based on an interpolation scheme involving a grid of local LTI models referring to different operating points. The presented strategy for interpolation is applicable in an m-dimensional EOC space.

To demonstrate the efficacy of the proposed method, a variety of simulation studies were investigated. To this end, a simple cantilever model featuring linear and nonlinear temperature dependence was modeled as an LPV system under varying temperatures and healthy as well as damaged conditions using Simulink. The LPV-based SP2E method was employed using PALS-tuned Kalman as well as Riccati-based and LMI-based $\mathcal{H}_\infty$ filters. The investigations showed that the presented method can intrinsically remove the effect of the exogenous scheduling effect while facilitating the detection and localization of small damages simultane-

ously. In this regard, the Kalman and Riccati-based $\mathcal{H}_\infty$ filters outperformed the LMI-based $\mathcal{H}_\infty$ filters. The latter showed a reduced sensitivity towards damage so that not all instances of damage could be detected as such. A variance-based normalization approach was considered to reduce the disturbing effects of varying excitation intensities, resulting in the successful detection and localization of damage under nonstationary excitation.

The investigations were completed by a sensitivity study regarding the sampling grid distance for the interpolation. It was observed that a dense grid of local LTI models is likely to improve damage detection and localization when the monitored structure manifests a nonlinear dependence on EOCs. However, in a completely linear problem, the grid density has a minor influence on the normalization performance.

7

MONITORING A TEST STRUCTURE FOR SHM

This chapter combines the central contributions presented in Chapters 4 to 6 and provides a real-life validation of the corresponding approaches and techniques. The Leibniz University Test Structure for Monitoring (LUMO) gives the validation object, which comprises a steel lattice mast located outside near Hanover, Germany, and which was originally planned, designed, and constructed by the author and his colleagues. It is densely equipped with accelerometers that help to continuously acquire vibration data applicable for SHM. Reversible damage mechanisms distributed along the structure can be activated to realize changes in stiffness and mass to varying extents. This chapter considers six damages introduced on three different positions that shall be studied after describing the test structure. Parts of this chapter are based on a submitted article [211].

7.1 STRUCTURE DESCRIPTION

LUMO is situated on a meadow next to an agricultural field, 20 km south of Hanover (Lower Saxony, Germany). It constitutes a steel lattice mast mounted on a concrete block foundation linked to a data acquisition system. The mast features reversible damage mechanisms installed on six levels. The block foundation was built in October 2019, the tower was erected in June 2020, and the continuous measurements started in August 2020. In the following, a characterization is given of the test structure, the environmental conditions, and the corresponding open-access data set. For further information, see [211].

7.1.1 General description

The lattice mast is made of galvanized and painted structural steel. It consists of three identical segments with a length of 3 m each, resulting in a total height of 9 m. The overall weight without sensors is approximately 90 kg. Each segment has three tubular legs forming a cross-section similar to an isosceles triangle and consists of seven bracing levels and short connecting sections at the ends. The sections end in an elliptical flange which allows the connection of the segments in arbitrary order employing regular M10 steel bolts. Figure 7.1 contains a photograph of the lattice mast.

The test structure is mounted on a concrete block foundation with the dimensions 1.5 m × 1.5 m × 0.8 m, which is embedded in cohesive soil. Therefore, an anchor plate with eight head bolts attached to it was integrated during the manufacturing of the foundation. To safely erect and modify the mast, the anchor plate was designed as a hinge consisting of two metal plates with a thickness of 30 mm each. The latter is kept shut by 12 M12 bolts during monitoring measurements to provide a rigid mast fixture. A photograph of the foundation and connector plate is given in Figure 7.2.

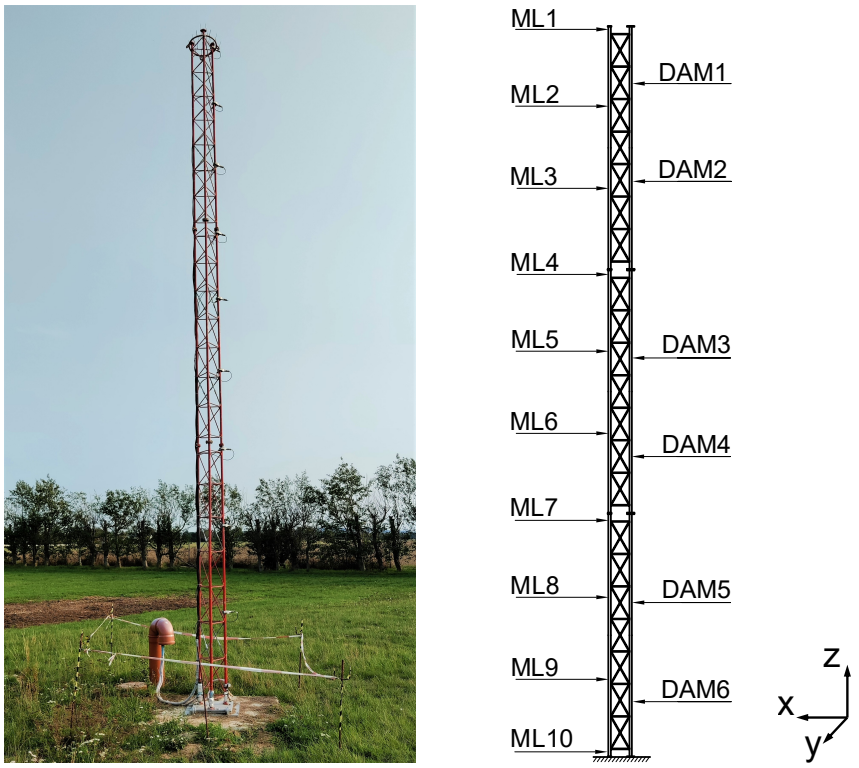

Figure 7.1: Photograph of the test structure (left), and schematic drawing including the measurement levels (ML) and the damage locations (DAM) (right) [211].

7.1.2 Reversible damage features and environmental conditions

The key features of the test structure are local reversible damage mechanisms that can be used to introduce stiffness and, if desired, mass alterations. For this purpose, on six levels of the structure, which are depicted in Figure 7.1, these mechanisms enable the disconnection of individual bracings. At each damage level, all three bracings were equipped with damage mechanisms, resulting in 18 potential positions for introducing localized stiffness and mass alterations. The damage mechanisms, which are depicted in Fig. 7.3, consist of an M10 threaded rod with a coupling nut on each end – one with a left-hand and one with a right-hand thread. Two simple M10 nuts between the coupling nuts can be used to lock the damage mechanism when set in place. Another photograph of the installed damage mechanisms at damage level 6 is given in Figure 7.2. Damage of LUMO can be realized by loosening the coupling nuts so that the corresponding bracing is severed (stiffness reduction) or by removing the entire damage mechanism. The last-mentioned damage scenario also results in a reduction of mass of approximately 155 g per damage mechanism. The damage cases considered herein generally imply the complete removal of damage mechanisms.

As LUMO is located outside, the primary excitation source constitutes aerodynamic forces exerted by the wind, which mainly blows from west to south. Further, variations of the structural dynamic behavior are mainly caused by daily and seasonal temperature cycles. During visual inspections, it was also recognized that birds occasionally seek the mast as a place to rest.

Figure 7.2: Photograph of the foundation and anchor plate (left), and photograph of the first bay and damage mechanisms in place (right).

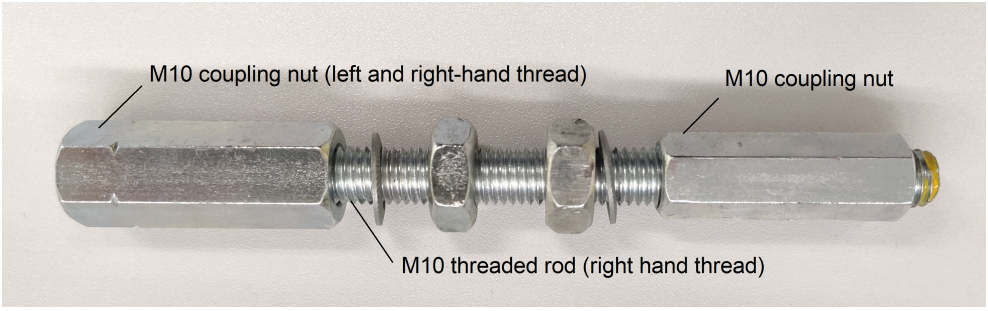

Figure 7.3: Photograph of removable damage mechanism.

7.1.3 Sensor equipment and data acquisition

The structure is equipped with 18 uniaxial accelerometers, three strain sensors, and one material temperature sensor. They are distributed across ten horizontal measurement levels, which are schematically displayed in Figure 7.1. Note that accelerometers are positioned at ML1-9, whereas ML10 is only used for the measurements of strains and temperature, cf [211]. The strain measurements are not considered in this work, and therefore, are not assessed any further. MEAS 8811LF-01-005 piezoelectric accelerometers with IEPE current supply are mounted in pairs using 90° mounting brackets to measure in orthogonal directions in the horizontal plane and to capture the spatial motion. There are no acceleration sensors in the vertical direction (z-axis) because of their low relevance for beam-like structures and the primary focus on bending deformation. One Pt100-type thermocouple is mounted at ML10 and provides the reference material temperature.

The data acquisition system consists of a National Instruments NI-cDAQ-9189 chassis connected to a host computer, both protected from the environment in a shack approximately 40 m away from the test structure. The chassis contains five NI-9234 modules for the measurements of the accelerometers, one NI-9237 module for the strain gauges, and one NI-9291 module for the temperature sensor. The data is acquired continuously at a sampling rate

of 1651.61 Hz and locally stored as data blocks of 10 min on the hard drive of the host computer.

A meteorology mast erected by the Institute of Meteorology and Climatology (IMUK) of Leibniz University Hannover is positioned 20 m away from the test structure. There, the meteorological data is measured and saved as one-minute mean values. This information precisely describes the prevailing environmental conditions. Previous studies [211] showed that among all the meteorological data acquired, besides the temperature, the maximum wind speed constitutes an essential parameter, as the lattice mast exhibits nonlinear dynamics in terms of amplitude-dependent behavior, cf. Section 7.2.

For this chapter, data from September 2020 until May 2021 was considered, which is available in an online open-access repository of Leibniz University Hannover and can be accessed through `https://doi.org/10.25835/0027803`. Besides measurements referring to the structure under healthy conditions, the mentioned data acquisition period also covers several damage cases, as listed in Tab. 7.1.

Table 7.1: Data recordings according to structural state and damage position [211].

Period of data acquisition	Structural state	Damage position
Aug. 1st, 2020 - Oct. 13th, 2020	healthy	–
Oct. 13th, 2020 - Oct. 27th, 2020	damaged	damage level 6 (all damage mechanisms removed)
Oct. 27th, 2020 - Nov. 9th, 2020	healthy	–
Nov. 9th, 2020 - Nov. 24th, 2020	damaged	damage level 4 (all damage mechanisms removed)
Nov. 24th, 2020 - Mar. 18th, 2021	healthy	–
Mar. 18th, 2021 - Apr. 20th, 2021	damaged	damage level 3 (all damage mechanisms removed)
Apr. 20th, 2021 - May 4th, 2021	healthy	–
May 4th, 2021 - May 19th, 2021	damaged	damage level 6 (one damage mechanisms removed)
May 19th, 2021 - May 28th, 2021	healthy	–
May 28th, 2021 - Jun. 14th, 2021	damaged	damage level 4 (one damage mechanisms removed)
Jun. 14th, 2021 - Jun. 25th, 2021	healthy	–
Jun. 25th, 2021 - Jul. 12th, 2021	damaged	damage level 3 (one damage mechanisms removed)
Jul. 12th, 2021 - Jul. 31st, 2021	healthy	–

7.2 CHARACTERIZATION OF DYNAMIC BEHAVIOR

When monitoring a structure, methods and approaches must be chosen properly according to its dynamic behavior. For instance, if the system exhibits strong nonlinearities or nonstationary dynamics on short-term scales, say during periods of 10 min, as considered here, then, identifying the system as LTI will most probably lead to poor damage identification performance. Hence, before launching automated SHM routines, engineers in charge should assess the dynamic behavior of the observed system in a supervised manner for a certain period. In the case of LUMO, this was conducted in [211] by observing natural frequencies and modal damping. As a result, it was shown that the lattice mast exhibits nonlinear and parameter-varying dynamic behavior on both short-term as well as long-term time scales. Nonlinear dynamics manifested as amplitude dependency are caused by varying wind forces; daily and seasonal temperature fluctuations further influence the dynamic behavior. Despite these observations, the authors concluded that the short-term dynamics (10 min) might as well be approximated as LTI since the mentioned properties, especially the maximum wind speed, seldom show non-smooth and extreme variations. Therefore, assuming it constant for 10 min intervals is reasonable. For completeness and understanding regarding the dynamics of the lattice mast, parts of investigations conducted in [211] are presented here in a condensed and extended fashion.

To obtain a general overview of the variations of structural dynamics, consider the period of September 1st, 2020, until September 30th, 2020. During this time, LUMO was observed under healthy conditions. Fig. 7.4 depicts the history of damped natural frequency[1] of the first 15 modes identified with the help of the unweighted SSI-COV algorithm, cf. Tab. 2.1. Further, stabilization diagrams were employed to discard spurious modes. To reduce the numerical burden of the long-term modal analysis, only data blocks acquired every 30 min were taken into account. The identification results for the frequency range from 0 to 120 Hz were classified with the help of a simple clustering algorithm and the settings given in Tab. 7.2. Characterization of these modes follows from Tab. 7.3. A close-up of the evolution of the

Table 7.2: Criteria for modal clustering of identified modes of LUMO based on 10-min data sets.

Criterion for modal clustering	Value
Min. MAC value within cluster	0.95
Max. absolute frequency deviation within cluster	1 Hz
Min. absolute frequency difference between mean frequencies of clusters	0.02 Hz

natural frequency of mode B2-x is presented in Fig. 7.5, which exhibits the mentioned variation most clearly. Additionally, an exemplary plot of the corresponding mode shape is depicted in Fig. 7.6. In both Figs. 7.4 and 7.5, it can be observed that natural frequencies vary heavily during the considered time interval. As mentioned before, these fluctuations are caused by varying excitation intensity and temperature, see [211]. In the following, these properties shall be examined separately.

1 In the present chapter, damped natural frequencies are generally implied when writing *natural frequencies*. As mentioned in [211], comparable results and interpretations can be achieved by considering the undamped natural frequencies instead.

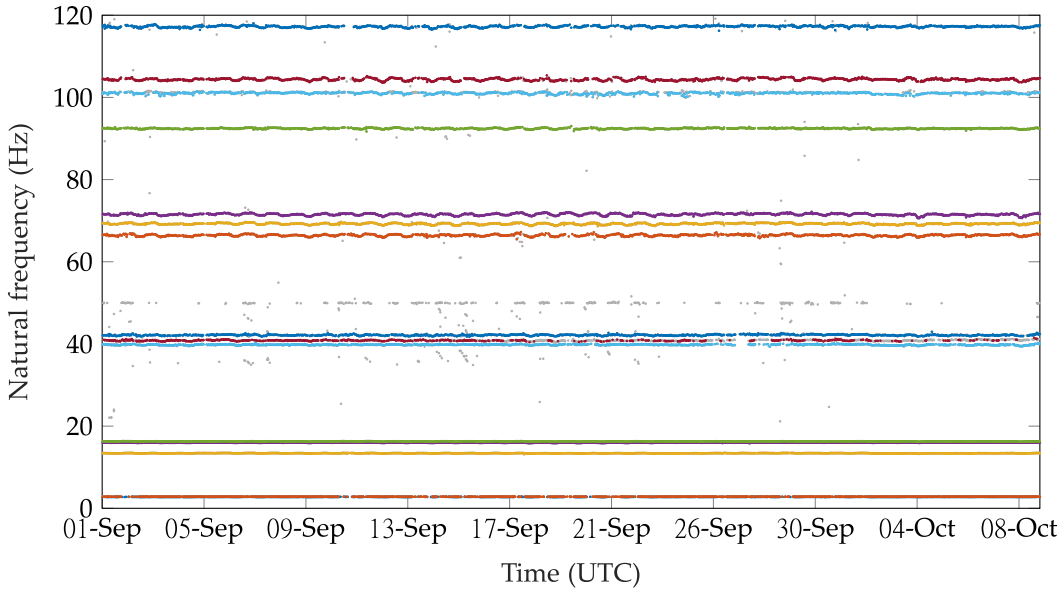

Figure 7.4: All identified and classified natural frequencies of LUMO from September 1st until October 13th, 2020 and between 0 to 120 Hz (unclassified frequencies in gray).

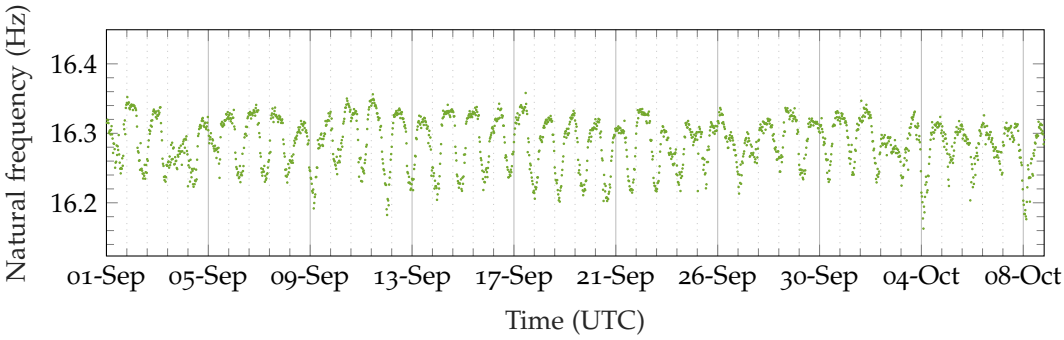

Figure 7.5: Close-up of evolution of natural frequency of B2-x from September 1st until October 13th, 2020.

AMPLITUDE DEPENDENCE

To observe the effect of amplitude dependence, again, measurements at an interval of 30 min were considered during the period from September 1st, 2020, until September 30th, 2020. The natural frequency values corresponding to B2-x (see Tab. 7.3) and obtained for 10-min data sets are presented in dependency plots in Fig. 7.7. To exclude the effect of temperature, all identification results outside the window of material temperature from 9 to 13 °C were discarded. The dependency plots display the maximum wind speed (MW) and its substitute $\log(\mathrm{var}\{\mathrm{accelo9}\})$ over the natural frequency and modal damping ratio. Here, var{accelo9} represents the absolute value of the variance of the acceleration measurements in x- and y-direction acquired at ML9 (see Fig. 7.1), which are denoted as $\mathrm{accelo9_x}$ and $\mathrm{accelo9_y}$, respectively, so that

$$\mathrm{var}\{\mathrm{accelo9}\} = \sqrt{\mathrm{var}\{\mathrm{accelo9_x}\}^2 + \mathrm{var}\{\mathrm{accelo9_y}\}^2}.$$

Table 7.3: Characterization of first 15 vibration modes and natural frequencies obtained using SSI-COV and modal clustering using parameters given in Table 7.2.

Index	Average natural frequency, Sep. 1st - Oct. 13th, 2020	Type of vibration mode (dominating direction)	Identifier
1	2.76 Hz	1st bending mode (y)	B1-y
2	2.81 Hz	1st bending mode (x)	B1-x
3	13.40 Hz	1st torsional mode	T1
4	15.94 Hz	2nd bending mode (y)	B2-y
5	16.28 Hz	2nd bending mode (x)	B2-x
6	39.78 Hz	2nd torsional mode	T2
7	40.76 Hz	3rd bending mode (y)	B3-y
8	42.14 Hz	3rd bending mode (x)	B3-x
9	66.40 Hz	3rd torsional mode	T3
10	69.15 Hz	4th bending mode (y)	B4-y
11	71.51 Hz	4th bending mode (x)	B4-x
12	92.40 Hz	4th torsional mode	T4
13	100.98 Hz	5th bending mode (y)	B5-y
14	104.33 Hz	5th bending mode (x)	B5-x
15	117.16 Hz	5th torsional mode	T5

Note that in [211], $\log(\mathrm{var}\{\mathrm{accelo9}\})$, i.e., the common logarithm of var{accelo9}, was identified as a suitable proxy for the maximum wind speed, which can be alternatively considered for periods of missing wind measurements, e.g., from May 7th, 2021 until June 21st, 2021. In fact, in the cited publication, it was shown that the maximum wind speed and $\log(\mathrm{var}\{\mathrm{accelo9}\})$ computed for 10-min data sets are linearly correlated, which was quantified by a Pearson coefficient [60] of 0.96. In Fig. 7.7, additional plots presenting the material temperature (MT) vs. natural frequency and damping ratio are included to visualize that the temperature effect has truly been isolated.

The dependency plot confirms the amplitude dependence of LUMO, as the considered natural frequency decreases with rising wind speeds, representing a softening behavior. At the same time, the damping ratio increases, possibly because of higher aerodynamic damping effects. Note that Fig. 7.7 displays the undamped natural frequency values. Thus, their decrease cannot be explained by an increase in modal damping, cf. Eq. 2.13. Further, it can be seen that $\log(\mathrm{var}\{\mathrm{accelo9}\})$ determined for the 10-min data sets is indeed a suitable substitute for the maximum wind speed measurements. This conclusion follows by comparing the left and middle column of Fig. 7.7. Therefore, in the following, the auxiliary parameter will be solely considered.

TEMPERATURE DEPENDENCE

The temperature dependence can be investigated similarly by utilizing dependency plots. Therefore, the same data acquisition period was considered as before, and the data were

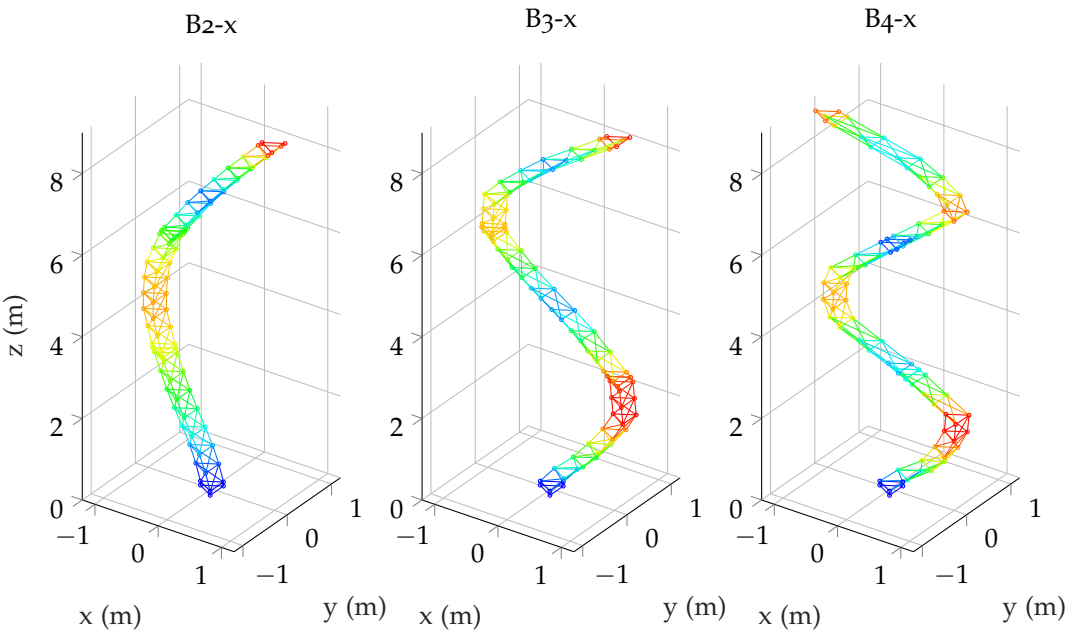

Figure 7.6: Exemplary plot of mode shapes of B2-x, B3-x, and B4-x.

filtered, allowing maximum wind speeds to range from 3 to 5 $\mathrm{m\,s^{-1}}$ only. In Fig. 7.8, the natural frequency values corresponding to the mode B2-x are plotted over the material temperature, air temperature (AT) averaged over 10 min, as well as the corresponding maximum wind speed. The latter was considered to reassess the neglected effect of strongly varying excitation intensity. It can be seen the natural frequency values decrease with rising temperature, confirming a thermal dependency of the lattice mast.

7.3 DAMAGE DETECTION AND LOCALIZATION UNDER VARYING ENVIRONMENTAL CONDITIONS

According to Tab. 7.1, two damage cases are considered in this chapter that constitute the removal of all, or a single damage mechanism (cf. Fig. 7.3) positioned at one measurement level. These cases shall be investigated in the proceeding sections employing the LPV-based SP2E method introduced in Chapter 6. Thus, the goal is to detect and localize damage under realistic EOV.

7.3.1 Preliminary investigations

Before conducting the actual damage analysis, preliminary investigations shall be first performed in view of Assumption 4.1, which was formulated to enable the a priori assessment of the estimators' applicability for damage identification. As in the previous studies, this is carried out by regarding the PSDs of estimation errors (S_e). The type of filter that exhibits the best estimation performance will be considered for damage identification. To this end, regard Fig. 7.9. Therein, the PSD of an exemplary measurement of LUMO is depicted. The graph refers to the upmost accelerometer pointing in the x-direction. Additionally, the analytical

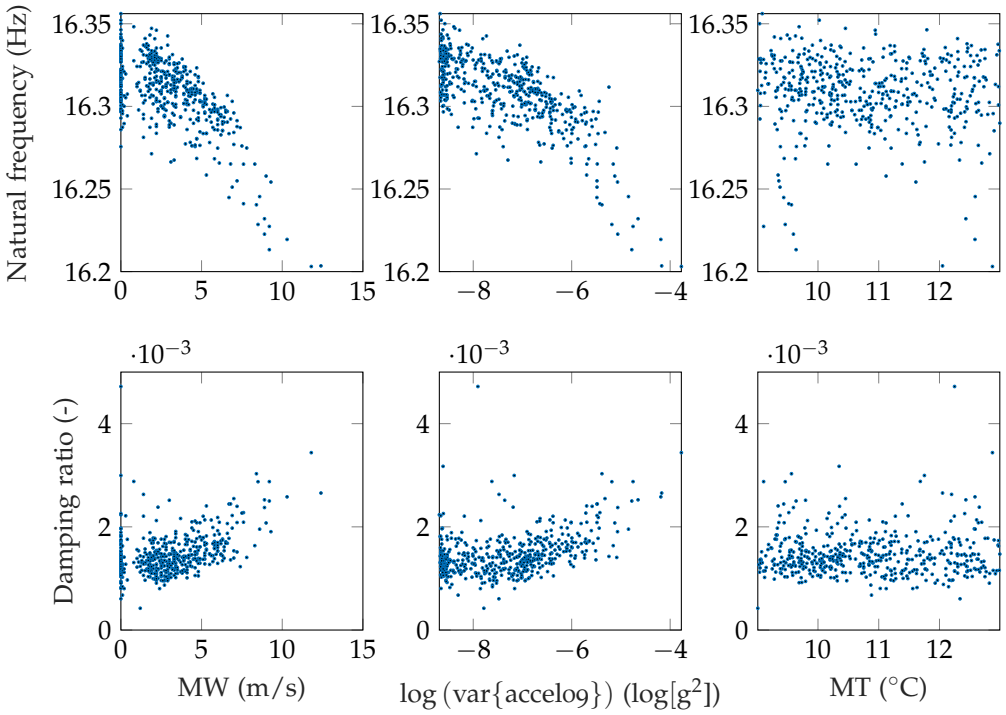

Figure 7.7: Dependency plot to examine amplitude dependence of LUMO. Natural frequency values and damping ratios of B2-x plotted vs. maximum wind speed (MW), log (var{accelo9}), and material temperature (MT) for corresponding 10-min datasets.

spectrum ($S_{y,\mathrm{SSI}}$) obtained via SSI-COV is presented as well. It follows the PSD of measured acceleration, as desired. At first, note that both axes are scaled logarithmically and that the entire frequency range up to $f_s/2$ was depicted. The previous section focused on modes below 120 Hz for three reasons that can be explained well in view of Fig. 7.9:

(i) Characterizing higher frequency modes as in Tab. 7.3 is particularly challenging, as the spatial resolution given by the sensor network is too low to distinguish between the corresponding mode shapes.

(ii) Few signal energy is contained in higher frequency ranges suggesting a minor relevance concerning the global structural dynamics.

(iii) Numerous spikes appear near 200 Hz that possibly represent local vibrations of the struts of the girder mast and no global dynamics, which are relevant for the considered SHM strategy.

That being mentioned, regard the PSDs of the estimation errors (S_e) also depicted in Fig. 7.9. They represent three different linear quadratic estimators, namely a Kalman filter and a Riccati-based and LMI-based $\mathcal{H}_\infty$ filter (see Chapter 3) that were designed given the identified dynamics of LUMO (blue line in Fig. 7.9). The noise covariance matrices of the former were identified using PALS in combination with the CVX framework and the solver SeDuMi. The alternative solver resulted in faster convergence compared to SDPT3, which was employed for Chapters 5 and 6. The LMI-based $\mathcal{H}_\infty$ filter was designed with the help of YALMIP and SDPT3.

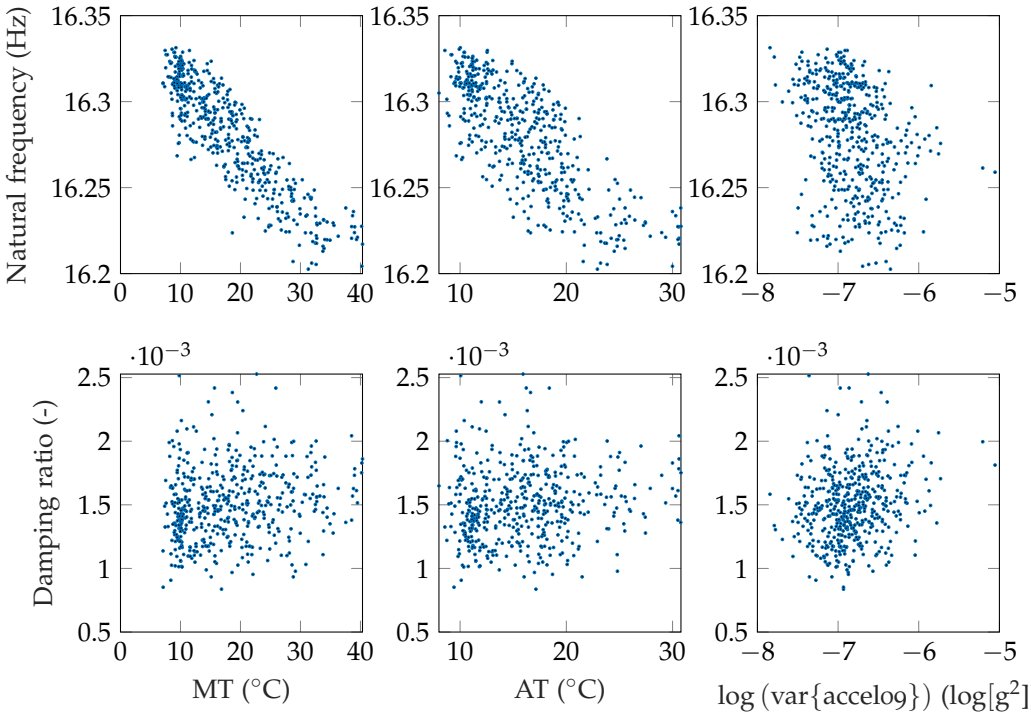

Figure 7.8: Dependency plot to examine temperature dependence of LUMO. Natural frequency values and damping ratios of B2-x plotted vs. material temperature (MT), air temperature (MT), and log (var{accelo9}) for corresponding 10-min datasets.

In Fig. 7.9 it can be seen that the LMI-based $\mathcal{H}_\infty$ estimator fails to filter the measured signal at all, whereas its Riccati-based pendant succeeds to cope with the first identified mode at around 3 Hz at least. On the other hand, the Kalman filter performs best, which can be observed from the estimation error spectrum that spreads well over all frequencies, not indicating any correlation with the measurement signal. A possible explanation for the bad performance of the $\mathcal{H}_\infty$ filters follows from their design objective. According to Problem 3.3, the $\mathcal{H}_\infty$ filters aim to minimize the $\mathcal{H}_\infty$ norm of the system $\boldsymbol{T}_{e\bar{w}} : \bar{w} \to e$, where $\bar{w}$ represents the unknown excitation and measurement noise (w and v), and $e = y_k - \hat{y}_{k|k-1}$ is the estimation error. Hence, the filters strive to minimize the maximal gain of $\boldsymbol{T}_{e\bar{w}}$, cf. Section 3.1.4. Now, regarding Fig. 7.9, it appears that the first mode at around 3 Hz comprises most of the measured signal's average power. Especially compared to the vibration modes beyond 30 Hz, the signal energy is exceeded by orders of magnitude. For the $\mathcal{H}_\infty$ filters, this suggests that filtering the vibrations associated with the first mode has the greatest impact on minimizing the maximum gain of $\boldsymbol{T}_{e\bar{w}}$, and thus, the estimation error e. This effect can be observed in the case of the Riccati-based $\mathcal{H}_\infty$ filter but not for the LMI-related design. The latter observation suggests that the LMI-based synthesis approach for $\mathcal{H}_\infty$ filters proposed in Section 3.5.2 is simply not as efficient as its pendant, which is in line with the investigation results obtained in Chapter 6. As a consequence and in accordance with Assumption 4.1, Kalman filters should be realized for the damage identification of LUMO.

To complete this discussion, the two noise covariance estimation approaches, namely ALS and PALS, shall be compared in the following. Therefore, the same data set is considered.

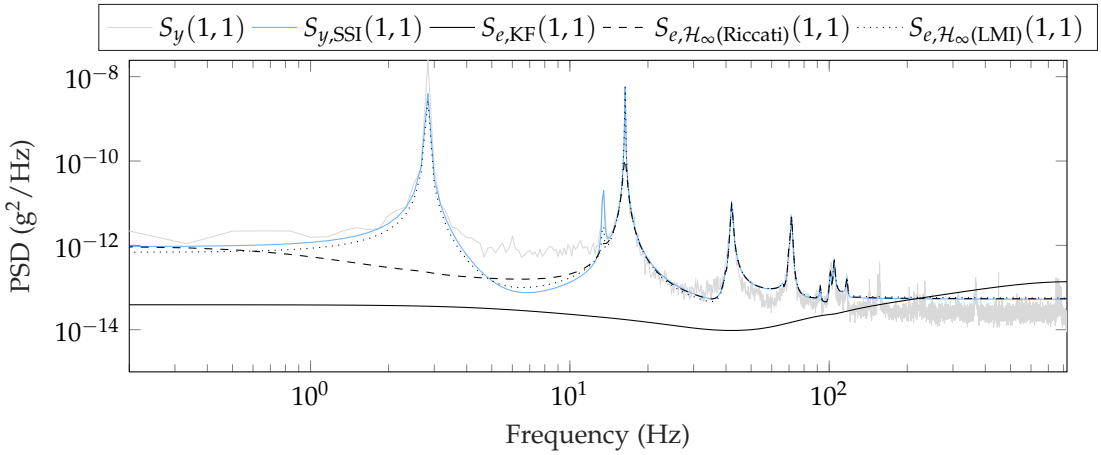

Figure 7.9: PSD of exemplary measurement of LUMO (S_y), analytical PSD using identified system ($S_{y,\mathrm{SSI}}$), and PSDs resulting from estimators (S_e).

As before, the PSDs of the acceleration signal acquired at the upmost measurement position in the x-direction and its analytical counterpart are depicted in Fig. 7.10. These graphs are

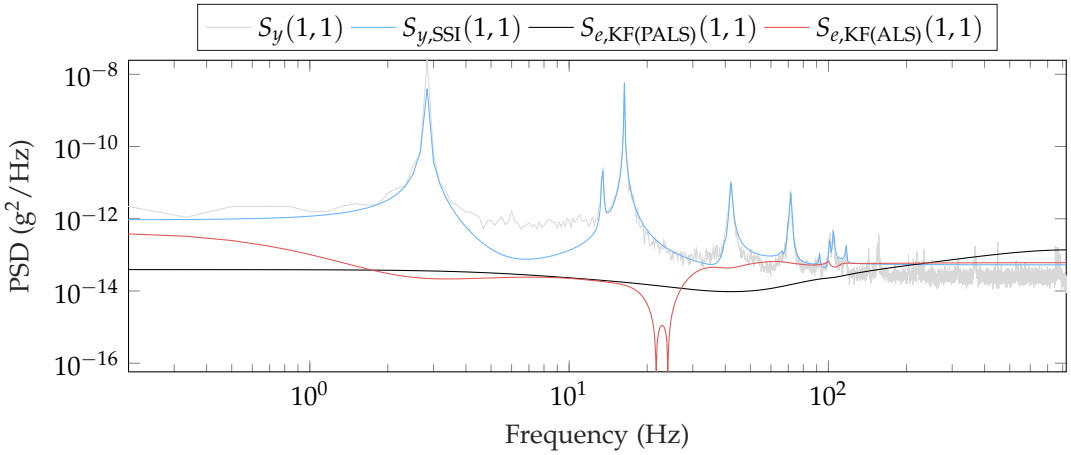

Figure 7.10: PSD of exemplary measurement of LUMO (S_y), analytical PSD using identified system ($S_{y,\mathrm{SSI}}$), and PSDs of estimation errors resulting from Kalman filters (S_e) tuned with the help of ALS and PALS.

accompanied by the spectra of the estimation errors resulting from Kalman filters tuned with ALS- or PALS-estimated noise covariance matrices. It can be seen that the Kalman filter designed with the help of covariance matrices estimated with PALS is more suitable for damage analysis. The reason is that the average power of the estimation error is lower in the relevant frequency range (cf. $S_{y,\mathrm{SSI}}$) and, more importantly, $S_{e,\mathrm{KF(ALS)}}$ shows little spikes at around 100 Hz, which indicates correlation with the measured data. As discussed in Chapter 5, this was likely triggered by the discrepancy between the dynamics represented by the identified system model ($S_{y,\mathrm{SSI}}$) and those encompassed in the measured data (S_y). Consequently, in accordance with Assumption 4.1, PALS-tuned Kalman filters were employed for the damage analysis of LUMO.

7.3.2 Damage analysis procedure

Deciding on the type of linear quadratic estimation according to Assumption 4.1 is a crucial step for the SP2E-based damage identification. Moreover, the second assumption formulated in Section 4.4, which is essentially dedicated to the model selection problem, should also be considered to lay a proper foundation for damage analysis. When monitoring a structure under ambient excitation, EOV, and significant uncertainty, it is practically impossible to enable the identification of the same vibration modes for all time. Hence, one could disregard Assumption 4.2 and simply apply stable systems $\boldsymbol{G}_i$ and estimators $\boldsymbol{\Pi}_i^{-1}$. Alternatively, one might consider only specific vibration modes by making use of $\boldsymbol{G}_3$, see Section 4.2.2. Depending on the identification rate of the considered modes, the latter approach might come at the price of skipping significant amounts of incoming data sets. Then, the state of the structure under surveillance can be assessed less frequently but possibly more thoroughly. To study this assertion, both approaches shall be investigated at LUMO in the following sections. From there, procedures can be derived that are applicable for different cases and experiments. The two different strategies of model selection and damage identification, which will be further elaborated on in the proceeding paragraphs, are formally defined:

Table 7.4: Different strategies for model selection in the context of SP2E-based damage analysis of LUMO.

Strategy 1	Defining $\boldsymbol{G}_3 = \boldsymbol{G}_2$, cf. Fig. 4.2. Performing no modal reductions concerning a static set of reference modes.
Strategy 2	Defining $\boldsymbol{G}_3$ as a reduced form of $\boldsymbol{G}_2$. Performing the model reductions with respect to a static set of reference modes.

Despite the differences in the model selection strategies, the unweighted SSI-COV in combination with stabilization diagrams was generally applied for the system identification of LUMO, as mentioned before. Also, only the frequency range from 0 to 140 Hz was considered. Hence, spurious modes and such that are difficult to interpret (cf. Tab. 7.3) were also neglected in view of strategy 1.

DEFINING THE GRID OF LOCAL REFERENCE SYSTEMS

Section 7.2 proved that the dynamic behavior of LUMO depends strongly on the temperature and excitation intensity. Thus, the material temperature and $\log\left(\mathrm{var}\{\mathrm{accelo9}\}\right)$ were considered for data normalization. These quantities define a two-dimensional EOC space in which local reference estimators are interpolated. To obtain a grid of these systems, the EOC space was segmented first by defining $\Delta\theta$, see Fig. 6.3. In the present case, $\Delta\theta_1$ was defined to refer to the material temperature, whereas $\Delta\theta_2$ represents $\log\left(\mathrm{var}\{\mathrm{accelo9}\}\right)$. Under consideration of Figs. 7.7 and 7.8, these values were chosen as $\Delta\theta_1 = 2\,\mathrm{K}$ and $\Delta\theta_2 = 1\,\log\left(\mathrm{g}^2\right)$. That is, small changes in the structure's dynamics could theoretically be realized by the LPV model to be identified. Apparently, the grid associated with θ_1 has a finer resolution than θ_2. This was realized to enable a representation of the grid elements with a reasonable amount of potential reference systems. It should be mentioned that defining a particularly fine grid for all

relevant EOCs is desirable but practically infeasible, as too many grid elements are likely to be non-represented. This circumstance complicates the interpolation problem.

In the next step and for a defined data acquisition period, the EOC-labeled estimators were assigned to the resulting grid. This procedure was handled differently for the strategies defined in Tab. 7.4. **Strategy 1**: Because of the likely case of multiple systems falling into a certain grid field, the system with the highest model order was chosen as the local reference system. **Strategy 2**: To conduct a modal-based model selection, a set of reference modes needs to be defined first. In the present case, these followed from the cluster analysis presented in Section 7.2, resulting in the mode set listed in Tab. 7.3. The associated mode shapes were chosen as the ones that showed the greatest similarity with the remaining mode shapes contained in the corresponding mode cluster. Given that and the systems assigned to the EOC grid, the list of reference modes was updated (reduced) so that local reference models could be found that represented the same modes across the entire EOC space. For the comparison of the updated list of reference modes and the ones comprised by the identified system models, the criteria given in Tab. 7.2 were considered. Finally, the estimators were chosen as local references that showed the highest compliance with the reference mode set.

PERFORMING THE LPV-BASED SP2E METHOD

Damage identification under EOV was performed using the two-dimensional grid of local LTI models for the LPV-based SP2E method introduced in Chapter 6. Hence, the SP2E related damage indicators $r_{d\mathcal{V}}([i_1, i_2]))$ and $P_{d\mathcal{V}}$ (see Section 4.3) were computed by identifying $\mathbf{\Pi}_1^{-1}$ for some θ_k via interpolation (see Fig. 6.4), and then, applying the original SP2E method, see Section 4.1. The EOCs observed at time k (defining θ_k) referred to the analysis system $\mathbf{\Pi}_2^{-1}$. The input y_3 to both estimators $\mathbf{\Pi}_1^{-1}$ and $\mathbf{\Pi}_2^{-1}$ followed from the definition of $\boldsymbol{G}_3$ according to Tab. 7.4. Thus, in the case of strategy 1, $\boldsymbol{G}_3 = \boldsymbol{G}_2$ was simply defined, whereas, for strategy 2, $\boldsymbol{G}_3$ was derived from $\boldsymbol{G}_2$ so that it was only comprised by those modes relatable to the set of reference modes. Note that in either case (strategy 1 or 2) the estimators $\mathbf{\Pi}_1^{-1}$ and $\mathbf{\Pi}_2^{-1}$ featured the original model order that followed from the system identification via SSI-COV and a simple model reduction based on stabilization diagrams, generally considering the frequency range from 0 to 140 Hz. Thus, differences of the mentioned model selection strategies manifest themselves solely in the construction of the grid of local reference estimators (see above) and in the definition of $\boldsymbol{G}_3$, and thus, y_3.

Now, to enable the execution of **strategy 2** in accordance with Assumption 4.2, a modal comparison must be conducted between $\boldsymbol{G}_3$ and $\boldsymbol{G}_{1,i}$, where the latter refers to the identified systems associated with $\mathbf{\Pi}_1^{-1}$, cf. Fig. 6.3. Recall that $\boldsymbol{G}_3$ is derived from $\boldsymbol{G}_2$ and should comprise only reference modes defined during the LTI grid identification. For the modal comparison, it was tested if a reduced version of $\boldsymbol{G}_2$ ($\boldsymbol{G}_3$) existed, where each of its modes could be linked to those comprised by each $\boldsymbol{G}_{1,i}$. As long as this pertained, the damage analysis proceeded with $\boldsymbol{G}_3$; otherwise, the current data set referring to $\boldsymbol{G}_2$ was skipped. The case where $\boldsymbol{G}_{1,i}$ contains more vibration modes than $\boldsymbol{G}_3$ is not critical and was therefore disregarded. Also, a comparison of $\boldsymbol{G}_3$ and $\boldsymbol{G}_2$ was not considered, as $\boldsymbol{G}_3$ was directly derived from $\boldsymbol{G}_2$. Obviously, to enable the modal comparison, certain criteria had to be defined. The ones applied in the present studies are summarized in Tab. 7.5. These criteria were chosen particularly high to ensure modal tracking even when severe damage occurs. **Strategy 1** was conducted in such a way that Assumption 4.2 was respected at least for each data set separately. That is, it was

Table 7.5: Criteria for modal comparison of $\boldsymbol{G}_{1,i}$ and $\boldsymbol{G}_3$.

Criterion for modal comparison	Value
min. MAC	0.2
max. relative exceedance of natural frequency	20 %
max. relative lower deviation of natural frequency	30 %

assured that only analyses were performed where the entire dynamics of $\boldsymbol{G}_3 = \boldsymbol{G}_2$ could be linked to $\boldsymbol{G}_{1,i}$ by means of the criteria listed in Tab. 7.5. Thus, the modal compliance was ensured for all data sets differently.

Finally, to remove the effect of different excitation intensity, which affects the magnitude of damage indicators, the amplitude-related normalization via the average power of y_3 (see Eq. 6.11) was carried out additionally.

7.3.3 Localizing the complete removal of damage mechanisms

In the following, the damage analysis results for the complete removal of damage mechanisms, namely the severing of all three struts, are presented. The corresponding periods are given in Tab. 7.1. Data acquired under particularly low temperatures were generally discarded to disregard the effect of icing encountered in some periods, see [211]. This concerns a material temperature smaller than 1 °C. As mentioned before, no frequencies greater than 140 Hz were considered for the system identification. This choice is in line with Tabs. 7.5 and 7.3. Thus, systems that potentially represented the first 15 modes could be considered. An important remark is made with respect to the periods considered for training and validation. Generally, the phase after the repair of the preceding damage case and before the first occurrence of damage was taken into account. To illustrate this issue, regard Tab. 7.1 and consider the damage at DAM3, which was introduced on March 18th, 2021, and repaired on April 20th, 2021. For this case, the relevant period for training and validation comprises November 24th, 2020, until March 18th, 2021. This selection was conducted to facilitate a proper realization of the reference state, as the repair of LUMO must be associated with slight alterations of the structural dynamics, see [211]. The data representing the healthy structure was split into two parts, where 2/3 was assigned for training and the remainder was used for validation, cf. Section 4.4.3. Nevertheless, the grid of local LTI reference systems was assembled by considering the totality of training and validation data to provide better coverage of the grid. Though, during validation, the corresponding data instances were disregarded to avoid biased statistics, leading to an artificially lower threshold for damage detection. The corresponding hypothesis test was formulated based on the damage indicators' CDFs and a significance level of $\alpha = 3\,\%$.

Figs. 7.11 to 7.16 as well as Figs. 7.17, 7.19, and 7.21 show the damage identification results for the removal of all damage mechanisms at DAM6, DAM4, and DAM3, respectively, see Fig. 7.2. The presentation style of the damage analysis results is similar to the one used in Chapter 6. However, the type I (false-positive) and type II (false-negative) error rate for validation and testing, respectively, are additionally provided. Figs. 7.11 to 7.16 are dedicated to the model

selection strategy 1 defined in Tab. 7.4. The corresponding figures display the variance-based damage-sensitve feature $r_{d\mathcal{V}}([i_1, i_2]))$ for $i_1 = 1$ and $i_2 = 550$ as well as the power-based feature $P_{d\mathcal{V}}$. The latter was computed to allow a comparison in a more practical scenario.

Given these results, it can be observed that damage detection is successful for all three damage cases even when minor attention is paid to Assumption 4.2. Concerning the damage localization, a good success rate can be confirmed for the complete removal of damage mechanisms at all damage levels. In the figures, the relevant measurement levels are highlighted by a grey area. Some outliers concerning damage localization exist for all damage cases, especially damage at DAM3, see Figs. 7.15 and 7.16. A special comment should be made in view of the damage indicators' evolution during training and validation. Especially in Figs. 7.13 to 7.16, different deterministic trends can be observed, which can be described as oscillatory (in Fig. 7.13) or nonlinear (linear in log-scaled plot) in Fig. 7.15. This might indicate a change in the intact system or improper data normalization. In any case, this disturbance might have caused an increase in the type I error compared to the first damage case, cf. Figs. 7.11 and 7.12.

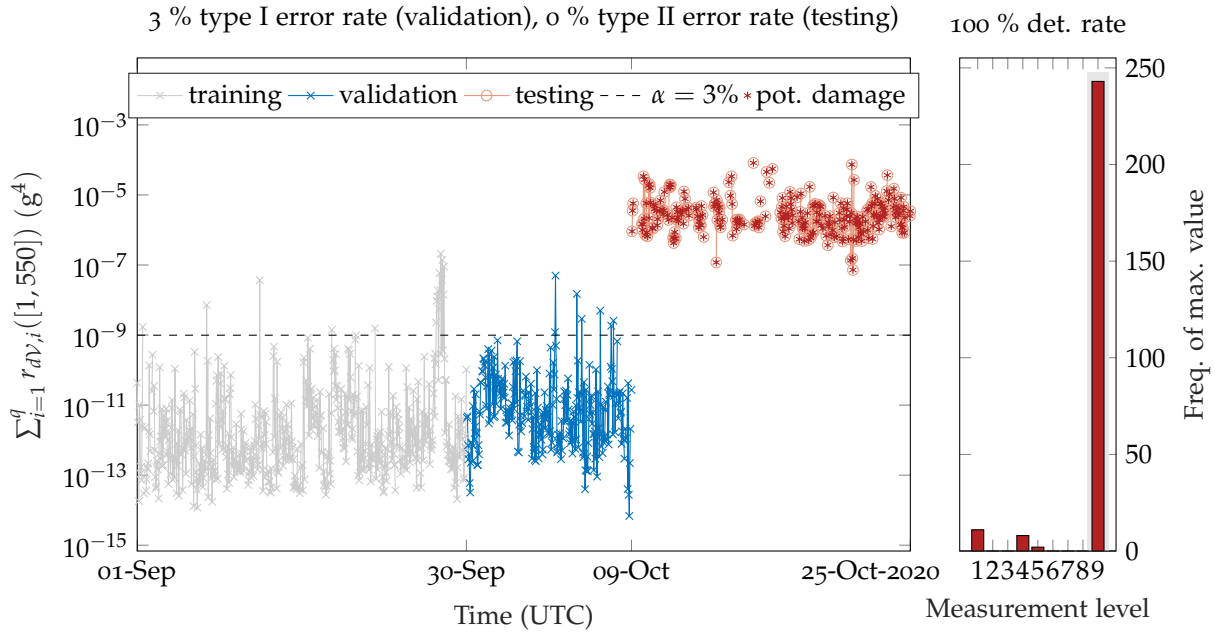

Figure 7.11: Variance feature for localization of complete removal of damage mechanisms at damage level 6. Damage localization and data normalization by LPV-based SP2E. Model selection according to strategy 1 defined in Tab. 7.4.

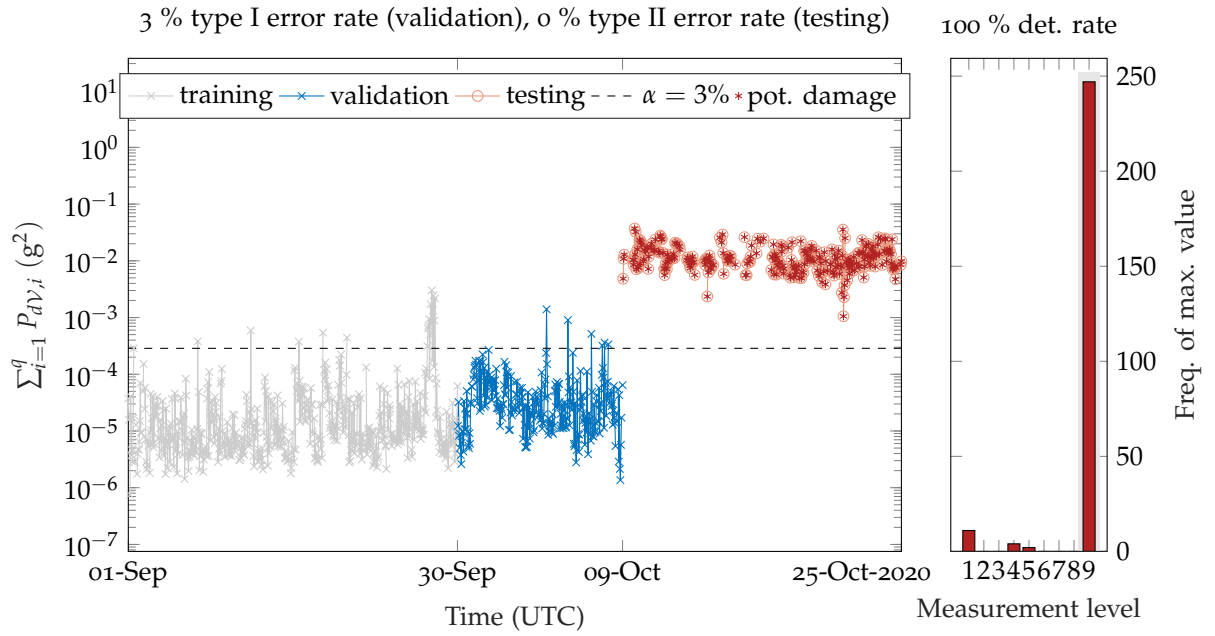

Figure 7.12: Power feature for localization of complete removal of damage mechanisms at damage level 6. Damage localization and data normalization by LPV-based SP2E. Model selection according to strategy 1 defined in Tab. 7.4.

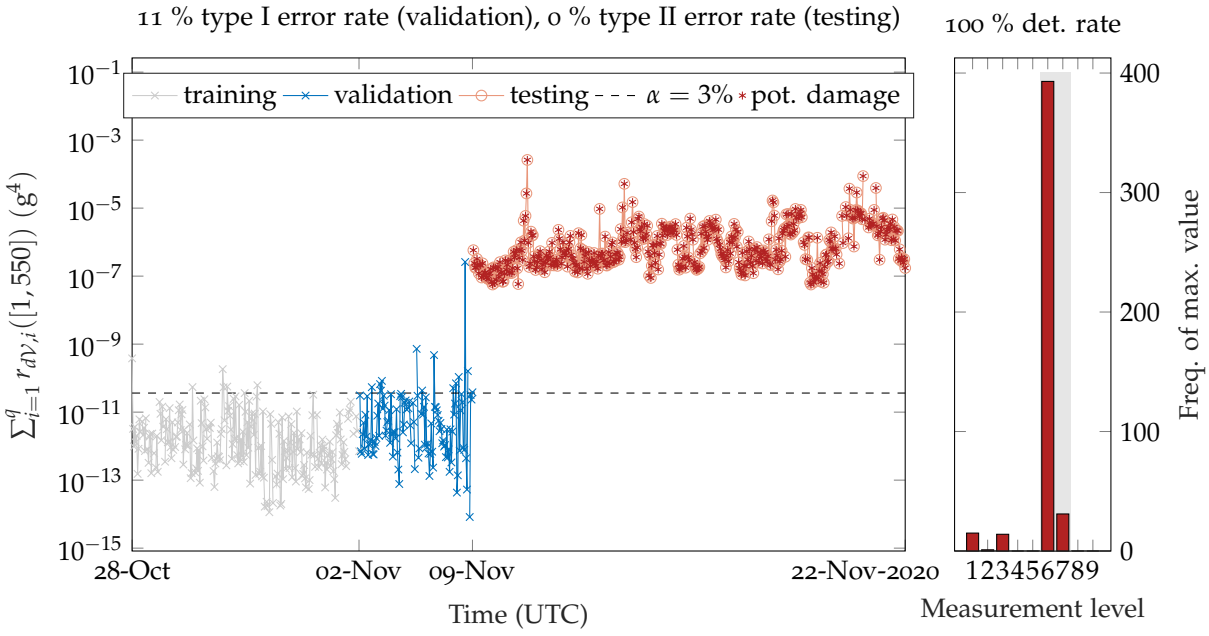

Figure 7.13: Variance feature for localization of complete removal of damage mechanisms at damage level 4. Damage localization and data normalization by LPV-based SP2E. Model selection according to strategy 1 defined in Tab. 7.4.

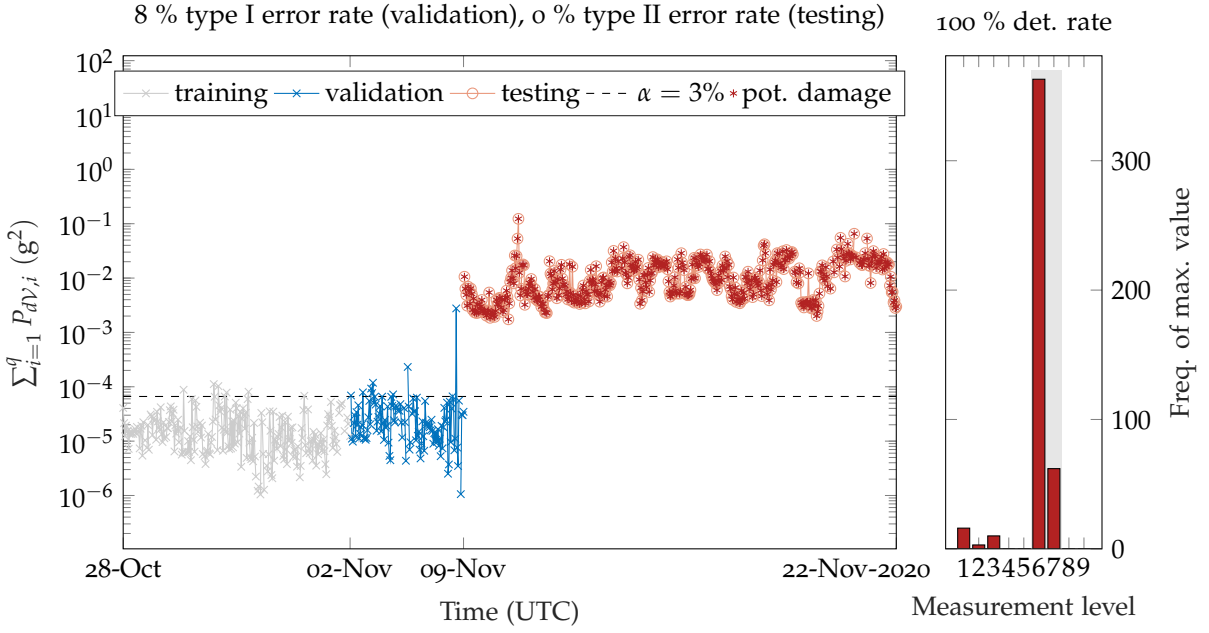

Figure 7.14: Power feature for localization of complete removal of damage mechanisms at damage level 4. Damage localization and data normalization by LPV-based SP2E. Model selection according to strategy 1 defined in Tab. 7.4.

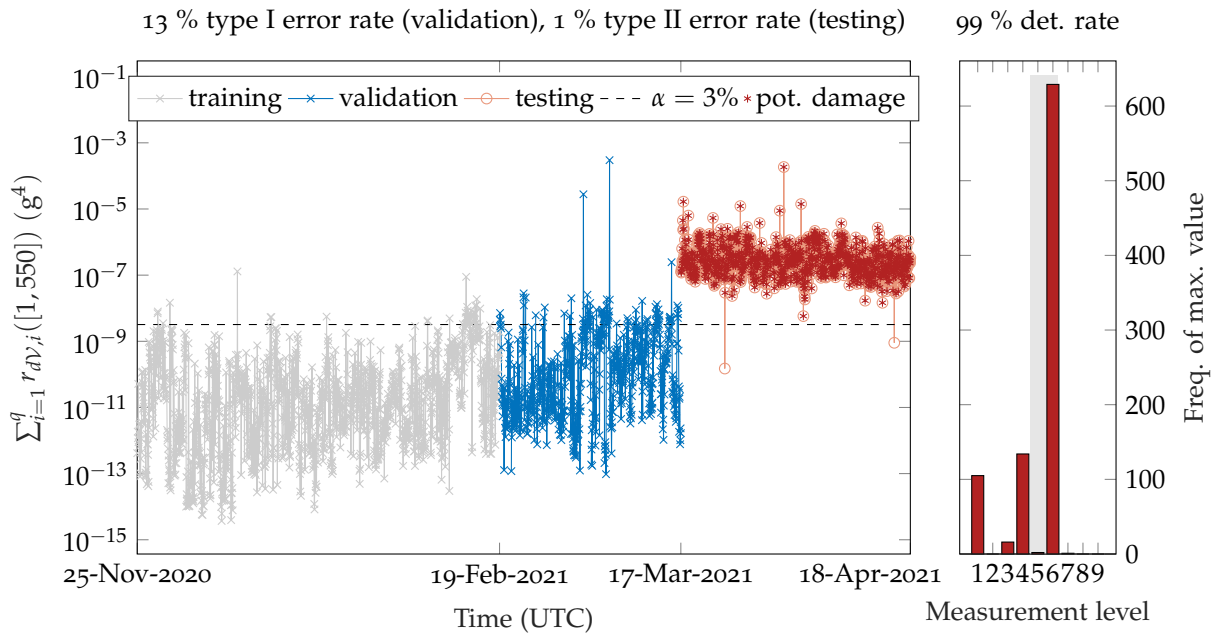

Figure 7.15: Variance feature for localization of complete removal of damage mechanisms at damage level 3. Damage localization and data normalization by LPV-based SP2E. Model selection according to strategy 1 defined in Tab. 7.4.

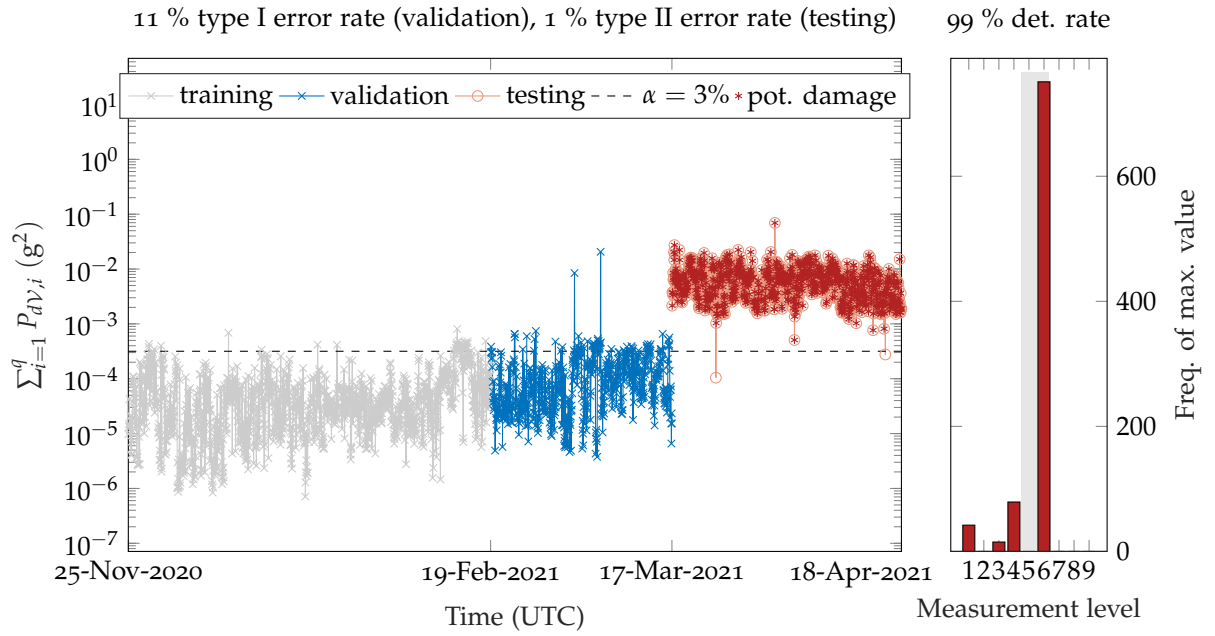

Figure 7.16: Power feature for localization of complete removal of damage mechanisms at damage level 3. Damage localization and data normalization by LPV-based SP2E. Model selection according to strategy 1 defined in Tab. 7.4.

Concerning the different damage indicators (variance-based and power-based), only minor differences regarding the precision of damage localization can be seen. That is, the power-

based feature leads to slightly fewer outliers. This can be best observed for the case of damage at DAM3, see 7.15 and 7.16. More importantly, the damage analysis with the power-based damage indicator produced a smaller type I error rate, cf. Figs. 7.13 to 7.16. Hence, it can be assumed that in practice, when the LPV-based SP2E method is applied, the variance feature derived in Section 4.2 is less suitable for damage identification. However, to prove this assumption, more experimental studies are required. Based on this observation, the power-based damage indicator is presented in the remainder of this chapter; results obtained for the variance-based feature are provided in Section A.4.1.

Figs. 7.17 to 7.22 are dedicated to the damage analysis under consideration of model selection strategy 1. That is, for these analyses, fixed sets of reference modes were employed, which implies that only changes in the corresponding modal properties are taken into account. Hence, Figs. 7.18, 7.20, and 7.22 are provided that depict the evolution of the natural frequencies, representing the reference modes during training, validation, and testing. It can be seen that due to the soft criteria defined in Tab. 7.5, the tracking of modes was successful even after the introduction of damage. However, it also led to false assignments of the modes, which is observable in all phases of damage analysis. Notably, the considered set of modes varied significantly throughout the damage cases. This can be justified by the demand for a consistent representation for all local reference estimators by means of the same modes.

Despite the minor mode assignment issues, which suggest a more elaborate modal tracking strategy, damage detection and localization were mostly successful for all damage cases. Comparing Figs. 7.12, 7.14, and 7.16 with 7.17, 7.19, and 7.21 shows that the type I error rate could be reduced in all cases except damage at damage level 6, where the false-positive rate was already at 3 %. Nevertheless, because of the more thorough model selection procedure, more pronounced damage detection results or, at least, less variance of the damage features would have been expected. This expectation is raised in view of the natural frequencies' evolution, which displays distinct jumps once the damage is introduced. The fact that the variance of the damage features is rather high, independent of the applied model selection strategy, suggests that either of the applied data normalization strategies does not function properly. I.e., the LPV-based data normalization (see Chapter 6) could not model the dependency of the structure's dynamics and the EOCs correctly. Also, the power-related normalization method concerning varying levels of excitation might have failed to clean up the data. The latter scenario is most likely, since the spectral characteristic of the excitation most probably varies significantly, while the proposed amplitude-normalization assumes at least equal spectral distribution of signal energy.

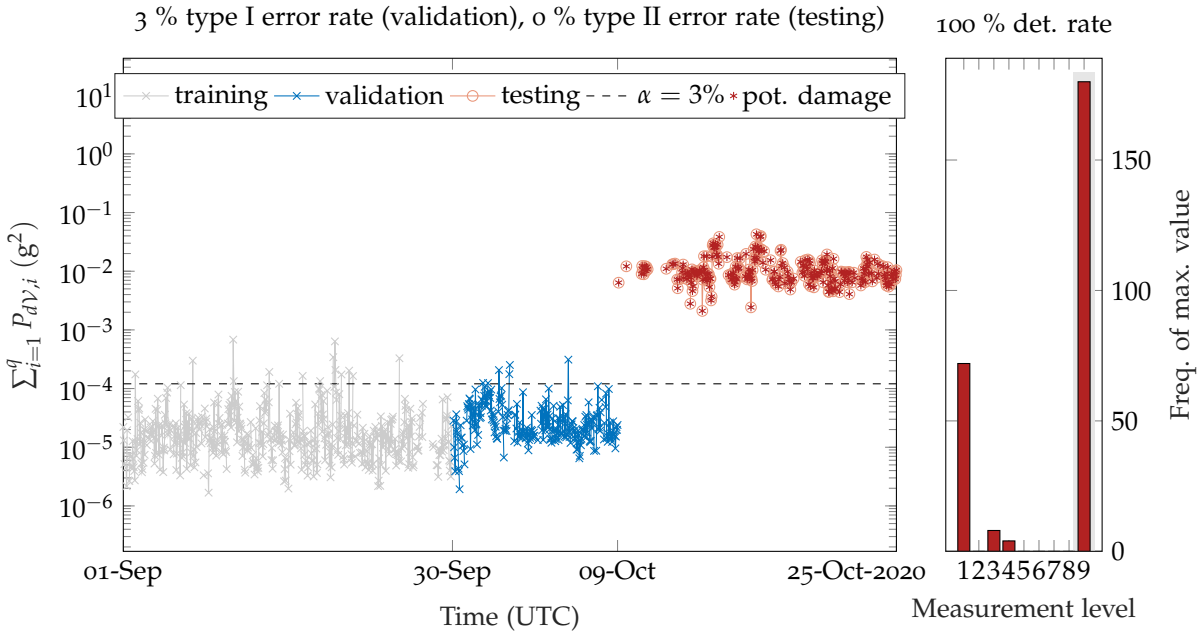

Figure 7.17: Power feature for localization of complete removal of damage mechanisms at damage level 6. Damage localization and data normalization by LPV-based SP2E. Model selection according to strategy 2 defined in Tab. 7.4.

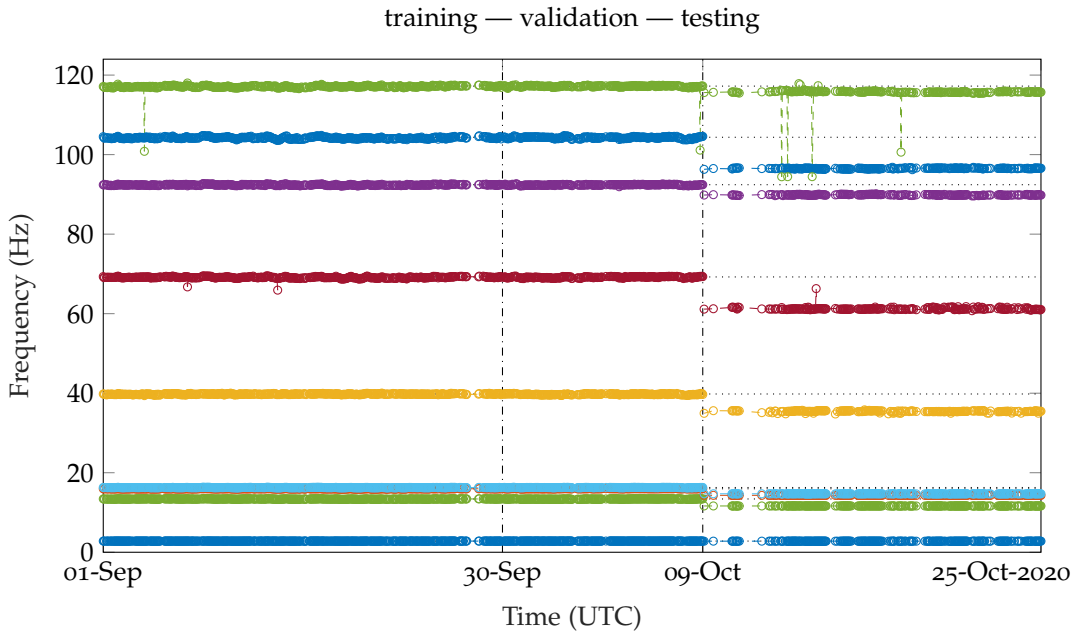

Figure 7.18: Natural frequencies corresponding to model selection strategy 2 defined in Tab. 7.4. Localization of complete removal of damage mechanisms at damage level 6.

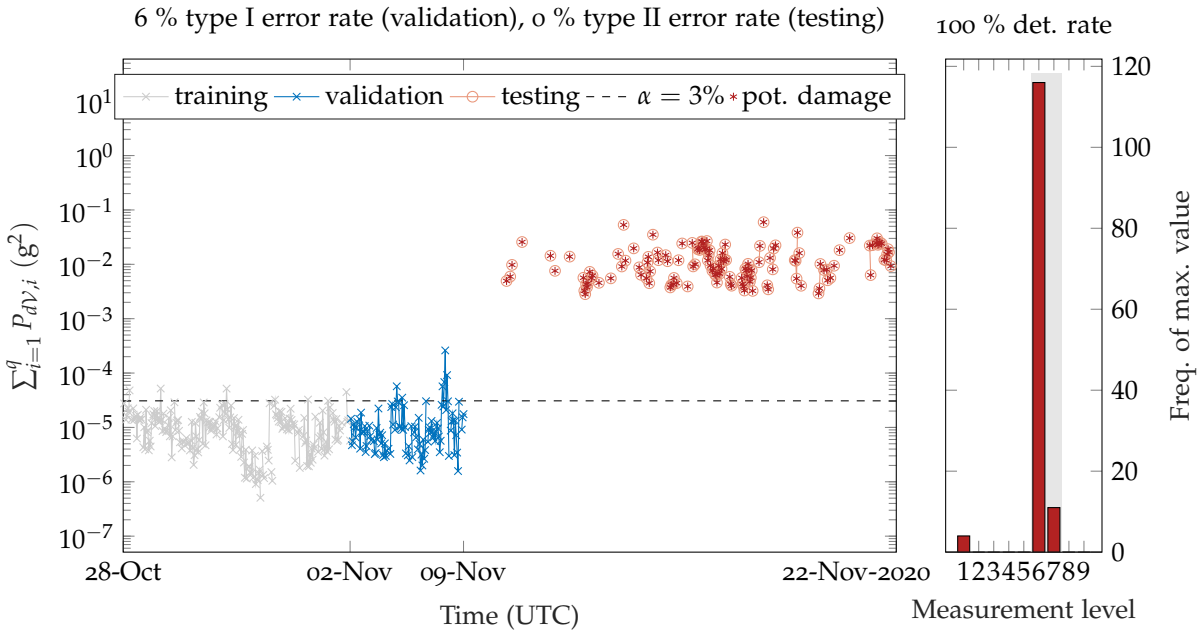

Figure 7.19: Power feature for localization of complete removal of damage mechanisms at damage level 4. Damage localization and data normalization by LPV-based SP2E. Model selection according to strategy 2 defined in Tab. 7.4.

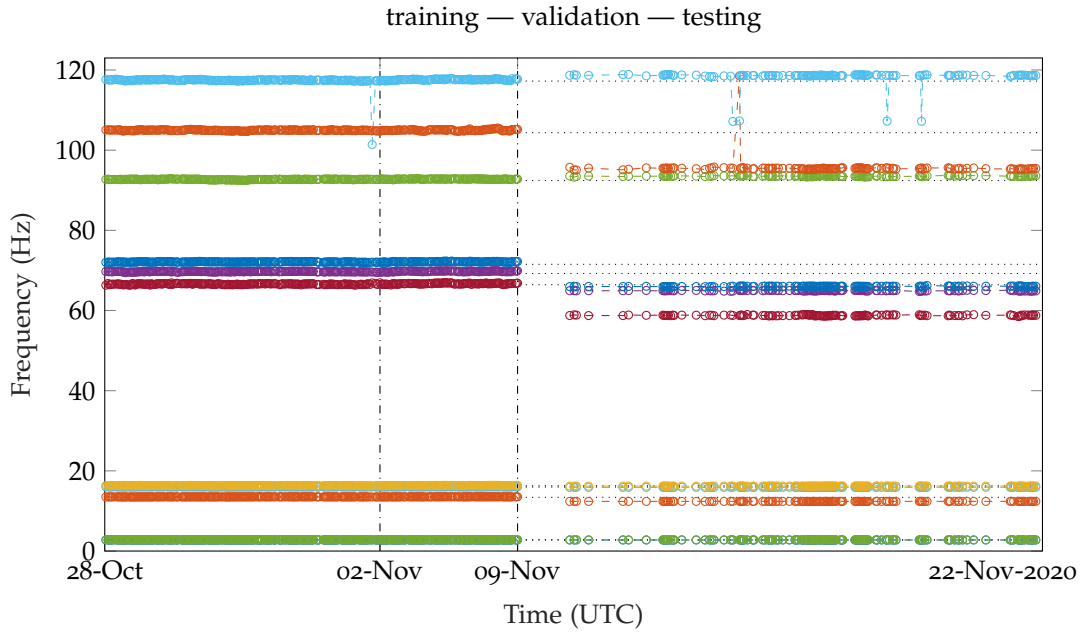

Figure 7.20: Natural frequencies corresponding to model selection strategy 2 defined in Tab. 7.4. Localization of complete removal of damage mechanisms at damage level 4.

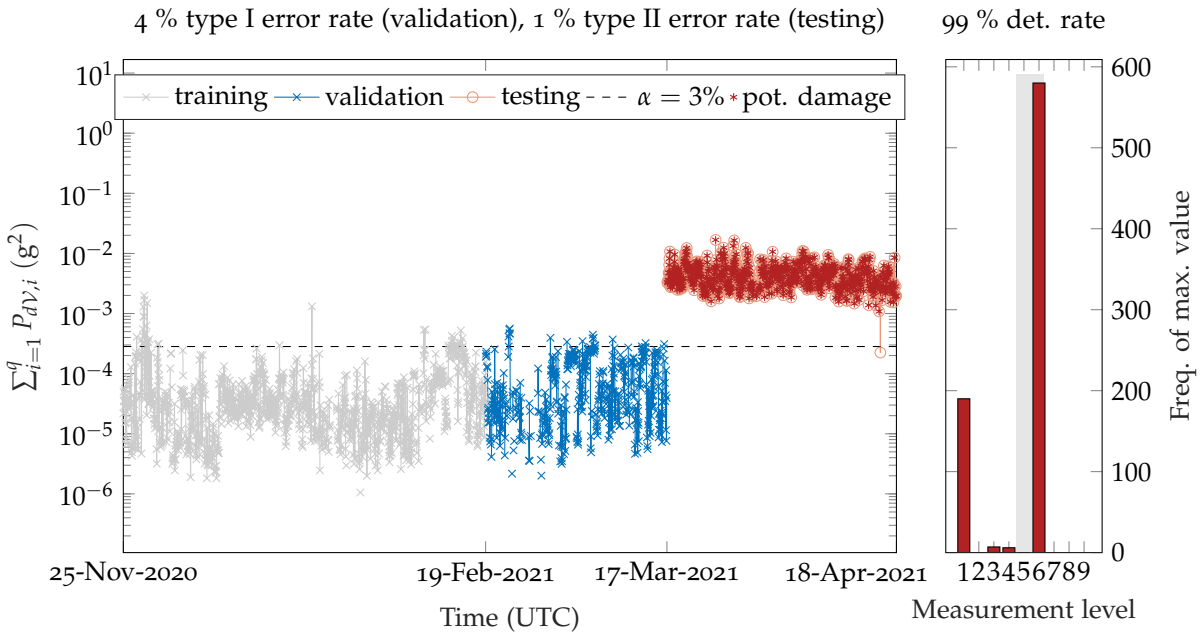

Figure 7.21: Power feature for localization of complete removal of damage mechanisms at damage level 3. Damage localization and data normalization by LPV-based SP2E. Model selection according to strategy 2 defined in Tab. 7.4.

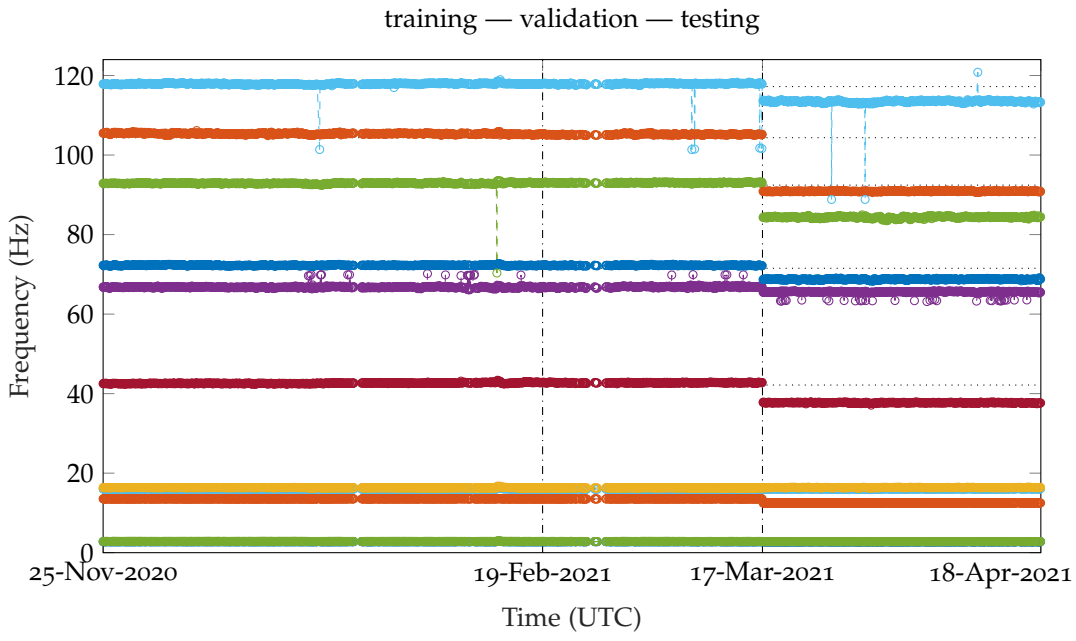

Figure 7.22: Natural frequencies corresponding to model selection strategy 2 defined in Tab. 7.4. Localization of complete removal of damage mechanisms at damage level 3.

7.3.4 Localizing the removal of a single damage mechanism

After investigating the more severe damage cases, the minor scenarios shall be regarded, which manifest themselves in the removal of a single damage mechanism at DAM6, DAM4, or DAM3. The corresponding results can be found in Figs. 7.23 to 7.25 for model selection strategy 1 (see Tab. 7.4) and in Figs. 7.26, 7.28, and 7.30 for strategy 2. Again, results concerning the variance-based damage indicator can be found in Section A.4.2.

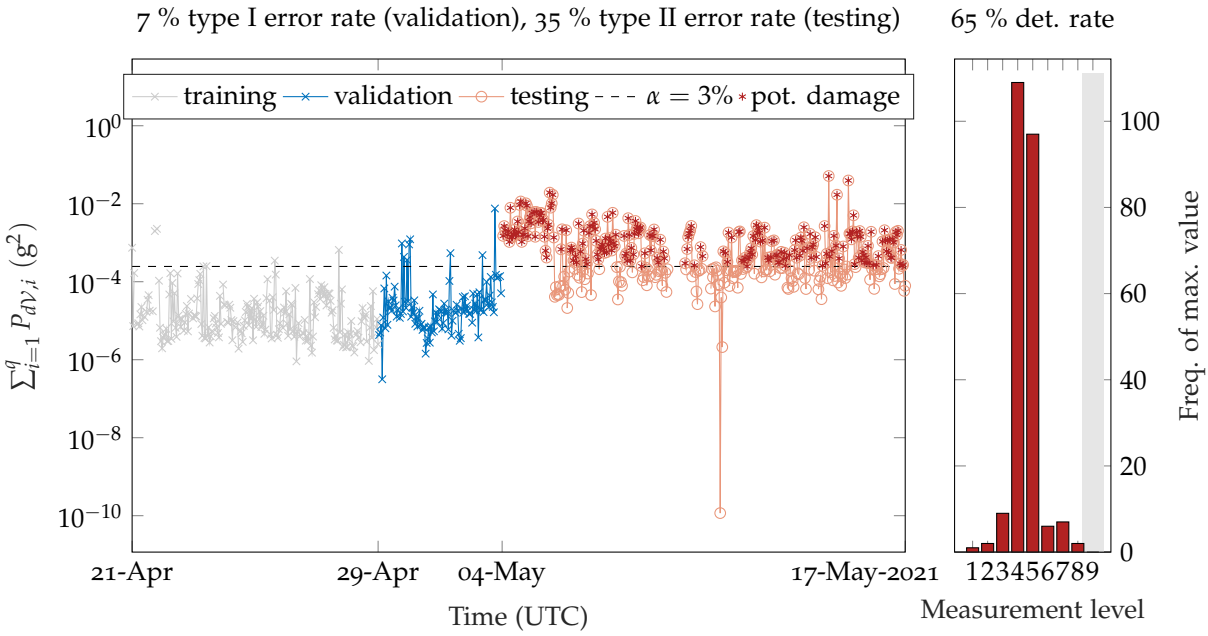

Figure 7.23: Power feature for localization of removal of single damage mechanism at damage level 6. Damage localization and data normalization by LPV-based SP2E. Model selection according to strategy 1 defined in Tab. 7.4.

Starting with the modal tracking-free approach (strategy 1), it can be recognized that the success rate for damage detection and localization is significantly reduced compared to the more severe damage scenarios studied in the previous section. Damage at DAM6 could only be detected in 65 % of the cases, resulting in a 35 % type II error (false-negative) rate. The removal of a single damage mechanism at DAM4 constitutes the case with the highest detection rate, which amounted to 85 %. Damage detection at the upmost position (DAM3) among the considered cases was barely feasible. Further, except for damage at DAM4, which triggered a fair amount of alarms in the remote proximity of the actual damage position (DAM3 instead of DAM4), damage localization can hardly be confirmed in any case.

Notably, the strictly modal-based model selection approach for damage identification (strategy 1 in Tab. 7.4) improves the damage detection rate tremendously, as can be seen in Figs. 7.26, 7.28, and 7.30. By following this enhanced approach, the damages could be detected in at least 91 % (damage at DAM3) and at a maximum of 94 % (DAM4) of the cases. Thus, the type II error rate was reduced accordingly. Unfortunately, the localization of damage was not improved significantly, although a few more alarms were triggered at the correct locations in the cases of damage at DAM4 and DAM3.

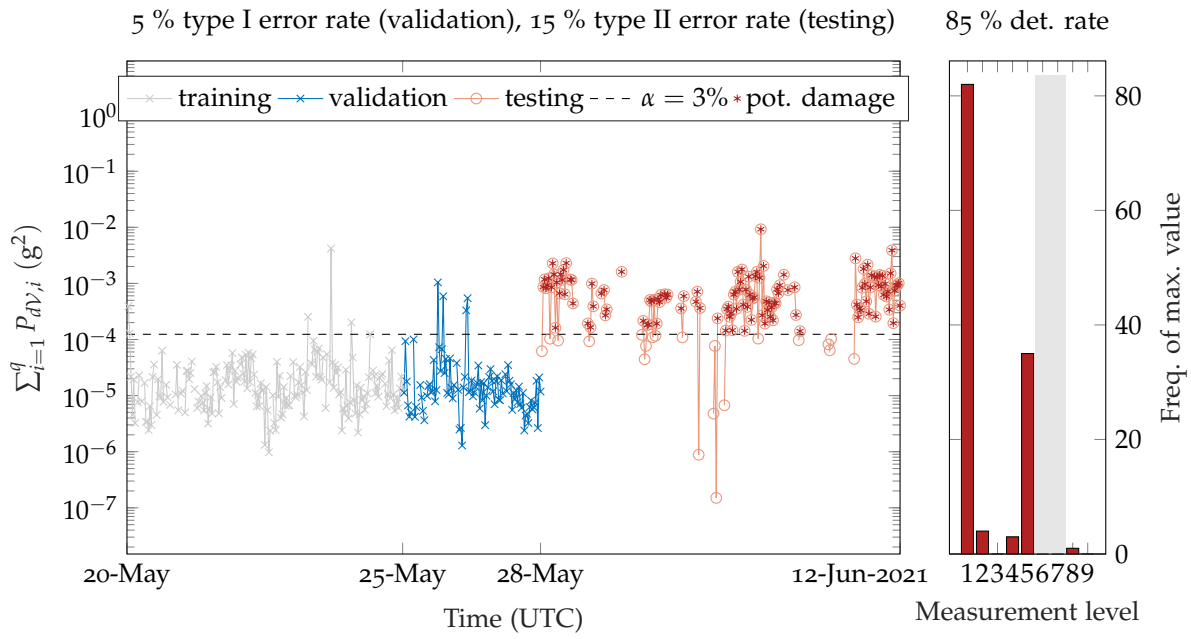

Figure 7.24: Power feature for localization of removal of single damage mechanism at damage level 4. Damage localization and data normalization by LPV-based SP2E. Model selection according to strategy 1 defined in Tab. 7.4.

An interesting effect can be observed in Fig. 7.26, where the damage indicator exceeds the damage detection threshold significantly during validation. This instance can be explained with a faulty mode assignment of mode B5-x at around 104 Hz visible in Fig. 7.27, which emphasizes the necessity of performing a thorough model selection. The erroneous classification of modes can also be recognized in Fig. 7.29 and Fig. 7.31 but without showing a strict correlation with the corresponding damage indicators.

Despite the improved damage analysis results that could be achieved with the help of the model selection strategy 2, the effectiveness of the employed data normalization approaches is still questionable. Figs. 7.27, 7.29, and 7.31 show again distinct jumps of some natural frequencies, indicating a substantial change of the structure's dynamics. Since these changes can be easily observed even under the presence of EOV, they should also be picked up by the LPV-based SP2E method. In the following section, the change of modal properties will be further studied.

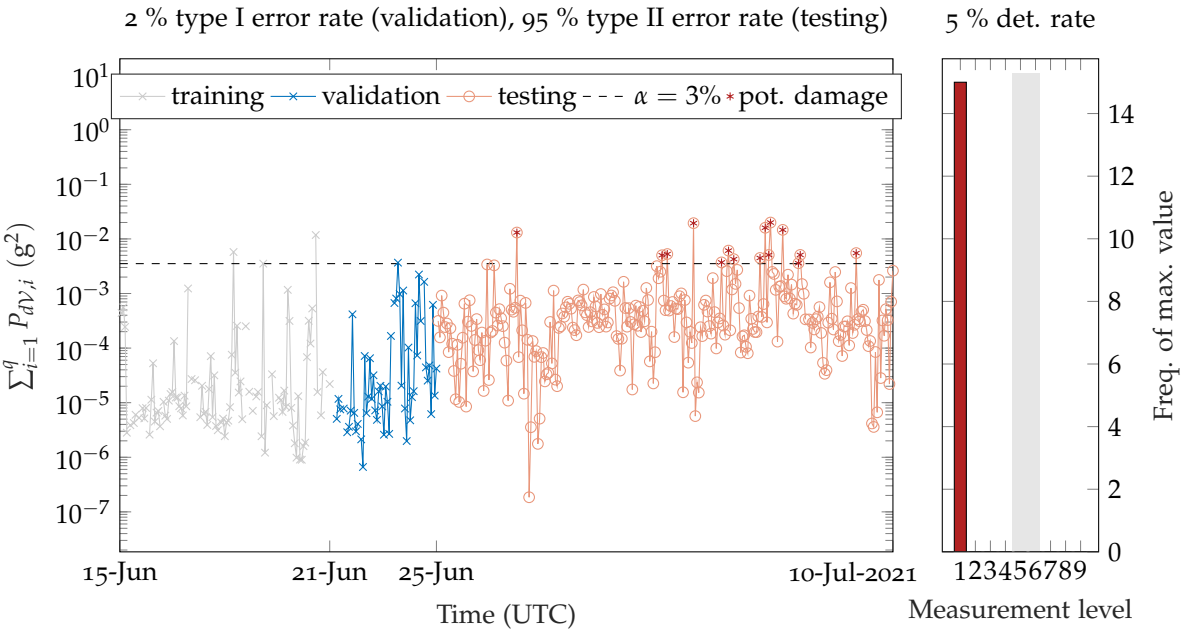

Figure 7.25: Power feature for localization of removal of single damage mechanism at damage level 3. Damage localization and data normalization by LPV-based SP2E. Model selection according to strategy 1 defined in Tab. 7.4.

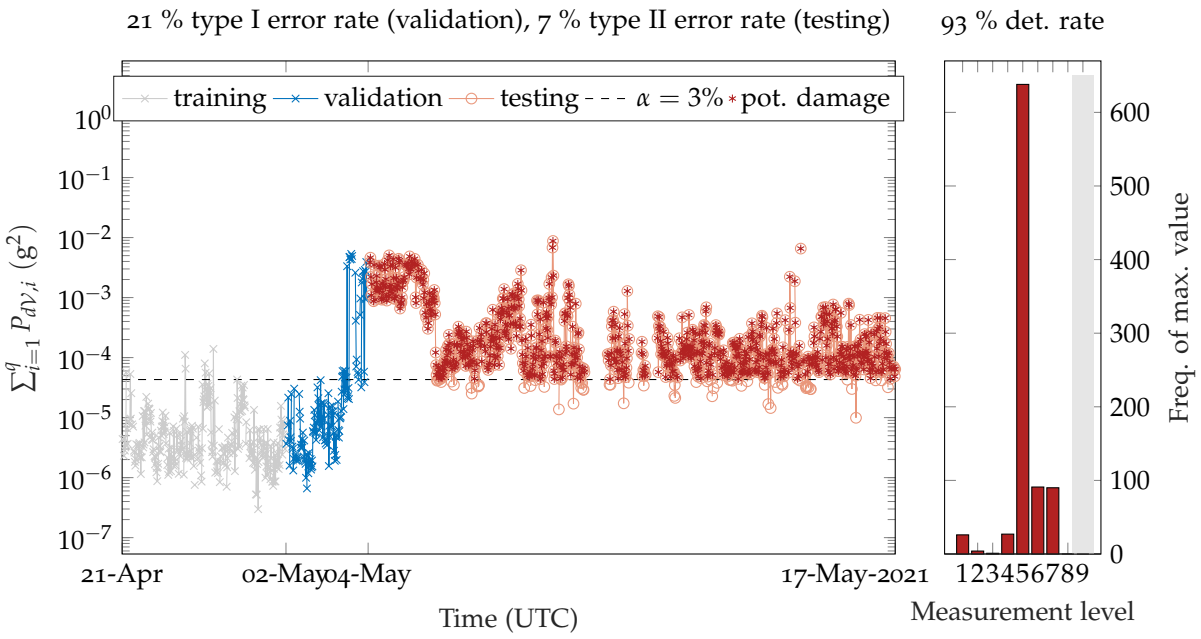

Figure 7.26: Power feature for localization of removal of single damage mechanism at damage level 6. Damage localization and data normalization by LPV-based SP2E. Model selection according to strategy 2 defined in Tab. 7.4.

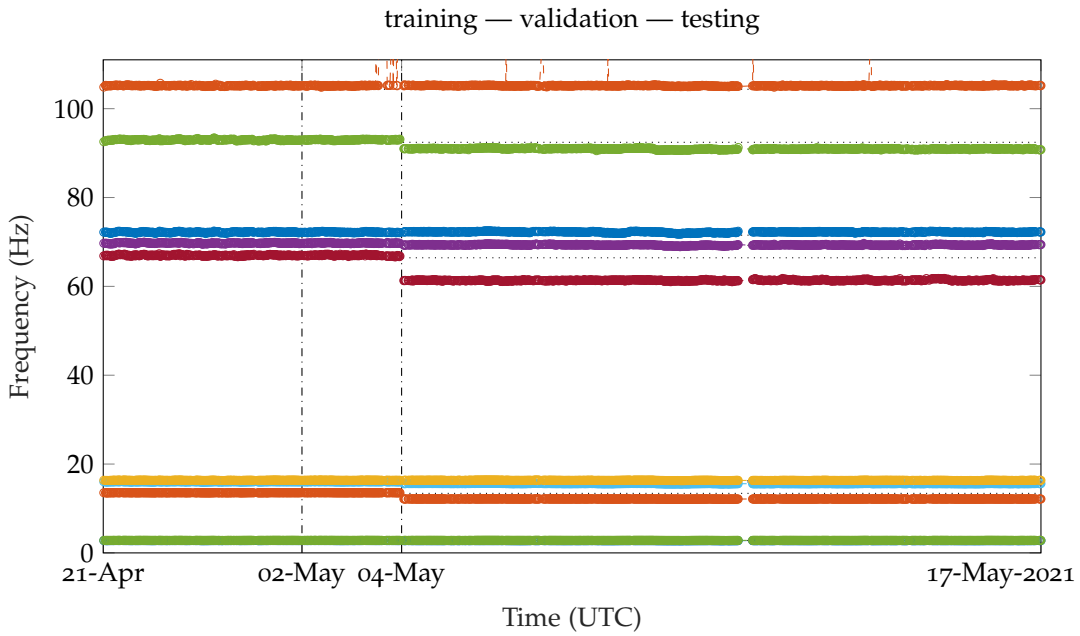

Figure 7.27: Natural frequencies corresponding to model selection strategy 2 defined in Tab. 7.4. Localization of removal of single damage mechanism at damage level 6.

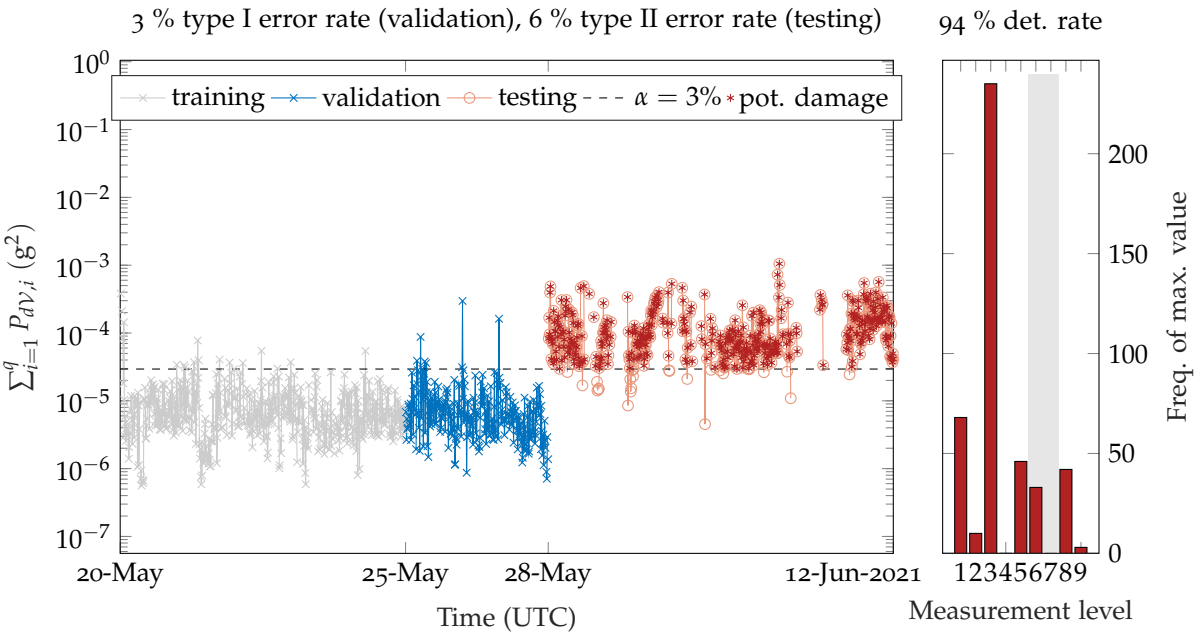

Figure 7.28: Power feature for localization of removal of single damage mechanism at damage level 4. Damage localization and data normalization by LPV-based SP2E. Model selection according to strategy 2 defined in Tab. 7.4.

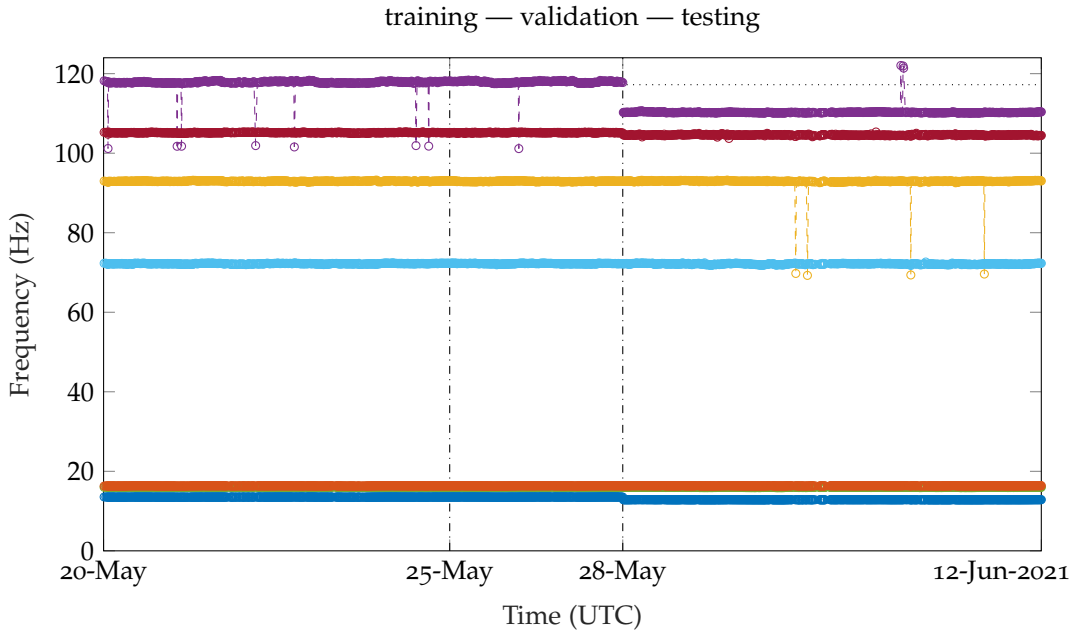

Figure 7.29: Natural frequencies corresponding to model selection strategy 2 defined in Tab. 7.4. Localization of removal of single damage mechanism at damage level 4.

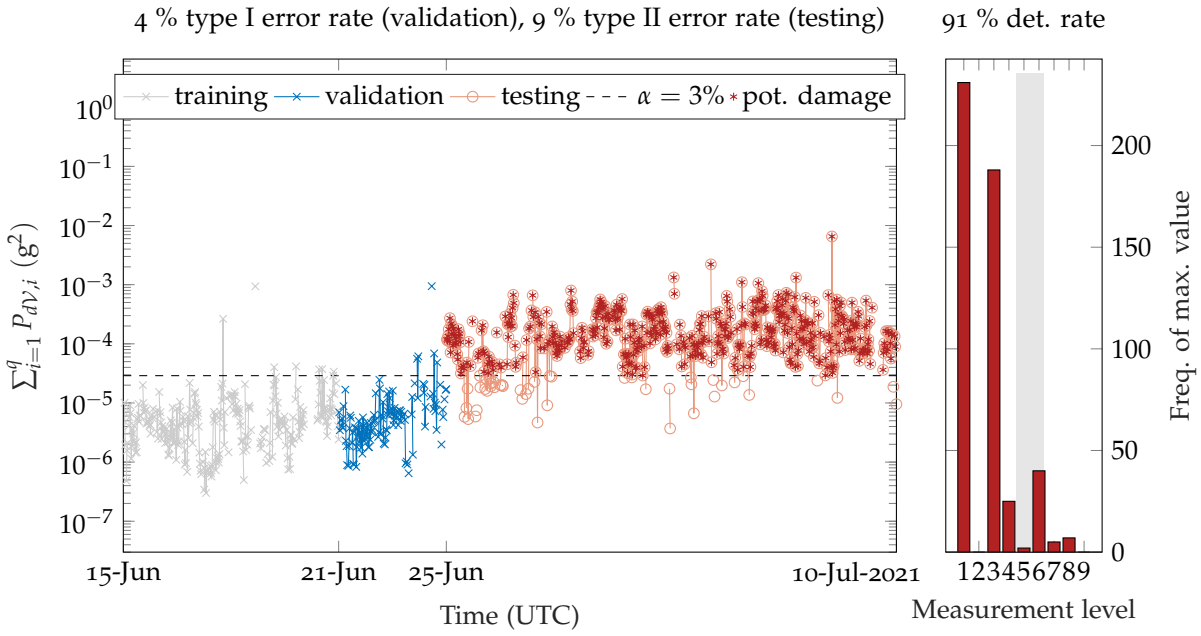

Figure 7.30: Power feature for localization of removal of single damage mechanism at damage level 3. Damage localization and data normalization by LPV-based SP2E. Model selection according to strategy 2 defined in Tab. 7.4.

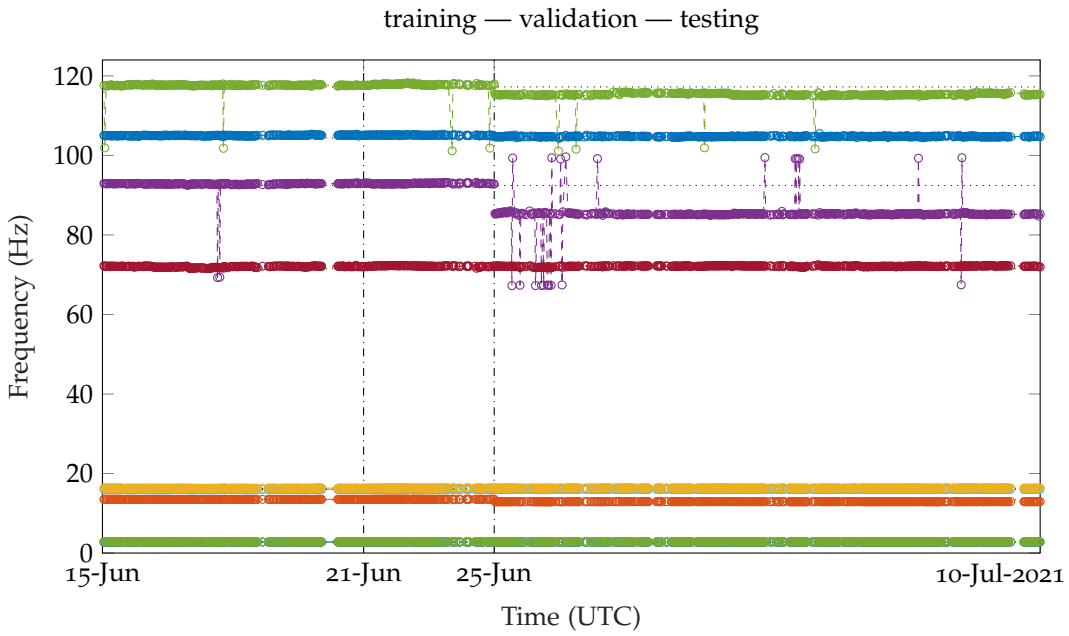

Figure 7.31: Natural frequencies corresponding to model selection strategy 2 defined in Tab. 7.4. Localization of removal of single damage mechanism at damage level 3.

7.4 FURTHER ASSESSMENT OF DAMAGE IDENTIFICATION RESULTS

The results presented before suggest that a thorough model selection is required to increase the chance of detecting small damages. Moreover, the corresponding modal tracking provides valuable insight into the structure's dynamic behavior before and after the occurrence of damage. As for the regarded experiment, the results associated with the less severe damage (Figs. 7.27, 7.29, and 7.31) reveal that removing a single damage mechanism mainly affects the torsional modes, while, on first sight, the bending modes appear to be unaffected by the damage. This makes perfect sense since the diagonal struts almost entirely contribute to the lattice mast's torsional stiffness. Thus, to complete the studies associated with the considered experiment and to provide a better basis for evaluating the outcome of the damage analyses, the lastly presented damage case (removal of a single damage mechanism at DAM3) shall be further investigated from a modal perspective. Therefore, modes T4 and B4-x are studied in terms of MAC values and natural frequencies.

Figs. 7.32 and 7.33 depict these quantities with respect to the material temperature and $\log(\mathrm{var}\{\mathrm{accel09}\})$. Similar plots for the severe damage case are additionally provided in Section A.4.3. The MAC values were computed by considering the reference mode shape determined before. Fig. 7.32 contains the results associated with the torsional mode T4 for the healthy and damaged structure, and Fig. 7.33 depicts the values corresponding to the bending mode B4-x. Basically, Fig. 7.32 repeats the information contained in Fig. 7.30, i.e., that the damage leads to a significant drop of the natural frequency, which is accompanied by a reduction of the MAC to approximately 0.9. This change can be recognized without the employment of any data normalization technique. On the other hand, the bending mode represented by Fig. 7.33 is clearly less affected by the damage, as mentioned before. This is manifested by the natural frequency values of the healthy and damaged structure, which spread similarly across the considered parameter space. However, the corresponding MAC values display a significant drop caused by the damage. Figs. 7.32 and 7.33 confirm the impression that the removal of even a single damage mechanism has a tremendous impact on LUMO's structural dynamics. The damage leads to a change in natural frequencies and MAC values that can be recognized even without the use of data normalization strategies. This circumstance stands in contrast to the damage identification results presented in the previous section that fail to reflect the significance of the considered damage scenario.

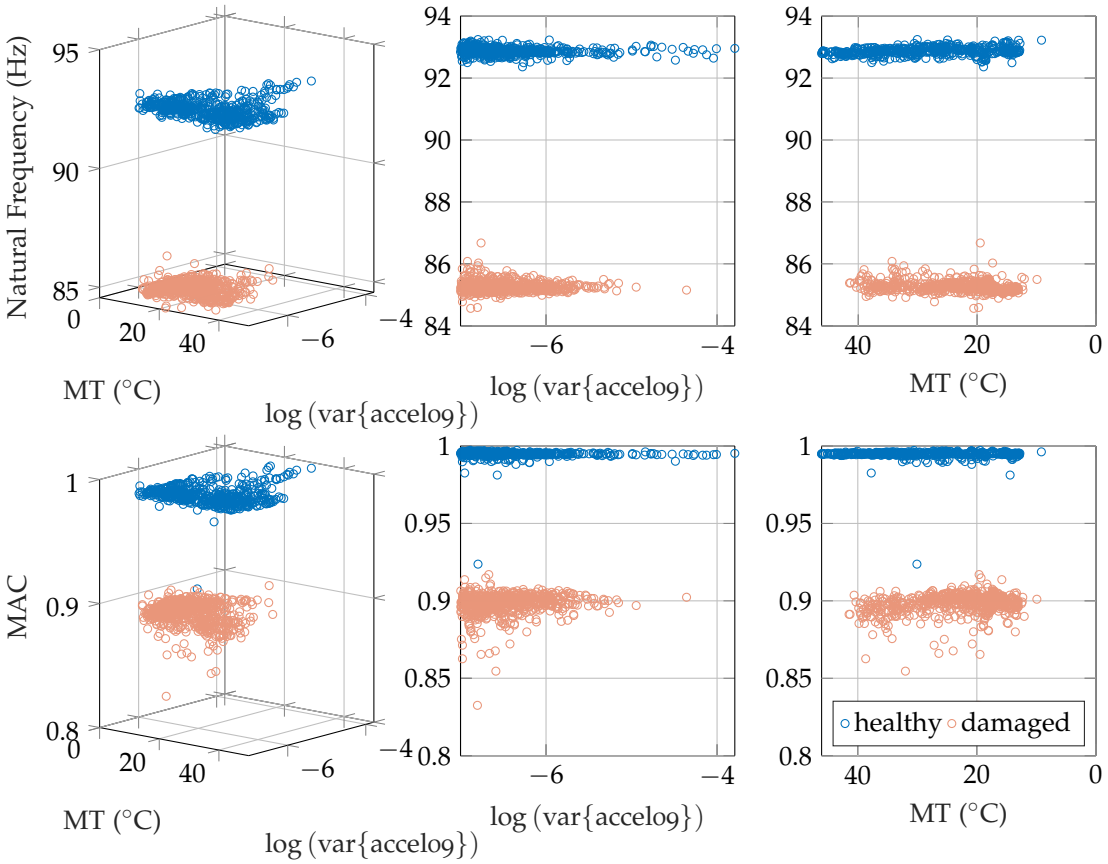

Figure 7.32: Comparison of natural frequencies and MAC values of mode T4 (plotted against material temperature [MT] and log[var{accelo9}] [log (g^2)]) referring to healthy structure and with single damage mechanism removed at damage level 3.

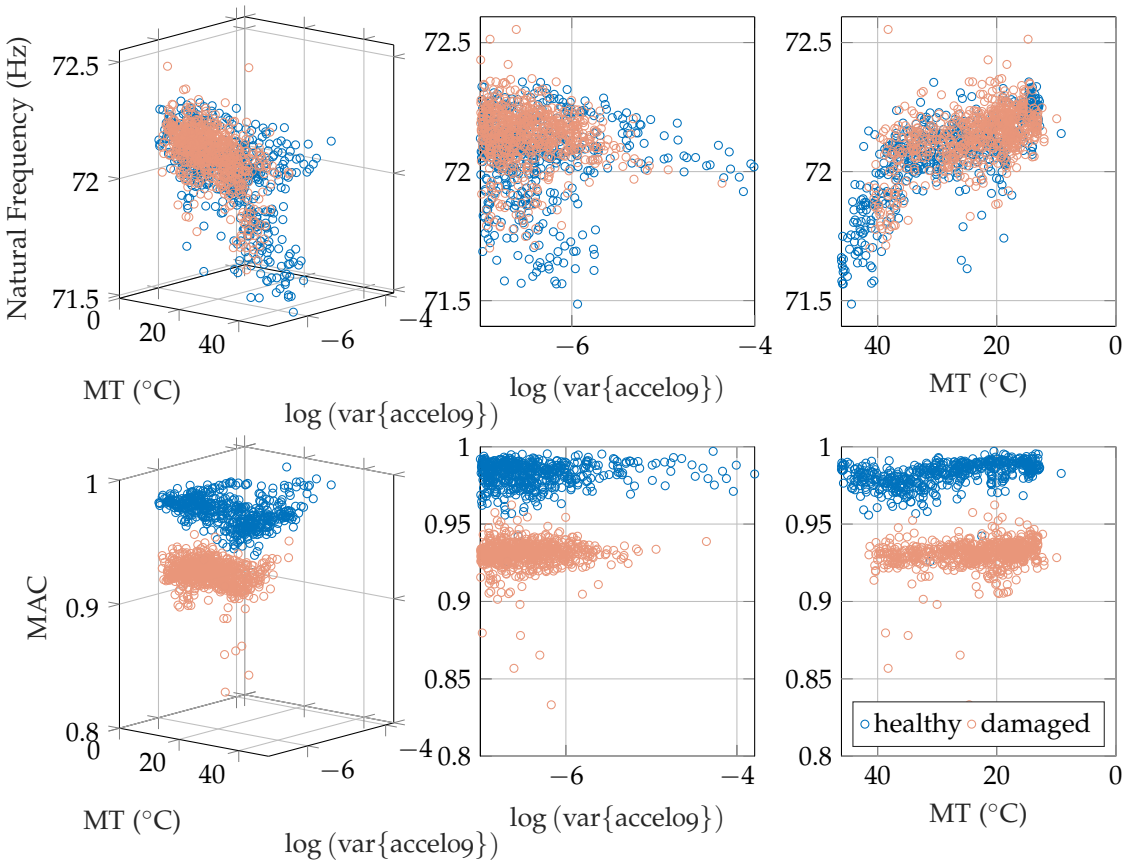

Figure 7.33: Comparison of natural frequencies and MAC values of mode B4-x (plotted against material temperature [MT] and log[var{accelo9}] [log (g^2)]) referring to healthy structure and with single damage mechanism removed at damage level 3.

7.5 CONCLUDING REMARKS

This chapter provides a real-life validation of the methods introduced in Chapters 4, 5, and 6. The corresponding techniques and procedures are applied to localizing joint stiffness and mass alterations at a lattice mast (LUMO) located outside. The presented investigations show that the parametric ALS and the LPV-based SP2E approach are practically applicable for monitoring structures with approximately linear and stationary short-term dynamics and parameter-varying (or nonstationary) and nonlinear long-term dynamics. Damages at three different levels and with two different degrees of severity could be detected under ambient excitation and EOV. Proper localization could only be announced for the more severe case. It was demonstrated that a modal-based model selection should be followed to achieve the highest sensitivity towards damage. However, all damages could even be noted by means of natural frequency and MAC shifts without further data normalization. Therefore, given the extent of damage and its effect on the considered damage indicators, it is doubtful that damage detection would have been feasible if minor and practically relevant damages occurred.

It is not trivial to explain the reduced sensitivity towards damage compared to one observed in simulation studies (cf. Chapter 6). One might argue that the signal quality associated with simulations is higher than when real measurements are involved. However, this fact probably has only a minor impact on the final damage analysis. The reason is that once the observed system is identified and a parametric system model exists, the processing of data is no longer required, and the quality of the numerical models is always equal. Thus, it could be concluded that if the data quality is sufficient to derive proper images of the structure under surveillance, damage identification should be feasible with high sensitivity. In the case of LUMO, the signal quality is excellent, and the modeling of the structure via SSI works properly. This can be recognized by the identification of a high number of modes. More importantly, the greatest differences between simulations and experimental studies are manifested in the signal characteristics, which are intrinsically linked to the excitation. When ambient excitation is present, which is generally the case for structures located outdoors, the whiteness assumption is always violated, and not only the magnitude of excitation but only the spectral distribution of the signal energy varies continuously. These variations and violations are not accounted for by the considered damage analysis and system modeling schemes (short- and long-term modeling), and therefore, could be picked up by the considered damage indicators, leading to increased values even when the structure is entirely intact. In future research, more elaborate strategies for the normalization concerning the excitation should be developed and tested. This demand for innovation is complicated by the output-only nature of the applied methods. That is, information regarding the signal characteristics of the input is generally not available, and thus, should be derived from measured vibrations of the structure.

8

SUMMARY, CONCLUSION, AND OUTLOOK

In the following, a summary of the present thesis is given, and the work is concluded. Finally, recommendations for future research are presented.

8.1 SUMMARY

This thesis is dedicated to the use of linear quadratic estimation theory for damage localization in data-driven vibration-based SHM. Therefore, the central elements of the latter are defined and reviewed first. Since in SHM, damage is inferred from changes in the dynamic behavior of mechanical systems under EOV, this engineering discipline comprises (i) the capturing of short-term dynamics, (ii) the capturing of long-term dynamics, (iii) the actual damage analysis, and (iv) the consideration of uncertainty in tasks (i) to (iii). This work addresses the damage localization problem under consideration of all four subtasks, and thus, constitutes a validation of the proposed methods for the real-life application in SHM. Contributions are made concerning all subjects (i) to (iv).

On a short-term scale, structures are viewed as LTI systems throughout this thesis. Therefore, after introducing the scope and objectives, the fundamental theory of structural dynamics of such systems is presented. That is followed by introducing the SSI technique considered for their realization based on measured vibration data. Two different theories are considered for the design of filters or predictors for the acquired outputs, namely, the Kalman filter ($\mathcal{H}_2$) and $\mathcal{H}_\infty$ filter theories. They are subsequently summarized. A general framework for optimal control is introduced, and the theoretical basis is laid before providing unified formulations for the related design problems. The fundamentals part is closed by presenting the adapted damage analysis framework, which employs identified LTI systems and linear quadratic estimators in a purely parametric fashion. Here, a contribution is made by formulating an alternative (variance-based) damage indicator that can increase the sensitivity towards localized damage. Another contribution is manifested by providing criteria that help to assess the potential of linear quadratic estimators for damage identification prior to application.

The second part of this thesis constitutes the main novelties and application and validation cases. To pave the way for proper consideration of Kalman filters within the parametric damage analysis framework, a modified version of the well-known ALS technique is presented. The proposed method links the ability of the SSI to parameterize the PSD and correlation function of data applied for system identification to the ALS technique. By that, a data-free estimation for noise covariance matrices, applicable for Kalman filter tuning, is enabled. The implementation of the ALS method is validated in several simulations by comparing the estimated covariance matrices with those used for the simulation studies. Finally, the effectiveness of the parametric ALS in the context of Kalman filter-based damage localization is demonstrated in both simulation and experimental cases. Next, the problem of monitoring

under varying EOCs is addressed. Therefore, an interpolation-based identification scheme is introduced, which interprets the monitored structures as LPV systems. For this data normalization approach, local LTI systems associated with certain operational points are interpolated through weightings determined through barycentric coordinates. The resulting identified LPV systems are readily considered within the proposed damage analysis framework and thus, enable damage localization under varying EOCs. This approach is also applicable when the long-term dynamics are affected nonlinearly by varying EOCs, as shown in a simulation study of an LPV system. Finally, the central contributions, namely the PALS technique and the interpolation-based LPV identification, are applied in a real-life scenario by considering an outdoor test structure for SHM. The study shows that the methods are applicable in practice and that localized damage can be identified under consideration of realistic environmental factors that significantly influence the structure's dynamic behavior. Six different damage cases, constituting three different positions and two different extents of damage, are considered. While the continuous localization of the more severe cases is successful, the minor damages cases emphasize the potential for further advancements and research in the field of system identification and model selection.

8.2 CONCLUSION

Individual concluding remarks are presented for Chapters 3, 5, 6, and 7. This section constitutes an overall conclusion in view of the main goals and objectives of this thesis.

This thesis confirms the practical usability of linear quadratic estimators for data-driven vibration-based SHM by successfully detecting and localizing damages at a girder mast located outdoors and exposed to natural sources of excitation and uncertainty. Therefore, the central objective of the present work, the validation under realistic conditions, is fulfilled. However, the effect of the considered damage cases exceeded the influence of the environmental variability, so the efficacy of proposed data normalization strategies could not be proven. In fact, it must be suspected that in the regarded case, the detection of minor damages under the presence of changing environmental conditions would have failed. Nevertheless, the potential for improvements in view of the input-related normalization was recognized.

The presented validation study is essentially enabled through several contributions concerning the main subjects of SHM, which comprise the capturing of short-term and long-term dynamics, the actual damage analysis, and uncertainty consideration. The proposed approach to SHM assumes LPV characteristics of the structure under surveillance. This defines the long-term dynamic behavior. On shorter time scales, the observed structures are approximated as LTI systems. Capturing the long-term dynamics of structures refers to the problem of data normalization that can be performed implicitly or explicitly. The latter was aimed for in this thesis. It constitutes an interesting approach from a system theoretical point of view, as it attempts to identify functional dependence models of the structure's dynamic behavior and EOCs. In this work, a damage analysis framework designed for linear quadratic estimators is combined with a local approach for LPV system identification. Therefore, an interpolation scheme was adapted to identify interpolated reference estimators within m-dimensional EOC spaces. These systems can then be applied for damage detection and localization. By that, the long-term dynamic behavior of the observed system is inherently captured, and the de-

pendence on EOCs is explicitly identified. This interpolation scheme is tempting, as, on the one hand, even nonlinear dependencies can be modeled, and, on the other hand, many affecting EOCs can be considered. This thesis provides validation examples for the one-parameter ($m = 1$) and two-parameter ($m = 2$) case. First, the interpolation approach was employed in a simulation study involving an LPV system and finally in the outdoor experiment. In both cases, damages manifested as mass and/or stiffness alterations could be detected and localized. This confirms the suitability of the proposed explicit, interpolation-based data normalization strategy, and thus, contributes to the problem of capturing the long-term dynamics of systems.

The effective utilization of Kalman filters for this LPV-based damage identification was enabled by using the ALS method for noise covariance estimation. This well-known approach was extended so that the direct use of measurement data becomes obsolete in the actual least-squares problem. Hence, the developed PALS method, which constitutes the parametric extension of ALS, can be employed when the plants for the Kalman filter synthesis are identified with the help of SSI. This case pertains to the entire thesis. PALS is advantageous as it decreases the disturbing effect of dynamics encompassed in the measurement data but not represented by the identified systems. In this work, the efficacy of this approach could be demonstrated in several laboratory experiments and the final validation case. Since in the latter, the alternative $\mathcal{H}_\infty$ filter theory failed to produce estimators featuring a decent estimation performance, PALS-tuned Kalman filters could be employed instead. Therefore, these estimators provide a valuable alternative for the SP2E-based damage analysis, which was initially developed for the use of $\mathcal{H}_\infty$ filters.

The development of the PALS technique, the adaption of the interpolation-based LPV identification, and its combination with the SP2E-based damage analysis framework constitute the novelties put forward in this thesis. Two further contributions are made for damage analysis and the consideration of uncertainty. First, an alternative variance-based damage indicator was derived from the SP2E method. The feature was applied with success for all investigations regarding damage identification. More importantly, two assumptions were formulated in this regard to enable the a priori assessment of the suitability of linear quadratic estimators for damage identification. They are hoped to increase the confidence when predictors and filters are applied in future applications. As for the cases considered in this thesis, the postulated criteria proved to be helpful for the setup of the proposed SHM methodology.

8.3 OUTLOOK

Since this thesis only considers systems that exhibit approximately linear and stationary dynamics on a short-term scale, future work should concentrate on extending the proposed methodologies for nonstationary and possibly nonlinear systems. The former describes a straightforward step concerning the linear quadratic estimation theory. These techniques were developed for finite-horizon applications and can thus be adapted for monitoring systems that feature significant time variance. A greater challenge is posed by the output-only identification and realization of state-space models for such systems, which must be addressed first. In the present work, systems were identified using the SSI technique, resulting in the realization of LTI systems. Naturally, this method cannot be applied in the case of LTV systems, and thus,

alternative approaches must be considered. The extension to significantly nonlinear systems appears particularly challenging but would constitute an exciting research objective.

Besides these potential developments concerning different dynamic behavior of systems, some of the presented methods hold potential for improvements as well. For instance, the noise covariance estimation by (P)ALS could be enhanced concerning the solution of the central least-squares problem. Throughout this work, the number of lags of the innovations covariance function was chosen to be relatively small, although one would preferably set it as large as possible. Unfortunately, this parameter strongly impacts the computational burden manifested by the least-squares problem and, therefore, has to be reduced for pragmatic reasons. An attractive alternative, which is worth investigating, would be to skip a few lags and to define a sparse least-squares problem instead. Further improvements could be achieved by performing (P)ALS for different lag ranges in parallel.

One of the thesis's central contributions is applying interpolated LTI systems in combination with the SP2E framework. Interpolation is enabled by assigning weightings to the output equation of state-space models representing different operating points. The dynamic behavior for a given set of EOCs is indirectly interpolated, although it would be more desirable to obtain new models that feature interpolated poles. In addition to this being particularly appealing from a system theoretical point of view, it would also result in a more parsimonious system representation and allow the further analysis of the interpolated system, e.g., for modal analysis.

At last, particular attention should be paid to the practical application of the proposed techniques. The presented validation case confirms the applicability of the methodology in real life, yet it demands improvement regarding the sensitivity towards damage. A possible strategy to achieve that is, besides the aforementioned points, to improve normalization concerning structural excitation. When ambient excitation is present, the whiteness assumption of the inputs is violated, and the spectral distribution of the signal energy varies strongly. These points are not considered by the considered damage analysis scheme and system identification approaches of short- and long-term modeling. Hence, they should be considered by an enhanced normalization scheme, which is particularly challenging in the regarded output-only context. Therefore, the relevant information must be extracted from the acquired measurement data. Finally, to further assess the performance of the proposed SHM methodologies, comparisons to other methods would be of particular interest. That is readily facilitated through the open-access availability of the LUMO data.

Part III

APPENDIX

A

APPENDIX

This chapter chapter contains supplementary material for Chapters 2, 4, 6, and 7.

A.1 APPENDIX OF CHAPTER 2

In the following, the factorization of the covariance function $R_y(i) = \mathrm{E}\{y_{k+i}y_k^{\mathrm{T}}\}$ of y is derived for a state-space system as given in Eq. 2.74.

Note that the process noise w_k and measurement noise v_k are independent of the states x_k. Therefore,

$$\mathrm{E}\Big\{x_k w_k^{\mathrm{T}}\Big\} = 0,$$
$$\mathrm{E}\Big\{x_k v_k^{\mathrm{T}}\Big\} = 0,$$

and thus,

$$\mathrm{E}\Big\{y_k w_k^{\mathrm{T}}\Big\} = 0,$$
$$\mathrm{E}\Big\{y_k v_k^{\mathrm{T}}\Big\} = 0.$$

First, the covariance $R_y(0)$ is determined as

$$\begin{aligned} R_y(0) &= \mathrm{E}\Big\{y_k y_k^{\mathrm{T}}\Big\} \\ &= \mathrm{E}\Big\{\left[Cx_k + v_k\right]\left[Cx_k + v_k\right]^{\mathrm{T}}\Big\} \\ &= C\mathrm{E}\Big\{x_k x_k^{\mathrm{T}}\Big\}C^{\mathrm{T}} + C\mathrm{E}\Big\{x_k v_k^{\mathrm{T}}\Big\} + C\mathrm{E}\Big\{v_k x_k^{\mathrm{T}}\Big\} + \mathrm{E}\Big\{v_k v_k^{\mathrm{T}}\Big\} \\ &= C\Sigma C^{\mathrm{T}} + R. \end{aligned} \tag{A.1}$$

Further, to derive $R_y(i) = \mathrm{E}\{y_k y_k + i^{\mathrm{T}}\}$ for $i > 0$, it is helpful to formulate the evolution of the states:

$$\begin{aligned} x_{k+1} &= Ax_k + w_k, \\ x_{k+2} &= A(Ax_k + w_k) + w_{k+1} \\ &= A^2 x_k + Aw_k + w_{k+1}, \\ x_{k+3} &= A(A^2 x_k + Aw_k + w_{k+1}) + w_{k+2} \\ &= A^3 x_k + A^2 w_k + Aw_{k+1} + w_{k+2} \end{aligned}$$

etc., which can be summarized as

$$x_{k+i} = A^i x_k + \sum_{l=1}^{i} A^{l-1} w_{k+i-l}. \tag{A.2}$$

With the help of that, $R_y(i) = \mathrm{E}\{y_k y_k + i^\mathrm{T}\}$ for $i > 0$ finally yields

$$\begin{aligned}
R_i &= \mathrm{E}\Big\{y_{k+i} y_k^\mathrm{T}\Big\} \\
&= \mathrm{E}\Big\{\left[Cx_{k+i} + v_{k+i}\right]\left[Cx_k + v_k\right]^\mathrm{T}\Big\} \\
&= \mathrm{E}\left\{\left[C\left(A^i x_k + \sum_{l=1}^{i-l=0} A^{i-l} w_{k+l-1}\right) + v_{k+i}\right]\left[Cx_k + v_k\right]^\mathrm{T}\right\} \\
&= \mathrm{E}\left\{\left[CA^i x_k + C\sum_{l=1}^{i-l=0} A^{i-l} w_{k+l-1} + v_{k+i}\right]\left[Cx_k + v_k\right]^\mathrm{T}\right\} \\
&= CA^i \mathrm{E}\Big\{x_k x_k^\mathrm{T}\Big\} C^\mathrm{T} + CA^i \mathrm{E}\Big\{x_k v_k^\mathrm{T}\Big\} + C\sum_{l=1}^{i-l=0} A^{i-l} \mathrm{E}\Big\{w_{k+l-1} x_k^\mathrm{T}\Big\} C^\mathrm{T} \\
&\quad + C\sum_{l=1}^{i-l=0} A^{i-l} \mathrm{E}\Big\{w_{k+l-1} v_k^\mathrm{T}\Big\} + \mathrm{E}\Big\{v_{k+i} x_k^\mathrm{T}\Big\} C^\mathrm{T} + \mathrm{E}\Big\{v_{k+i} v_k^\mathrm{T}\Big\} \\
&= CA^i \mathrm{E}\Big\{x_k x_k^\mathrm{T}\Big\} C^\mathrm{T} + CA^{i-1} \mathrm{E}\Big\{w_k v_k^\mathrm{T}\Big\} \\
&= CA^i \Sigma C^\mathrm{T} + CA^{i-1} S \qquad \text{(A.3a)} \\
&= CA^{i-1} N. \qquad \text{(A.3b)}
\end{aligned}$$

Eqs. A.1 and A.3b together yield Eq. 2.81. Note that the transition from Eq. A.3a to Eq. A.3b is enabled by the covariance of future states and output:

$$\begin{aligned}
N &= \mathrm{E}\Big\{x_{k+1} y_k^\mathrm{T}\Big\} \\
&= \mathrm{E}\Big\{\left[Ax_k + w_k\right]\left[Cx_k + v_k\right]^\mathrm{T}\Big\} \\
&= A\mathrm{E}\Big\{x_k x_k^\mathrm{T}\Big\} C^\mathrm{T} + A\mathrm{E}\Big\{x_k v_k^\mathrm{T}\Big\} + \mathrm{E}\Big\{w_k x_k^\mathrm{T}\Big\} C^\mathrm{T} + \mathrm{E}\Big\{w_k v_k^\mathrm{T}\Big\} \\
&= A\Sigma C^\mathrm{T} + S. \qquad \text{(A.4)}
\end{aligned}$$

A.2 APPENDIX OF CHAPTER 4

If $\mathbf{\Omega}$ is assembled according to Eq. 4.9, then $Z = I$ in Eq. 4.18.

Proof. Substitute Eq. 4.18 into Eq. 4.17, and then, assemble $A_\Omega X = X\Lambda$ according to Eq. 4.13 with the help of Eq. 4.9a. This yields

$$\begin{bmatrix} A_{p,1}X_{11} & 0 & A_{p,1}X_{13} + K_{p,1}C_2X_{33} \\ 0 & A_{p,2}X_{22} & A_{p,2}X_{23} + K_{p,2}C_2X_{33} \\ 0 & 0 & A_2X_{33} \end{bmatrix} = \begin{bmatrix} X_{11}\Lambda_1 & 0 & X_{13}\Lambda_3 \\ 0 & X_{22}\Lambda_2 & X_{23}\Lambda_3 \\ 0 & 0 & X_{33}\Lambda_3 \end{bmatrix}. \tag{A.5}$$

Multiplying this equation with X_{33}^{-1} from the right leads to

$$\begin{bmatrix} A_{p,1}X_{11} & 0 & A_{p,1}X_{13}X_{33}^{-1} + K_{p,1}C_2 \\ 0 & A_{p,2}X_{22} & A_{p,2}X_{23}X_{33}^{-1} + K_{p,2}C_2 \\ 0 & 0 & A_2 \end{bmatrix} = \begin{bmatrix} X_{11}\Lambda_1 & 0 & X_{13}\Lambda_3X_{33}^{-1} \\ 0 & X_{22}\Lambda_2 & X_{23}\Lambda_3X_{33}^{-1} \\ 0 & 0 & X_{33}\Lambda_3X_{33}^{-1} \end{bmatrix}, \tag{A.6}$$

and reveals that

$$\Lambda_3 = X_{33}^{-1}A_2X_{33}, \tag{A.7}$$

by regarding the lowest block row. Consequently, Λ_3 contains the eigenvalues of A_2. Further, substituting Eq. A.7 into Eq. A.6 shows that

$$A_{p,1}Y + K_{p,1}C_2 = YA_2 \quad \text{and} \quad A_{p,2}Z + K_{p,2}C_2 = ZA_2. \tag{A.8}$$

Since the closed-loop matrix $A_{p,2}$ is defined as $A - K_{p,2}C_2$, Z must be identity. □

A.3 APPENDIX OF CHAPTER 6

Algorithmus 1 : Interpolation-based LPV identification

Input : grid of local LTI models (local reference estimators)
corresponding sets of EOC values $\bar{\theta}$
EOC grid distance $\Delta\theta$
current set of EOCs θ_k

Output : LPV system $\mathbf{\Pi}_1^{-1}$
weightings κ

$\dim\bar{\theta} \leftarrow$ dimension of considered EOC space
define $\tilde{\bar{\theta}} = \bar{\theta}$ and $\tilde{\theta}_k = \theta_k$
normalize $\tilde{\bar{\theta}}$ and $\tilde{\theta}_k$ such that $\tilde{\bar{\theta}} \in [0, 1]$
discard all local LTI models as well as EOC sets in $\bar{\theta}$ and $\tilde{\bar{\theta}}$ that correspond to $\bar{\theta} > \theta_k + 2\Delta\theta$ or $\bar{\theta} < \theta_k - 2\Delta\theta$
perform $\dim\bar{\theta}$-dimensional Delaunay triangulation for $\tilde{\bar{\theta}}$ (Matlab: `delaunayn`)

if $\tilde{\theta}_k$ *is included in some simplex obtained through Delaunay triangulation* (Matlab: `tsearchn`) **then**
  $V_{\tilde{\bar{\theta}}} \leftarrow$ vertices of surrounding simplex
  $a \leftarrow$ indeces of corresponding local LTI models
  $\kappa \leftarrow$ barycentric coordinates according to Eq. 6.7 given $V_{\tilde{\bar{\theta}}}$ and $\tilde{\theta}_k$
else
  $n_{\text{Close}} \leftarrow$ number of points represented by $\bar{\theta}$ that are in close vicinity of θ_k, i.e., $\bar{\theta} < \theta_k + \Delta\theta$ and $\bar{\theta} > \theta_k - \Delta\theta$
  if $n_{Close} > 0$ **then**
    $V_{\tilde{\bar{\theta}}} \leftarrow \min[n_{\text{Close}}, \dim\bar{\theta}]$ sets of EOCs contained in $\tilde{\bar{\theta}}$ closest to $\tilde{\theta}_k$
    $d_{V_{\tilde{\bar{\theta}}}} \leftarrow$ Euclidean distance between $V_{\tilde{\bar{\theta}}}$ and $\tilde{\theta}_k$
    $a \leftarrow$ indices of corresponding local LTI models
    $\kappa \leftarrow$ inverse distance weights such that $\kappa_i = \dfrac{1/d_{i,V_{\tilde{\bar{\theta}}}}}{\sum d_{V_{\tilde{\bar{\theta}}}}}$
  else
    $\kappa = 0$
  end
end

if $\kappa \neq 0$ **then**
  assemble $\mathbf{\Pi}_1^{-1}$ according to Eq. 6.3
end

A.4 APPENDIX OF CHAPTER 7

A.4.1 Appendix of Section 7.3.3

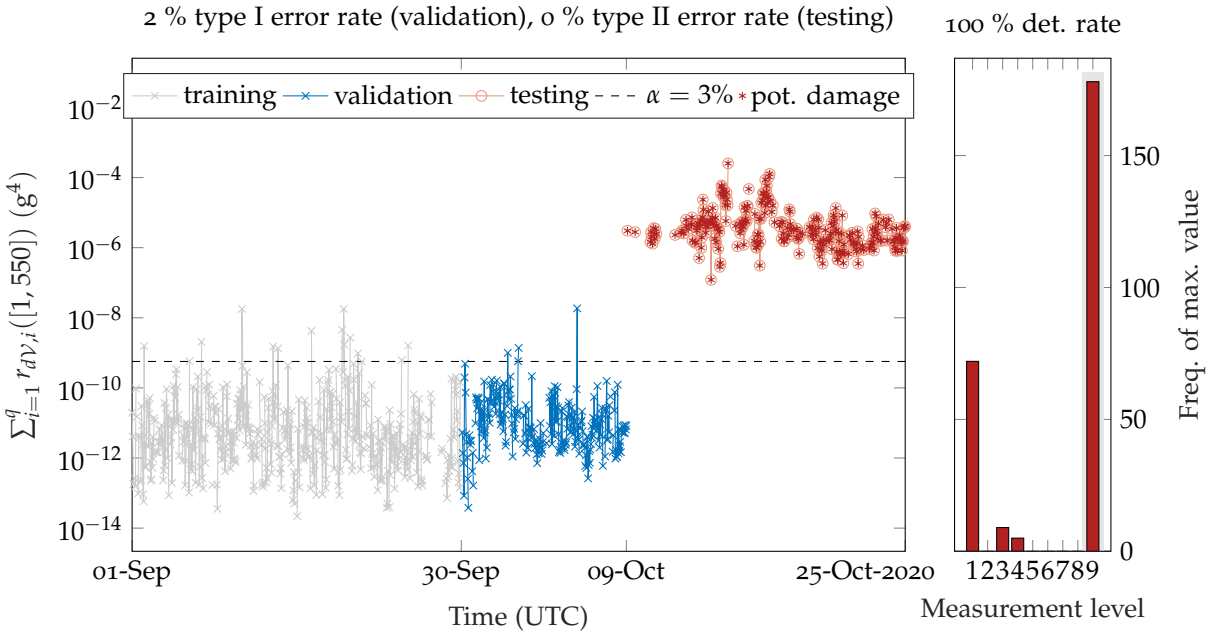

Figure A.1: Variance feature for localization of complete removal of damage mechanisms at damage level 6. Damage localization and data normalization by LPV-based SP2E. Model selection according to strategy 2 defined in Tab. 7.4.

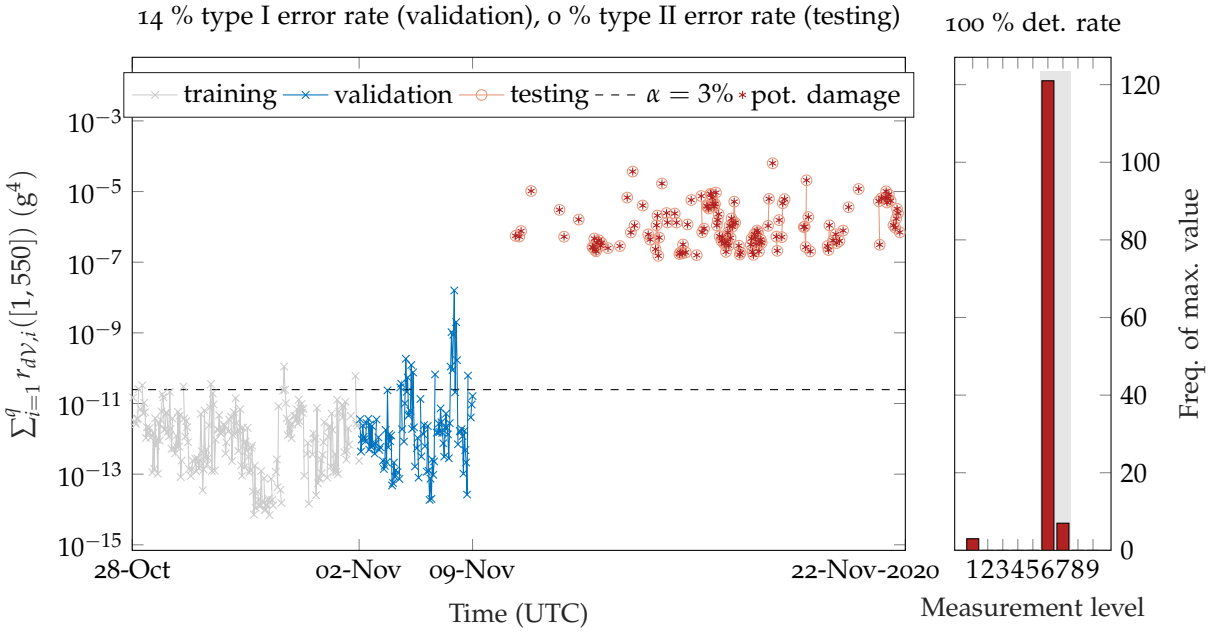

Figure A.2: Variance feature for localization of complete removal of damage mechanisms at damage level 4. Damage localization and data normalization by LPV-based SP2E. Model selection according to strategy 2 defined in Tab. 7.4.

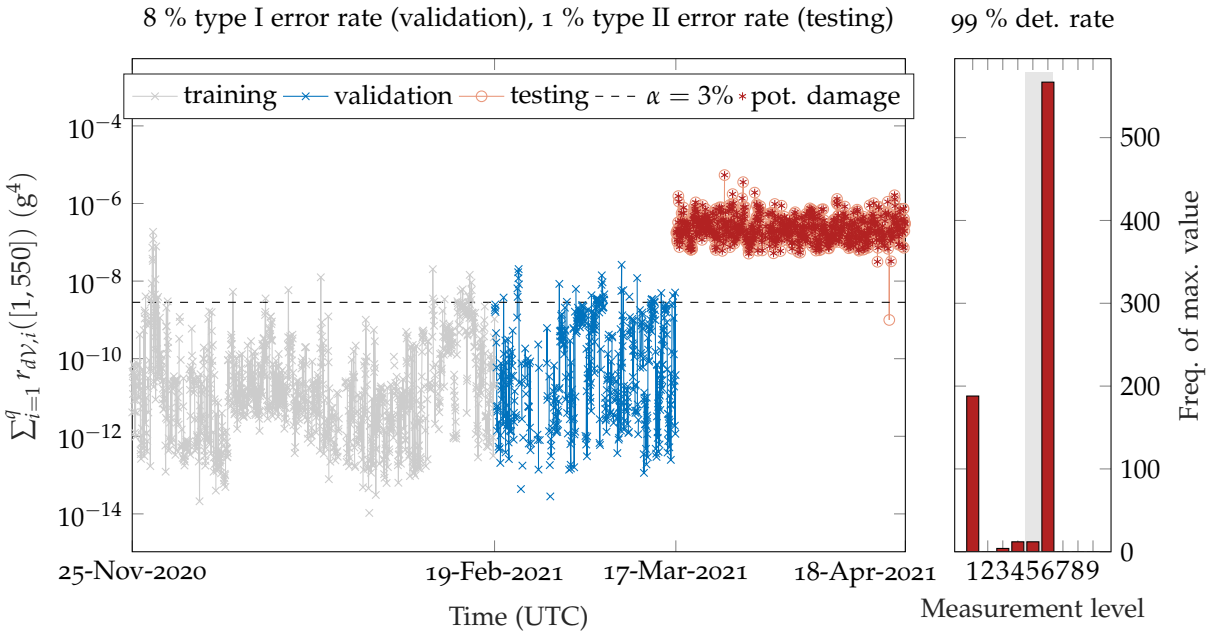

Figure A.3: Variance feature for localization of complete removal of damage mechanisms at damage level 3. Damage localization and data normalization by LPV-based SP2E. Model selection according to strategy 2 defined in Tab. 7.4.

A.4.2 Appendix of Section 7.3.4

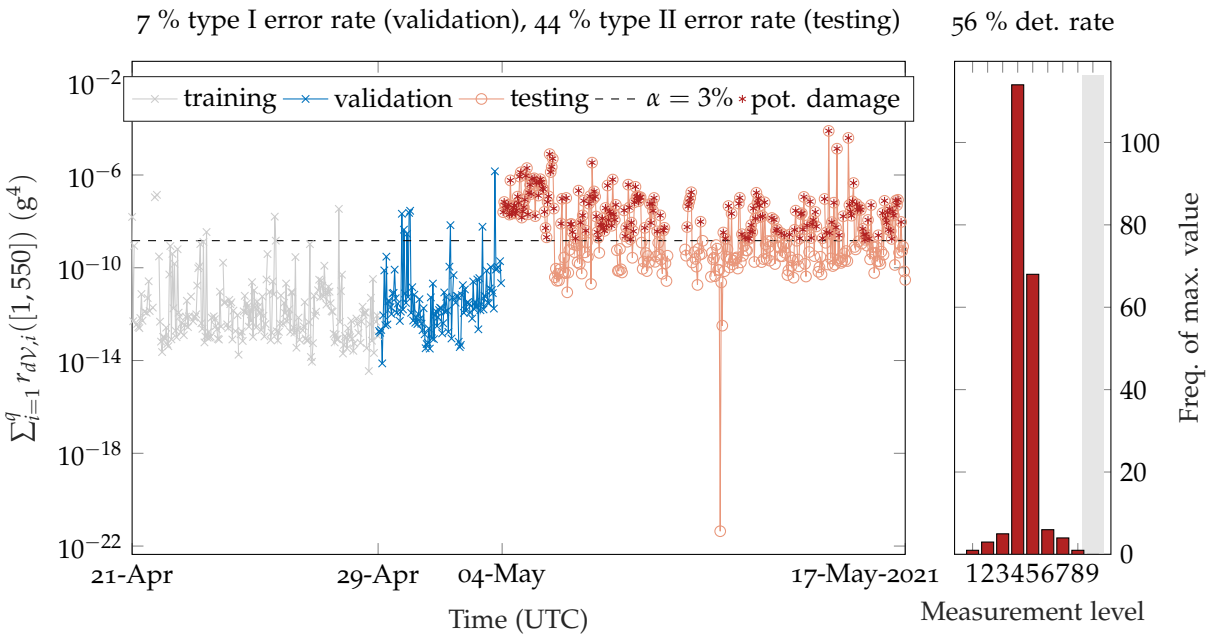

Figure A.4: Variance feature for localization of removal of single damage mechanism at damage level 6. Damage localization and data normalization by LPV-based SP2E. Model selection according to strategy 1 defined in Tab. 7.4.

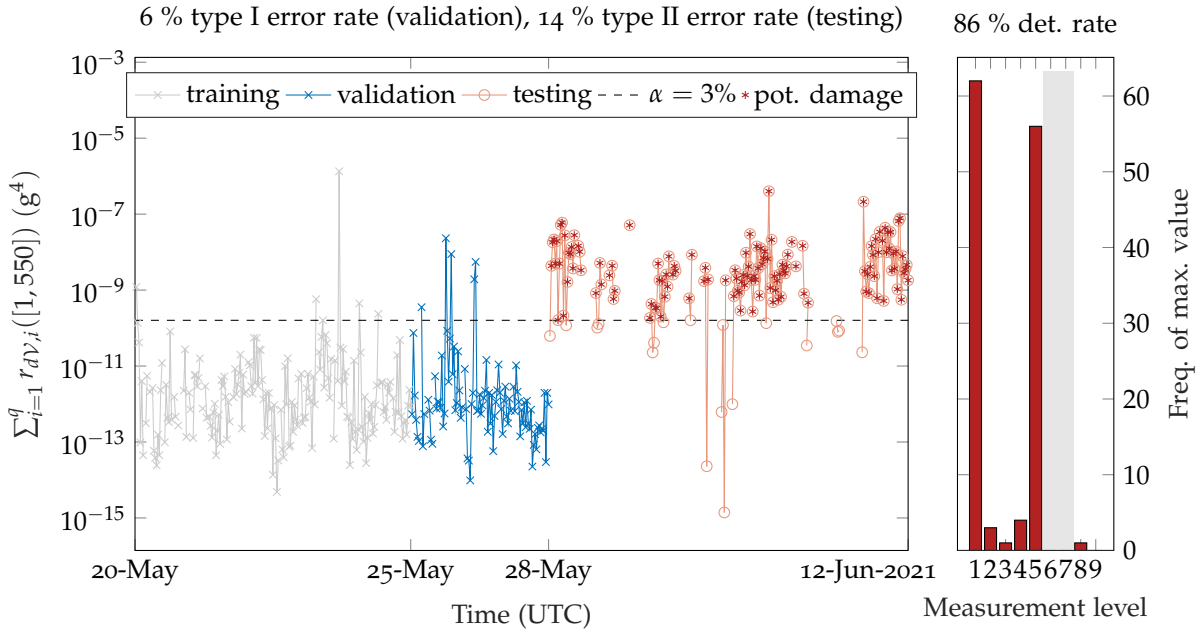

Figure A.5: Variance feature for localization of removal of single damage mechanism at damage level 4. Damage localization and data normalization by LPV-based SP2E. Model selection according to strategy 1 defined in Tab. 7.4.

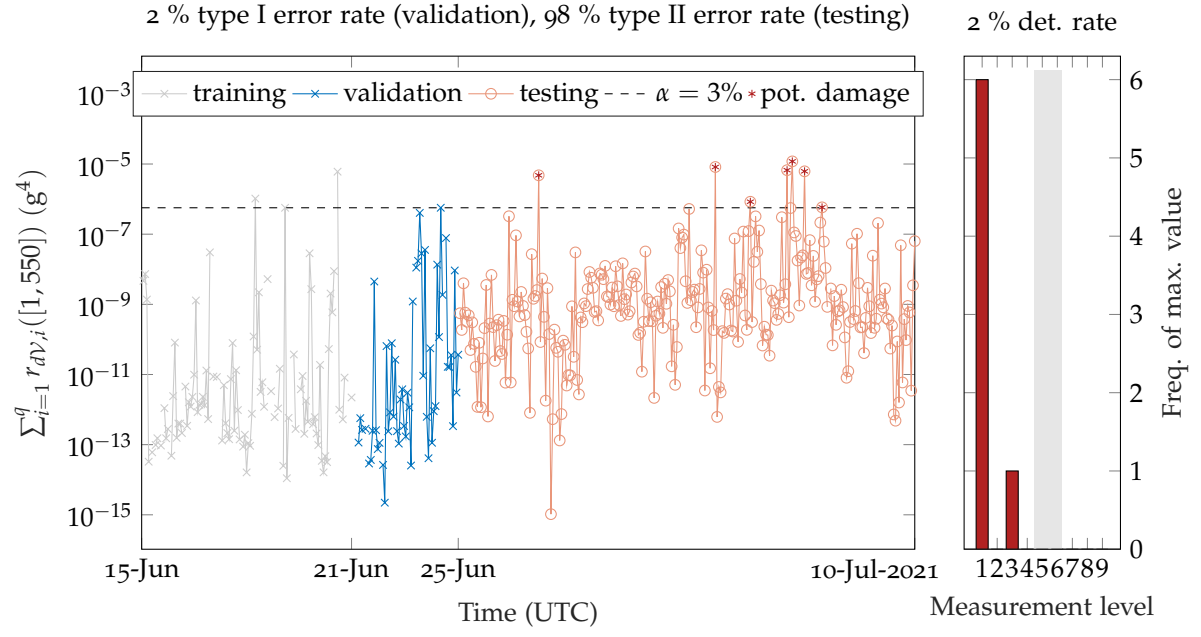

Figure A.6: Variance feature for localization of removal of single damage mechanism at damage level 3. Damage localization and data normalization by LPV-based SP2E. Model selection according to strategy 1 defined in Tab. 7.4.

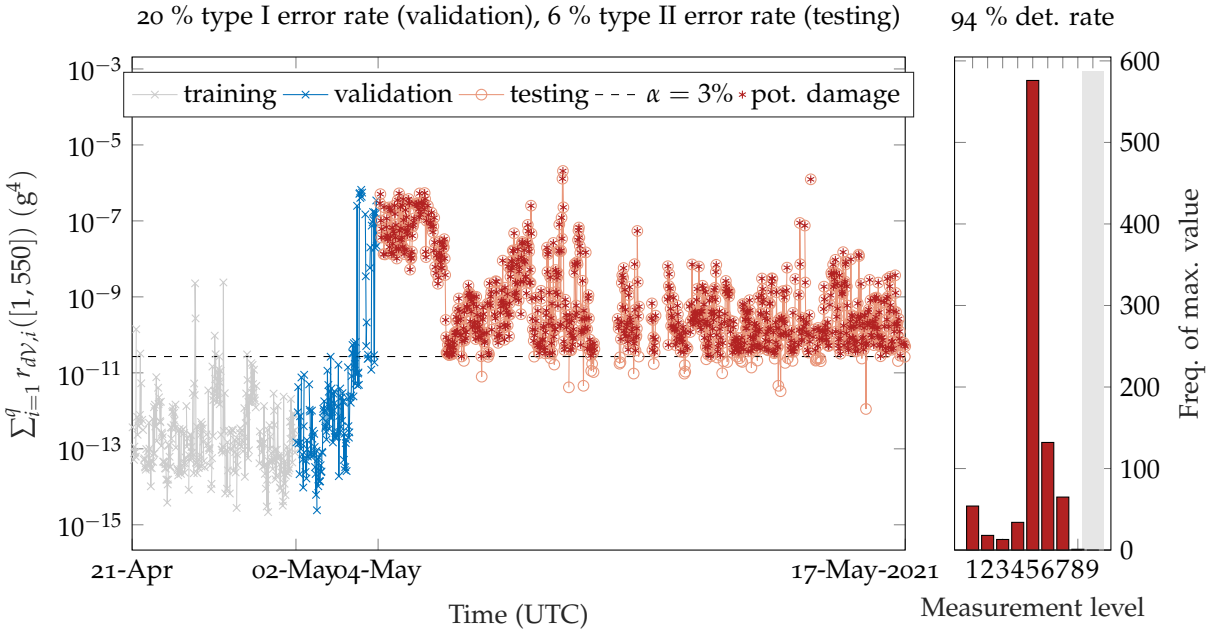

Figure A.7: Variance feature for localization of removal of single damage mechanism at damage level 6. Damage localization and data normalization by LPV-based SP2E. Model selection according to strategy 2 defined in Tab. 7.4.

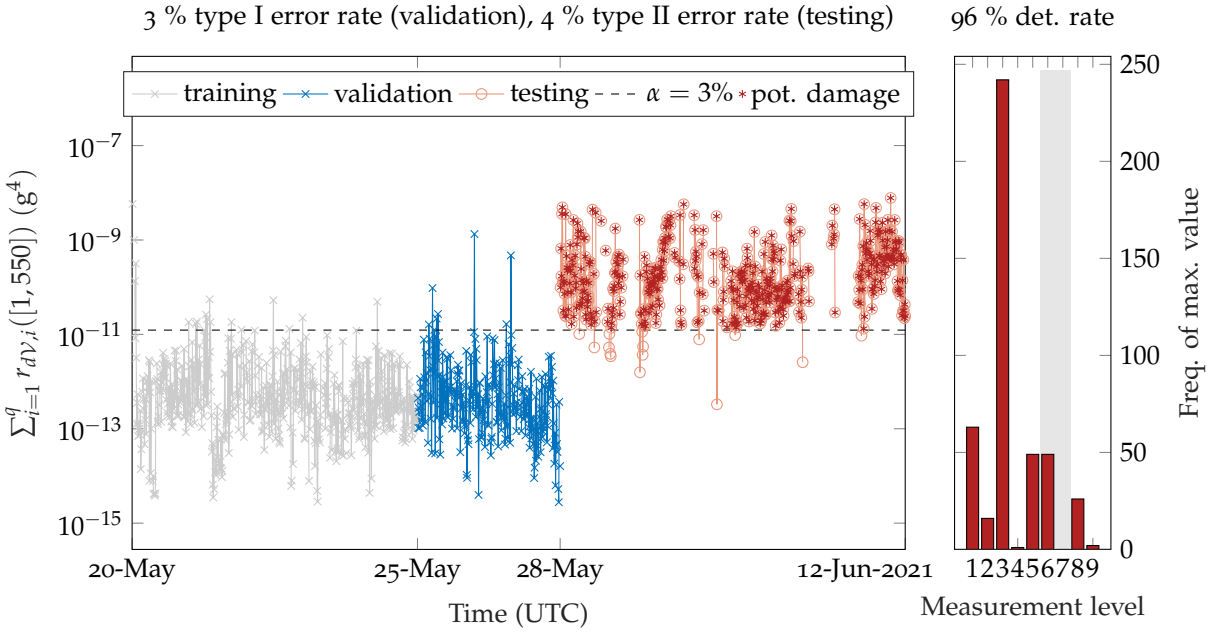

Figure A.8: Variance feature for localization of removal of single damage mechanism at damage level 4. Damage localization and data normalization by LPV-based SP2E. Model selection according to strategy 2 defined in Tab. 7.4.

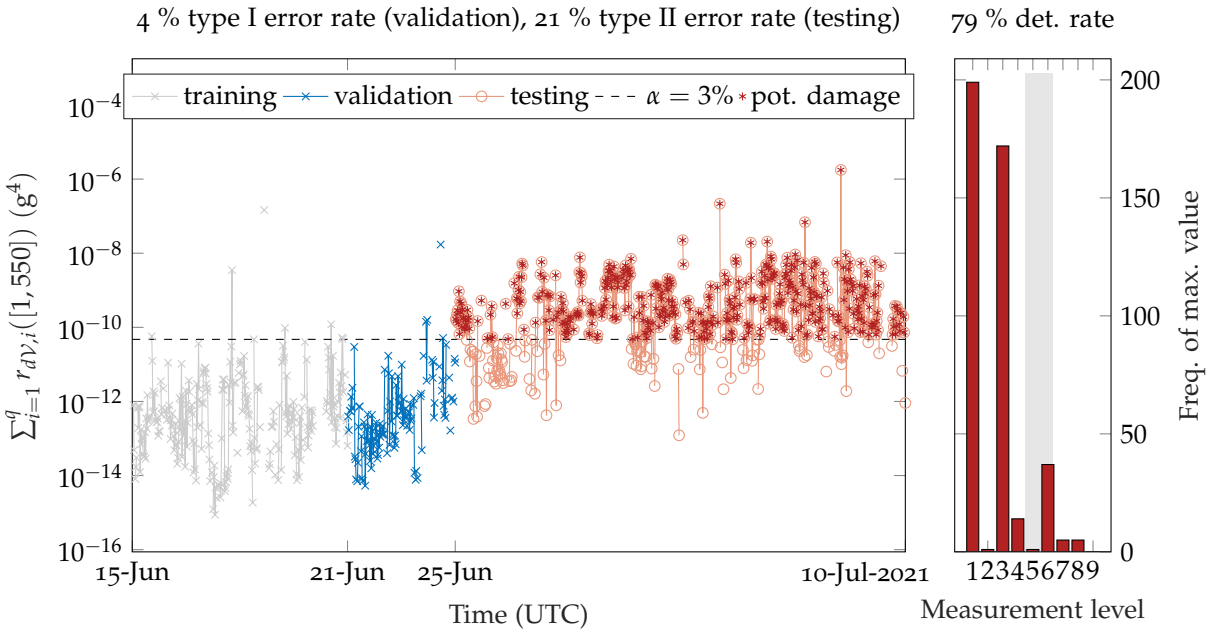

Figure A.9: Variance feature for localization of removal of single damage mechanism at damage level 4. Damage localization and data normalization by LPV-based SP2E. Model selection according to strategy 2 defined in Tab. 7.4.

A.4.3 Appendix of Section 7.3.5

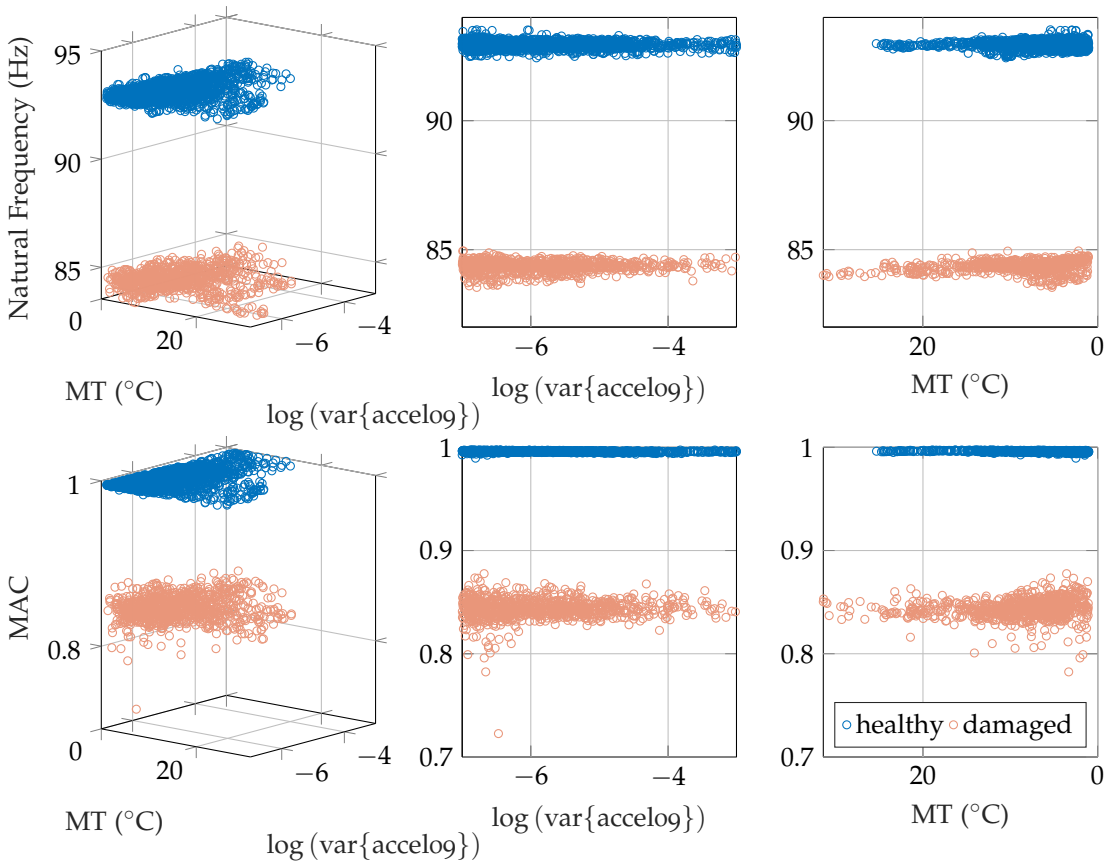

Figure A.10: Comparison of natural frequencies and MAC values of mode T4 (plotted against material temperature [MT] and log[var{accelo9}] [log (g^2)]) referring to healthy structure and with all damage mechanisms removed at damage level 3.

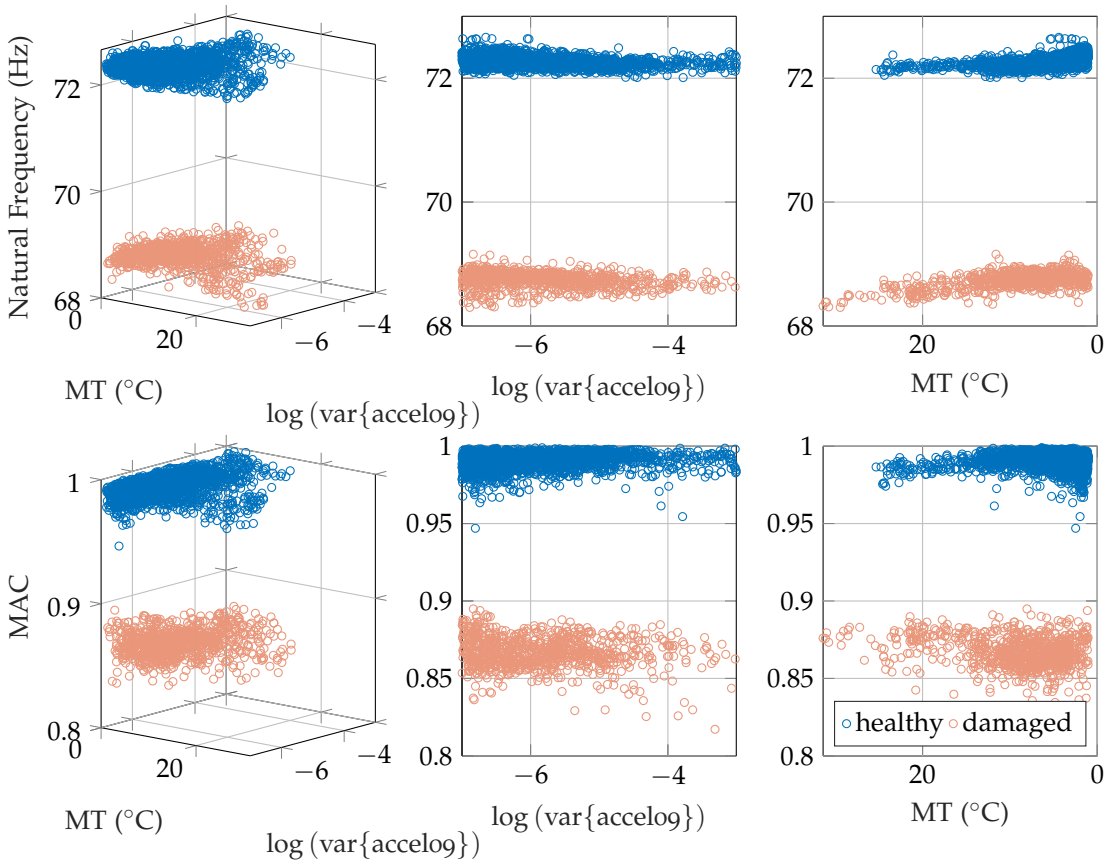

Figure A.11: Comparison of natural frequencies and MAC values of mode B4-x (plotted against material temperature [MT] and log[var{accelo9}] [log (g^2)]) referring to healthy structure and with all damage mechanisms removed at damage level 3.

BIBLIOGRAPHY

[1] H. Akaike. "Stochastic theory of minimal realization." In: *IEEE Transactions on Automatic Control* 19.6 (1974), pp. 667–674. DOI: 10.1109/TAC.1974.1100707 (cited on pages 40, 41).

[2] H. Akaike. "Markovian Representation of Stochastic Processes by Canonical Variables." In: *SIAM Journal on Control* 13.1 (1975), pp. 162–173. DOI: 10.1137/0313010 (cited on pages 42, 46).

[3] H. Akaike. "Canonical Correlation Analysis of Time Series and the Use of an Information Criterion." In: *System Identification Advances and Case Studies*. Ed. by R. K. Mehra and D. G. Lainiotis. Vol. 126. Mathematics in Science and Engineering. Elsevier, 1976, pp. 27–96. DOI: 10.1016/S0076-5392(08)60869-3 (cited on pages 6, 42, 46).

[4] B. M. Åkesson, J. B. Jørgensen, N. K. Poulsen, and S. B. Jørgensen. "A generalized autocovariance least-squares method for Kalman filter tuning." In: *Journal of Process Control* 18.7 (2008), pp. 769 –779. DOI: 10.1016/j.jprocont.2007.11.003 (cited on pages 88, 89, 91).

[5] R. J. Allemang. "The modal assurance criterion - Twenty years of use and abuse." In: *Sound & Vibration* 37 (Aug. 2003), pp. 14–23 (cited on page 7).

[6] Y. An, B. Błachowski, and J. Ou. "A degree of dispersion-based damage localization method." In: *Structural Control and Health Monitoring* 23.1 (June 2015), pp. 176–192. DOI: 10.1002/stc.1760 (cited on page 12).

[7] P. Andersen. "Identification of Civil Engineering Structures using Vector ARMA Models." English. PDF for print: 258 pp. PhD thesis. 1997 (cited on page 6).

[8] S.-K. Au. *Operational Modal Analysis*. Springer Singapore, 2017. DOI: 10.1007/978-981-10-4118-1 (cited on pages 7, 14).

[9] S.-K. Au, F.-L. Zhang, and Y.-C. Ni. "Bayesian operational modal analysis: Theory, computation, practice." In: *Computers & Structures* 126 (Sept. 2013), pp. 3–14. DOI: 10.1016/j.compstruc.2012.12.015 (cited on pages 7, 14).

[10] H. V. der Auweraer and B. Peeters. "Discriminating physical poles from mathematical poles in high order systems: use and automation of the stabilization diagram." In: *Proceedings of the 21st IEEE Instrumentation and Measurement Technology Conference (IEEE Cat. No.04CH37510)*. IEEE. DOI: 10.1109/imtc.2004.1351525 (cited on page 6).

[11] O. Avci, O. Abdeljaber, S. Kiranyaz, M. Hussein, M. Gabbouj, and D. J. Inman. "A review of vibration-based damage detection in civil structures: From traditional methods to Machine Learning and Deep Learning applications." In: *Mechanical Systems and Signal Processing* 147 (Jan. 2021), p. 107077. DOI: 10.1016/j.ymssp.2020.107077 (cited on page 7).

[12] L. D. Avendaño-Valencia, E. N. Chatzi, and S. D. Fassois. "In-Operation Wind Turbine Modal Analysis via LPV-VAR Modeling." In: *Rotating Machinery, Hybrid Test Methods, Vibro-Acoustics & Laser Vibrometry, Volume 8*. Springer International Publishing, 2017, pp. 47–57. DOI: 10.1007/978-3-319-54648-3_6 (cited on pages 7, 113).

[13] L. Avendaño-Valencia and S. Fassois. "Stationary and non-stationary random vibration modelling and analysis for an operating wind turbine." In: *Mechanical Systems and Signal Processing* 47.1-2 (Aug. 2014), pp. 263–285. DOI: 10.1016/j.ymssp.2013.07.022 (cited on pages 7, 113).

[14] L. D. Avendaño-Valencia and E. N. Chatzi. "Modelling long-term vibration monitoring data with Gaussian Process time-series models." In: 52.28 (2019), pp. 26–31. DOI: 10.1016/j.ifacol.2019.12.343 (cited on pages 113, 114).

[15] L. D. Avendaño-Valencia and E. N. Chatzi. "Multivariate GP-VAR models for robust structural identification under operational variability." In: *Probabilistic Engineering Mechanics* 60 (Apr. 2020), p. 103035. DOI: 10.1016/j.probengmech.2020.103035 (cited on page 14).

[16] L. D. Avendaño-Valencia, E. N. Chatzi, and D. Tcherniak. "Gaussian process models for mitigation of operational variability in the structural health monitoring of wind turbines." In: *Mechanical Systems and Signal Processing* 142 (Aug. 2020), p. 106686. DOI: 10.1016/j.ymssp.2020.106686 (cited on pages 4, 10).

[17] L. D. Avendaño-Valencia, E. N. Chatzi, K. Y. Koo, and J. M. W. Brownjohn. "Gaussian Process Time-Series Models for Structures under Operational Variability." In: *Frontiers in Built Environment* 3 (2017), p. 69. DOI: 10.3389/fbuil.2017.00069 (cited on pages 1, 4, 7–10, 14, 113).

[18] R. N. Banavar and J. L. Speyer. "A Linear-Quadratic Game Approach to Estimation and Smoothing." In: *1991 American Control Conference*. 1991, pp. 2818–2822. DOI: 10.23919/ACC.1991.4791915 (cited on page 59).

[19] J. S. Bendat and A. G. Piersol. *Random data: Analysis and measurement procedures*. Hoboken, N.J: Wiley, 2010 (cited on pages 32–34, 36–38).

[20] D. Bernal. "Load Vectors for Damage Localization." In: *Journal of Engineering Mechanics* 128.1 (Jan. 2002), pp. 7–14. DOI: 10.1061/(asce)0733-9399(2002)128:1(7) (cited on page 12).

[21] D. Bernal. "Flexibility-Based Damage Localization from Stochastic Realization Results." In: *Journal of Engineering Mechanics* 132.6 (June 2006), pp. 651–658. DOI: 10.1061/(asce)0733-9399(2006)132:6(651) (cited on page 12).

[22] D. Bernal. "Kalman filter damage detection in the presence of changing process and measurement noise." In: *Mechanical Systems and Signal Processing* 39.1 (2013), pp. 361–371. DOI: 10.1016/j.ymssp.2013.02.012 (cited on pages 57, 104).

[23] M. Bertha and J.-C. Golinval. "Identification of non-stationary dynamical systems using multivariate ARMA models." In: *Mechanical Systems and Signal Processing* 88 (May 2017), pp. 166–179. DOI: 10.1016/j.ymssp.2016.11.024 (cited on page 7).

[24] S. Bogoevska, M. Spiridonakos, E. Chatzi, E. Dumova-Jovanoska, and R. Höffer. "A Data-Driven Diagnostic Framework for Wind Turbine Structures: A Holistic Approach." In: *Sensors* 17.4 (2017). DOI: 10.3390/s17040720 (cited on page 10).

[25] L. Bornn, C. R. Farrar, G. Park, and K. Farinholt. "Structural Health Monitoring With Autoregressive Support Vector Machines." In: *Journal of Vibration and Acoustics* 131.2 (Feb. 2009). DOI: 10.1115/1.3025827 (cited on page 10).

[26] G. E. P. Box and D. A. Pierce. "Distribution of Residual Autocorrelations in Autoregressive-Integrated Moving Average Time Series Models." In: *Journal of the American Statistical Association* 65.332 (1970), pp. 1509–1526 (cited on page 57).

[27] G. E. P. Box, G. M. Jenkins, G. C. Reinsel, and G. M. Ljung. *Time series analysis : forecasting and control*. Hoboken, New Jersey: John Wiley & Sons, Inc, 2016 (cited on page 6).

[28] S. Boyd and L. Vandenberghe. *Convex optimization*. Cambridge, UK New York: Cambridge University Press, 2004 (cited on pages 63, 88, 91, 117).

[29] A. Brandt. *Noise and vibration analysis : signal analysis and experimental procedures*. Chichester Hoboken, N.J: Wiley, 2011 (cited on pages 5, 33–35, 38, 39, 81).

[30] R. Brincker, L. Zhang, and P. Andersen. "Modal identification of output-only systems using frequency domain decomposition." In: *Smart Materials and Structures* 10.3 (June 2001), pp. 441–445. DOI: 10.1088/0964-1726/10/3/303 (cited on pages 5, 7, 25).

[31] J. Brown, D. Su, H. Kong, S. Sukkarieh, and E. Kerrigan. "Improved Noise Covariance Estimation in Visual Servoing Using an Autocovariance Least-squares Approach." In: *IFAC-PapersOnLine* 52.22 (2019). 1st IFAC Workshop on Robot Control WROCO 2019, pp. 37–42. DOI: https://doi.org/10.1016/j.ifacol.2019.11.044 (cited on page 88).

[32] Y. Bulut. "Applied Kalman filter theory." PhD thesis. Northeastern University, 2011 (cited on pages 89–91).

[33] I. CVX Research. *CVX: Matlab Software for Disciplined Convex Programming, version 2.0*. http://cvxr.com/cvx. Aug. 2012 (cited on pages 63, 88, 97).

[34] J. D. Caigny, R. Pintelon, J. F. Camino, and J. Swevers. "Interpolated Modeling of LPV Systems." In: 22.6 (Nov. 2014), pp. 2232–2246. DOI: 10.1109/tcst.2014.2300510 (cited on page 116).

[35] M. Cao, W. Xu, W. Ostachowicz, and Z. Su. "Damage identification for beams in noisy conditions based on Teager energy operator-wavelet transform modal curvature." In: *Journal of Sound and Vibration* 333.6 (Mar. 2014), pp. 1543–1553. DOI: 10.1016/j.jsv.2013.11.003 (cited on page 12).

[36] B. Carew and P. Bélanger. "Identification of optimum filter steady-state gain for systems with unknown noise covariances." In: *IEEE Transactions on Automatic Control* 18.6 (1973), pp. 582–587. DOI: 10.1109/TAC.1973.1100420 (cited on page 88).

[37] B. Cauberghe. "Applied Frequency-Domain System Identification in the Field of Experimental and Operational Modal Analysis." PhD thesis. Vrije Universiteit Brussel, 2004 (cited on page 6).

[38] R. J. Caverly and J. R. Forbes. *LMI Properties and Applications in Systems, Stability, and Control Theory*. 2021 (cited on pages 63, 64).

[39] S. Chandrasekaran. *Structural Health Monitoring with Application to Offshore Structures*. WORLD SCIENTIFIC, May 2019. DOI: 10.1142/11302 (cited on page 14).

[40] C.-T. Chen. *Linear system theory and design*. New York: Oxford University Press, 1999 (cited on pages 24, 26–29, 31).

[41] J. Chen and R. J. Patton. *Robust Model-Based Fault Diagnosis for Dynamic Systems*. Springer US, 1999. DOI: 10.1007/978-1-4615-5149-2 (cited on pages 67, 68).

[42] T. Chen and B. Francis. *Optimal sampled-data control systems*. London New York: Springer, 1995 (cited on pages 49–51).

[43] S. Chesné and A. Deraemaeker. "Damage localization using transmissibility functions: A critical review." In: *Mechanical Systems and Signal Processing* 38.2 (July 2013), pp. 569–584. DOI: 10.1016/j.ymssp.2013.01.020 (cited on page 13).

[44] R. W. Clough and J. Penzien. *Dynamics of Structures*. 3rd ed. Berkley: Computers & Structures, 2003 (cited on pages 22, 24).

[45] *Control Toolbox™ User's Guide*. Revised for Version 10.4 (Release 2018a). Natick, MA, USA: The MathWorks, Inc, 2018 (cited on page 119).

[46] H. S. M. Coxeter. *Introduction to geometry*. New York: Wiley, 1969 (cited on page 117).

[47] E. J. Cross, G. Manson, K. Worden, and S. G. Pierce. "Features for damage detection with insensitivity to environmental and operational variations." In: *Proceedings of the Royal Society A: Mathematical, Physical and Engineering Sciences* 468.2148 (Oct. 2012), pp. 4098–4122. DOI: 10.1098/rspa.2012.0031 (cited on page 8).

[48] E. J. Cross and K Worden. "Approaches to nonlinear cointegration with a view towards applications in SHM." In: *Journal of Physics: Conference Series* 305 (July 2011), p. 012069. DOI: 10.1088/1742-6596/305/1/012069 (cited on page 9).

[49] E. J. Cross, T. J. Rogers, and T. J. Gibbons. "Grey-box Modelling for Structural Health Monitoring: Physical Constraints on Machine Learning Algorithms." In: *Structural Health Monitoring 2019*. DEStech Publications, Inc., Nov. 2019. DOI: 10.12783/shm2019/32349 (cited on page 5).

[50] E. J. Cross, K. Worden, and Q. Chen. "Cointegration: a novel approach for the removal of environmental trends in structural health monitoring data." In: *Proceedings of the Royal Society A: Mathematical, Physical and Engineering Sciences* 467.2133 (Apr. 2011), pp. 2712–2732. DOI: 10.1098/rspa.2011.0023 (cited on page 9).

[51] J. D'Errico. *nearestSPD*. Ed. by M. C. F. Exchange. URL: https://de.mathworks.com/matlabcentral/fileexchange/42885-nearestspd (cited on page 93).

[52] A. Dahlén, A. Lindquist, and J. Mari. "Experimental evidence showing that stochastic subspace identification methods may fail." In: *Systems & Control Letters* 34.5 (1998), pp. 303–312. DOI: 10.1016/S0167-6911(98)00020-6 (cited on page 42).

[53] G. Dazi, M. Azimmohseni, and F. Yaghmaie. "Rank-based statistics for testing the whiteness hypothesis of time series." In: *Communications in Statistics - Simulation and Computation* 48.8 (2019), pp. 2452–2466. DOI: 10.1080/03610918.2018.1458127 (cited on page 57).

[54] F. M. Dekking, C. Kraaikamp, H. P. Lopuhaä, and L. E. Meester. *A Modern Introduction to Probability and Statistics*. Springer London, 2005. DOI: 10.1007/1-84628-168-7 (cited on page 35).

[55] A. Deraemaeker and K. Worden. "A comparison of linear approaches to filter out environmental effects in structural health monitoring." In: *Mechanical Systems and Signal Processing* 105 (May 2018), pp. 1–15. DOI: 10.1016/j.ymssp.2017.11.045 (cited on page 8).

[56] A. Deraemaeker and A. Preumont. "Vibration based damage detection using large array sensors and spatial filters." In: *Mechanical Systems and Signal Processing* 20.7 (Oct. 2006), pp. 1615–1630. DOI: 10.1016/j.ymssp.2005.02.010 (cited on page 12).

[57] V. Dertimanis, M. Spiridonakos, and E. Chatzi. "Data-driven uncertainty quantification of structural systems via B-spline expansion." In: *Computers & Structures* 207 (Sept. 2018), pp. 245–257. DOI: 10.1016/j.compstruc.2017.03.006 (cited on page 10).

[58] N. Dervilis, M. Choi, S. Taylor, R. Barthorpe, G. Park, C. Farrar, and K. Worden. "On damage diagnosis for a wind turbine blade using pattern recognition." In: *Journal of Sound and Vibration* 333.6 (Mar. 2014), pp. 1833–1850. DOI: 10.1016/j.jsv.2013.11.015 (cited on page 8).

[59] Y. Diao, X. Men, Z. Sun, K. Guo, and Y. Wang. "Structural Damage Identification Based on the Transmissibility Function and Support Vector Machine." In: *Shock and Vibration* 2018 (June 2018), pp. 1–13. DOI: 10.1155/2018/4892428 (cited on page 13).

[60] Y. Dodge. *The concise encyclopedia of statistics*. New York: Springer, 2008 (cited on page 143).

[61] M. Döhler. "Subspace-based system identification and fault detection: Algorithms for large systems and application to structural vibration analysis." Theses. Université Rennes 1, Oct. 2011 (cited on page 129).

[62] M. Döhler, X.-B. Lam, and L. Mevel. "Uncertainty quantification for modal parameters from stochastic subspace identification on multi-setup measurements." In: *Mechanical Systems and Signal Processing* 36.2 (Apr. 2013), pp. 562–581. DOI: 10.1016/j.ymssp.2012.11.011 (cited on page 14).

[63] M. Döhler and L. Mevel. "Efficient multi-order uncertainty computation for stochastic subspace identification." In: *Mechanical Systems and Signal Processing* 38.2 (July 2013), pp. 346–366. DOI: 10.1016/j.ymssp.2013.01.012 (cited on page 14).

[64] G.-R. Duan and H.-H. Yu. *LMIs in Control Systems*. CRC Press, June 2013. DOI: 10.1201/b15060 (cited on page 63).

[65] J. Duník, O. Straka, O. Kost, and J. Havlík. "Noise covariance matrices in state-space models: A survey and comparison of estimation methods—Part I." In: *International Journal of Adaptive Control and Signal Processing* 31.11 (), pp. 1505–1543. DOI: 10.1002/acs.2783 (cited on page 87).

[66] J. Duník, O. Straka, and M. Šimandl. "On Autocovariance Least-Squares Method for Noise Covariance Matrices Estimation." In: *IEEE Transactions on Automatic Control* 62.2 (2017), pp. 967–972. DOI: 10.1109/TAC.2016.2571899 (cited on page 87).

[67] A. Entezami and H. Shariatmadar. "An unsupervised learning approach by novel damage indices in structural health monitoring for damage localization and quantification." In: *Structural Health Monitoring* 17.2 (Feb. 2017), pp. 325–345. DOI: 10.1177/1475921717693572 (cited on page 7).

[68] K. Erazo, D. Sen, S. Nagarajaiah, and L. Sun. "Vibration-based structural health monitoring under changing environmental conditions using Kalman filtering." In: *Mechanical Systems and Signal Processing* 117 (2019), pp. 1 –15. DOI: 10.1016/j.ymssp.2018.07.041 (cited on pages 13, 104).

[69] W. Fan and P. Qiao. "Vibration-based Damage Identification Methods: A Review and Comparative Study." In: *Structural Health Monitoring* 10.1 (Apr. 2010), pp. 83–111. DOI: 10.1177/1475921710365419 (cited on page 7).

[70] C. Farrar and K. Worden. *Structural Health Monitoring: A Machine Learning Perspective*. Wiley, 2012 (cited on pages 1, 7–11, 14, 15, 67, 130).

[71] C. R. Farrar, P. J. Cornwell, S. W. Doebling, and M. B. Prime. *Structural Health Monitoring Studies of the Alamosa Canyon and I-40 Bridges*. Tech. rep. July 2000. DOI: 10.2172/766805 (cited on page 4).

[72] C. R. Farrar, S. W. Doebling, and D. A. Nix. "Vibration–based structural damage identification." In: *Philosophical Transactions of the Royal Society of London. Series A: Mathematical, Physical and Engineering Sciences* 359.1778 (Jan. 2001). Ed. by N. A. J. Lieven and D. J. Ewins, pp. 131–149. DOI: 10.1098/rsta.2000.0717 (cited on page 1).

[73] C. R. Farrar, T. A. Duffey, S. W. Doebling, and D. A. Nix. "A Statistical Pattern Recognition Paradigm for Vibration-Based Structural Health Monitoring." In: *Proceedings of*

the 2 nd International Workshop on Structural Health Monitoring. 1999, pp. 764–773 (cited on page 1).

[74] S. Fassois. "Parametric identification of vibrating structures." In: *Encyclopedia of Vibration* (Jan. 2001), pp. 673–685 (cited on pages 4, 6).

[75] P. L. Faurre. "Stochastic Realization Algorithms." In: *System Identification Advances and Case Studies*. Ed. by R. K. Mehra and D. G. Lainiotis. Vol. 126. Mathematics in Science and Engineering. Elsevier, 1976, pp. 1–25. DOI: 10.1016/S0076-5392(08)60868-1 (cited on pages 40, 41).

[76] R. Feynman, R. Leighton, and M. Sands. *The Feynman Lectures on Physics, Vol. I: The New Millennium Edition: Mainly Mechanics, Radiation, and Heat*. The Feynman Lectures on Physics. Basic Books, 2011 (cited on page 21).

[77] E. Figueiredo, G. Park, C. R. Farrar, K. Worden, and J. Figueiras. "Machine learning algorithms for damage detection under operational and environmental variability." In: *Structural Health Monitoring* 10.6 (Nov. 2010), pp. 559–572. DOI: 10.1177/1475921710388971 (cited on page 7).

[78] E. Figueiredo, G. Park, J. Figueiras, C. Farrar, and K. Worden. "Structural health monitoring algorithm comparisons using standard data sets." In: (Mar. 2009). DOI: 10.2172/961604 (cited on page 36).

[79] C. Flexa, W. Gomes, and C. Sales. "Data Normalization in Structural Health Monitoring by Means of Nonlinear Filtering." In: *2019 8th Brazilian Conference on Intelligent Systems (BRACIS)*. IEEE, Oct. 2019. DOI: 10.1109/bracis.2019.00044 (cited on page 11).

[80] U. Forssell. *On H2 and H-infinity Optimal Estimation*. Tech. rep. 1885. Linköping University, Department of Electrical Engineering, 1996, p. 24 (cited on page 59).

[81] M. L. Fugate, H. Sohn, and C. R. Farrar. "Vibration-based damage detection using statistical process control." In: *Mechanical Systems and Signal Processing* 15.4 (July 2001), pp. 707–721. DOI: 10.1006/mssp.2000.1323 (cited on page 15).

[82] S. GRES, M. DOHLER, P. Andersen, L. Damkilde, and L. Mevel. "Hankel matrix normalization for robust damage detection." In: *IOMAC 2019 - 8th International Operational Modal Analysis Conference*. Copenhagen, Denmark, May 2019, pp. 1–8 (cited on page 130).

[83] P. Gahinet and P. Apkarian. "A linear matrix inequality approach toH∞ control." In: *International Journal of Robust and Nonlinear Control* 4.4 (1994), pp. 421–448. DOI: 10.1002/rnc.4590040403 (cited on page 63).

[84] H. Gao and X. Li. *Robust filtering for uncertain systems: a parameter-dependent approach*. Springer, Cham, 2014 (cited on page 63).

[85] M. Ge and E. C. Kerrigan. "Noise covariance identification for time-varying and nonlinear systems." In: *International Journal of Control* 90.9 (2017), pp. 1903–1915. DOI: 10.1080/00207179.2016.1228123 (cited on page 87).

[86] J.-C. Golinval. "Damage Detection in Structures Based on Principal Component Analysis of Forced Harmonic Responses." In: *Procedia Engineering* 199 (2017), pp. 1912–1918. DOI: 10.1016/j.proeng.2017.09.449 (cited on page 8).

[87] M. Grant and S. Boyd. "Graph implementations for nonsmooth convex programs." In: *Recent Advances in Learning and Control*. Ed. by V. Blondel, S. Boyd, and H. Kimura. Lecture Notes in Control and Information Sciences. http://stanford.edu/~boyd/graph_dcp.html. Springer-Verlag Limited, 2008, pp. 95–110 (cited on pages 63, 88, 97).

[88] M. Green and D. Limebeer. *Linear robust control*. Englewood Cliffs, N.J: Prentice Hall, 1995 (cited on pages 47, 49–51, 54).

[89] J. Gu, M. Gul, and X. Wu. "Damage detection under varying temperature using artificial neural networks." In: *Structural Control and Health Monitoring* 24.11 (Feb. 2017), e1998. DOI: 10.1002/stc.1998 (cited on page 11).

[90] P. Guillaume, P. Verboven, S. Vanlanduit, H. Van der Auweraer, and B. Peeters. "A poly-reference implementation of the least-squares complex frequency-domain estimator." In: Kissimmee (FL), USA, Jan. 2003 (cited on page 6).

[91] M. W. Häckell and R. Rolfes. "Monitoring a 5MW offshore wind energy converter — Condition parameters and triangulation based extraction of modal parameters." In: *Mechanical Systems and Signal Processing* 40.1 (2013), pp. 322 –343. DOI: 10.1016/j.ymssp.2013.04.004 (cited on page 7).

[92] M. W. Häckell, R. Rolfes, M. B. Kane, and J. P. Lynch. "Three-Tier Modular Structural Health Monitoring Framework Using Environmental and Operational Condition Clustering for Data Normalization: Validation on an Operational Wind Turbine System." In: *Proceedings of the IEEE* 104.8 (Aug. 2016), pp. 1632–1646. DOI: 10.1109/jproc.2016.2566602 (cited on page 9).

[93] M. W. Häckell. *A holistic evaluation concept for long-term structural health monitoring*. 2015. DOI: 10.15488/8469 (cited on pages 14, 80).

[94] M. Häckell and R. Rolfes. "A Modular SHM-Scheme for Engineering Structures under Changing Conditions: Application to an Offshore Wind Turbine." In: *EWSHM - 7th European Workshop on Structural Health Monitoring*. Ed. by L. Cam, Vincent, Mevel, Laurent, Schoefs, and Franck. IFFSTTAR, Inria, Université de Nantes. Nantes, France, July 2014 (cited on page 1).

[95] J. Han and M. Kamber. *Data mining : concepts and techniques*. Amsterdam Boston San Francisco, CA: Elsevier Morgan Kaufmann, 2006 (cited on page 9).

[96] P. C. Hansen. "Regularization tools – a Matlab package for analysis and solution of discrete ill-posed problems." In: *Numerical Algorithms* 6 (1994), pp. 1–35. DOI: 10.1007/BF02149761 (cited on page 91).

[97] P. C. Hansen. *Rank-Deficient and Discrete Ill-Posed Problems*. Society for Industrial and Applied Mathematics, 1998. DOI: 10.1137/1.9780898719697 (cited on page 91).

[98] P. C. Hansen. "Regularization tools version 4.0 for MATLAB 7.3." In: *Numerical Algorithms* 46 (Nov. 2007), pp. 189–194. DOI: 10.1007/s11075-007-9136-9 (cited on page 91).

[99] B. Hassibi, A. H. Sayed, and T. Kailath. "Linear estimation in Krein spaces. I. Theory." In: *IEEE Transactions on Automatic Control* 41.1 (1996), pp. 18–33. DOI: 10.1109/9.481605 (cited on pages 59, 60).

[100] B. Hassibi, A. H. Sayed, and T. Kailath. "Linear estimation in Krein spaces. II. Applications." In: *IEEE Transactions on Automatic Control* 41.1 (1996), pp. 34–49. DOI: 10.1109/9.481606 (cited on page 59).

[101] B. Hassibi, A. Sayed, and T. Kailath. *Indefinite-Quadratic Estimation and Control: A Unified Approach to H2 and H-infinity Theories*. SIAM Studies in Applied Mathematics. Society for Industrial and Applied Mathematics, 1999 (cited on pages 56, 58–62).

[102] J. a. P. Hespanha. *Linear systems theory*. Princeton: Princeton University Press, 2018 (cited on pages 30, 31, 54).

[103] N. J. Higham. "Computing a nearest symmetric positive semidefinite matrix." In: *Linear Algebra and its Applications* 103 (1988), pp. 103 –118. DOI: 10.1016/0024-3795(88)90223-6 (cited on page 93).

[104] B. L. Ho and R. E. Kalman. "Editorial: Effective construction of linear state-variable models from input/output functions." In: *at - Automatisierungstechnik* 14.1-12 (1966), pp. 545–548. DOI: 10.1524/auto.1966.14.112.545 (cited on pages 41–43).

[105] O. Huth, G. Feltrin, J. Maeck, N. Kilic, and M. Motavalli. "Damage Identification Using Modal Data: Experiences on a Prestressed Concrete Bridge." In: *Journal of Structural Engineering* 131.12 (Dec. 2005), pp. 1898–1910. DOI: 10.1061/(asce)0733-9445(2005)131:12(1898) (cited on pages 7, 12).

[106] I. Hwang, S. Kim, Y. Kim, and C. E. Seah. "A Survey of Fault Detection, Isolation, and Reconfiguration Methods." In: *IEEE Transactions on Control Systems Technology* 18.3 (May 2010), pp. 636–653. DOI: 10.1109/tcst.2009.2026285 (cited on page 12).

[107] T. Kailath, A. Sayed, and B. Hassibi. *Linear Estimation*. Prentice-Hall Information and System Sciences Series. Prentice Hall, 2000 (cited on page 49).

[108] R. E. Kalman. "A New Approach to Linear Filtering and Prediction Problems." In: 82.1 (Mar. 1960), pp. 35–45. DOI: 10.1115/1.3662552 (cited on page 58).

[109] F. Kang, X. Liu, and J. Li. "Temperature effect modeling in structural health monitoring of concrete dams using kernel extreme learning machines." In: *Structural Health Monitoring* 19.4 (Sept. 2019), pp. 987–1002. DOI: 10.1177/1475921719872939 (cited on page 10).

[110] T. Katayama. *Subspace Methods for System Identification*. Communications and Control Engineering. Springer London, 2006 (cited on pages 6, 41–46, 51, 56, 88).

[111] T. Katayama. "A Note on LQ Decomposition in Stochastic Subspace Identification." In: *Perspectives in Mathematical System Theory, Control, and Signal Processing: A Festschrift in Honor of Yutaka Yamamoto on the Occasion of his 60th Birthday*. Ed. by J. C. Willems, S. Hara, Y. Ohta, and H. Fujioka. Berlin, Heidelberg: Springer Berlin Heidelberg, 2010, pp. 355–364. DOI: 10.1007/978-3-540-93918-4_32 (cited on page 42).

[112] E. Kreyszig. *Introductory functional analysis with applications*. New York: Wiley, 1978 (cited on page 48).

[113] J. Kullaa. "Eliminating Environmental or Operational Influences in Structural Health Monitoring using the Missing Data Analysis." In: *Journal of Intelligent Material Systems and Structures* 20.11 (Sept. 2008), pp. 1381–1390. DOI: 10.1177/1045389x08096050 (cited on page 9).

[114] J. Kullaa. "Vibration-Based Structural Health Monitoring Under Variable Environmental or Operational Conditions." In: *New Trends in Vibration Based Structural Health Monitoring*. Ed. by A. Deraemaeker and K. Worden. Vienna: Springer Vienna, 2010, pp. 107–181. DOI: 10.1007/978-3-7091-0399-9_4 (cited on page 8).

[115] C. Lanczos. *The Variational Principles of Mechanics*. New York: Courier Corporation, 1986 (cited on page 22).

[116] A. Lenzen, M. Rohrer, and M. Vollmering. "Damage localization of mechanical structures considering environmental and operational conditions based on output-only system identification and H∞-estimation." In: *Mechanical Systems and Signal Processing* 156 (July 2021), p. 107572. DOI: 10.1016/j.ymssp.2020.107572 (cited on pages 13, 74, 115).

[117] A. Lenzen and M. Vollmering. "A new technique for damage localisation using estimates in Krein spaces." In: May 2015 (cited on page 13).

[118] A. Lenzen and M. Vollmering. "An output-only damage identification method based on H∞ theory and state projection estimation error (SP2E)." In: *Structural Control and Health Monitoring* 24 (2017). DOI: 10.1002/stc.2003 (cited on pages 13, 67, 73, 74, 76).

[119] A. Lenzen and M. Vollmering. "On experimental damage localization by SP2E: Application of H∞ estimation and oblique projections." In: *Mechanical Systems and Signal Processing* 104 (2018), pp. 648 –662. DOI: 10.1016/j.ymssp.2017.11.028 (cited on pages 13, 67, 71, 73, 74, 76).

[120] A. Lenzen and M. Vollmering. "Mechanical system scaling based on output only identification and mass perturbations by state projections." In: *Mechanical Systems and Signal Processing* 144 (Oct. 2020), p. 106863. DOI: 10.1016/j.ymssp.2020.106863 (cited on page 74).

[121] A. Lenzen and H. Waller. "From Black to White Box Models in Structural Mechanics." In: *2nd International Conference Lifetime Oriented Design Concepts (ICLODC)*. Bochum, Germany, Mar. 2004 (cited on page 5).

[122] L. Ljung. *System identification : theory for the user*. 2nd ed. Upper Saddle River, NJ: Prentice Hall PTR, 1999 (cited on page 6).

[123] J. Lofberg. "YALMIP : a toolbox for modeling and optimization in MATLAB." In: *2004 IEEE International Conference on Robotics and Automation (IEEE Cat. No.04CH37508)*. 2004, pp. 284–289. DOI: 10.1109/CACSD.2004.1393890 (cited on page 63).

[124] T.-T. Lu and S.-H. Shiou. "Inverses of 2 × 2 block matrices." In: *Computers & Mathematics with Applications* 43.1 (2002), pp. 119–129. DOI: https://doi.org/10.1016/S0898-1221(01)00278-4 (cited on pages 72, 76).

[125] *MATLAB Optimization Toolbox Release 2018a*. The MathWorks, Inc, Natick, MA, USA. 2018 (cited on pages 88, 91).

[126] F. Magalhães, A. Cunha, and E. Caetano. "Vibration based structural health monitoring of an arch bridge: From automated OMA to damage detection." In: *Mechanical Systems and Signal Processing* 28 (Apr. 2012), pp. 212–228. DOI: 10.1016/j.ymssp.2011.06.011 (cited on pages 7, 10).

[127] J. Magnus and H. Neudecker. "The elimination matrix: Some lemmas and applications." English. In: *SIAM Journal on Algebraic and Discrete Methods* 1.4 (1980). Pagination: 28, pp. 422–449 (cited on page 92).

[128] J. Magnus and H. Neudecker. *Matrix Differential Calculus with Applications in Statistics and Econometrics*. PROBABILISTICS AND STATISTICS. Wiley, 1999 (cited on page 90).

[129] H. Martín-Sanz, K. Tatsis, V. K. Dertimanis, L. D. Avendaño-Valencia, E. Brühwiler, and E. Chatzi. "Monitoring of the UHPFRC strengthened Chillon viaduct under environmental and operational variability." In: *Structure and Infrastructure Engineering* 16.1 (Sept. 2019), pp. 138–168. DOI: 10.1080/15732479.2019.1650079 (cited on page 10).

[130] R. Mehra. "On the identification of variances and adaptive Kalman filtering." In: *IEEE Transactions on Automatic Control* 15.2 (1970), pp. 175–184. DOI: 10.1109/TAC.1970.1099422 (cited on pages 88, 90).

[131] R. Mehra. "Approaches to adaptive filtering." In: *IEEE Transactions on Automatic Control* 17.5 (1972), pp. 693–698. DOI: 10.1109/TAC.1972.1100100 (cited on pages 87, 88).

[132] K. Mendrok and P. Kurowski. "Operational modal filter and its applications." In: *Archive of Applied Mechanics* 83.4 (Sept. 2012), pp. 509–519. DOI: 10.1007/s00419-012-0700-y (cited on page 12).

[133] K. Mendrok and T. Uhl. "Experimental verification of the damage localization procedure based on modal filtering." In: *Structural Health Monitoring* 10.2 (June 2010), pp. 157–171. DOI: 10.1177/1475921710373292 (cited on pages 12, 13).

[134] C. D. Meyer. *Matrix Analysis and Applied Linear Algebra*. Philadelphia: SIAM, 2000 (cited on pages 24, 43, 45, 71, 72).

[135] M. Meyer. *Signalverarbeitung*. Springer Fachmedien Wiesbaden, 2014. DOI: 10.1007/978-3-658-02612-7 (cited on page 39).

[136] N. Mohd Razali and B. Yap. "Power Comparisons of Shapiro-Wilk, Kolmogorov-Smirnov, Lilliefors and Anderson-Darling Tests." In: *Journal of Statistical Modelling and Analytics* 2 (Jan. 2011) (cited on page 57).

[137] D. Montgomery. *Introduction to statistical quality control*. 6th ed. Hoboken, N.J: Wiley, 2009 (cited on page 15).

[138] A. Mosavi, D. Dickey, R. Seracino, and S. Rizkalla. "Identifying damage locations under ambient vibrations utilizing vector autoregressive models and Mahalanobis distances." In: *Mechanical Systems and Signal Processing* 26 (Jan. 2012), pp. 254–267. DOI: 10.1016/j.ymssp.2011.06.009 (cited on pages 7, 13).

[139] P. Moser and B. Moaveni. "Environmental effects on the identified natural frequencies of the Dowling Hall Footbridge." In: *Mechanical Systems and Signal Processing* 25.7 (Oct. 2011), pp. 2336–2357. DOI: 10.1016/j.ymssp.2011.03.005 (cited on page 10).

[140] C. Neethling and P. Young. "Comments on "Identification of optimum filter steady-state gain for systems with unknown noise covariances"." In: *IEEE Transactions on Automatic Control* 19.5 (1974), pp. 623–625. DOI: 10.1109/TAC.1974.1100694 (cited on page 88).

[141] Y. Ni, X. Hua, K. Fan, and J. Ko. "Correlating modal properties with temperature using long-term monitoring data and support vector machine technique." In: *Engineering Structures* 27.12 (Oct. 2005), pp. 1762–1773. DOI: 10.1016/j.engstruct.2005.02.020 (cited on page 10).

[142] B. J. Odelson, M. R. Rajamani, and J. B. Rawlings. "A new autocovariance least-squares method for estimating noise covariances." In: *Automatica* 42.2 (2006), pp. 303 –308. DOI: 10.1016/j.automatica.2005.09.006 (cited on pages 87–89).

[143] C. K. Oh and H. Sohn. "Damage diagnosis under environmental and operational variations using unsupervised support vector machine." In: *Journal of Sound and Vibration* 325.1 (2009), pp. 224–239. DOI: https://doi.org/10.1016/j.jsv.2009.03.014 (cited on page 11).

[144] G. Oliveira, F. Magalhães, Á. Cunha, and E. Caetano. "Vibration-based damage detection in a wind turbine using 1 year of data." In: *Structural Control and Health Monitoring* 25.11 (Sept. 2018), e2238. DOI: 10.1002/stc.2238 (cited on page 10).

[145] A. V. Oppenheim, A. S. Willsky, and H. S. Nawab. *Signals & systems*. Upper Saddle River, N.J: Prentice Hall, 1997 (cited on pages 27–29).

[146] *Optimization Toolbox™ User's Guide*. Revised for Version 9.2 (Release 2018a). Natick, MA, USA: The MathWorks, Inc, 2018 (cited on pages 88, 91).

[147] P. Overschee and B. de Moor. *Subspace identification for linear systems : theory, implementation, applications*. Boston: Kluwer Academic Publishers, 1996 (cited on pages 6, 42, 45, 46, 88).

[148] P. van Overschee and B. de Moor. "Subspace algorithms for the stochastic identification problem." In: *Automatica* 29.3 (May 1993), pp. 649–660. DOI: 10.1016/0005-1098(93)90061-w (cited on pages 6, 42).

[149] A. Pandey, M. Biswas, and M. Samman. "Damage detection from changes in curvature mode shapes." In: *Journal of Sound and Vibration* 145.2 (1991), pp. 321–332. DOI: 10.1016/0022-460X(91)90595-B (cited on pages 7, 12).

[150] A. Papoulis and S. U. Pillai. *Probability, random variables, and stochastic processes*. Boston: McGraw-Hill, 2002 (cited on pages 32, 33, 35).

[151] M. Paz and Y. H. Kim. *Structural Dynamics - Theory and Computation*. Berlin, Heidelberg: Springer, 2018 (cited on page 21).

[152] B. Peeters. "System identification and damage detection in civil engineering." eng. PhD thesis. KU Leuven, 2000 (cited on pages 10, 23, 42, 45).

[153] B. Peeters, H. V. der Auweraer, P. Guillaume, and J. Leuridan. "The PolyMAX Frequency-Domain Method: A New Standard for Modal Parameter Estimation?" In: *Shock and Vibration* 11.3-4 (2004), pp. 395–409. DOI: 10.1155/2004/523692 (cited on page 6).

[154] B. Peeters and G. D. Roeck. "One-year monitoring of the Z24-Bridge: environmental effects versus damage events." In: *Earthquake Engineering & Structural Dynamics* 30.2 (2001), pp. 149–171. DOI: 10.1002/1096-9845(200102)30:2<149::aid-eqe1>3.0.co;2-z (cited on page 128).

[155] N. Penner, T. Grießmann, and R. Rolfes. "Monitoring of suction bucket jackets for offshore wind turbines: Dynamic load bearing behaviour and modelling." In: *Marine Structures* 72 (July 2020), p. 102745. DOI: 10.1016/j.marstruc.2020.102745 (cited on page 128).

[156] S. Pereira, E. Reynders, F. Magalhães, Á. Cunha, and J. P. Gomes. "The role of modal parameters uncertainty estimation in automated modal identification, modal tracking and data normalization." In: *Engineering Structures* 224 (Dec. 2020), p. 111208. DOI: 10.1016/j.engstruct.2020.111208 (cited on pages 7, 10).

[157] R. Pintelon, P. Guillaume, and J. Schoukens. "Uncertainty calculation in (operational) modal analysis." In: *Mechanical Systems and Signal Processing* 21.6 (Aug. 2007), pp. 2359–2373. DOI: 10.1016/j.ymssp.2006.11.007 (cited on page 14).

[158] R. Pintelon and J. Schoukens. "Nonparametric Techniques in System Identification." In: *Encyclopedia of Systems and Control*. Springer London, 2015, pp. 907–918. DOI: 10.1007/978-1-4471-5058-9_109 (cited on page 6).

[159] D. Pitchforth, T. Rogers, U. Tygesen, and E. Cross. "Grey-box models for wave loading prediction." In: *Mechanical Systems and Signal Processing* 159 (2021), p. 107741. DOI: 10.1016/j.ymssp.2021.107741 (cited on page 5).

[160] A. Poulimenos and S. Fassois. "Parametric time-domain methods for non-stationary random vibration modelling and analysis — A critical survey and comparison." In: *Mechanical Systems and Signal Processing* 20.4 (May 2006), pp. 763–816. DOI: 10.1016/j.ymssp.2005.10.003 (cited on page 7).

[161] C. Priori, M. De Angelis, and R. Betti. "On the selection of user-defined parameters in data-driven stochastic subspace identification." In: *Mechanical Systems and Signal Processing* 100 (2018), pp. 501–523. DOI: 10.1016/j.ymssp.2017.07.045 (cited on page 44).

[162] G. Quaranta, B. Carboni, and W. Lacarbonara. "Damage detection by modal curvatures: numerical issues." In: *Journal of Vibration and Control* 22.7 (Aug. 2014), pp. 1913–1927. DOI: 10.1177/1077546314545528 (cited on page 12).

[163] C. Rainieri. *Operational modal analysis of civil engineering structures : an introduction and guide for applications*. New York: Springer, 2014 (cited on pages 4, 6, 42, 45).

[164] M. Rajamani. "Data-based Techniques to Improve State Estimation in Model Predictive Control." Doctoral thesis. University of Wisconsin–Madison, 2007 (cited on pages 88, 89, 91, 92).

[165] M. R. Rajamani and J. B. Rawlings. "Estimation of the disturbance structure from data using semidefinite programming and optimal weighting." In: *Automatica* 45.1 (2009), pp. 142 –148. DOI: 10.1016/j.automatica.2008.05.032 (cited on page 92).

[166] M. R. Rajamani, J. B. Rawlings, and T. A. Soderstrom. "Application of a new data-based covariance estimation technique to a nonlinear industrial blending drum." In: *Texas-Winsconsin Modeling and Control Consortium, Tech. Report* 3 (2007) (cited on pages 87, 88).

[167] K Rao. *Signals and systems*. Cham, Switzerland: Birkhäuser, 2018 (cited on page 38).

[168] E. Reynders. "System Identification and Modal Analysis in Structural Mechanics." eng. PhD thesis. KU Leuven, 2009 (cited on pages 5, 26).

[169] E. Reynders, K. Maes, G. Lombaert, and G. D. Roeck. "Uncertainty quantification in operational modal analysis with stochastic subspace identification: Validation and applications." In: *Mechanical Systems and Signal Processing* 66-67 (Jan. 2016), pp. 13–30. DOI: 10.1016/j.ymssp.2015.04.018 (cited on page 14).

[170] E. Reynders, R. Pintelon, and G. De Roeck. "Uncertainty bounds on modal parameters obtained from stochastic subspace identification." In: *Mechanical Systems and Signal Processing* 22.4 (2008). Special Issue: Crack Effects in Rotordynamics, pp. 948 –969. DOI: 10.1016/j.ymssp.2007.10.009 (cited on page 14).

[171] E. Reynders and G. D. Roeck. "Reference-based combined deterministic–stochastic subspace identification for experimental and operational modal analysis." In: *Mechanical Systems and Signal Processing* 22.3 (2008), pp. 617–637. DOI: 10.1016/j.ymssp.2007.09.004 (cited on page 44).

[172] E. Reynders, G. Wursten, and G. D. Roeck. "Output-only structural health monitoring in changing environmental conditions by means of nonlinear system identification." In: *Structural Health Monitoring* 13.1 (Oct. 2013), pp. 82–93. DOI: 10.1177/1475921713502836 (cited on pages 7, 8).

[173] T. J. Rogers, G. R. Holmes, E. J. Cross, and K. Worden. "On a Grey Box Modelling Framework for Nonlinear System Identification." In: *Special Topics in Structural Dynamics, Volume 6*. Springer International Publishing, 2017, pp. 167–178. DOI: 10.1007/978-3-319-53841-9_15 (cited on page 5).

[174] A. Rytter. "Vibrational Based Inspection of Civil Engineering Structures." English. PhD thesis. Denmark: Dept. of Building Technology and Structural Engineering, Aalborg University, 1993 (cited on page 11).

[175] S. Sharma and S. Sen. "Bridge Damage Detection in Presence of Varying Temperature Using Two-Step Neural Network Approach." In: *Journal of Bridge Engineering* 26.6 (June 2021), p. 04021027. DOI: 10.1061/(asce)be.1943-5592.0001708 (cited on page 11).

[176] H Shi, K Worden, and E. J. Cross. "A nonlinear cointegration approach with applications to structural health monitoring." In: *Journal of Physics: Conference Series* 744 (Sept. 2016), p. 012025. DOI: 10.1088/1742-6596/744/1/012025 (cited on page 9).

[177] H. Shi, K. Worden, and E. J. Cross. "A cointegration approach for heteroscedastic data based on a time series decomposition: An application to structural health monitoring." In: *Mechanical Systems and Signal Processing* 120 (Apr. 2019), pp. 16–31. DOI: 10.1016/j.ymssp.2018.09.036 (cited on page 9).

[178] Y. Shokrani, V. K. Dertimanis, E. N. Chatzi, and M. N. Savoia. "On the use of mode shape curvatures for damage localization under varying environmental conditions." In: *Structural Control and Health Monitoring* 25.4 (2018), e2132. DOI: 10.1002/stc.2132 (cited on pages 7, 8, 12, 13).

[179] D. Simon. "From Here to Infinity." In: *Embedded Systems Programming* 14 (11 2001), pp. 20–32 (cited on page 59).

[180] D. Simon. *Optimal State Estimation: Kalman, H-Infinity, and Nonlinear Approaches*. Wiley-Interscience, 2006 (cited on pages 53, 55, 56, 58, 59).

[181] *Simulink® User's Guide*. Revised for Version 10.4 (Release 2018a). Natick, MA, USA: The MathWorks, Inc, 2018 (cited on page 119).

[182] H. Sohn. "Effects of environmental and operational variability on structural health monitoring." In: *Philosophical Transactions of the Royal Society A: Mathematical, Physical and Engineering Sciences* 365.1851 (Dec. 2006), pp. 539–560. DOI: 10.1098/rsta.2006.1935 (cited on page 7).

[183] H. Sohn, K. Worden, and C. R. Farrar. "Statistical Damage Classification Under Changing Environmental and Operational Conditions." In: *Journal of Intelligent Material Systems and Structures* 13.9 (Sept. 2002), pp. 561–574. DOI: 10.1106/104538902030904 (cited on page 11).

[184] M. Spiridonakos, A. Poulimenos, and S. Fassois. "Output-only identification and dynamic analysis of time-varying mechanical structures under random excitation: A comparative assessment of parametric methods." In: *Journal of Sound and Vibration* 329.7 (Mar. 2010), pp. 768–785. DOI: 10.1016/j.jsv.2009.10.005 (cited on page 7).

[185] M. D. Spiridonakos, E. N. Chatzi, and B. Sudret. "Polynomial Chaos Expansion Models for the Monitoring of Structures under Operational Variability." In: *ASCE-ASME Journal of Risk and Uncertainty in Engineering Systems, Part A: Civil Engineering* 2.3 (Sept. 2016). DOI: 10.1061/ajrua6.0000872 (cited on pages 7, 10).

[186] P. Stoica and Y. Selen. "Model-order selection." In: *IEEE Signal Processing Magazine* 21.4 (July 2004), pp. 36–47. DOI: 10.1109/msp.2004.1311138 (cited on page 6).

[187] J. F. Sturm. "Using SeDuMi 1.02, A Matlab toolbox for optimization over symmetric cones." In: *Optimization Methods and Software* 11.1-4 (1999), pp. 625–653. DOI: 10.1080/10556789908805766 (cited on pages 63, 88).

[188] M. Thirumarimurugan, N. Bagyalakshmi, and P. Paarkavi. "Comparison of fault detection and isolation methods: A review." In: *2016 10th International Conference on Intelligent Systems and Control (ISCO)*. IEEE, Jan. 2016. DOI: 10.1109/isco.2016.7726957 (cited on page 12).

[189] K. C. Toh, M. J. Todd, and R. H. Tütüncü. "SDPT3 — A Matlab software package for semidefinite programming, Version 1.3." In: *Optimization Methods and Software* 11.1-4 (1999), pp. 545–581. DOI: 10.1080/10556789908805762 (cited on pages 63, 88, 97).

[190] G. Tondreau and A. Deraemaeker. "Local modal filters for automated data-based damage localization using ambient vibrations." In: *Mechanical Systems and Signal Processing* 39.1-2 (Aug. 2013), pp. 162–180. DOI: 10.1016/j.ymssp.2013.03.020 (cited on page 12).

[191] G. Tondreau and A. Deraemaeker. "Automated data-based damage localization under ambient vibration using local modal filters and dynamic strain measurements: Experimental applications." In: *Journal of Sound and Vibration* 333.26 (Dec. 2014), pp. 7364–7385. DOI: 10.1016/j.jsv.2014.08.021 (cited on page 12).

[192] S. Tøoffner-Clausen. *System Identification and Robust Control : a Case Study Approach*. London: Springer London, 1996 (cited on pages 47, 48, 50).

[193] R. Tóth. *Modeling and Identification of Linear Parameter-Varying Systems*. Springer Berlin Heidelberg, 2010. DOI: 10.1007/978-3-642-13812-6 (cited on pages 114, 115).

[194] S. Tsiapoki. *Transmissibility-based monitoring and combination of damage feature decisions within a holistic structural health monitoring framework*. 2018. DOI: 10.15488/5584 (cited on page 9).

[195] S. Tsiapoki, O. Bahrami, M. W. Häckell, J. P. Lynch, and R. Rolfes. "Combination of damage feature decisions with adaptive boosting for improving the detection performance of a structural health monitoring framework: Validation on an operating wind turbine." In: *Structural Health Monitoring* 20.2 (Mar. 2020), pp. 637–660. DOI: 10.1177/1475921720909379 (cited on page 9).

[196] V. B. Tymchyshyn and A. Khlevniuk. "Beginner's guide to mapping simplexes affinely." en. In: (2019). DOI: 10.13140/RG.2.2.13787.41762 (cited on pages 117, 118).

[197] H. Ulrich and H. Weber. *Laplace-, Fourier- und z-Transformation : Grundlagen und Anwendungen*. Wiesbaden: Springer Vieweg, 2017 (cited on pages 28–30).

[198] M. D. Ulriksen, D. Tcherniak, P. H. Kirkegaard, and L. Damkilde. "Operational modal analysis and wavelet transformation for damage identification in wind turbine blades." In: *Structural Health Monitoring* 15.4 (July 2016), pp. 381–388. DOI: 10.1177/1475921715586623 (cited on pages 12, 13).

[199] R. J. Vaccaro and T. Vukina. "A solution to the positivity problem in the state-space approach to modeling vector-valued time series." In: *Journal of Economic Dynamics and Control* 17.3 (1993), pp. 401–421. DOI: https://doi.org/10.1016/0165-1889(93)90004-C (cited on page 93).

[200] L. Vandenberghe and S. Boyd. "Semidefinite Programming." In: *SIAM Rev.* 38.1 (Mar. 1996), 49–95. DOI: 10.1137/1038003 (cited on pages 88, 91).

[201] P. Verboven. "Frequency-domain system identification for modal analysis." PhD thesis. Vrije Universiteit Brussel, 2002 (cited on page 6).

[202] V. Verdult and M. Verhaegen. "Subspace identification of piecewise linear systems." In: IEEE, 2004. DOI: 10.1109/cdc.2004.1429336 (cited on page 115).

[203] M. Verhaegen. "Identification of the deterministic part of MIMO state space models given in innovations form from input-output data." In: *Automatica* 30.1 (1994). Special issue on statistical signal processing and control, pp. 61–74. DOI: https://doi.org/10.1016/0005-1098(94)90229-1 (cited on page 42).

[204] M. Vollmering. "Damage Localization of Mechanical Structures by Subspace Identification and Krein Space Based H-infinity Estimation." PhD thesis. Bauhaus-Universität Weimar, 2018, p. 205 (cited on pages 23, 60–62, 70, 72).

[205] M. Vollmering and A. Lenzen. "Theory and numerical application of damage localization method state projection estimation error (SP2E)." In: *Structural Control and Health*

Monitoring 25.10 (Aug. 2018), e2237. DOI: 10.1002/stc.2237 (cited on pages 13, 71, 74–76).

[206] M. A. Wahab and G. D. Roeck. "Damage detection in bridges using modal curvatures: Application to real damage scenario." In: *Journal of Sound and Vibration* 226.2 (Sept. 1999), pp. 217–235. DOI: 10.1006/jsvi.1999.2295 (cited on page 12).

[207] W. Weijtjens, G. D. Sitter, C. Devriendt, and P. Guillaume. "Operational modal parameter estimation of MIMO systems using transmissibility functions." In: *Automatica* 50.2 (Feb. 2014), pp. 559–564. DOI: 10.1016/j.automatica.2013.11.021 (cited on page 6).

[208] W. Weijtjens, T. Verbelen, G. D. Sitter, and C. Devriendt. "Foundation structural health monitoring of an offshore wind turbine—a full-scale case study." In: *Structural Health Monitoring* 15.4 (July 2016), pp. 389–402. DOI: 10.1177/1475921715586624 (cited on page 10).

[209] P. Welch. "The use of fast Fourier transform for the estimation of power spectra: A method based on time averaging over short, modified periodograms." In: *IEEE Transactions on Audio and Electroacoustics* 15.2 (1967), pp. 70–73. DOI: 10.1109/TAU.1967.1161901 (cited on page 39).

[210] S. Wernitz, E. Chatzi, B. Hofmeister, M. Wolniak, W. Shen, and R. Rolfes. "On noise covariance estimation for Kalman filter-based damage localization." In: *Mechanical Systems and Signal Processing* 170 (May 2022), p. 108808. DOI: 10.1016/j.ymssp.2022.108808 (cited on pages 13, 58, 67, 70, 73, 74, 87, 88, 92, 102–104).

[211] S. Wernitz, B. Hofmeister, C. Jonscher, T. Grießmann, and R. Rolfes. "A New Open-Database Benchmark Structure for Vibration-Based Structural Health Monitoring." In: (2022). DOI: 10.13140/RG.2.2.26051.48163 (cited on pages 89, 137–141, 143, 150).

[212] S. Wernitz, D. Pache, T. Grießmann, and R Rolfes. "Performance of an H-infinity estimation based damage localization approach in the context of automated Structural Health Monitoring." In: *Proceedings of the 9th European Workshop on Structural Health Monitoring (EWSHM 2018)*. July 2018 (cited on pages 13, 74).

[213] S. Wernitz, D. Pache, T. Grießmann, and R. Rolfes. "Damage Localization with SP2E Under Changing Conditions." In: *Structural Health Monitoring 2019*. DEStech Publications, Inc., Nov. 2019. DOI: 10.12783/shm2019/32505 (cited on pages 8, 13, 74, 80, 87, 108, 115).

[214] R. L. Williams II and D. A. Lawrence. *Linear State-Space Control Systems*. New York: John Wiley & Sons, 2007 (cited on pages 23, 25, 26, 93).

[215] K. Worden and J. M. Dulieu-Barton. "An Overview of Intelligent Fault Detection in Systems and Structures." In: *Structural Health Monitoring* 3.1 (Mar. 2004), pp. 85–98. DOI: 10.1177/1475921704041866 (cited on pages 2, 11, 14).

[216] K. Worden, H. Sohn, and C. Farrar. "Novelty detection in A changing environment: Regression and interpolation approaches." In: *Journal of Sound and Vibration* 258.4 (Dec. 2002), pp. 741–761. DOI: 10.1006/jsvi.2002.5148 (cited on page 9).

[217] K. Worden, T. Baldacchino, J. Rowson, and E. J. Cross. "Some Recent Developments in SHM Based on Nonstationary Time Series Analysis." In: *Proceedings of the IEEE* 104.8 (Aug. 2016), pp. 1589–1603. DOI: 10.1109/jproc.2016.2573596 (cited on page 9).

[218] A.-M. Yan, G. Kerschen, P. D. Boe, and J.-C. Golinval. "Structural damage diagnosis under varying environmental conditions—Part I: A linear analysis." In: *Mechanical Systems and Signal Processing* 19.4 (July 2005), pp. 847–864. DOI: 10.1016/j.ymssp.2004.12.002 (cited on pages 8, 12).

[219] A.-M. Yan, G. Kerschen, P. D. Boe, and J.-C. Golinval. "Structural damage diagnosis under varying environmental conditions—part II: local PCA for non-linear cases." In: *Mechanical Systems and Signal Processing* 19.4 (July 2005), pp. 865–880. DOI: 10.1016/j.ymssp.2004.12.003 (cited on pages 7, 8).

[220] A.-M. Yan, P. D. Boe, and J.-C. Golinval. "Structural Damage Diagnosis by Kalman Model Based on Stochastic Subspace Identification." In: *Structural Health Monitoring* 3.2 (2004), pp. 103–119. DOI: 10.1177/1475921704042545 (cited on page 13).

[221] A. Yan and J.-C. Golinval. "Structural damage localization by combining flexibility and stiffness methods." In: *Engineering Structures* 27.12 (Oct. 2005), pp. 1752–1761. DOI: 10.1016/j.engstruct.2005.04.017 (cited on page 12).

[222] M. A. Zagrobelny and J. B. Rawlings. "Practical improvements to autocovariance least-squares." In: *AIChE Journal* 61.6 (2015), pp. 1840–1855. DOI: 10.1002/aic.14771 (cited on page 88).

[223] H. Zeiger and A. McEwen. "Approximate linear realizations of given dimension via Ho's algorithm." In: *IEEE Transactions on Automatic Control* 19.2 (1974), pp. 153–153. DOI: 10.1109/TAC.1974.1100525 (cited on page 42).

[224] Q. Zhang. "LPV System Local Model Interpolation Based on Combined Model Reduction." In: 51.15 (2018), pp. 1104–1109. DOI: 10.1016/j.ifacol.2018.09.046 (cited on page 115).

[225] Q. Zhang and L. Ljung. "LPV System Common State Basis Estimation from Independent Local LTI Models." In: 48.28 (2015), pp. 190–195. DOI: 10.1016/j.ifacol.2015.12.123 (cited on page 115).

[226] Q. Zhang and L. Ljung. "From structurally independent local LTI models to LPV model." In: 84 (Oct. 2017), pp. 232–235. DOI: 10.1016/j.automatica.2017.06.006 (cited on page 115).

[227] Q. Zhang, L. Ljung, and R. Pintelon. "On Local LTI Model Coherence for LPV Interpolation." In: 65.8 (Aug. 2020), pp. 3671–3676. DOI: 10.1109/tac.2019.2948898 (cited on page 115).

[228] S. Zhang, T. J. Rogers, and E. J. Cross. "Gaussian Process Based Grey-Box Modelling for SHM of Structures Under Fluctuating Environmental Conditions." In: *Lecture Notes in Civil Engineering*. Springer International Publishing, 2021, pp. 55–66. DOI: 10.1007/978-3-030-64908-1_6 (cited on page 5).

[229] Z. Zhang and A. Kusiak. "Monitoring Wind Turbine Vibration Based on SCADA Data." In: *Journal of Solar Energy Engineering* 134.2 (Feb. 2012). DOI: 10.1115/1.4005753 (cited on page 9).

[230] K. Zhou, J. C. Doyle, and K. Glover. *Robust and Optimal Control*. London: Prentice Hall, 1996 (cited on pages 29, 47–49, 51).

[231] S.-D. Zhou, W. Heylen, P. Sas, and L. Liu. "Parametric modal identification of time-varying structures and the validation approach of modal parameters." In: *Mechanical Systems and Signal Processing* 47.1-2 (Aug. 2014), pp. 94–119. DOI: 10.1016/j.ymssp.2013.07.021 (cited on page 7).

[232] K. Zolna, P. B. Dao, W. J. Staszewski, and T. Barszcz. "Nonlinear Cointegration Approach for Condition Monitoring of Wind Turbines." In: *Mathematical Problems in Engineering* 2015 (2015), pp. 1–11. DOI: 10.1155/2015/978156 (cited on page 9).

[233] K. Zolna, P. B. Dao, W. J. Staszewski, and T. Barszcz. "Towards homoscedastic nonlinear cointegration for structural health monitoring." In: *Mechanical Systems and Signal*

Processing 75 (June 2016), pp. 94–108. DOI: 10.1016/j.ymssp.2015.12.014 (cited on page 9).

MITTEILUNGEN DES INSTITUTS FÜR STATIK UND DYNAMIK DER LEIBNIZ UNIVERSITÄT HANNOVER

1	R. Rolfes/ C. Hühne	Eröffnungskolloquium (Tagungsband)	2005
2	H. Rothert/ M. Kaliske/ L. Nasdala	Entwicklung von Materialmodellen zur Alterung von Elastomerwerkstoffen unter besonderer Berücksichtigung des Sauerstoffeinflusses (DFG-Abschlußbericht)	2005
3	L. Nasdala	Simulation von Materialinelastizitäten bei Nano-, Mikro- und Makrostrukturen – Stabilitätsprobleme, Schädigungs- und Alterungsprozesse bei Kohlenstoffnanoröhren und Elastomerwerkstoffen (Habilitationsschrift)	2005
4	C. Hühne	Robuster Entwurf beulgefährdeter, unversteifter Kreiszylinderschalen aus Faserverbundwerkstoff (Dissertationsschrift)	2006
5	L. Nasdala/ K.-U. Schröder	Finite Element Applications in Structural Analysis (Skript zur Hörsaalübung)	2006
6		Klausuraufgabensammlung, 4. Auflage	2007
7	R. Rolfes/ W.-J. Gerasch/ D. Rotert	Vorlesung Tragwerksdynamik	2007
8	K.-H. Elmer/ K. Betke/ Th. Neumann	Standardverfahren zur Ermittlung und Bewertung der Belastung der Meeresumwelt durch die Schallimmission von Offshore-Windenergieanlagen (Abschlussbericht zum BMU-Forschungsvorhaben)	2007
9	K.-U. Schröder	Zur nichtlinearen Berechnung von Stahlbeton- und Verbundbauteilen (Dissertationsschrift)	2007
10	G. Ernst	Multiscale Analysis of Textile Composites – Stiffness and Strength (Dissertationsschrift)	2008
11	G. Haake	Systemidentifikation mit Autoregressiven Modellen und Validierung numerischer Strukturmodelle bei Offshore-Windenergieanlagen (Dissertationsschrift)	2010
12	T. Grießmann	Dynamisches Tragverhalten von Stahlbetonbiegebalken im Experiment und in der Simulation (Dissertationsschrift)	2011
13	S. Zerbst	Global Approach for Early Damage Detection on Rotor Blades of Wind Energy Converters (Dissertationsschrift)	2011

14	N. Wieczorek	Semiaktive Schwingungsdämpfung leichter Fußgängerbrückenkonstruktionen (Dissertationsschrift)	2011
15	B. Kriegesmann	Probabilistic Design of Thin-Walled Fiber Composite Structures (Dissertationsschrift)	2012
16	J. Reetz	Schadensdiagnose an Tragstrukturen von Windenergieanlagen mit der Multiparameter-Eigenwertproblem-Methode (Dissertationsschrift)	2012
17	R. Rolfes/ D. Rotert	Vorlesung Baustatik	2012
18	R. Rolfes/ D. Rotert	Vorlesung Stabtragwerke	2012
19	H. Krüger	Ein physikalisch basiertes Ermüdungsschädigungsmodell zur Degradationsberechnung von Faser-Kunststoff-Verbunden (Dissertationsschrift)	2012
20	S. Czichon	Multi scale Failure Analysis of Fibre Reinforced Polymers with production induced Porosity Defects (Dissertationsschrift)	2013
21	T. Pahn	Inverse Load Calculation for Offshore Wind Turbines (Dissertationsschrift)	2013
22	M. Fricke/ B. Neddermann/ A. Lübben/ J. Gabriel	Realistische Hydroschallszenarien auf der Basis von Prognosemodellen und Monitoring für den Bau von Offshore-Windparks in der deutschen Nordsee (''HyproWind'') (Abschlussbericht zum BMU-Forschungsvorhaben)	2014
23	M. Vogler	Anisotropic Material Models for Fiber Reinforced Polymers (Dissertationsschrift)	2014
24	M. Fricke	Ein physikalisch basiertes Gesamtmodell für hydroakustische Immissionsprognosen bei Offshore-Pfahlrammungen (Dissertationsschrift)	2015
25	M. Häckell	A holistic evaluation concept for long-term structural health monitoring (Dissertationsschrift)	2015
26	J. Rustemeier	Optimierung von Blasenschleiern zur Minderung von Unterwasser-Rammschall (Dissertationsschrift)	2016
27	S. Hühne	A two-way loose coupling procedure for buckling and damage analysis of composite structures (Dissertationsschrift)	2016
28	A. Meurer	Filtering Geometric Imperfection Patterns for Analysis and Design of Composite Shell Structures (Dissertationsschrift)	2017
29	A. Dean	Material Modeling of Short Fiber Reinforced Polymeric Composites: Theory, Numerical Aspects, and Applications (Dissertationsschrift)	2017

30	M. Bishara	Compressive Failure of Polymer Composites Including Fiber Kinking and Interaction of Failure Mechanisms (Dissertationsschrift)	2017
31	K. Schröder	Advanced Model Updating Strategies for Structural Dynamic Systems (Dissertationsschrift)	2018
32	S. Tsiapoki	Transmissibility-Based Monitoring and Combination of Damage Detection Decisions within a Holistic Structural Health Monitoring Framework (Dissertationsschrift)	2018
33	S. R. Nabavi	Failure analysis of polycrystalline silicon-based photovoltaic modules considering the effects of residual stresses and mechanical loading (Dissertationsschrift)	2018
34	S. Scheffler	Ein neuer Modellierungsansatz zur systematischen numerischen Untersuchung des Versagensverhaltens von Verbindungen in FVK (Dissertationsschrift)	2018
35	J. Häfele	A numerically efficient and holistic approach to design optimization of offshore wind turbine jacket substructures (Dissertationsschrift)	2019
36	C. Hübler	Efficient probabilistic analysis of offshore wind turbines based on time-domain simulations (Dissertationsschrift)	2019
37	M. Akterskaia	Global-local progressive failure analysis of composite panels including skin-stringer debonding and intralaminar damage (Dissertationsschrift)	2019
38	C. Gebhardt	Robust computational procedures for the nonlinear dynamic analysis of beam and shell structures (Habilitationsschrift)	2020
39	A. Haldar	Multistable morphing structures using variable stiffness laminates (Dissertationsschrift)	2020
40	R. Unger	Multi-scale constitutive modelling of nanoparticle/epoxy nanocomposites: Molecular simulation-based methods and experimental validation (Dissertationsschrift)	2020
41	J. Fankhänel	A Multi-Scale Framework for Nanocomposites including Interphase and Agglomeration Effects (Dissertationsschrift)	2020
42	N. Penner	Monitoring ambient angeregter baudynamischer Systeme durch mehrschichtige Perzeptren (Dissertationsschrift)	2021
43	C. Gerendt	A finite element-based continuum damage model for mechanical joints in fiber metal laminates under static and fatigue loading: Theory and experimental validation (Dissertationsschrift)	2022
44	M. Brod	Damage prediction of unidirectional fiber composites under cyclic loading with different amplitudes (Dissertationsschrift)	2022

45	R. Berger	Multi-Objective Structural Optimization of Repairs of Blisk Blades (Dissertationsschrift)	2022
46	G. Balokas	Metamodel-based uncertainty quantification for the mechanical behavior of braided composites (Dissertationsschrift)	2022
47	S. Wernitz	Damage Localization in Data-Driven Vibration-Based Structural Health Monitoring Using Linear Quadratic Estimation Theory (Dissertationsschrift)	2022